Measurement of Properties of the Lunar Surface Using the Diviner Lunar Radiometer Experiment on the NASA Lunar Reconnaissance Orbiter

Ian Richard Thomas

Lincoln College

Atmospheric, Oceanic and Planetary Physics

University of Oxford

Trinity Term 2011

Thesis submitted for the degree of Doctor of Philosophy

Abstract

Measurement of Properties of the Lunar Surface Using the Diviner Lunar Radiometer Experiment on the NASA Lunar Reconnaissance Orbiter

Ian Richard Thomas

Lincoln College
Atmospheric, Oceanic and Planetary Physics
Thesis submitted for the degree of Doctor of Philosophy in the University of Oxford.
Trinity Term, 2011

The Diviner Lunar Radiometer is a nine-channel radiometer on board the Lunar Reconnaissance Orbiter, launched in June 2009 and currently orbiting the Moon. Diviner is the first orbiting multi-spectral instrument to observe the lunar surface in the mid- and far-infrared, therefore this thesis details the first steps towards utilising observations in this new spectral region.

The author, as part of the Diviner instrument team, contributed to the pre-launch testing and calibration of Diviner. Specifically, the transmission profiles of the B2 and B3 filters, which could not be measured after integration into the instrument due to their long wavelength passbands, were determined. Further investigations of the far-infrared mesh filters were also conducted, as the spectral responses of similar mesh filters were found to have broadened after integration into the Mars Climate Sounder instrument, the pre-cursor instrument to Diviner. To test if this would occur in Diviner also, a new setup was made to approximately re-create the instruments' optical layout. No such spectral broadening was measured in the B1, B2 or B3 filters. The linearities of Diviner's detectors were also confirmed through analysis of the pre-flight calibration data.

Laboratory emission spectra taken under ambient conditions differ from those taken in a lunar environment, which induces a temperature gradient in soil and mineral samples. Due to a lack of spectra measured under such conditions, which are directly comparable to Diviner's measurements, a new chamber for performing high-resolution emission measurements in a simulated lunar environment was built and calibrated. This setup induces a temperature gradient in each sample by heating it from below while it is surrounded by a cooled radiation shield, all enclosed in a very low pressure vacuum chamber. Lunar analogue minerals have been measured, first in reflectance, and then in simulated lunar conditions, forming the basis of a new lunar spectral library.

The uses of the mid- and far-infrared have been described herein, utilising calibrated Diviner observations to: [1] map the temperatures of the lunar poles; [2] investigate regions containing higher than average abundances of rocks; and [3] determine the composition of regions of the lunar surface by combining observations with the new spectral library made during this project.

Acknowledgements

The Diviner instrument owes its success to an incredible effort by many people; many more than can be personally named here. I would like to begin by thanking everyone involved, from mission conception, through construction, calibration, spacecraft integration and launch, to those working on post-launch operations and data analysis.

First and foremost, I need to thank my primary supervisor, Dr. Neil Bowles, and my 1st and 2nd year supervisor, Dr. Simon Calcutt, for their guidance and assistance over the years, without whom none of this would have been possible.

Many others in AOPP have also helped me invaluably, especially Jon Temple and Andy Clack in the Electronics Workshop, and Jason Perry and Duncan Constable in the Mechanical Workshop. I must also thank: Dr. Bob Watkins for his knowledge, assistance (and occasional lending) of vacuum, cryogenic and electronic components; Dr. Adam Camilletti for his expertise in everything hardware-related; Dr. Con Tsang and Dr. Remco De Kok for their amazing knowledge of IDL; Ramin Lolachi for his help in the construction of the filter measurement jig; and everyone else who has helped to keep the department running smoothly behind the scenes.

Outside of AOPP, I must also thank all the Clarendon workshop staff - especially Rob Harris - and everyone who I've had the opportunity to work with at home and abroad, most notably the Diviner Instrument and Science Teams. In particular, I would like to thank Dr. Marc Foote and Dr. Tim Schofield from the former and Dr. Ben Greenhagen, Prof. David Paige, Kerri Donaldson-Hanna and Prof. Tim Glotch from the latter. I am very grateful to Dr. Paul Turner from Brüker Optics, Dr. Jeff Johnson of the USGS, and Dr. Alessandro Maturilli and Dr. Jörn Helbert of DLR for all their help.

Many thanks also to my D.Phil. examiners, Prof. Fred Taylor and Dr. Ian Crawford, and to the Science and Technology Facilities Council for funding this project.

...And last but definitely not least: to my mum, Carol, my dad, Tony, my sister, Heather, my girlfriend, Margherita, and the rest of my family and friends for keeping me sane, whether back home in Huddersfield, in Durham or during the past four years in Oxford – thanks for everything!

Commonly Used Abbreviations

Below is a list of abbreviations seen in the text; some with a small description. All are defined throughout the thesis, but are also listed here for quick reference.

ALSEP	Apollo Lunar Surface Experiments Package
AO	Announcement of Opportunity
AOPP	Atmospheric, Oceanic and Planetary Physics. A sub-department of the Department of Physics at Oxford University
ASTER	Advanced Spaceborne Thermal Emission and Reflection Radiometer
ASU	Arizona State University
BB	Blackbody
CAD	Computer Aided Design
CAM	Computer Aided Manufacturing
CF	Christiansen Feature
CMM	Coordinate Measuring Machine
DLaTGS	Deuterated L-alanine doped Triglycine Sulphate. A type of infrared detector
DLRE	Diviner Lunar Radiometer Experiment. The full name of the Diviner Instrument
DLR	Deutsches Zentrum für Luft- und Raumfahrt
DREB	Diviner Remote Electronics Box
ESMD	Exploration Systems Mission Directorate
FIR	Far-Infrared
FIR DTGS	Far-Infrared Deuterated Triglycine Sulphate. A type of far-infrared detector
FOV	Field Of View
FFT	Fast Fourier Transform
FPA/FPB	Focal Plane A/B
FTIR	Fourier Transform Infrared

FWHM	Full Width at Half Maximum
HITRAN	High Resolution Transmission Molecular Absorption Database
ISAMS	Improved Stratospheric and Mesospheric Sounder
JPL	Jet Propulsion Laboratory. A NASA laboratory in Pasadena, California, USA
KBr	Potassium Bromide. A material transparent in the mid-infrared, used as reflectance standards, windows and beamsplitters
KCl	Potassium Chloride. A material transparent in the visible, near- and mid-infrared
KREEP	Potassium, Rare Earth Elements and Phosphorus
LALT	Laser Altimeter. An instrument on board the SELENE/Kaguya lunar satellite
LCROSS	Lunar Crater Observation and Sensing Satellite
LN_2	Liquid Nitrogen
LOLA	Lunar Orbiter Laser Altimeter
LRO	Lunar Reconnaissance Orbiter
MCS	Mars Climate Sounder. A radiometer on Mars Reconnaissance Orbiter
MCT	Mercury Cadmium Telluride. A type of infrared detector
MI	Multiband Imager. An instrument on board the SELENE/Kaguya lunar satellite
MIR	Mid-Infrared
NIR	Near-Infrared
NPL	National Physical Laboratory
OAP	Off-Axis Paraboloid
OPUS	Optical User Software. The software used to control Brüker Spectrometers
PAN	Pure Anorthosite

PMIRR	Pressure Modulator Infrared Radiometer. A pre-cursor to Mars Climate Sounder, flown on both Mars Observer (PMIRR-1) and Mars Climate Orbiter (PMIRR-2)
PTFE	Polytetrafluoroethylene
PRT	Platinum Resistance Thermometer. A type of temperature sensor
PSR	Permanently Shadowed Region
SELENE	Selenological and Engineering Explorer. Also known as 'Kaguya'
SLE	Simulated Lunar Environment
SMD	Science Mission Directorate
SNR	Signal-to-Noise Ratio
SOM	Supporting Online Material (of a journal article)
SPICE	Spacecraft, Planet, Instrument, C-matrix and Events. Software describing the location, time, pointing direction etc. of the spacecraft and planets
SSTL	Surrey Satellite Technology Ltd.
TIR	Thermal Infrared
UCLA	University of California, Los Angeles
UV	Ultraviolet

Contents

1 Introduction

1.1 Pre-Apollo Knowledge of the Moon

1.1.1 Historical Lunar Observations

Until the middle of the 20th century, our knowledge of the Moon was extremely limited. While appearing to be composed of lighter and darker materials, to the naked eye our only natural satellite appears smooth and circular, a belief that existed until the invention of the telescope in the Middle Ages. After Galileo's initial telescope observations in 1609, more was gradually discovered about the Moon in the following centuries, and by the 20th century much had been ascertained.

As telescope technology improved, it became clear that the lunar surface was covered in craters, mountains and ridges, many of which were named and had their heights determined by observations from Earth. Laboratory experiments and observations concluded that the craters were not volcanic in origin, but were instead formed by impacts [Wilhelms, 1993]. By examining photographs of the surface, scientists began to piece together the relative history of such craters, for example, by determining which impacts covered older craters with their ejecta, and which newer craters then formed within these regions [Wilhelms, 1993]. Theories regarding the origins of the compositionally-distinct regions of the Moon were also made, with Baldwin [Wilhelms, 1993] concluding that the optically dark areas were actually lava-filled impact basins. These and other discoveries allowed scientists to begin to understand the geology and evolutionary history of the Moon, but as observations were only possible from the Earth's surface, a significant proportion of the Moon could never be seen: due to tidal locking, the same side of the Moon always points towards the Earth, therefore only 59% [Burke, 2011] of the lunar surface can ever be viewed. Also, the Earth's atmosphere allows measurements to be made only in certain spectral regions, and

even the largest available ground telescopes have limited spatial resolution when viewing an object as distant as the Moon. For example, the largest diameter mid-infrared (MIR) telescope, the 3.8m UKIRT in Hawaii has a lunar surface spatial resolution of ~1km when measuring at 8μm, assuming diffraction-limited operation.

1.1.2 Precursor Missions

The next milestone was achieved when further technological advances enabled the use of remote sensing satellites; their use accelerated when the Moon became a target for human exploration and so required more detailed reconnaissance. The objective of the unmanned NASA Lunar Orbiter Program was to photograph the Moon to determine possible landing sites for crewed landers, which between its five satellites mapped 99% of the surface at 60m or better resolution [Angelo, 2006]. Meanwhile, the Soviet Union's Luna Program consisted of fifteen satellites destined for lunar orbit or impact. Despite many initial failures, there were some notable successes in the advancement of remote sensing. Luna 10, an orbiter launched in 1966, contained several scientific instruments aside from photographic cameras, such as a gamma-ray spectrometer, magnetometer, meteorite detector, photon counter and infrared detector [Johnson, 1979]. The success of the remote sensing programs then led to the first samples being returned from the Moon.

1.2 The NASA Apollo Missions to the Moon: 1969-1972

1.2.1 Lunar Sample Return

The Apollo 11 mission brought back to Earth 22kg of lunar rock in July 1969, which was catalogued and stored at the Johnson Space Centre in Houston, Texas, USA. Each subsequent mission brought back increasing amounts of Moon rock, culminating in 111kg

by Apollo 17 in December 1972. Three of the Soviet unmanned Luna programmes also returned 326g of samples, making a total of 382kg between the two superpowers [Heiken et al., 1991]. Some samples were made available to scientists for analysis, which allowed new insights to be made not only into the history of the Moon, but also the Earth and the solar system.

1.2.2 Key results from Lunar Sample Analysis

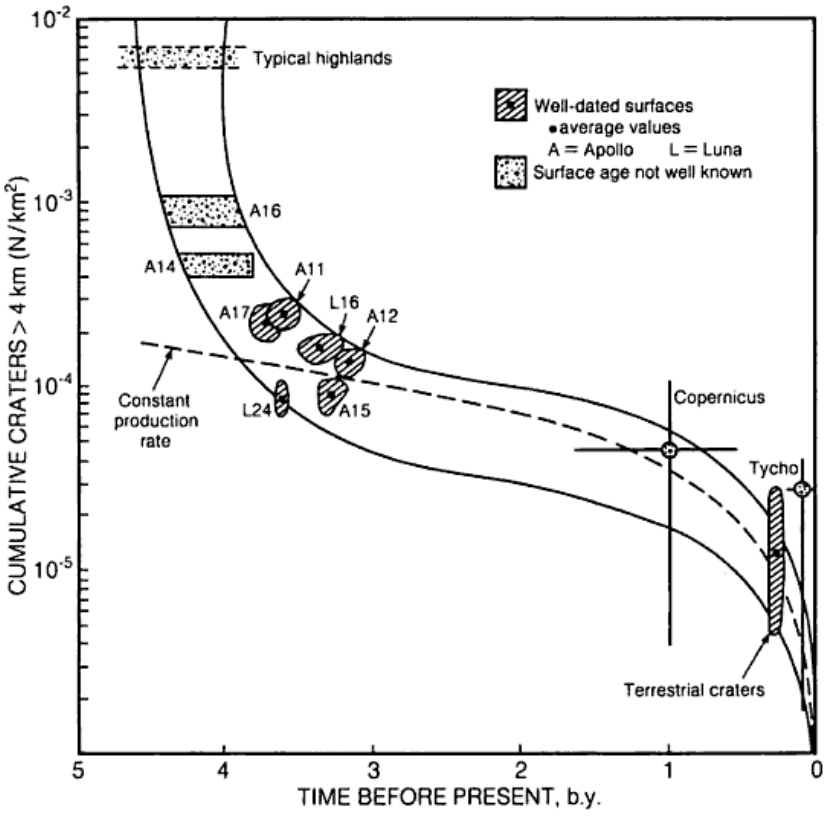

Figure 1-1: Relative ages of the Apollo and Luna landing sites, from Heiken et al. [1991]. Ages were derived from crater counts and sample dating techniques.

Analysis of these returned samples indicated that, besides unusual parts of Oceanus Procellarum (Apollo 12) and Mare Imbrium (Apollo 15), the surface is composed of rocks and minerals also found on Earth, with similar isotope ratios suggesting a common origin of both bodies. Further studies were able to quantify the differences between the distinct

regions of the Moon, confirming the theories of Baldwin (Section 1.1.1). Radioactive isotope dating showed that the rocks from the areas of higher albedo, known as the highlands, were older than the lower albedo maria [Heiken et al., 1991] (Figure 1-1), around the age of the oldest known Earth rocks [e.g. Todd, 2011]. Methods such as X-ray fluorescence [e.g. Bansal et al., 1972], atomic absorption and neutron spectroscopy [e.g. Maxwell and Wiik, 1971] revealed distinct compositional differences between the two. The lunar highlands are composed primarily of anorthosite, a rock composed mainly of plagioclase feldspar, a mineral containing sodium, calcium, aluminium, silicon and oxygen [Heiken et al., 1991]. Conversely, the maria are composed of basaltic lava flows, of pyroxenes predominantly containing iron and magnesium in addition to sodium, calcium, aluminium, silicon and oxygen [Heiken et al., 1991].

The extremely old age of the surface (Figure 1-1) combined with the lack of surface-altering processes such as erosion, weathering, or plate tectonics, has allowed the Moon to retain a record of the history of the solar system. Bombardment by meteorites, comets and asteroids, particularly in the early Solar system, and by micrometeorites and radiation, has gradually altered the surface over time, as evidenced in the returned samples.

1.2.3 Rock Classification

The composition of returned samples were found to be structurally complex, as the different types had been altered and mixed by processes over billions of years, but it was possible to make several generalisations. Lunar materials were classified into three generations, depending on their age and amount of time exposed to incoming particles and radiation from space [Jolliff et al. (eds.), 2006]:

1. First Generation: These are old plutonic and volcanic igneous rocks unaffected by impacts, and are formed from molten material. Plutonic (or intrusive) refers to material that solidified beneath the lunar surface, and volcanic (or extrusive) refers to material that solidified on the surface.

2. Second Generation: These are materials formed from bombardment of the surface, such as recrystallised rocks and impact breccias, which are composite rocks formed from all other rock types through crushing, mixing, and sintering during meteorite impacts [Todd, 2011].

3. Third Generation: These are the youngest class, and are formed from repeated micrometeorite bombardment of the surface. The bombardment breaks down rocks and rock fragments into powders that are then overturned and transported across the surface by further impacts, a process known as impact gardening. This creates a top layer of fine-grained unconsolidated surface material, known as the regolith. This regolith covers almost all the surface, except for bedrock exposures, to an average depth of a few metres. Small impacts can also redistribute the regolith laterally across the surface without affecting the composition, changing the location of expected rock types and obscuring other minerals. Regolith breccias are examples of third generation materials, which are impact breccias that have been broken down and transported in this way. Agglutinates, commonly found in the Apollo soils, are fragments of regolith that have been fused with glass created by the heat of impacts, whose abundance in soils increases with exposure age [Jolliff et al. (eds.), 2006].

1.2.4 Geological History

By piecing all this information together, from sample analyses, photographs and observations from Earth, a timeline of the Moon's history was able to be made, from formation to the present day.

1.2.4.1 Early Formation: The Giant Impact Hypothesis

From radioactive dating it was discovered that the Moon formed approximately 4.5 Gyr ago. The large degree of commonality found between lunar and Earth rocks, calculations by Hartmann & Davis [1975] and numerical simulations by Stevenson [1987] favour the theory that the Moon was formed when a Mars-sized planet collided with the Earth. The ejected material then coalesced into a molten spherical body orbiting the Earth, which then began to cool.

1.2.4.2 The Magma Ocean Hypothesis

The diagram originally presented here cannot be made freely available via ORA due to copyright restrictions. See the Nash et al. [1993] reference for the original image.

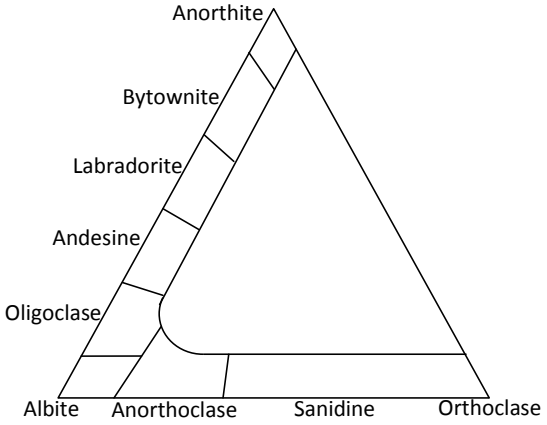

Figure 1-2: Lunar Ternary diagrams. Characteristic lunar rocks can be represented by a plagioclase-pyroxene-olivine ternary (left; from Nash et al. [1993]), while iron-free plagioclase and alkali feldspars are shown on an orthoclase-anorthite-albite diagram (right; e.g. Gupta, [1998]).

The lunar highlands, composed of less-dense, older anorthositic rocks could have been formed by the crystallisation of plagioclase in magma [Wood et al., 1970]. Their existence, therefore, above denser mafic (magnesium and ferric i.e. iron-containing) rocks provides crucial evidence for the existence of a magma ocean on the lunar surface. This, known as the 'magma ocean hypothesis', states that a magma ocean at least 100 - 300 km deep [Solomon & Longhi, 1977] covered most of the early Moon's surface, which crystallised and then sank or floated depending on the constituent's relative densities [Warren, 1985]. As such, the denser mafic pyroxenes and olivines crystallised first and sank, while the anorthosites crystallised later and floated, forming a crust approximately 20–120 km thick [e.g. Wood et al., 1970; Neumann et al., 1996]. The order of crystallisation is determined by Bowen's reaction series [Wicander et al., 2005], where the minerals are ordered by their relative crystallisation temperatures. For example, the minerals that comprise plagioclase are described as follows (Figure 1-2), with the former crystallising at the highest temperature:

- Anorthite (90-100% $CaAl_2Si_2O_8$, 0-10% $NaAlSi_3O_8$)
- Bytownite (70-90% $CaAl_2Si_2O_8$, 30-10% $NaAlSi_3O_8$)
- Labradorite (50-70% $CaAl_2Si_2O_8$, 50-30% $NaAlSi_3O_8$)
- Andesine (30-50% $CaAl_2Si_2O_8$, 50-70% $NaAlSi_3O_8$)
- Oligoclase (10-30% $CaAl_2Si_2O_8$, 70-90% $NaAlSi_3O_8$)
- Albite (0-10% $CaAl_2Si_2O_8$, 90-100% $NaAlSi_3O_8$)

Bowen's reaction series also states how other non-anorthositic minerals are ordered. For example, beginning with the highest crystallisation temperatures, there are:

- Olivines (e.g. Forsterite, Mg_2SiO_4; Fayalite, Fe_2SiO_4)

- Pyroxenes (e.g. Augite, $(Ca,Na)(Mg,Fe,Al)(Si,Al)_2O_6$; Diopside, $MgCaSi_2O_6$; Enstatite, $MgSiO_3$)
- Orthoclase ($KAlSi_3O_8$)
- Quartz (SiO_2)

While plagioclase, olivines and pyroxenes were commonly found [Heiken et al., 1991] in the lunar samples, minerals with relatively low crystallisation temperatures, such as orthoclase, microcline (a polymorph of orthoclase, i.e. a mineral with the same chemical composition but different atomic arrangement) and quartz were not, but were speculated to exist.

1.2.4.3 Lunar Maria

After the anorthositic crust had solidified and the late heavy bombardment period had ended approximately 4 Gyr ago, the lunar maria began to form. Magma erupted from the interior of the Moon covering mainly low-lying impact basins with basalt, a rock formed from the rapid cooling of lava [Jolliff et al. (eds.), 2006]. This basalt originated from below the crust, and therefore is predominantly composed of heavier, metal-containing mafic materials, such as pyroxene and ilmenite ($FeTiO_3$). These eruptions produced the regions of lower albedo that are visible from the Earth, but are not uniformly distributed on the lunar surface. Nearly all the maria are located on the lunar nearside (the side which currently always points towards the Earth) and are generally distributed away from the poles, even though the oldest and deepest observable impact basin [Jolliff et al. (eds.), 2006], the South Pole-Aitken Basin, is found on the lunar farside.

1.2.4.4 Younger Craters and Space Weathering

Since the maria formed, many other impacts have occurred. Large craters such as Copernicus, Aristarchus, Tycho and Jackson craters, are believed to have formed within approximately the last 1 Gyr [Jolliff et al. (eds.), 2006; Hartmann, 1968] from impacts by meteors, asteroids or comets. The lunar surface is gradually altered over time by a process known as space weathering. Many small rock particles, known as micrometeorites, cosmic rays and particles from the solar wind hit the surface of the Moon continually causing changes to the mineral structure of the upper surface layers (Section 1.2.3). The most mature, third generation rocks have been broken down by successive bombardments, transported around the surface, mixed together with other rock types and then reformed into new material. After billions of years, these processes have gradually changed the lunar surface into the form that exists today, hence the mixture of rock and mineral types that were found in the returned lunar samples.

1.2.5 Detection of Water in Lunar Samples

When analysed on Earth, the returned samples were found to contain small (12 - 20 μmole/g) traces of water. As the regions around the landing sites were believed to be completely without water, these findings were assumed to be due to contamination from the Earth's atmosphere [Epstein & Taylor, 1973]. However, new analyses and remote sensing data have now overturned this conclusion (Section 2.3.1.5).

All successful Apollo landings after Apollo 11 placed a group of scientific instruments on the surface known as the Apollo Lunar Surface Experiments Packages (ALSEP) [Lauderdale & Eichelman, 1974]. These ALSEPs contained Suprathermal Ion Detector Experiment (SIDE) mass spectrometers, which may have detected water vapour *in situ* during the lunar night-time. Detection of energetic ions during daylight would suggest that

the ions were part of the solar wind, but the existence of such particles at night could not be definitively explained [Neugebauer, 1972].

As the Apollo Program progressed, the missions became increasingly scientific. In addition to the ALSEP packages, remote sensing instruments were included on the orbiting command modules, with the first infrared mapping instrument, the Infrared Scanning Radiometer (ISR) on Apollo 17 [Mendell, 1976]. The crew of the Apollo 17 craft was the first and only mission to contain a geologist.

1.3 Unanswered Questions

While the sample return missions were invaluable to understanding the geology and history of the Moon, the limited scope of landing sites, times of day, instruments and limited mass of returned samples meant that many questions were left unanswered when the Apollo and Luna Programs ended.

1.3.1 Apollo's Limited Regional Landing sites

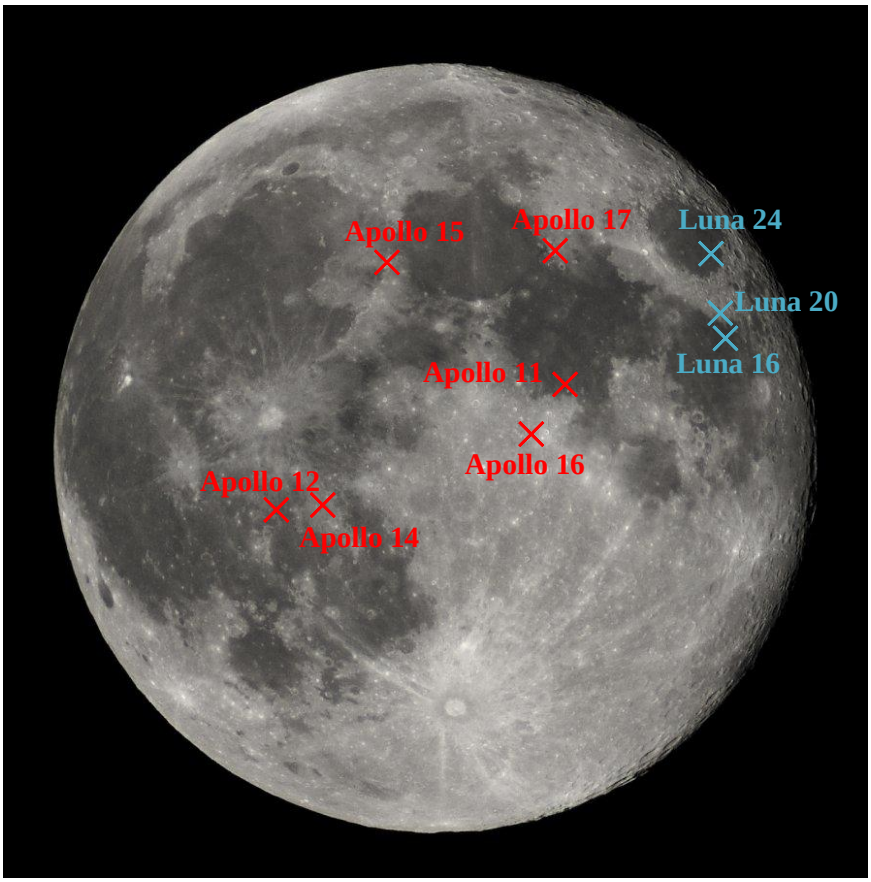

Figure 1-3: The lunar nearside as observed from Earth (Viatour © [2006]), with the locations of the Apollo and Luna probes overlaid by the author.

The localised nature of the landing sites was a disadvantage. The missions required flat locations containing minimal craters, for the safety of the astronauts. As no communications satellites were in orbit around the Moon, all landing sites needed to be on the lunar nearside so communication with mission control remained possible. For safety, the approach trajectory to the Moon needed to be close to equatorial so that the astronauts could slingshot themselves back to Earth using lunar gravity in case of engine failure [Compton, 1989]. Hence, all of the Apollo sites are within the equatorial region and are all located on the lunar nearside, as are most of the Luna sample return missions (Figure 1-3). No Apollo or Luna mission ever went to either of the lunar poles, or even greater than ±40° from the lunar equator.

The need to maximise safety also influenced the geological variation observed at landing sites. Landing areas were chosen based on the number of slopes and craters in an area, in addition to the previous constraints of requiring a nearside, equatorial region. Therefore, the flatter maria were preferred for landing sites over the cratered highlands, so all the missions landed within maria, except for Apollo 16 which set down in the Descartes Highlands [Jolliff et al (eds.), 2006]. The first missions were only able to explore the area directly around the lunar module, but from Apollo 15 onwards the use of a lunar roving vehicle allowed several kilometres to be traversed [Compton, 1989]. While these expanded the range of samples possible, variations were still lacking. For example, in a comparison to modern spectroscopic data taken in the 1990s, it was suggested that of all the types of mare basalts, samples of less than half were returned [Jolliff et al (eds.), 2006]. Other more-recently discovered geologically distinct regions, such as the Procellarium KREEP (Potassium , Rare Earth Elements and Phosphorus) Terrane, have never been sampled. More information regarding landing site selection can be found in Compton [1989].

1.3.2 Limited Samples

The lack of mass available for outgoing or return trips affected the equipment taken and amount of samples returned. While a lunar rover accompanied the astronauts on Apollo 15, 16 and 17, no deep drills (>3m) were taken and hence all samples were taken of material close to the surface. Even though previous large impacts had excavated material from deep and re-distributed it across the surface, many rock types remain un-sampled, while of those that have, these movements have removed much of their geological context [Jolliff et al (eds.), 2006].

1.3.3 The Hiatus in Lunar Exploration

The Apollo Program ended in 1972 and since then no astronauts have been to the Moon. Likewise, the last samples returned by the Luna Program were in 1976, and it was not until 1994, with the onset of the US Department of Defense's Clementine Mission that another mission dedicated to the Moon was launched [Williams, 2011]. This was followed by another American orbiter, Lunar Prospector, in 1998, and then a resurgence in lunar remote sensing missions in the 21st century, all of which owe much to the earlier work of the Apollo and Luna Programs.

1.4 The Use of Lunar Samples for Future Missions

These returned samples are essential to the field of remote sensing, both by providing the geological context for global observations made by remote sensing instruments and by guiding instrument design. For example: many modern instruments use the Apollo landing sites as known calibration sites for their sensors [e.g. Nozette et al., 1994; Ohtake, 2010], while laboratory analysis of samples helps instrument designers, such as in the choice of filter wavelengths [e.g. Greenhagen & Paige, 2006] or sensitivity of radioactivity detectors.

2 Previous Lunar Remote Sensing Instruments

2.1 Introduction

This chapter describes the timeline of previous projects designed to determine the properties of the Moon as precursors to measurements made by Diviner. These can be divided into two distinct types:

- Surface temperature. This constrains the regions of permanent illumination and shadow, in the search for cold traps potentially containing water (Section 2.3.2), optimum future landing site locations (Section 2.4) and allows the presence of rocks to be detected (Section 2.6), a major landing site hazard.
- Surface composition. Mapping lunar composition from orbit gathers much information regarding the formation and geological history of the Moon (Section 2.7).

Post Apollo, and after a hiatus of over twenty years, lunar exploration restarted with the launch of the Clementine spacecraft in 1994, as a joint project by the United States Department of Defence and NASA. Clementine's ability to map the Moon's surface properties on a global scale meant that the new results gained from this instrument led to an increased understanding of the Moon. This lead to a resurgence in interest in the Moon, and was followed by another satellite, NASA's Lunar Prospector, in 1998 to further map the surface and confirm some results speculated from the data returned by Clementine. This chapter describes the timeline of previous projects designed to determine the Moon's surface composition, rock abundance, and temperature, as precursors to measurements made by Diviner.

2.2 Temperature Measurements

A global temperature map of the lunar surface can address three key questions, relevant to both lunar science and human lunar exploration:

- To constrain the possible regions in which water ice can remain
- To discover regions where the surface is permanently illuminated
- To detect large-scale rocks (i.e. >1 m)

The former two applications are crucial for the establishment of a human settlement on the lunar surface[1], which would require oxygen and water for sustaining astronauts and a constant power source, while the latter is important in identifying safe landing zones for future missions.

2.3 The Search for Water-Ice and Other Trapped Volatiles

The presence of H_2O, in the form of water vapour or ice, on the Moon is dependent on two mechanisms: one to deliver the water to the Moon, and another to keep it there in the harsh vacuum environment. It is believed that the Moon has been bombarded in the past by volatile-rich meteoroids and comets, depositing their water on the surface, which could then remain trapped given the right conditions, such as in regions of low temperatures (<100K) in shadowed regions [Watson et al, 1961]. The solar wind also contributes, both creating water through the reduction of iron in the lunar regolith and destroying it through sputtering and decomposition processes [Arnold, 1979]. Watson et al. [1961] concluded that the removal rate of volatiles from the Moon is limited by their evaporation rate, and therefore sufficiently cold locations could store water-ice for billions of years, hence surface diurnal

[1]So were a key driver in the eventual design and calibration of the Diviner instrument (Section 4)

and seasonal temperature maps are essential in determining the most likely locations of water-ice.

More recent studies by Vasavada et al. [1999] found that the temperature where each metre of ice takes 1Gyr to evaporate is ~112K. They used a 3D thermal model to simulate radiation scattering within lunar polar craters, finding that parts of permanently shaded craters within thirteen degrees of the poles should be sufficiently continually cold to store water ice for billions of years. These permanently shadowed regions (PSRs) exist due to the low axial tilt of the Moon of 1.5° relative to the ecliptical plane [Burke, 2011], limiting seasonal variation and causing some crater floors near the lunar poles to never directly receive incident sunlight. The absence of convection, owing to the lack of atmosphere, and the low thermal conductivity of the lunar soils [e.g. Birkebak et al., 1970] have allowed PSRs to remain extremely cold while in close proximity to much hotter regions. As the ice accumulates in cold trap regions only gradually over billions of years but can be sublimated by higher temperatures much more quickly[2] [Vasavada et al., 1999], large concentrations of ice require such cold regions to have been consistently cold over very long timescales. Studies of the Moon's obliquity history have shown that this axial tilt may have been significantly larger in the past [Ward, 1975], so while temperature maps may be useful in locating regions likely to contain ice (and hence guide observations), the actual amount present could be limited. Described below are some previous attempts at conclusively detecting lunar water ice.

[2]E.g. the evaporation rate of water increases 1000-fold for a temperature increase of 112 K to 130 K.

2.3.1 Direct Detection of Water Ice Signatures

2.3.1.1 Clementine Bistatic Radar Experiment

The Clementine Bistatic Radar Experiment was an extra experiment performed at the end of the Clementine mission [Nozette et al., 1994]. Signals sent from the on-board transmitter were reflected off the lunar surface and received by the Deep Space Network receivers on Earth, which measured the magnitude and polarisation of the radar echoes [Nozette et al., 1996]. The results showed that the echoes from PSRs near the lunar south pole exhibited an enhancement compared to other areas of the surface periodically exposed to solar illumination, suggesting that low-loss volume scattering volatiles, such as water ice, were present in these regions of permanent shadow [Nozette et al., 1996]. This discovery was enough to warrant another mission with a more specific instrument suite, the NASA Lunar Prospector.

2.3.1.2 Lunar Prospector Neutron Spectrometer

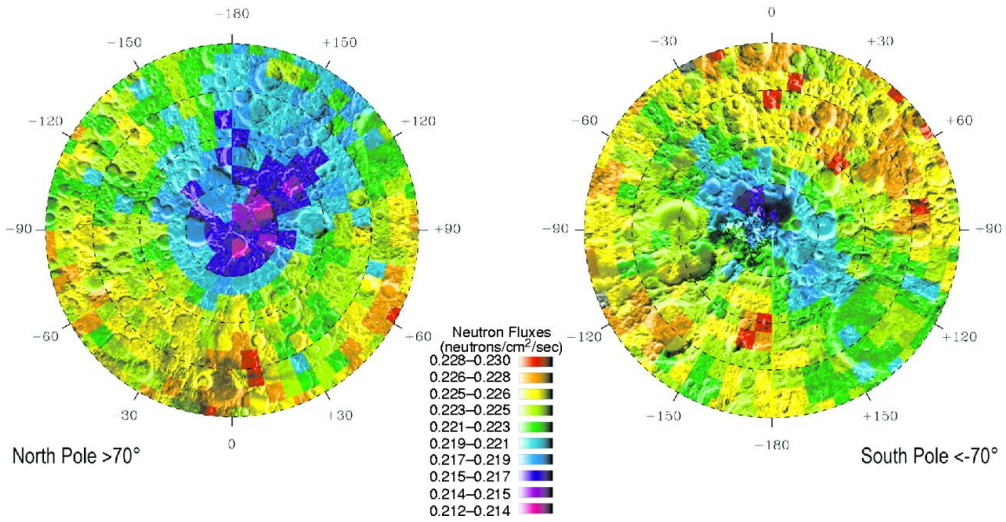

Figure 2-1: Epithermal neutron flux maps of the north and south poles from Feldman et al. [1998a] (reprinted with permission from AAAS). The reduced flux at the poles indicates increased concentrations of hydrogen. The 4° (latitudinal) resolution prevents detection of sub-crater deposits.

Another lunar remote sensing satellite, Lunar Prospector, was launched in 1998 that contained, amongst other instruments, a neutron spectrometer designed to continue the investigation into possible water-ice deposits [Feldman et al., 1998a]. Epithermal (i.e. intermediate energy) neutrons detected by this spectrometer were studied to estimate the magnitude of potential water ice deposits. Several large polar craters were again observed at the lunar south pole, together with polar plains containing many small craters at the north pole, to contain regions thought to be residing in permanent shadow. An increase in hydrogen concentration, [H] interpreted as a proxy for water ice, was observed in these craters (Figure 2-1) compared to the surrounding sunlit areas, again suggesting that the temperature (and hence rate of sublimation of water) of the lunar surface is the factor discriminating regions of enhanced [H] from those that are not. For the south pole, it was estimated that [H] = 1700±900ppm, which equates to a water concentration of [H_2O] = 1.5±0.8%, while for the north this was estimated at >10%, though this estimate is very uncertain [Feldman et al., 1998a].

2.3.1.3 Lunar Prospector Surface Impact

The Lunar Prospector mission ended when it was intentionally crashed into Shoemaker Crater, a permanently shaded crater at the lunar south pole, while Earth-based observatories monitored the crash site for evidence of water in the debris plume. No water ice was detected, but many reasons were speculated for this, including [Isbell, Morse & Rische, 1999]:

- The spacecraft missed the desired target site or hit an area of rock or dry soil
- The water molecules believed to be present only exist as hydrated minerals within rocks and the crash lacked the energy to separate this water from the minerals

- The telescopes on Earth, which have small fields of view, were not pointed correctly to observe the crash location
- The plume containing the water did not manage to rise above the crater wall or flew away from the telescopes' view.
- The target site did not contain any water, either because no water-ice exists on the Moon and the signals observed originate from hydrogen, possibly implanted by the solar wind, or because the site chosen was not representative of a typical lunar PSR.

With all these uncertainties, the question of whether or not water ice exists on the Moon could still not be answered definitively.

2.3.1.4 Arecibo Observatory Radio Telescope Radar measurements

The Arecibo Observatory Planetary Radar in Puerto Rico was used to map areas of the lunar poles visible from the Earth [Campbell et al, 2003]. Radar measurements showed that permanently shaded areas did not give rise to strong backscattering or the distinctive polarisation signatures associated with thick ice deposits. Any lunar ice present within the regions measureable by the Arecibo dish must therefore be in the form of distributed grains or thin layers, or be buried under several metres of dust, where the 70cm wavelength radar cannot probe. The radar echo from the floors of craters Hermite and Peary near the lunar north pole, and Shoemaker and Faustini near the south pole, showed no difference in radar-scattering from the lunar highlands. The floor of Shackleton crater where Clementine Bistatic radar images inferred the presence of thick ice deposits could not be viewed from the Arecibo dish, while the Lunar Prospector observations can be also be attributed to thin ice deposits, again leaving the presence of significant water-ice abundances unsubstantiated.

2.3.1.5 Detection of Hydroxyl and Water in Near Infrared Spectra

Recently, the results of three separate instruments confirmed the presence of water/hydroxyl (the -OH band) –bearing materials on the lunar surface. These instruments were:

- The Visual and Infrared Mapping Spectrometer (VIMS) on the Cassini Spacecraft (destined for Jupiter and Saturn) [Clark, 2009],
- The Near Infrared (NIR) spectrometer on the Deep Impact Spacecraft (destined for comet 103P/Hartley 2) [Sunshine et al., 2009], and
- The Moon Mineralogy Mapper (M^3) on the Chandrayaan-1 lunar orbiter [Pieters et al., 2009].

Water/hydroxyl appears as an absorption feature in the 2.8 – 3 μm region, and was widely distributed across the lunar surface, appearing strongest at higher latitudes and several fresh feldspathic craters [Pieters et al., 2009]. These results suggested water/hydroxyl is continually formed and retained in ongoing surface processes, and could provide a mechanism for increased deposition of water into permanent shadowed regions.

2.3.2 Detection of Cold Traps

Since the surface temperature is key to trapping volatile material, full diurnal and seasonal measurements of surface temperature are vital. As described previously, methods for remotely mapping water detect it indirectly by measuring either hydrogen concentrations or changes in behaviour of reflected radio waves; hence they depend on observing differences between regions of PSRs and those receiving sunlight, to discount global-scale surface property effects. To make cold temperature measurements to distinguish multiple PSRs, satellite-based infrared instruments are required. Surface temperature measurements from Earth are difficult due to the water vapour bands located in much of the far-infrared (FIR)

region [e.g. Murcray et al., 1969], a high surface resolution is required to map small regions of permanent shadow, and the entire surface needs to be observable.

Prior to Diviner only two instruments capable of determining surface brightness temperatures had made measurements of the surface from lunar orbit, the Infrared Scanning Radiometer on board the Apollo 17 Service Module and the Long Wave Infrared Camera on Clementine, neither of which could map PSR temperatures due to their limited wavelength and spatial coverage (below).

2.3.2.1 Apollo 17 Infrared Scanning Radiometer

The Infrared Scanning Radiometer (ISR) on board the Apollo 17 Command-Service Module was the first instrument to map the thermal emission of the lunar surface from orbit. It consisted of one channel, capable of measuring from 1.2 to 65μm, and used a bolometer as the detector [Mendell, 1976]. While the temperature range of this radiometer was sufficiently large (85K-400K) to measure the diurnal temperature variations of most of the lunar surface, it was not able to measure the lowest temperatures of permanently shaded craters and due to the orbit of the Service Module did not measure more than 25 degrees north or south of the lunar equator. The spatial resolution of the instrument was also relatively large, at 2.2km, impairing detection of smaller scale features.

2.3.2.2 Clementine Long Wavelength Infrared Camera

The Clementine orbiter contained a Long-Wavelength Infrared (LWIR) camera containing a single filter from 8.0 - 9.5 μm [Nozette et al., 1994], capable of observing both poles and had a higher resolution than the ISR at 55-136m per pixel. The camera successfully mapped 0.4% of the night-time surface of the Moon, before the spacecraft malfunctioned, but had a

minimum detectable temperature of approximately 200K, so no permanently shaded regions could be adequately thermally mapped [Nozette et al, 1994].

2.4 Permanent illumination

In the same way that the small axial tilt of the Moon gives rise to the PSRs, it should also cause some polar regions to be in near constant sunlight. Permanently illuminated ridges and crater rims etc. are distinguishable to instruments that measure reflected sunlight, such as ultraviolet/visible (UV/Vis) and NIR cameras, allowing these sites to be mapped by satellites such as Clementine [Bussey et al., 1999] and Small Missions for Advanced Research in Technology (SMART-1) . For example, the Advanced Moon micro-Imager Experiment (AMIE) onboard SMART-1 found an almost- permanently illuminated peak 17 km from the lunar south pole during its 18 month orbit [Grieger et al., 2008].

However, maps of surface temperature of such regions, across many diurnal cycles and lunar seasons, have never been made from lunar orbit prior to Diviner. The LWIR Clementine Camera lacked sufficient mapping coverage, while the orbit of the Apollo 17 ISR prevented it from observing the lunar poles during its short duration flight (above). The temperature of permanently illuminated regions is an important factor in the planning of extended human presence of the Moon, which has only previously been estimated from models.

2.5 Temperature Measurements Conclusion

While previous instruments have been capable of identifying polar permanently illuminated regions, clearly, insufficient temperature measurements have been made of the polar regions believed to exist in permanent shadow. Thus prior to the launch of LRO there was still

considerable debate about the temperatures in the polar regions, and while hydroxyl/water has been found in low concentrations (up to 770 parts per million) widely spread across the surface, the presence of trapped water-ice in these regions has not been definitively identified. Temperature measurements by an instrument such as Diviner will be able to tightly constrain regions sufficiently cold to trap water ice for billions of years, and will also be able to detect rocks on the surface by measuring a property known as thermal inertia, described below.

2.6 Thermal Measurements: Rock Abundance

2.6.1 Introduction

By measuring the heating and cooling rates of the lunar surface, it is possible to identify areas containing rocks. Rocks retain heat better than the surrounding regolith, and so appear to change in temperature slower and to a lesser magnitude during the course of a lunar day compared to the rest of the surface. These heating and cooling rates are related to the thermal inertia of the material, therefore rock abundances can be derived from measurements of this property.

2.6.2 Thermal Inertia

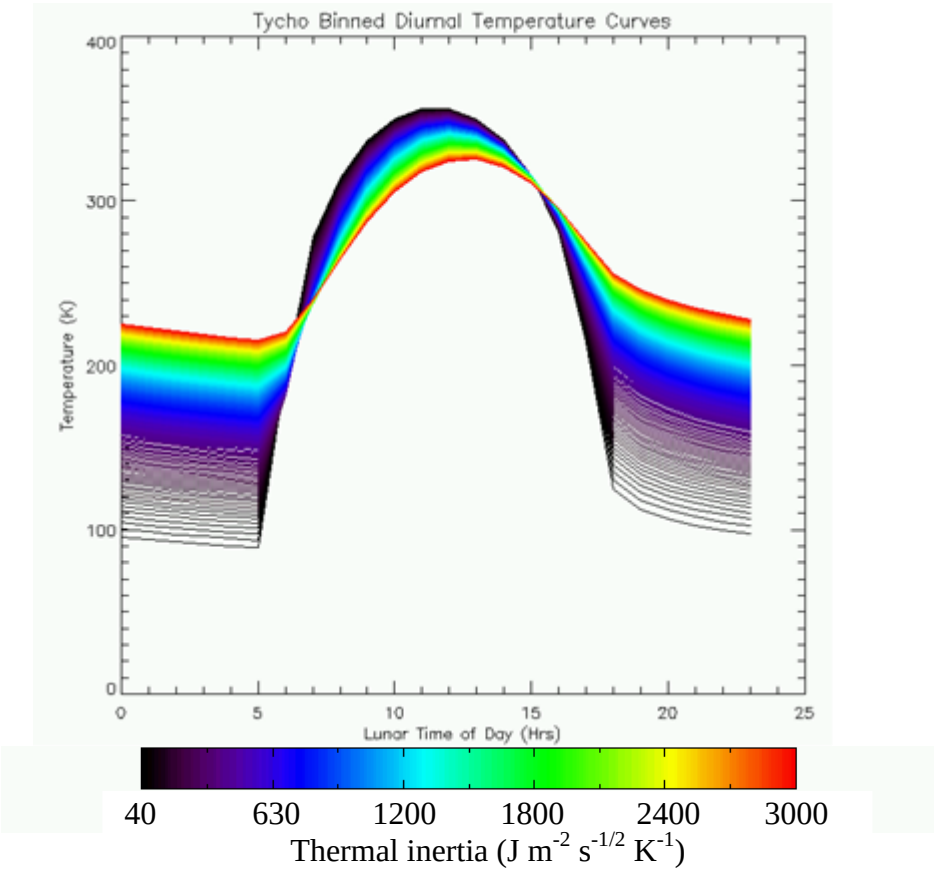

Figure 2-2: Computed diurnal curves for Tycho crater (-43° latitude; in the absence of topography), showing the difference in surface temperature between regolith (typical thermal inertia: 50 J m^{-2} $s^{-1/2}$ K^{-1} [Spencer et al., 1989]) through to rock (thermal inertia: 2500 J m^{-2} $s^{-1/2}$ K^{-1} [Jakosky, 1986]). The thermophysical model of Spencer [1990] was used for the calculation.

Thermal inertia (SI units: J m^{-2} K^{-1} $s^{-1/2}$) is best described as the resistance of a material to changes in heating and cooling; it is analogous to how, in classical mechanics, an object's inertia affects its ability to resist changes of motion, and is defined by the equation:

$$I = \sqrt{k\rho c} \qquad [2\text{-}1]$$

where k is the material's bulk thermal conductivity (W K^{-1} m^{-1}), ρ is the material's density (kg m^{-3}), and c is the material's specific heat capacity (J kg^{-1} K^{-1}) and follows from the equation of heat conduction [e.g. Hanel et al., 2003] . The temperature of the surface of an

airless body, such as the Moon, rotating with respect to a radiation source, i.e. the Sun, depends on the radiative equilibrium of incoming and outgoing radiation at each location on the surface throughout the body's diurnal cycle [Vasavada et al., 1999]. On the Moon, this equilibrium is governed by the thermal inertia of the material, with measured surface temperatures of low-inertia materials increasing faster during the daytime when heated by incident solar radiation, and decreasing faster during the lunar night-time. Lunar regolith typically has a lower thermal conductivity, lower density and lower heat capacity than lunar rocks and therefore much lower thermal inertia, typically 50 J m^{-2} K^{-1} $s^{-1/2}$ for regolith [Spencer, 1989] compared with 2500 J m^{-2} K^{-1} $s^{-1/2}$ for bare rock [Jakosky, 1986]. Therefore variations in regolith temperature throughout the diurnal cycle are greater than for those of rocks, as shown by the results of a 1-D thermophysical model in Figure 2-2, in the simplest form allowing rock abundances to be inferred by measuring surface temperatures across a range of local times of day. Prior to Diviner, the ISR was the best instrument to show thermal anomalies on the lunar surface.

2.6.2.1 ISR and LWIR Measurements

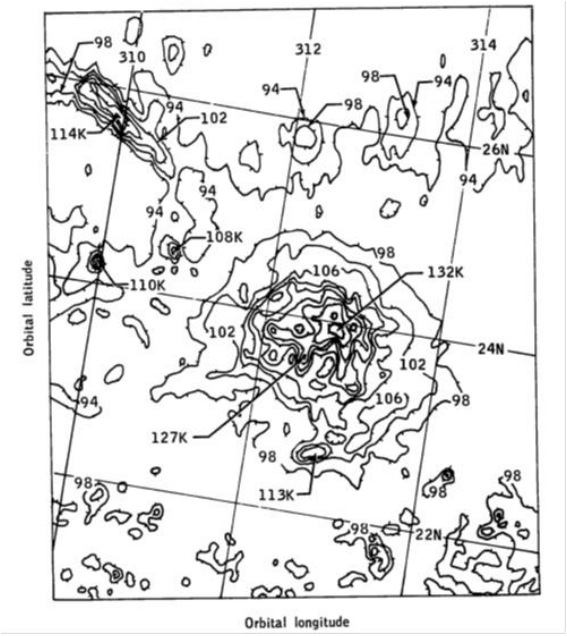

Figure 2-3: Aristarchus observed by the ISR seven hours before sunrise, from Paige et al., [2009]. A region of increased temperature is observed at 132 K, higher than the remaining regolith at 94 - 98 K.

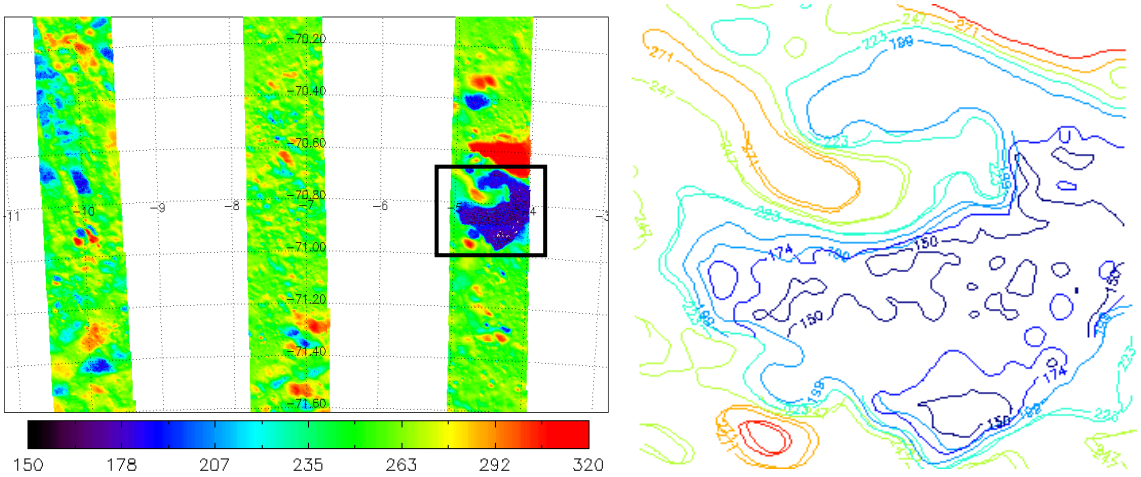

Figure 2-4: Clementine LWIR temperature data plotted in IDL by the author, showing gaps in coverage (left) and an enlarged view of a crater showing temperature variations of the surface, generated in IDL (right). The minimum detectable temperature of the instrument was ~200K for adequate signal to noise, and so the crater floor could not be mapped reliably, however differences in temperatures can be clearly observed.

Diurnal temperature variations were observed by the ISR and LWIR, and thermal anomalies were also observed in some locations, where the surface would cool down more slowly than surrounding areas when solar illumination ceased, believed to be the result of rocks on or close to the surface (e.g. Figure 2-3) [Mendell & Wieczorek, 1993]. The number of rocks exposed in an area depends on many factors, such as age (as all rocks are eventually comminuted to soil by impacts) and on processes that expose and cover rocks, such as mass-wasting[3], slumping and avalanching; hence from the ISR measurements alone, constraints can be placed on these surface evolution processes [Mendell & Wieczorek, 1993] for the latitudes that were accessible from Apollo 17's orbit. Clementine LWIR measurements however, lacked the required temperature range (Section 2.3.2.2) to determine regions of increased temperature at night, and so could only be used to detect reduced temperatures during the lunar day (e.g. Figure 2-4)

2.7 Mineralogy and Surface Processes

Until the launch of Lunar Reconnaissance Orbiter, the two most commonly used methods of determining surface composition from orbit were through detection of high-energy particles or spectral selection of reflected sunlight from the surface. Each of these methods has several advantages and disadvantages, described below.

[3]Movement of soil or regolith down a slope under the influence of gravity.

2.7.1 Elemental Abundance Mapping by High Energy Particle Detection

2.7.1.1 Lunar Prospector Neutron Spectrometer

The Neutron Spectrometer on board Lunar Prospector was able to detect fast (>10^5 eV) and thermal (<0.3 eV) neutrons in addition to epithermal neutrons (Section 2.3.1.2). Such neutrons are generated by galactic cosmic rays interacting with the lunar surface, with the energy of the detected neutrons depending on the nuclei present on the surface. Hence, through detection of these particles, elemental composition can be determined. Neutron fluxes are typically small; therefore only low resolution maps can be made, and only after repeated measurements, gathered on many spacecraft flybys, have been averaged together [Feldmann et al., 1998b].

2.7.1.2 Lunar Prospector Gamma-Ray Spectrometer

Similarly to the Neutron Spectrometer described above, the Gamma-Ray Spectrometer mapped elemental abundances by measuring the energy of emitted gamma-rays up to 8 MeV [Feldmann et al., 1998b]. These rays are caused by the de-excitation of nuclei, with energies corresponding to specific elements.

2.7.1.3 SMART-1 and Chandrayaan-1 Compact X-Ray Spectrometers

The D-CIXS instrument on SMART-1 and the C1XS instrument on Chandrayaan-1 were designed to detector X-rays emitted from the lunar surface. Excitation by solar X-rays incident on the Moon causes the surface to fluoresce, releasing x-rays with specific energies dependent on the excited element. Lower atomic number elements, such as Mg, Al and Si can be detected at typical levels of solar activity; however solar flares can excite transitions in heavier elements, allowing detection of many different compositions using this technique during periods of increased solar activity [Swinyard et al., 2009].

2.7.1.4 Discoveries from Elemental Abundance Mapping Instruments

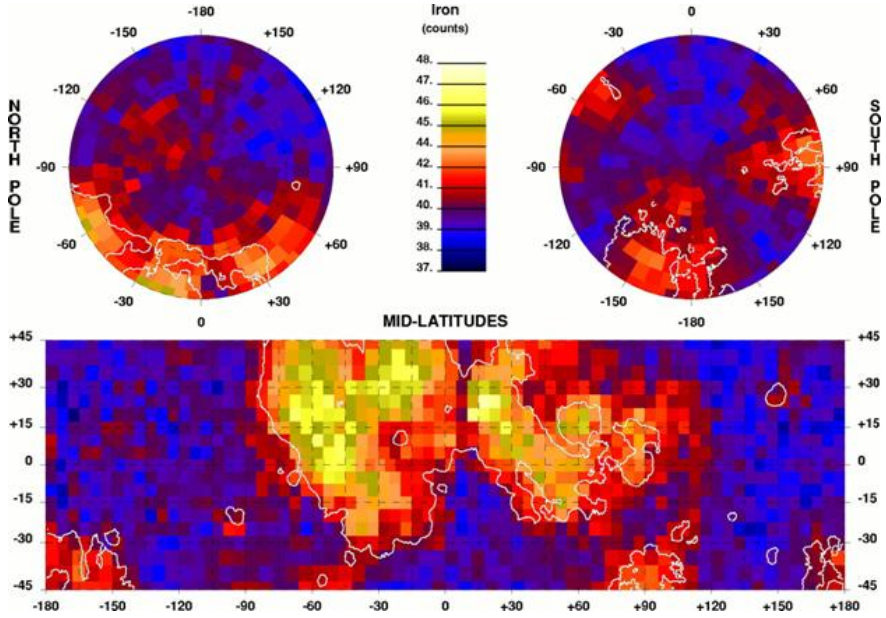

Figure 2-5: Lunar Prospector Fe abundance maps from Lawrence et al. [1998b] (reprinted with permission from AAAS). The regions of increased iron correlate well with the maria.

The Neutron Spectrometer data allowed feldspathic, mafic and basaltic rock types to be distinguished from one another at a resolution of 2° x 2°. The low altitude, mainly mafic compositions smoothly transitioned into feldspathic compositions at high altitudes [Feldmann et al., 1998b]. Iron and titanium abundance maps were also derived from the data [Elphic et al., 1998], and regions containing Gadolinium and Samarium were detected [Elphic et al., 2000]. The Gamma Ray spectrometer data, while at a lower resolution (5° x 5°), allowed comprehensive maps to be derived of iron (Figure 2-5), potassium and thorium, crucial in mapping the KREEP terrain, important for understanding crustal evolution (Section 1.2).The D-CIXS instrument detected magnesium, aluminium, silicon and calcium during its lifetime [Swinyard et al., 2009], but unfortunately the extended solar minimum prevented the C1XS instrument from extended mapping of the surface, however surface

elemental abundances of Mg, Al, Si, Ca and Fe were derived for a highland region near Tycho crater during a period of increased solar activity [Narendranath et al., 2010].

2.7.2 Ultraviolet/Visible and Near-Infrared Spectroscopy

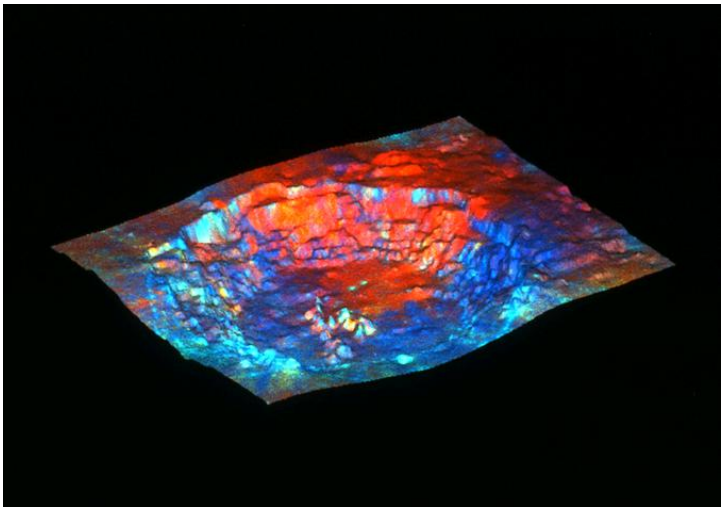

Figure 2-6: Copernicus crater, as an example of how UV/Vis and topography can be combined to investigate new regions of the lunar surface never visited by astronauts, from Spudis and Bussey [1997] (© Lunar and Planetary Institute). The colours represent ratios of Clementine channels, where red = 750/415 nm, green = 750/950 nm and blue = 415/750 nm. Variations in these ratios represent differences in composition, which can then be related to their location within the crater, allowing geological information to be derived, for example.

UV/Vis and NIR Cameras, which detect reflected sunlight, were flown on several missions beginning with Clementine in 1994. While such instruments are not able to detect the individual elements present in the surface like high energy particle detectors, they can detect rock/mineral types and have much higher spatial resolution and signal-to-noise ratios, meaning averaging observations over multiple orbits is usually not required. Reflected UV/Vis and NIR absorption spectra contain absorption bands characteristic of the surface composition, and by comparing with laboratory reflectance measurements of minerals found

in the Apollo samples and reflectance spectra of the Moon from Earth-based telescopes, it is possible to design instruments with appropriate filter wavelengths to map specific rock types and mineral compositions. In the recent, post Apollo period three missions have carried Vis/NIR instruments to lunar orbit.

2.7.2.1 Clementine

The Clementine payload included both UV/Vis and NIR cameras (channels at: 415, 750, 900, 950 and 1,000 nm [Pieters, 1999], and 1.1, 1.25, 1.5, 1.99, 2.6 and 2.7 μm [Lucey et al., 1998]), making it the first instrument able to map global lunar composition (Section 2.7.3.4). Clementine also carried a laser altimeter to map the lunar topography, allowing craters never explored by the Apollo astronauts to be studied in great detail for the first time (e.g. Figure 2-6).

2.7.2.2 Kaguya

The Japanese space agency's (JAXA) Kaguya lunar orbiter, launched in 2007, also contained instruments for measuring radiation reflected off the lunar surface. The Multiband Imager instrument was a combined UV/Vis and NIR camera with similar channels (415, 750, 900, 950, (2x) 1,000, 1,050, 1,250 and 1,550 nm)[4] to the Clementine cameras launched thirteen years earlier. The lower orbit (~100 km) and advances in detector technology allowed more detailed compositional maps to be made at up to 20 m surface resolution [Ohtake et al., 2009]. The Spectral Profiler (SP), also on-board Kaguya, was a line-profiling instrument, utilizing a diffraction grating to measure spectra from 0.5 - 2.6 μm in 296 bands with a spatial resolution of 500m [Yamamoto et al., 2010].

[4] The instrument had two telescopes, both with a 1000nm channel, to aid in combining the results of the two.

2.7.2.3 Chandrayaan-1

The M^3 imaging spectrometer was the latest instrument to observe the Moon from lunar orbit in the UV/Vis and NIR spectral regions. It contained 260 channels providing high spectral- (10 nm) and high spatial- resolution (up to 70m per pixel) [Pieters et al., 2010].

2.7.3 Relating Laboratory Measurements to UV/Vis and NIR Remote Sensing Data

In order to determine surface composition from remote sensing instruments such as hyper spectral imagers and spectrometers, representative rocks and minerals need to be measured in the laboratory in a comparable way to the orbiting instrument. For the NIR region, this typically requires reflectance spectroscopy measurements to be made usually by illuminating a sample rock or mineral sample and measuring the resulting reflected radiation with an instrument such as a Fourier Transform Infrared (FTIR) spectrometer.

2.7.3.1 Near Infrared Absorption Bands

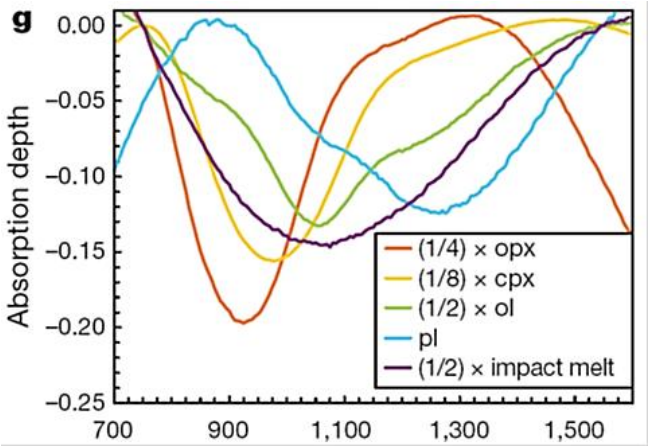

Figure 2-7: Mineral absorption depths for orthopyroxene (opx), clinopyroxene (cpx), olivine (ol), plagioclase (pl) and impact melt (Apollo sample 77075), from Ohtake et al. [2009] (reprinted by permission from Macmillan Publishers Ltd.).

Materials can be characterised through the shape and location of their spectral absorption bands (e.g. Figure 2-7), which depend on the properties of the material and hence on the material's composition. In the NIR these are reflectance absorption bands, which have distinctive shapes and can therefore be distinguished from one another through remote sensing if known samples are also measured in a similar way in a laboratory.

2.7.3.2 Laboratory Reflectance Measurements

Laboratory reflectance spectra are derived by making two measurements: one of the sample under investigation and one of a reference standard. The reference standard has a known reflectance in the geometry of the setup being used, and hence the sample reflectance spectrum can be inferred. Many lunar terrestrial analogues have been measured in this way, including rocks, minerals, returned lunar samples and analogues that have been artificially space-weathered. These reflectance spectra have then made publicly available in spectral libraries. Some relevant spectral libraries to this investigation are:

[1] The Reflectance Experiment Laboratory (RELab) at Brown University, RI, USA [e.g. Pieters, 1983]

[2] The Advanced Spaceborne Thermal Emission and Reflection Radiometer (ASTER) Spectral Library at the NASA Jet Propulsion Lab (JPL), CA, USA [e.g. Baldridge et al., 2009]

[3] The Arizona State University (ASU) Thermal Emission Spectroscopy Laboratory Spectral Library at ASU, AZ, USA [e.g. Christensen et al., 2000].

Library [1] is centred around providing measurements for the Clementine, Kaguya and M^3 instruments, and therefore primarily measures in the UV/Vis and NIR ranges, typically from 0.3 - 2.5 μm, but extends to 25 μm in some cases. [2] contains a collection of measurements

from several institutions containing reflectance spectra in both UV/Vis/NIR and Thermal Infrared (TIR) regions. Both [1] and [2] have also measured samples of different grain sizes, from fine particulates of less than 30 μm to coarse samples of 500 μm or greater [Baldridge et al., 2009]. [3] is typically used with the Thermal Emission Spectrometer (TES) instrument that orbited Mars as part of the Mars Global Surveyor mission to aid the derivation of Martian surface composition, hence contains measurements of thermal emission of only coarse samples typically consisting of 710 - 1000 μm sized grains, more comparable to measurements of Mars [Christensen et al., 2000].

Theoretical spectra can also be calculated of mixtures using spectral mixing models of compositions measured in the laboratory. In particular the high signal-to-noise ratio of UV/Vis/NIR instruments allows the relative strengths of their characteristic bands to be resolved, allowing % abundances to be derived for some compositional types (Section 2.7.3.4).

2.7.3.3 Photometric Correction and Calibration

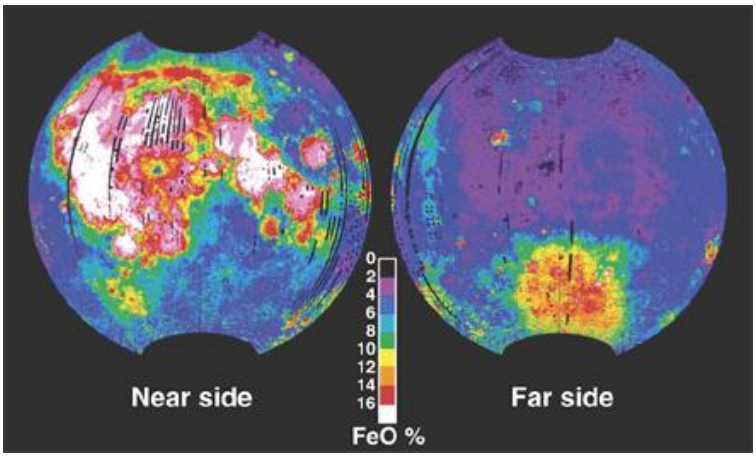

Figure 2-8: Clementine FeO concentrations derived from Clementine data, from Spudis [2001] (reprinted with permission from AAAS). The abundances correlate well with lunar prospector iron abundance maps and regions of mare.

One of the difficulties in comparing laboratory spectra to returned data from Vis/NIR instruments is that the geometry of both measurements must be the same, or one dataset must be converted into the geometry of the other using a photometric function, and for the Moon, albedo and soil maturity effects must be accounted for. For both Clementine [Pieters, 1999] and Kaguya [Ohtake et al., 2009], the returned data were converted into the geometry of the RELab spectral library using the photometric function of McEwen [1996] (modified by McEwen et al., [1998]), the form and method of which is described in more detail in Section 6.4.3.1.

A method to remove surface albedo and maturity effects, using only Clementine UV/Vis camera data was developed in stages by Blewett et al. [1997], Lucey et al. [1998] and Lucey et al. [2000], allowing accurate maps of iron and titanium abundances (Figure 2-8) to be made successfully from Clementine data.

2.7.3.4 Discoveries

UV/Vis and NIR instruments have the ability to categorise the surface into distinct compositional groups. Orthopyroxene, clinopyroxene, olivine and plagioclase reflectance spectra have different absorption bands (e.g. Figure 2-7), and as such can be identified by instruments with well-chosen spectral band-passes.

The Clementine UV/Vis and NIR camera datasets were used to create high-resolution (125 m/pixel [Lucey et al., 2000]) maps of iron (in the form of FeO) and titanium (in the form of TiO_2) of the lunar surface (e.g. Figure 2-8), allowing the distribution of the most common rock types to be found. Titanium maps of the lunar mare highlight the compositional differences between different regions of these younger regions, allowing distinct types of

mare (high-Ti and low-Ti types) with further subdivisions possible. For example, Staid and Pieters [1996] found that the high-Ti basalts could be separated into three further compositionally- and stragraphically- distinct areas, with implications for formation and evolution of such areas.

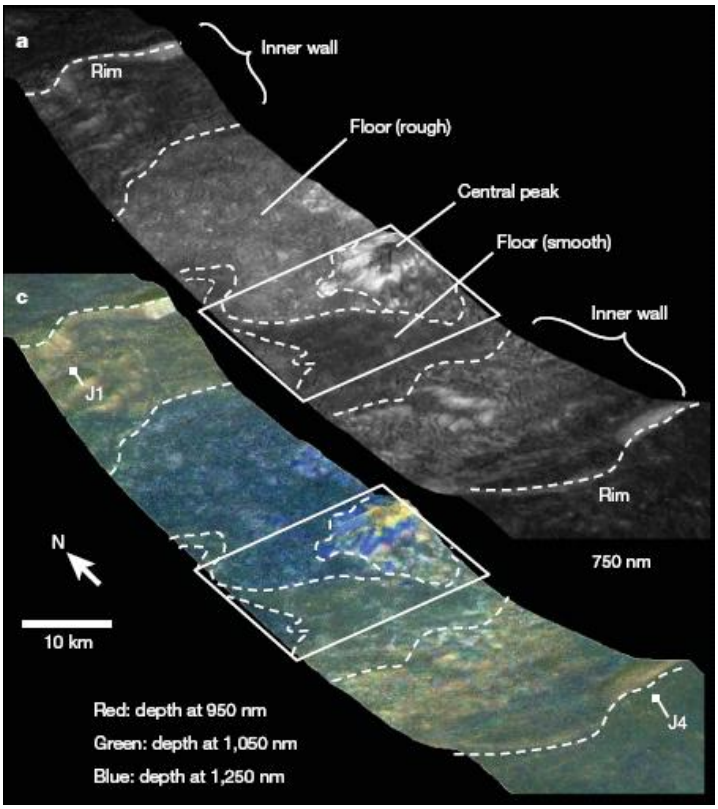

Figure 2-9: Single- and multi-spectral imaging of Jackson Crater by the Multiband Imager on Kaguya, from Ohtake et al. [2009] (reprinted by permission from Macmillan Publishers Ltd.). The yellow regions on the central peak were identified as >98% plagioclase.

Ohtake et al. [2009] used data from the Multiband Imager on Kaguya to discover regions of pure anorthosite, containing greater than 98% plagioclase (e.g. Figure 2-9). Yamamoto et al. [2010] used the Spectral Profiler, also on Kaguya, to find surface olivine outcrops, which they found to be located around places where the crust is relatively thin, around South Pole-Aitken, Imbrium and Moscoviense impact basins, suggesting that these olivine outcrops

either originated in the lunar mantle or are a type of rock known as a troctolite formed mainly from later mixing of plagioclase and olivine [Lucey, 2010]. Matching laboratory and M^3spectra found new regions of more unusual compositional types, such as spinel [Pieters et al., 2011], that had only been found previously in very small amounts in lunar sample analyses [Eckhert et al., 1991].

2.8 Mineralogy and Surface Processes: Thermal Infrared Spectroscopy

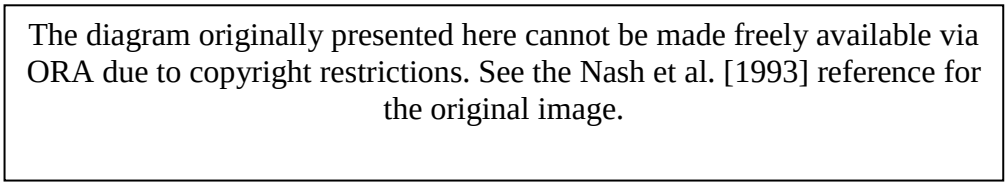

Figure 2-10: Typical absorption bands observed in the transition region between NIR and TIR (left), and the TIR restrahlen band region (right), both from Nash et al. [1993]. CF locations are shown by tick marks (right), which occur at minima here, as this figure shows reflectance (not emission) spectra.

The TIR region, like the NIR, also contains compositionally-distinct spectral bands (Figure 2-10), mostly originating from the silicon – oxygen and aluminium – oxygen bands (Nash et al., 1993):

- In the 4 – 7 μm region, most of the bands observed are either overtones or combination tones of the stretching and bending fundamentals of these bands.
- The 7 – 12 μm region contains stretching vibration bands known as Restrahlen bands, however the spectral contrast (i.e. the difference in contrast between the band and the surrounding continuum) of these are reduced on the Moon due to the small particle size of the regolith. This region is dominated by the Christiansen Feature (CF), a compositionally-dependent, prominent emission maximum typically observed around 8 μm, described in detail later (Section 2.9.3.2). Above 12 μm there are bending vibration and lattice bands. There also exists an emission minimum known as the transparency feature [Salisbury & Walter, 1989].

2.8.1 Earth-Based Spectroscopy

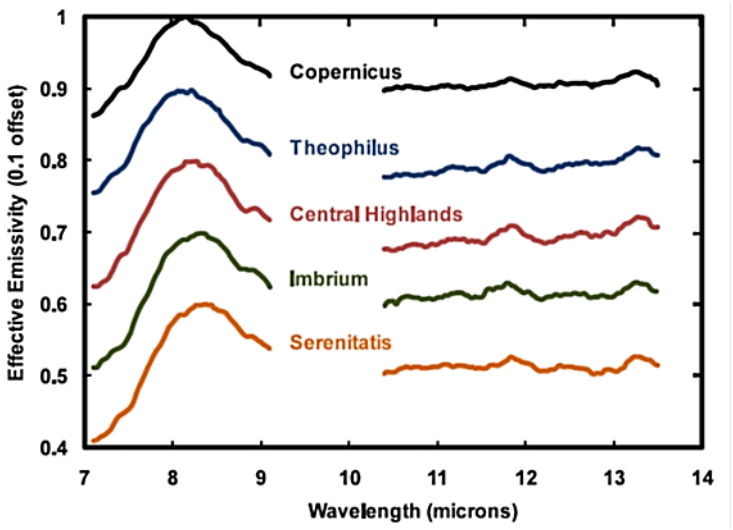

Figure 2-11: Balloon-borne TIR observations of several lunar regions by Murcray et al., 1970 (digitised by Paige et al., [2009]). The ozone absorption band around 9 - 10 μm is not plotted.

As described in Section 1.1.1, observations from the Earth can only yield a limited amount of information. Observations of the lunar farside and some regions of the poles are inaccessible, and the lack of broad atmospheric windows limits spectral coverage, but it has been shown [Murcray et al., 1970; Lucey et al., 1989; Potter and Morgan, 1981] that compositional differences between observable regions can be seen. The only work to contradict this, by Goetz [1968], determined that there was no spectral difference in all but two of twenty-three locations, but a different analysis of the same dataset by Lucey [1991] found discernable differences in keeping with other subsequent Earth-based measurements.

To observe the Moon from Earth, measurements must be taken in a spectral region not obscured by the atmosphere, with corrections made to remove atmospheric spectral features or must be made by an instrument above the atmosphere. Murcray et al. [1970] used a balloon-borne radiometer, flown to an altitude of 32km, to measure the Moon in the 7 - 13.5 μm spectral region (Figure 2-11). While the residual atmospheric absorption spectrum was not removed, the variation in CF wavelength was seen to shift between compositionally distinct regions of the lunar surface. These compositional differences are highlighted by Lucey [1991], who compared four previous TIR datasets to show that variations in the spectral location of the CF agreed with one another. Sprague et al. [1992] was able to remove atmospheric artefacts from ground-based telescope observations using the HITRAN molecular absorption database to model Earth's atmosphere at their location, removing the ozone band prominent in the spectra of Murcray et al. [1970]. See Lucey [1991] for a thorough comparative analysis of all lunar TIR spectra taken from 1968-1990.

2.9 Relating Laboratory Measurements to Thermal Infrared Remote Sensing Data

While some solar radiation is reflected from the lunar surface in the TIR region of the spectrum, it is dominated by thermal emission. This implies that any measured spectrum will be driven by variations in emissivity that are diagnostic of the rocks and minerals present in the instrument's field of view rather than reflectivity, so ideally laboratory measurements (or calculations if possible) of mineral emissivity spectra are required to allow confident identification.

2.9.1 Laboratory Emission Measurements

The scale of the laboratory work performed for NIR instruments has never been repeated in the TIR, presumably due to the lack of any instruments capable of measuring the lunar surface in this spectral region compared to the numerous shorter-wavelength instruments. The ASTER spectral library (Section 2.7.3.2) contains measurements of suitably sized grain samples (compared to returned Apollo regolith, below), but generally measured in reflectance in the TIR region. These can be converted from total reflectance, R, to emissivity, ε, using Kirchhoff's Law: $\varepsilon = 1 - R$, but are not well suited to lunar comparisons due to the measurement conditions, discussed later (Section 2.9.3). The ASU spectral library discussed in Section 2.7.3.2, whilst having measured TIR emission spectra, is also not well suited to lunar comparisons due to the sample grain sizes and experimental setup. The reasons for the discrepancies seen between existing spectral libraries and those expected to be measured when observing the Moon are discussed below.

2.9.2 Grain size

Measured emission spectra are affected by particle size of the sample (Section 2.9.3.3), and so representative samples should be measured. The 710-1000 µm size distributions of the ASU spectral library are much larger than the median lunar particle size, found to be 48 - 105 µm (Apollo 11), 42 - 94 µm (Apollo 12) [Carrier, 1973], 75 - 802 µm (Apollo 14) [McKay et al., 1972] and 51 - 108 µm (Apollo 15) [Carrier, 1973] from laboratory investigations of the respective returned Apollo soils. The amount of variation of grain size within a sample also affects TIR results; hence relatively narrow grain size ranges are preferred, allowing such effects to be quantified.

2.9.3 Experimental Setup

2.9.3.1 The Lunar Environment

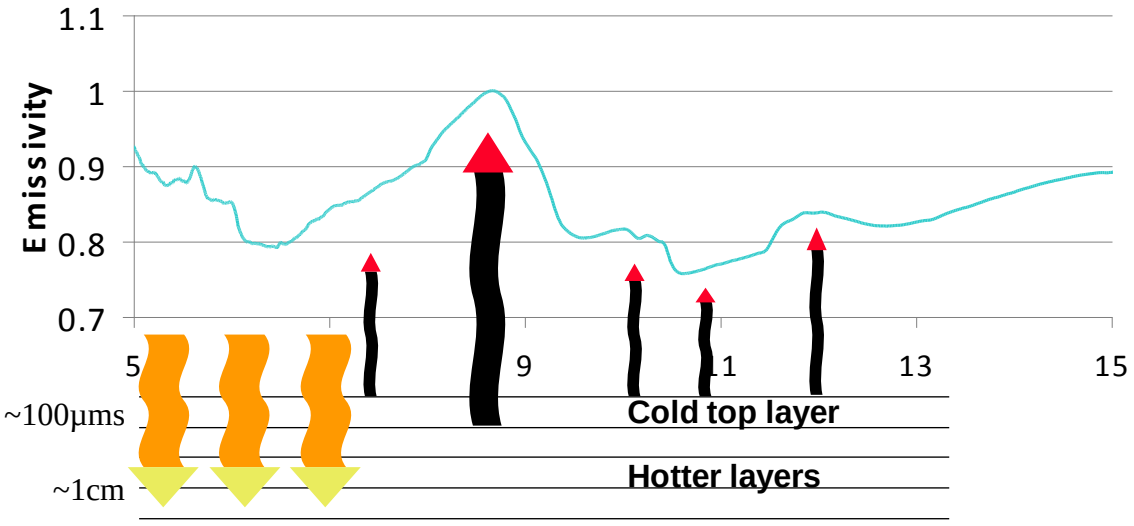

Figure 2-12: Diagram showing how the effective emissivity of a non-isothermal sample is affected by its transparency. The solar wave heats the top few centimetres of the soil, while radiation is only emitted from the top few hundred microns. Within this top few hundred micron layer, more radiation originates from the hotter, deeper layers at wavelengths where the material is most transparent, increasing the measured emissivity.

As well as by particle size, emission spectra are also strongly affected by the environment in which the samples are measured, which is the primary reason that the ASTER library cannot be used. Previous laboratory measurements [Logan and Hunt, 1970] and radiative transfer models [Henderson and Jakosky, 1994, 1997; Millan et al., 2011] have shown that the lunar thermal environment alters the measured emission spectra by creating a temperature gradient in the lunar surface. This thermal gradient exists due to the radiation absorption depth of a silicate mineral being larger (and hence more transparent) at shorter wavelengths, so the sample is heated to a depth of a few centimetres by solar radiation. The Moon reradiates in the infrared, but the absorption depth is much shorter at these wavelengths, therefore only the top layer of the sample can radiate to cold space (Figure 2-12). This cools the top few microns of the surface, thereby creating a large thermal gradient in the surface [Logan and Hunt, 1970]. The very low pressure ($<10^{-12}$ mbar) atmosphere on the Moon increases this temperature gradient, as the lack of interstitial gases within the regolith prevent heat transport by convection [Wechsler and Glaser, 1965], which under higher pressures (e.g. as is the case for the Earth and Mars) would have almost removed any temperature gradient. This thermal gradient affects the infrared spectra by increasing the spectral contrast (i.e. the difference in emissivity between the feature and the surrounding spectrum) and altering the spectral location of the CF emissivity maximum; usually shifting it to a shorter wavelength. There has been much discussion regarding how the lunar environment produces these observed effects, discussed below.

2.9.3.2 The Christiansen Feature

The CF is named for Christian Christiansen, after discovering an optical effect where light is transmitted perfectly through a liquid containing suspended particles, when both the liquid and the suspension have the same refractive index at that wavelength [Christiansen, 1884].

In a mineral or rock sample this occurs when the refractive index of the surface is equal to the refractive index of the atmosphere (or vacuum in the case of the Moon, i.e. = 1), which results in a transmission maximum at that wavelength. In regions of the spectrum with higher transmission (i.e. where the absorption depth is larger), such as around the CF, radiation originates from deeper, hotter layers within the sample, contributing to an increase in measured effective emissivity. Therefore, different temperatures are effectively being measured at different wavelengths, with higher emissivities corresponding to regions of increased transmission, explaining the observed increase in spectral contrast.

Several possible explanations for the wavelength shift of the CF have been proposed: Hapke [1996] theorised that because the Planck function shifts to shorter wavelengths at warmer temperatures deeper in the surface, the emissivity maximum would also be observed to shift. Salisbury and Walter [1989] suggested that the shift in the peak of the CF could be explained by the broadening of the Restrahlen band (Section 2.8) located on the long wavelength side of the emissivity peak. Also, as the atmospheric pressure is reduced, the refractive index tends towards 1, which therefore should shift the CF to slightly shorter wavelengths.

Thorough radiative transfer models of quartz in the lunar environment [Henderson and Jakosky, 1994, 1997; MillanValle et al., 2011], using the refractive indices and incorporating Mie scattering theory into a multi-layer model have also been able to reproduce the effects of the thermal gradient on the measured emissivity spectrum. Models such as these are important to understand how and why the spectra are altered by the lunar thermal and vacuum environment, but are of limited use in the creation of a lunar TIR spectral library. At present they can only be used to model minerals with simple structures and well known optical constants such as quartz, so to create a relevant spectral library

measurements need to be made of actual samples in a laboratory. The aim of such laboratory setups is to simulate an equal thermal gradient to that experienced by the same sample if it were on the lunar surface, thereby allowing emissivity spectra to be measured that should then be directly comparable to lunar observations.

2.9.3.3 Simulating the Lunar Environment 1: Heating from Above

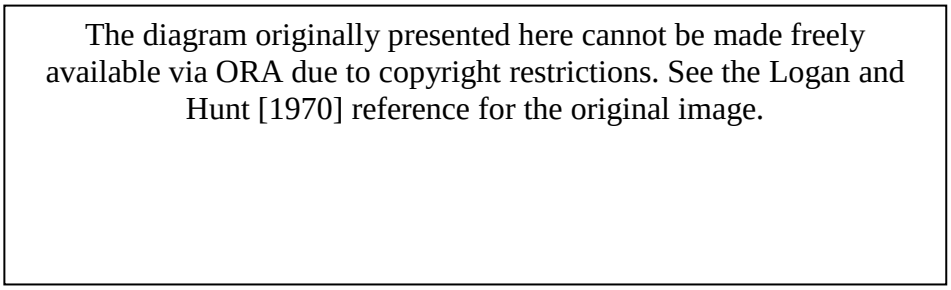

Figure 2-13: The laboratory setup of Logan and Hunt [1970] for measuring emission spectra in a SLE, using the balloon-borne spectrometer of Murcray et al. [1970].

Initial laboratory measurements of samples in a simulated lunar environment (SLE) were conducted in the early 1970's, after the balloon-borne radiometer of Murcray et al. [1970] had recorded TIR spectra of the Moon. The most comprehensive studies were made by Logan and Hunt [1970] and Logan et al. [1973], who measured six samples (quartz, albite, anorthoclase, labradorite, hornblende and olivine), each separated into two grain sizes (0 - 5 μm and 0 - 74 μm), under lunar conditions. Their setup (Figure 2-13) consisted of a 5mm deep sample cup surrounded by a radiation shield containing two apertures. A 500W quartz iodine lamp was placed behind one aperture and shone radiation of wavelengths 0.35 - 5 μm

through a filter to heat the sample, as the incident solar radiation does on the lunar surface. Radiation emitted through the other aperture was measured by a radiometer similar to that of Murcray et al. [1970]. The radiation shield could be cooled to 77 K to simulate space. Although this isn't as cold as space, it is an acceptable approximation since the radiance emitted from a blackbody at 77K is negligible compared to room temperature at the wavelengths under investigation. The apparatus was then enclosed in a vacuum chamber capable of maintaining a pressure of 10^{-4} mbar, sufficiently low that the lack of interstitial gases within the sample prevents heat transport by convection, as occurs on the Moon [Wechsler and Glaser, 1965].

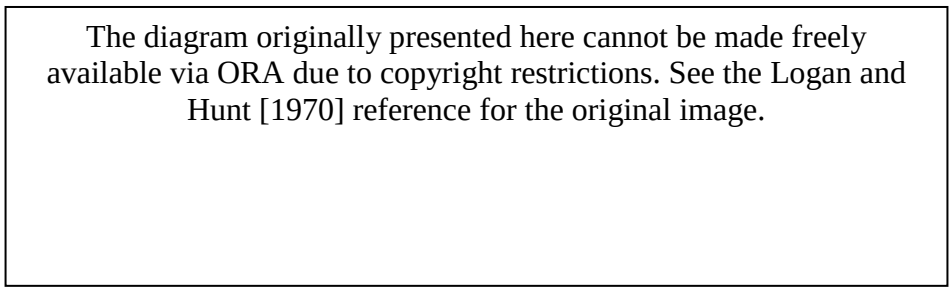

Figure 2-14: The effects on the CF of varying the environmental conditions, from Logan and Hunt [1970]. The SLE environment produces the greatest spectral contrast.

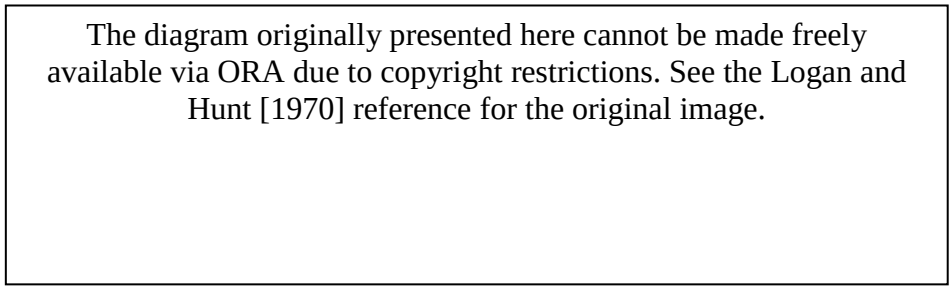

Figure 2-15: The effects of varying the sample grain size, from Logan and Hunt [1970]. The smallest grain size produces the greatest spectral contrast; however this size distribution is not representative of the lunar surface.

Samples were measured by Logan and Hunt [1970] in four environments: low pressure ($<10^{-3}$ mbar) with a cold radiation shield (77 K); low pressure and a warm radiation shield (290 K); and atmospheric pressure of dry Nitrogen with a warm radiation shield. They found that the CF is the most prominent emissivity maximum in the wavelength region measured (6 - 12 μm), and that the conditions on the lunar surface were ideal in enhancing the CF (Figure 2-14) compared with other diagnostic spectral features, with smaller-sized particles showing the most enhancement (Figure 2-15), contrary to measurements made in ambient conditions [Lyon, 1964].

A more comprehensive study using the same setup by Logan et al. [1973] investigated further variables that could affect the location and spectral contrast of the CF when measured in a SLE, such as composition and sample packing, summarised below:

- Increasing the particle size generally (in 4/5 of the samples) causes the spectral contrast to increase in packed samples but affects 'fairy castle'[5] samples randomly (2/5 increase, 3/5 decrease). The CF mainly shifts to shorter wavelengths with increasing particle sizes (4/5 for packed, 5/5 for fairy castle samples)

[5] Samples were made to have the consistency of fine dust by using an air elutriation column or by gentle sieving; these were dubbed 'fairy castle' samples

- Packing the samples causes the spectral contrast to decrease in all samples (10/10), while the CFs shift to shorter wavelengths for all small particle sized samples (6/6) but shift randomly (2/4 at shorter wavelength, 2/4 longer) for the larger particle size.

No details of sample preparation are given in Logan and Hunt [1970], but Logan et al. [1973] state that the samples for that study were obtained from Ward's Natural Science Establishment (no initial origins given) and were ground using a fluid energy mill (for 0 - 5 μm samples) or using mortars and sieves.

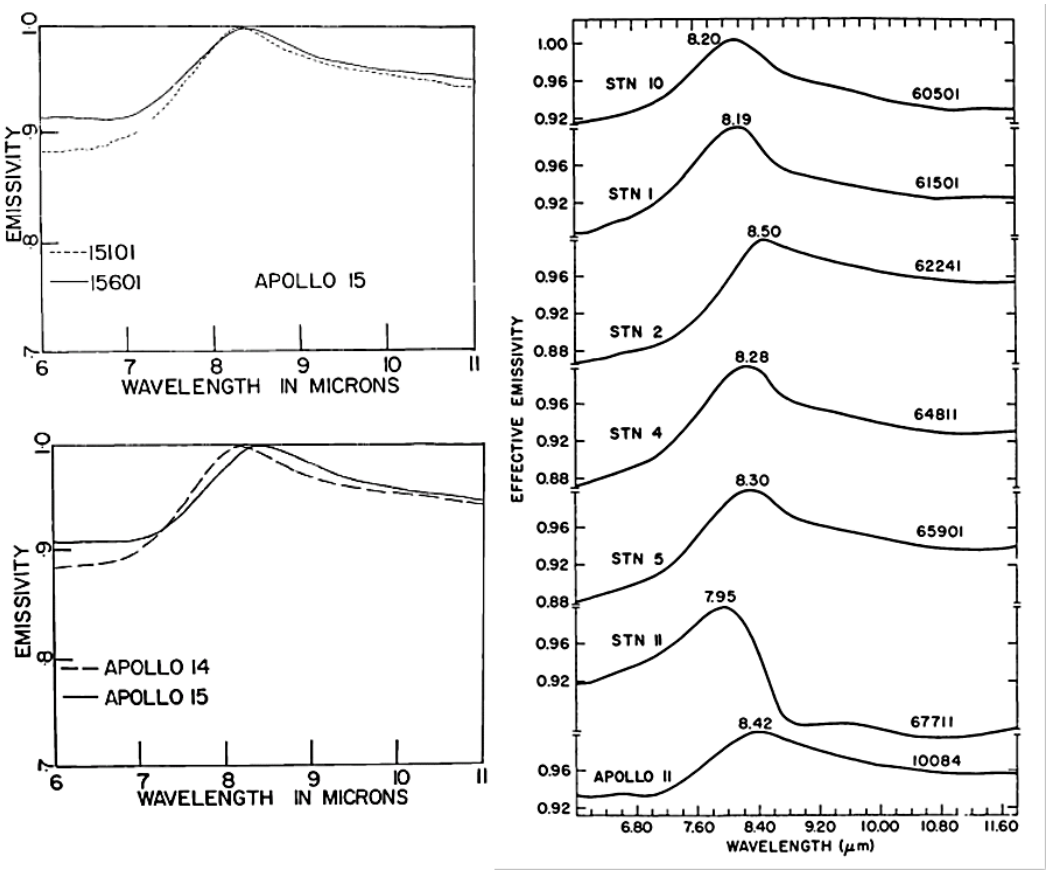

Figure 2-16: Apollo 11, 14, 15 and 16 samples measured in a SLE, from Logan et al. [1972] (left) and Salisbury et al. [1973] (right). Less spectral contrast is observed than in mineral SLE measurements. © Lunar and Planetary Institute.

The same setup was used again by Logan et al. [1972] and Salisbury et al. [1973] to demonstrate that the spectral contrast of the CF occurs not only when measuring terrestrial samples but also in returned lunar samples (Figure 2-16). 10084 (Apollo 11); 14259 (Apollo 14); 15101 and 15601 (Apollo 15); and 60501, 61501, 62241, 64811, 65901 and 67711 (Apollo 16) all displayed a prominent CF whose shape varied sufficiently that compositional information could be derived from lunar TIR observations. CF locations were found by Logan et al. [1972] to lie between those of basic rocks (gabbro, basalt, diabase, anorthosite) and ultrabasic (peridotite, pyroxenite) but spectral contrasts of all Apollo samples measured in this study were less than all but one gabbroic/basaltic sample.

2.9.3.4 Simulating the Lunar Environment 2: Heating from Below

Over twenty years later, this work was revisited: Henderson and Jakosky [1994] used a radiative transfer model to calculate the effects of the lunar environment on an ideal quartz spectrum. Henderson and Jakosky [1997] improved on this, incorporating Mie scattering into the model to accurately model quartz spectra under lunar, Martian and terrestrial environments for 3 μm, 10 μm, 30 μm and 100 μm particle sizes. By using their model, they were also able to calculate how the sample temperature varied with depth, showing how the magnitude of the thermal gradient affected the spectra.

Based on their modelling work, Henderson et al. [1996] devised a different method of simulating the lunar environment in laboratory setups. To investigate the thermal gradients present in their samples, they heated them from below, by heating the underside of the sample cup, rather than from above using a lamp, in the same non-convective, low pressure ($\sim 10^{-3}$ mbar) environment. As the sun (or lamp) heats the sample to a depth of several centimetres [Vasavada et al., 1999 etc.] and the MIR region radiates from the top few hundred microns, an equal thermal gradient can be produced in the sample if the correct

sample cup temperature is used. The study found that a temperature of ~500K with a radiation shield temperature of 100-150K created the correct thermal gradient, causing a quartz 0 - 50 μm sample to display the same CF location and spectral contrast as when heated from above by Logan et al. [1973]. Henderson et al. [1996] stated that:

> "This result suggests that visible absorption length scales for this grain size distribution of quartz are long enough that sunlight penetration effectively produces heating of the uppermost surface from below."

By extension, this measurement technique could be applied to measure any mineral with similar optical/infrared properties as the quartz sample, for example similarly fine-grained silicate minerals [e.g. Farmer, 1974].

2.9.3.5 Comparison of the Heating from Above and Below Methods

The advantages and disadvantages of heating-from-below versus heating-from-above are listed below:

- Ideally the sample must only be able to view the radiation shield. In both setups this is unfeasible due to the aperture required for emitted radiation to enter the detector/spectrometer, but the heating from above setup requires an extra aperture for the lamp radiation. This can be negated by placing a filter (Logan et al. [1973] used a Pyrex-glass filter) over the second aperture which is cooled with the shield, but this limits the amount of radiation incident on the sample and also heats the shield, requiring a more powerful cooling system. For example, a 2mm thickness Pyrex® 4470 glass typically has a transmission of ~90% from 0.3 - 2 μm, but falls to under 50% by 2.7 μm [Praezisions Glas & Optik GmbH, unknown year].
- Unless such a filter is used, some radiation from the lamp will be reflected off the sample and measured by the detector, which will need to be removed through either

the calibration algorithm or by a system of rapidly shuttering the lamp and only measuring spectra when shuttered, similar to that of a chopper used in a monochromator.

- Any new system will ideally need to cross-calibrate with existing emission setups [Christensen and Harrison, 1993; Ruff et al., 1997; Maturilli et al. 2006 etc.] such as those used by the ASTER or ASU spectral libraries (Section 2.7.3.2), in which case will require heated sample cups to replicate their setups anyway.
- A 500W lamp is a large source of heat to be contained within a vacuum chamber that also houses a radiation shield that needs to be cooled to cryogenic temperatures. A setup such as this is more complex technically, with an additional cooling system required for the lamp and a larger vacuum chamber needed to house it all, and therefore a larger pump required to maintain the same pressure. In comparison, vacuum compatible heater wire capable of heating a sample cup to >500K is commonly available.
- When heating-from-below, the sample cup temperature needs to be brought up to the required temperature and then held constant in order to set up the correct thermal gradient, requiring a temperature controller or similar.
- It is unknown whether heating-from-below and heating-from-above will create the same thermal gradient in all rocks and minerals. Transmission profiles of other silicate minerals [e.g. Hunt et al., 1950; Bradley et al., 1992] indicate that both types of experiment would give similar results, but samples containing mixtures of rock fragments, glasses, agglutinates, nano-phase iron etc., such as Apollo samples may not.

2.9.3.6 Comparison of Laboratory Measurements to Lunar Observations

Logan et al. [1972] compared SLE spectra of Apollo samples to TIR observations of the lunar surface from the balloon-borne radiometer of Murcray et al. [1970]. They found that the spectra correlated well with the most representative sample of that region, despite the large spot size of the radiometer. The two examples given are Mare Imbrium and Central Highlands: a CF of 8.37 μm was found by the radiometer, close to the 8.42 μm CF of Apollo 15 sample 15601 taken from Imbrium Basin. For the Central Highlands, the CF was observed at 8.24 μm while sample 14259, possibly composed of debris ejected from the lunar crust, had a laboratory CF of 8.22 μm. They also compared the highlands measurement to terrestrial anorthosites measured under SLE, concluding that such a long wavelength CF requires that this region must contain pyroxene or olivine in addition to plagioclase, as plagioclase minerals always exhibit CFs of less than 7.90 μm in a SLE. Without more lunar surface spectra at higher resolution though, the heterogeneity of the highland regions could not be investigated further. The shorter wavelength CF of all the Apollo soils measured under SLE was 7.95 μm, of sample 67711 taken from the lunar highlands by Apollo 16, which would suggest that a greater variation of CFs exist than those measured by Murcray et al. [1970].

The observation that the minerals of the plagioclase solid solution series (Section 1.2.4.2) display different CFs has been proposed as a way to distinguish such minerals from each other. In addition to general compositional determination being possible from the TIR region alone, combining with other datasets has significant advantages. For example, Donaldson-Hanna et al. [2009] showed that by using UV/Vis and NIR data to constrain regions of plagioclase and then TIR data to map CF wavelengths should allow each plagioclase mineral to be mapped individually, if the CFs of such minerals can be measured in the laboratory.

2.9.4 Previous Studies of Potential Thermal Infrared Instruments

Previous instruments capable of measuring in the TIR (ISR, LWIR etc. mentioned previously) have only contained one channel for temperature measurement purposes, and so without other spectral channels, have been unable to return any meaningful compositional information. A comprehensive analysis of the potential of TIR lunar observations was made by Nash et al. [1993], complete with a potential instrument design for a polar-orbiting lunar satellite, based on the Thermal Emission Spectrometer (TES), a similar instrument sent to Mars as part of the Mars Observer and re-flown on the Mars Global Surveyor mission. Their findings were that a spectrometer measuring the 4 - 25 μm region could be capable of:

- Distinguishing and deriving concentrations of the major lunar compositions, such as pyroxene, olivine and feldspars, plus absolute silica content
- Measuring glass and agglutinate concentrations to determine relative surface ages
- Deriving surface thermophysical properties and mapping of possible condensed volatiles in the polar regions.

While this requires an instrument with a relatively large mass and power consumption (14.5kg and 10.6W for TES [Christensen et al., 2001]) and would have a ground resolution of 1km (at an altitude of 100km [Nash et al., 1993]), Lucey [1991] concluded that:

> "multispectral imaging with as few as two or three well-chosen bands should be effective at determining relative and absolute differences in mineralogy between lunar locations".

2.10 Conclusions

2.10.1 Instrument Conclusions

From the details given in this chapter, several conclusions can be drawn:

- Important new information can be gained from completely mapping the surface temperature of the Moon at all lunar local times. From this, new investigations can be made into the environmental conditions of future landing sites, constraints can be placed on the potential locations of lunar water-ice deposits, and bulk rock abundances can be derived.
- The NIR region has been extensively studied, and elemental abundance mappers have been flown previously and have much lower resolution than 'camera' type instruments. However, compositional studies using the TIR region have only ever been conducted from Earth's orbit using outdated (by today's standards) measurement equipment. An instrument containing as little as two well-chosen channels should be sufficient to provide new constraints on surface composition.
- Such a TIR compositional study will require extensive laboratory mineral measurements, described below.

2.10.2 Laboratory Measurement Conclusions

- Clearly, the current number of TIR lunar spectra is insufficient for compositional analysis of the lunar surface in this spectral region, making new measurements a high priority. From sufficient measurements, it may be possible to quantitatively produce SLE spectra from reflectance or emissivity spectra taken under ambient conditions. This would be advantageous in that it would allow existing spectra to be used in studies, vastly increasing the number of measurements available for lunar

comparison. A study by Salisbury and Walter [1989] showed that CF peak wavelengths of samples when measured in emissivity in vacuum (with ambient temperature radiation shield) correlate well with reflectance measurements converted to emissivity using Kirchhoff's law. No studies were made between these isothermal emissivity spectra and SLE spectra though, or how this relationship was affected by particle size or sample packing.

- It is hard to draw definitive conclusions from the limited number of results of SLE experiments so far, but a few recommendations for future experiments can be made. Experiments will need to replicate the lunar thermal and vacuum environment, particularly the thermal gradient within the sample, and will ideally need to measure several particle sizes and types of packing for each rock or mineral measured. Particle size effects should have a limited outcome on CF peak wavelengths though: Logan et al. [1973] found that grinding samples for longer, reducing the particle size, did not affect the wavelength of the CF, agreeing with the findings of Salisbury and Walter [1989] that reducing the mean particle size did not shift the CF or the transparency peak. Salisbury and Walter [1989] concluded that:

  > "Particle size has the greatest effect on the wavelength of this feature, but only if taken to extremes. […] It appears that these spectral features are constant for reasonable variations in particle size distributions for an unsorted, fine particulate regolith."

- Spectra of Apollo samples are expected to exhibit CF wavelengths within the range of mineral and rock measurements, but past studies [Logan et al., 1972] have shown that spectral contrast will be reduced significantly. Spectral contrast varies significantly between different samples, even of those with equal, well-constrained particle sizes.

- The implementation of modern, high resolution and wider spectral coverage spectroscopy techniques would be advantageous. All previous SLE emission spectra have been acquired at relatively coarse resolutions using either a circular variable filter spectrometer (1.5% resolution, 6 - 11.8μm) [Logan and Hunt, 1970] or grating spectrometer (0.1μm resolution, 7 - 13μm) [Henderson et al., 1996]. A FTIR spectrometer would be capable of measuring at much higher resolution if desired (1 cm^{-1} = 0.006 μm^{-1} at 8 μm) through the MIR into the FIR.
- A combination of NIR and TIR datasets could allow new compositional constraints to be placed on certain locations of the surface, such as those composed of pure anorthosite.

3 The Diviner Lunar Radiometer

3.1 Introduction

From the previous work described in chapter 2 it is clear that new measurements from lunar orbit in the TIR can help answer several important unanswered questions, specifically the surface temperature range and whether there are regions that are consistently cold enough to trap volatiles such as water vapour for significant periods of time; plus constraints on composition from thermal IR measurements that cannot be resolved by VIS/NIR cameras or neutrons/gammas/x-ray. Therefore, when such an opportunity arose, the Diviner radiometer, described in detail in this chapter, was proposed.

3.2 Lunar Reconnaissance Orbiter (LRO)

The Lunar Reconnaissance Orbiter (LRO) mission was developed as part of the NASA Lunar Precursor Robotic Program [Chin et al., 2007], as one of series of missions envisaged from the National Security Presidential Directive 31, which stated:

> "starting no later than 2008, initiate a series of robotic missions to the Moon to prepare for and support future human exploration activities",

specifically, to:

> "extend human presence across the solar system, starting with a human return to the Moon by the year 2020" [Bush, 2004].

This led to an Announcement of Opportunity (AO) for instruments to be flown on LRO to investigate the following [Chin et al, 2007]:

- The radiation environment in lunar orbit and the effect this has on biological entities and radiation-shielding materials.
- High-resolution lunar topography at scales appropriate in assisting landing site selections, including metre- and smaller-scale features.
- Mapping of landforms, temperature and illumination conditions in the PSRs at the lunar poles.
- High-resolution global distribution maps of surface hydrogen, and detection of potential near-surface water-ice.

The instruments selected were [Chin et al., 2007]:

- The Lunar Orbiter Laser Altimeter (LOLA), for mapping the lunar global topography at high resolution, including surface roughness and slopes at potential landing sites, and possible polar near-surface water-ice.
- The Lunar Reconnaissance Orbiter Camera (LROC), composed of near- and wide-angle cameras capable of photographing meter-scale features at potential landing sites, and determining seasonal and time-of-day effects on polar illumination conditions to constrain water-ice regions.
- The Lunar Exploration Neutron Detector (LEND), to search for water-ice by measuring the neutrons released from the surface to a higher resolution than has previously been achieved, and make measurements of the lunar radiation environment.

- The Lyman-Alpha Mapping Project (LAMP) for making far-ultraviolet global maps to detect surface areas containing ice near to the lunar poles and to image PSRs through detection of reflected starlight
- The Cosmic Ray Telescope for the Effects of Radiation (CRaTER), containing tissue-equivalent plastics and radiation detectors to examine the biological effects of sustained lunar orbit due to galactic cosmic rays and background space radiation.
- Mini-RF, a synthetic aperture radar technology demonstrator capable of imaging in the S- and X-bands.
- The Diviner Lunar Radiometer Experiment (DLRE), of which this thesis is concerned.

3.3 The Diviner Lunar Radiometer

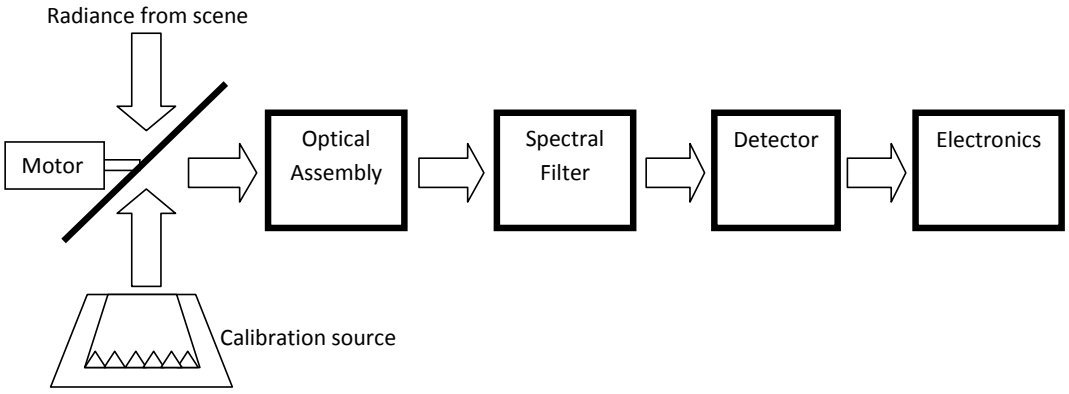

Figure 3-1: A block diagram of a typical radiometer (e.g. Taylor [2005]).

A radiometer (Figure 3-1) is a type of instrument used when high radiometric accuracy is preferable to high spectral resolution [Taylor, 2005]. Its spectral response is governed by the filters present, which only allow radiance of the desired wavelengths to reach the detectors.

3.3.1 Aims Outlined in the LRO AO

A multi-channel radiometer with well-chosen filters could contribute to six of the eight highest priority goals set out in the LRO AO [Paige et al, 2004], specifically [Paige et al, 2009]:

- To find and characterise permanently illuminated and shaded regions near the poles, helping in the search for water ice deposits, using long-wavelength high-resolution measurements to map global surface temperatures throughout the lunar diurnal and seasonal cycle
- To determine surface bulk thermal properties to aid in the mapping of surface rock abundance to assist in finding safe landing sites for future missions, by making TIR multi-spectral measurements of the surface.
- To provide new insights into regolith mineralogy and lunar geological processes, by mapping compositional spectral features from orbit.

3.3.2 Instrument Selection

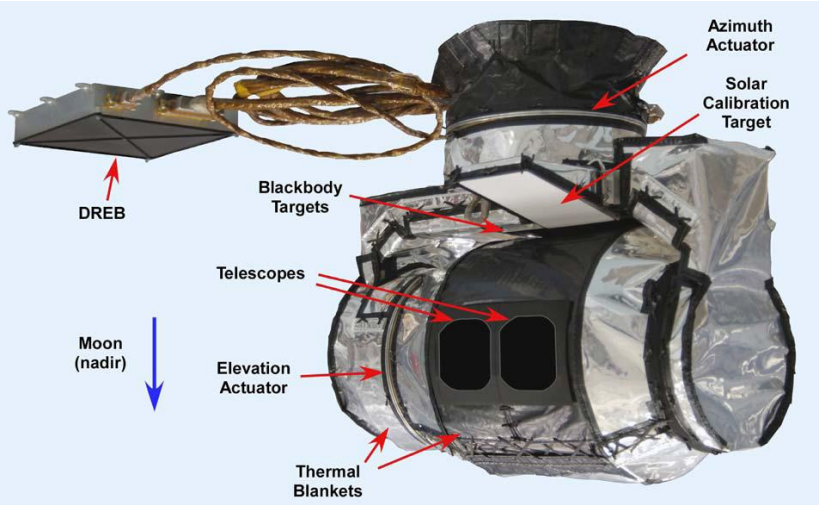

Figure 3-2: The Diviner Lunar Radiometer and Diviner Remote Electronics Box (DREB), from Paige et al. [2009].

Telescope number	Channel number	Band-pass (μm)	Function
A1	1	0.35–2.8	High Sensitivity Solar
A2	2	0.35–2.8	Mid Sensitivity Solar
A3	3	7.55–8.05	Mineralogy
A4	4	8.10–8.40	Mineralogy
A5	5	8.38–8.68	Mineralogy
A6	6	13–23	Thermal
B1	7	25–41	Thermal
B2	8	50-100	Thermal
B3	9	100-400	Thermal

Table 3-1: Properties of Diviner's spectral channels [Paige et al., 2009]

A suitable radiometer design capable of fulfilling the requirements of the LRO AO was already available based on the Mars Climate Sounder instrument (MCS, McCleese et al., 2007) that, at the time, was being integrated onto NASA's Mars Reconnaissance Orbiter (MRO). A near build-to-print copy of MCS, called the Diviner Lunar Radiometer (Figure 3-2), was proposed that could be ready for flight within the short schedule imposed by the mission [Paige et al., 2004; 2009].

Diviner was selected for the LRO mission in late 2004. After selection, it became clear that the signal to noise performance of three channels originally proposed to measure water ice was insufficient, and so these instrument filters were changed to map surface mineralogy instead [Greenhagen and Paige, 2006]. The other channels, consisting of two channels for

measuring surface albedo and four for measuring surface temperatures remained as described in the initial proposal (Table 3-1).

3.3.3 Design Heritage

3.3.3.1 Mars Climate Sounder

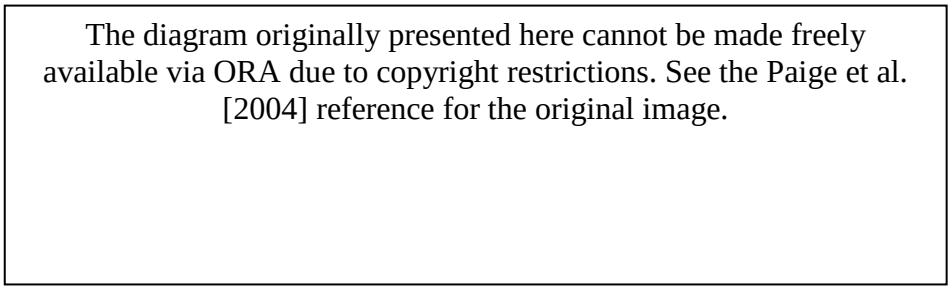

Figure 3-3: Diagram of the optical bench assembly of MCS and Diviner, showing the two telescopes, mirrors and focal plane and detector assemblies, from Paige et al. [2004].

MCS, flown on MRO in 2005, is a nine-channel radiometer designed to retrieve Martian atmospheric profiles of temperature, water vapour and opacity, much like an operational weather satellite orbiting the Earth [McCleese et al., 2007]. The instrument consists of two telescopes (A and B) (Figure 3-3) mounted on rotatable elevation and azimuth axes, allowing them to be pointed in the desired direction without requiring a change in spacecraft orientation. Each channel (A1-A6 in telescope A; B1-B3 in telescope B) contains a different filter, with a band centre ranging from 16.5μm to 42.1μm, located above an array of 21 un-cooled thermopile detectors (Foote et al., 1998). To achieve the required radiometric

accuracy when viewing the Martian limb, each detector has an integration time of 2.048 seconds per measurement [McCleese et al., 2007].

3.3.3.2 The Diviner Lunar Radiometer Experiment

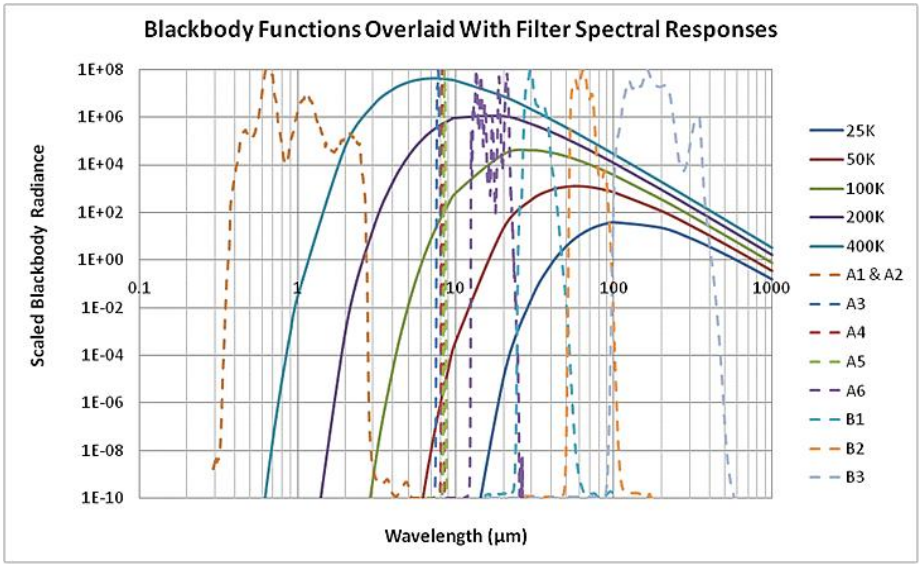

Figure 3-4: Planck blackbody functions of various temperatures and normalised Diviner filter responses. Spectral response data for channels A1 - B1 was provided by Foote [personal communication 2008].

To adapt the MCS to make lunar surface measurements, several modifications were made:

- Electronics: While MCS was primarily envisaged to be a mainly limb-viewing, Diviner is a nadir-pointing instrument, and so the MCS integration time for each detector was unsuitable. The low orbit of LRO, of only 50 km above the surface [Chin et al., 2007], required measurements to be made much faster to avoid elongated fields of view with surface detail smeared out. Therefore the integration time was decreased to a 16^{th} of that of MCS, to 0.128 seconds per measurement, though because a larger flux is measured from the warmer lunar surface than from the Martian atmosphere, radiometric accuracy is maintained. This increase in data

collection rate then meant that additional data processing and handling was required: the DREB was added to provide additional computational support and to communicate with the spacecraft bus, different to that of MRO [Paige et al., 2004].

- Thermal shielding: With the Moon being closer than Mars to the Sun, the solar flux and reflected radiation off the surface create a harsher thermal environment for the instrument to endure. It was painted black to increase heat dissipation and extra silver coated Teflon was used to shield the instrument, which is important to keep the instrument temperature stable, increasing accuracy and instrument lifetime [Paige et al., 2009].
- Filters: A larger spectral range was required to measure both short wave (≈300nm-2.2μm) solar reflectance and extremely low temperatures (>200μm, <50K) by the same instrument (Table 3-1; Figure 3-4); therefore different filters technologies were used in each of the two telescopes. The filters are described in more detail below.

3.3.4 MCS and Diviner Spectral Filters

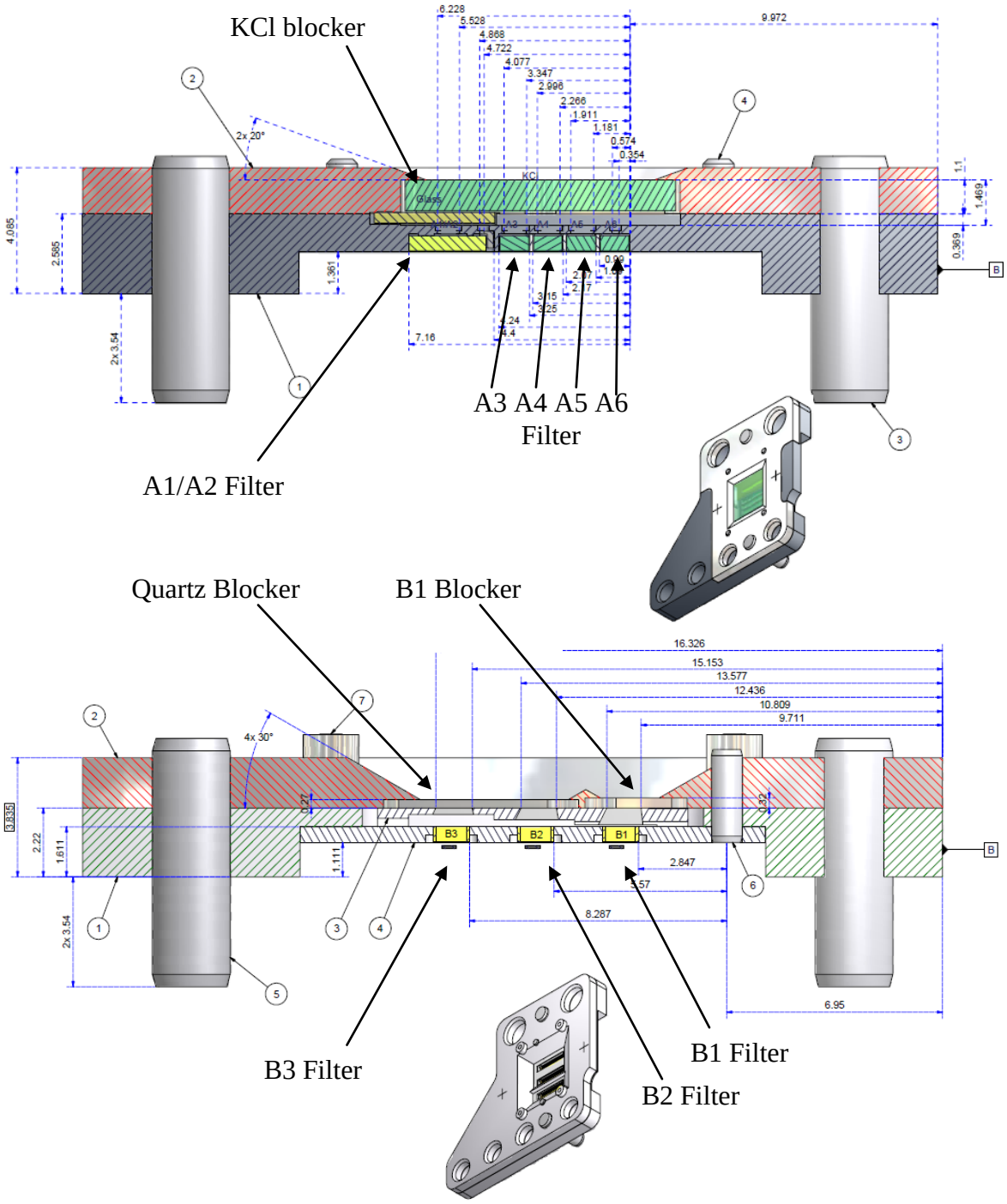

Figure 3-5: Schematic diagrams of the Diviner focal plane assemblies, showing the spectral filters and blockers (labelled) mounted with them. The detectors are located ~100 μm below the filters [Calcutt, personal communication 2008a].

The spectral responses of each of the channels are key to the instrument's operation, and are primarily determined by the band passes of the filters and out of band blockers in each channel (Figure 3-5). The large spectral range of both instruments required two types of filter, multi-layer dielectric and mesh filters, fabricated using different techniques. The operation of such filters is described more in detail elsewhere [Irwin, 1991; Taylor, 2005]; below is a summary of how the filters function and why additional spectral blockers are required.

3.3.4.1 Multi-layer Dielectric Filters

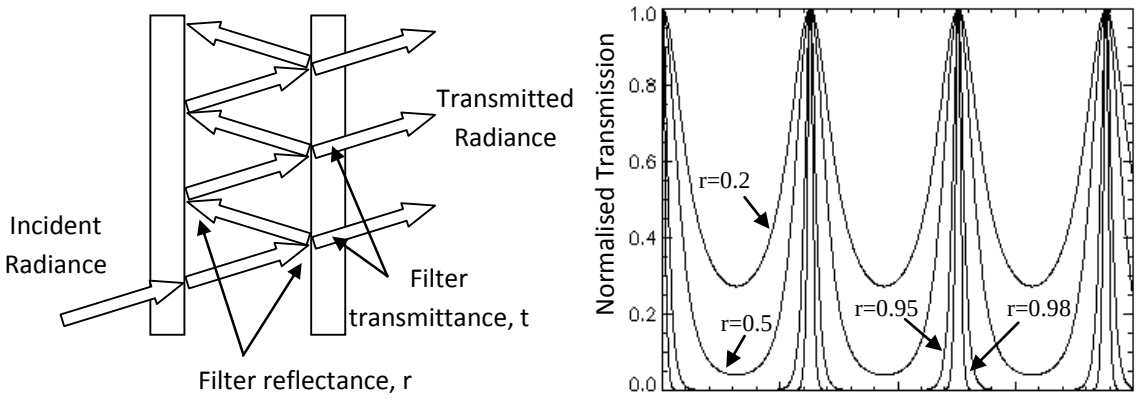

Figure 3-6: An incident beam is multiply reflected within the thin film. By varying r, different spectral responses can be made, which are periodic in wavelength (e.g. Taylor [2005]).

The filters in the 'A' telescope are effectively a set of Fabry-Perot etalons, which consist of two parallel surfaces separated by a distance *d* from each other. If these surfaces (or films in the case of the filter) have reflectance *r* and transmittance *t* then an incident beam of amplitude a_0 will reflect multiple times within the etalon (Figure 3-6). The transmitted beam will exhibit periodic maxima and minima (Figure 3-6) given by the following equations

from Taylor [2005]. The transmitted amplitude, summed over infinite reflections is calculated as:

$$a = a_0 t\left(1 + re^{-i\delta} + r^2 e^{-2i\delta} + \ldots\right) = a_0 t(1 - re^{-i\delta})^{-1} \qquad [3\text{-}1]$$

The transmitted power *T* is then:

$$T = aa^* = \frac{T_0}{[1 + F\sin^2\left(\frac{\delta}{2}\right)]} \qquad [3\text{-}2]$$

Where the maximum transmission T_0 is:

$$T_0 = \frac{a_0^2 t^2}{1 - r^2} \qquad [3\text{-}3]$$

And the finesse *F* is:

$$F = \frac{4r}{1 - r^2} \qquad [3\text{-}4]$$

Periodic transmission maxima occur when $\delta / 2 = m\pi$ where *m* = 1, 2, 3, etc, with the finesse affecting the spectral width as:

$$\Delta m = \frac{1}{\pi\sqrt{F}} \qquad [3\text{-}5]$$

The Diviner filters were made of many thin films of lead telluride and low-refractive index zinc selenide, deposited onto a substrate of zinc sulphide (A3-A5) or germanium (A6) by the Infrared Multilayer Laboratory at the University of Reading [Calcutt, 2007]. The A1 and A2 filters are made of uncoated phosphate glass. By using many layers of different thicknesses and refractive indices, the many maxima and minima block each other to remove the undesired periodic maxima while leaving the required spectral band passes. The substrate itself is also chosen to provide additional blocking of the undesired periodic transmission maxima, although for MCS and Diviner small spectral leaks were present where some out-of-band radiation was transmitted still, and so an extra broadband filter was

placed above the A1-A6 channels in both instruments. This blocker, made of parylene-coated KCl [Calcutt, 2007] has high transmission over all the filter pass bands in the A telescope, but switches off around 25 μm, stopping any longer-wavelength radiation from reaching the filters (Figure 3-5)

3.3.4.2 Telescope B Mesh Filters

For fabricating the longer wavelength B telescope filters however, the deposition technique proves difficult as the layer thicknesses necessarily become large and problems are encountered with adhesion when making filters with spectral responses greater than ~20 μm, [Irwin, 1991]. Instead, mesh filters made of two-dimensional copper grids are used in place of the thin films. These grids have specifically chosen grid -widths and -spacings to diffract out-of-band radiation while also acting as resonant meshes at the desired wavelengths, allowing transmission of radiation, which can be layered like the dielectric filters to produce the desired spectral band passes. The B1-B3 channels for both Diviner and MCS were made of layers of meshes of this type that suffered from similar spectral leaks due to periodic transmission maxima, and so were deposited on polypropylene substrates designed to block the out-of-band short-wave radiation.

Removing short-wave leaks such as these is essential, as they can affect the instrument significantly: although they may be small in absolute terms (e.g. <0.1% of a filter's maximum transmission), their effect can be large due to the peak in Planck radiance of thermally emitting surfaces such as the Moon or Mars lying in the MIR region (Figure 3-4), so a small out of band leak leads to a large out of band signal at the instrument's thermopile detectors.

3.3.4.3 MCS B-Telescope Spectral Responses

During the testing and development of the Mars Climate Sounder instrument, the mesh based filters and blockers all met their required specifications when measured separately in a FTIR spectrometer following their manufacture at Cardiff University. However, after integration into the instrument and during pre-flight testing and calibration it was discovered that the mesh filter spectral responses showed significant broadening compared to their pre-instrument integration performance. Of particular note was the B3 filter response, which had broadened by 45% (in wavenumber space) over its original design value [Lolachi, personal communication 2010] and showed significant variations in response between different detectors within the B3 detector array, leading to difficulties with the planned primary function of the B2 and B3 channels. The B2 and B3 channels were designed to detect water vapour independently of dust by using two channels with similar central wavelengths but different widths, with the wider B2 channel measuring water-vapour emission lines that the B3 channel did not [McCleese et al., 2007]. The narrower B3 channel was designed to measure the radiance in a 'gap' between two water vapour rotation bands around 45μm; however, since the B3 channel in the instrument was broader than designed it could also detect water vapour emission lines, complicating the derivation of water vapour abundance from MCS measurements.

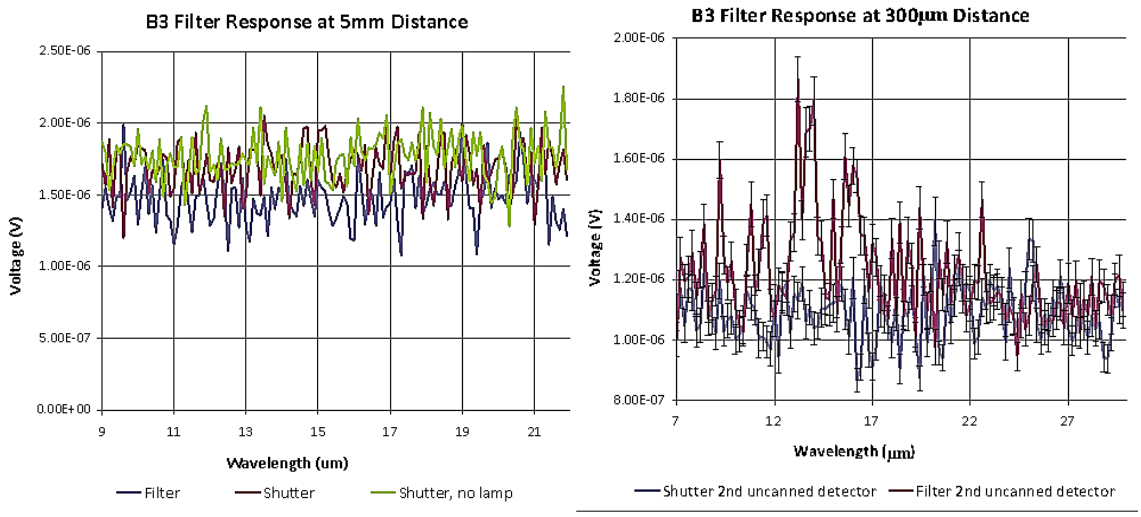

Figure 3-7: Difference in spectral transmission of the LRO B3 filter, by varying the distance between the filter and detector [Bowles et al., personal communication 2007]. At a distance of 300µm, an increase in transmission is clearly seen from 12-17µm, far outside of the range of the specification band-pass.

Investigations into the B3 filters for LRO by Bowles et al. [personal communication, 2007] showed evidence that the meshes and polypropylene substrate were not blocking all short-wavelength radiation when the detector was placed 300 µm behind the filter (similar to the MCS optical layout), with small transmission peaks observed between 12 - 17 µm (Figure 3-7). Investigations into the origins and effects of the changing filter band passes have so far been inconclusive, and methods of overcoming this problem are still being investigated [Lolachi, personal communication 2011].

3.3.4.4 Diviner Spectral Responses

Since Diviner is near-identical to MCS in optical design one immediate concern was that the performance of the B telescope mesh filters would also be compromised. Based on the experience gained from MCS a few alterations were made to the filters and out of band-pass

blockers were added to the mesh filters to improve performance (Figure 3-5) by reducing the shortwave leaks. A quartz piece was supplied by JPL that effectively blocked spectral leaks in the MIR up to 50 μm [Calcutt, personal communication 2008a], and therefore was used as the blocker for the B2 and B3 channels. For B1, however, crystalline materials were found that block the visible and near IR but transmit efficiently around the B1 band-pass, so a broadband multilayer dielectric filter was manufactured by the Infrared Multilayer Laboratory at Reading University from layers of cadmium selenide, lead telluride and germanium on a silicon substrate, to block out-of-band radiation below 25 μm.

Specification Number	Calibration Specification Description
DLRE-L2-4	DLRE must be capable of measuring surface brightness temperature with an accuracy of 5K from 40 to 55K, 2.5K from 55 to 75K, and 1K from 75 to 300 K.
DLRE-L2-5	DLRE must be capable of measuring night-time emitted thermal radiation of surfaces with temperature as low as 70K in at least two non-overlapping spectral channels that have brightness temperature accuracy better than 2.5K.
DLRE-FRD-66	The radiometric performance requirements summarized below shall apply to all 21 detectors in each DLRE spectral channel.
DLRE-FRD-68	In the DLRE thermal and mineralogy channels (A3, A4, A5, A6, B1, B2, and B3) the response to a 300 K blackbody source shall be calibrated to an absolute radiometric accuracy of better than ± 0.5% or to the noise level, whichever is larger.
DLRE-FRD-70	For the thermal channels, response to radiance from targets between

	40 K and 400 K shall be characterized to better than ± 0.1% of the reference radiance or to the noise level, whichever is larger. For the mineralogy channels, response to radiance from targets between 200 K and 400 K shall be characterized to better than ± 0.1% of the reference radiance or to the noise level, whichever is larger.
DLRE-FRD-83a	Signal to noise ratios for channels B1-B3 shall be no less than 80% of these values. Signal to noise ratios for channels A3-A5 shall be no less than 80% of these values. Signal to noise ratios for channel A6 shall be no less than 50% of these values. It shall be acceptable for the requirements for optical transmission or detector D* not to be met for a given channel, provided the signal-to-noise requirement is met.
DLRE-FRD-236	When viewed by the DLRE telescopes, the effective emissivity of the blackbody calibration target shall exceed 0.992 for the mineralogy spectral bands, 0.986 for the 12.5-25 micron band, 0.978 for the 25-50 micron band, 0.970 for the 50-100 micron band, and 0.965 for the 100-200 micron band. The emissivity values are averages over the spectral ranges weighted by a 300 K Planck distribution.

Table 3-2: The calibration specifications of Diviner that are required to be verified during pre-flight calibration by Foote [personal communication 2008]. Note that DLRE stands for Diviner Lunar Radiometer Experiment, which is usually shortened to Diviner.

A crucial part of the calibration and testing programme for Diviner was to determine if the same broadening that affected the MCS mesh filters was also present in the equivalent Diviner channels, which may have affected the instrument's ability to meet its required specifications (Table 3-2). A programme of measurements was designed to check for this as part of this work (Section 4.3).

3.3.4.5 Channel Nomenclature

It should be noted that the channels on Diviner are referred to differently after launch. When referring to post-launch operations, the channels are in general named from 1 to 9, unlike MCS where the convention was to include the telescope number, with names A1 to A6 and B1 to B3.

3.4 Instrument Observation and Data Collection

LRO's orbit is particularly suited to maximise the scientific output from Diviner, allowing it to fulfil the objectives set out in the AO. More details of this and the data returned from the instrument are given below.

3.4.1 Mapping Mode

Diviner has moderate spatial resolution; the instantaneous field of view of the instrument is 6.7 milliradians in the in-track direction and 3.4 mrad cross-track, corresponding to 320 m x 160m pixel spot size from 50 km orbit. The full cross-track swath width of the 21-detector instrument is 67 mrad (3.4 km ground swath). The instrument is designed to work as a pushbroom mapper, where the detector arrays are aligned perpendicular to the direction of spacecraft motion: therefore in-track refers to the direction of motion (i.e. North or South for a polar-orbiting instrument) while cross-track refers to East-West.

3.4.2 In-Orbit Calibration

Diviner is located on the nadir panel of the LRO spacecraft, giving it an unobstructed view of the lunar surface during measurements. To maintain radiometric accuracy, the instrument

carries out a regular calibration sequence as part of its standard observing mode by pointing away from the surface at regular intervals. Two calibration targets are attached to Diviner (Figure 3-2): a blackbody target within the base for calibration of the infrared channels, and a solar target attached to the base for calibration of the solar reflectance channels [Paige et al., 2009]. The thermal channels A3-B3 are calibrated approximately ten times per orbit, first by observing space for ten seconds, then viewing the internal blackbody for ten seconds, and finally viewing space again for ten seconds. The detectors are expected to have a linear response to infrared radiance based on ground calibration tests (Section 4.4) and therefore views of space and internal blackbody, both of known temperature and radiance are used to calibrate the instrument [Paige et al., 2009]. Channels A1 and A2 are calibrated once per orbit, in a similar method except that the solar target is viewed instead of the blackbody. The timings of the calibrations are chosen so that solar calibration is minimally affect by reflectance off the lunar surface and to ensure that the off-surface views do not occur at the same latitude each orbit, avoiding large gaps in surface observations. The solar reflectance target is a flight spare from the MCS instrument [Paige et al., 2009], which has well-characterised directional reflectance, allowing the reflected flux hitting the detectors to be calculated accurately.

3.4.3 Data Products

Data Product	Description
Level 1A	Calibrated radiances and housekeeping data
Level 1B	Calibrated radiances and housekeeping data merged with project-supplied geometry and timing information
Level 2	Gridded (Lat, Lon, Local time) global

	surface temperature and annual max, min and average surface temperature in query-able online database
Level 3	Gridded derived global fields: Lambert albedo, fine component thermal inertia, anisothermality, rock abundance, silicate mineralogy in queryable online \ database
Level 4	Polar resource products: maps of permanently shadowed regions, localized maps of derived surface and subsurface temperatures, illumination levels, water\ ice near-infrared reflectance maps for all regions potentially containing cold-trapped volatiles

Table 3-3: Description of the Diviner data products, taken from the Diviner website [unknown year]

As the LRO mission was designed primarily to supply engineering information for planning future human lunar exploration, there is a requirement for relatively rapid delivery of calibrated datasets to the science community. Calibrated, useable data (e.g. Level 1B, Table 3-3) were made public, via the NASA Planetary Data System (PDS), only six months after the mapping orbit began, with deliveries every three months thereafter. Derived, gridded products are released to the PDS every year. This is in contrast to, for example, M^3 where the first data taken (from 18th November 2008 to 14th February 2009) were not made available until June 2010 [Lundeen et al., 2008].

3.4.4 LRO Orbit Configuration

The LRO spacecraft was operated for its first year as an exploration mission, under the control of the NASA Exploration Systems Mission Directorate (ESMD), after which it was transferred to the Science Mission Directorate (SMD) for the remainder of the mission. This had implications for the choice of orbit and operations (e.g. targeted observations of possible future landing sites).

3.4.4.1 LRO Program under the Exploration Systems Mission Directorate

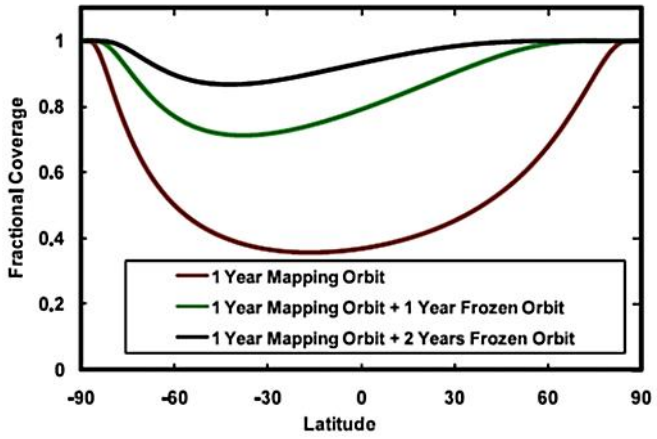

Figure 3-8: Predicted coverage of the surface at 10 am - 2 pm local lunar time for three possible orbit configurations by Paige et al. [2009].

After lunar orbit insertion, a commissioning phase took place during which the elliptical capture orbit was transformed into the 50 km circular mapping orbit. During this transition, the instruments were switched on and checked that they had survived launch and were working correctly. The one-year mapping orbit began 15th September 2009. The spacecraft flew in a roughly polar orbit, passing over or very close to the north and the south lunar pole approximately every two hours. The orbital plane was roughly fixed in inertial space (i.e. with respect to the stars), meaning that the Moon effectively rotated under the spacecraft

once per 28 days, with slight change in local time of day. After six months, measurements had been at all times of day. Diviner's swath width at most latitudes is too narrow for surface tracks to overlap, hence measurements made over many years will be required to map the surface at full resolution at multiple times of day [Vondrak et al., 2010] (Figure 3-8).

3.4.4.2 Science Mission Directorate

With the end of the ESMD supported mapping phase, several extended mission scenarios have been proposed [Vondrak et al., 2010; Tooley et al., 2010]. Currently the first year of the SMD is retaining the 50 km mapping orbit, but future plans have not been finalised, as of May 2011. Higher resolution measurements can be made from lower orbit but more fuel is expended to maintain the spacecraft position, whereas an elliptical orbit, such as that during the commissioning phase, would enable the spacecraft to remain in orbit for up to ten years, increasing temporal resolution (e.g. to map seasonal variations) and allowing opportunities for other observations to be made (e.g. lunar eclipse measurements).

3.5 Conclusions

A multi-channel radiometer such as Diviner should be easily capable of meeting the specified objectives of the LRO AO; however this may be compromised if the problems of MCS also affected the performance of Diviner flight instrument. To ensure that the instrument is able to meet the requirements, the flight instrument needed significant ground testing prior to launch. In particular:

- Some of the filters and blockers had not had their spectral responses measured. The mesh filters that in Diviner channels B2 and B3 needed measuring together as

stacks, as they are in the instrument, and the KCl blocker needed to be measured across the spectral range of the A1-A6 channels.

- All the Diviner (and MCS) mesh filters needed investigating for possible spectral broadening when measured in a way that replicates the optical design of the instrument.

- The complete instrument required thermal vacuum testing and field of view calibration to ensure that it can operate optimally in a space environment to the spatial and radiometric accuracy set out in the instrument calibration specifications (Table 3-2).

4 Diviner Instrument Calibration

4.1 Introduction

As discussed in the previous chapter, both during assembly and after the complete instrument had been assembled the Diviner instrument required a robust set of ground tests to demonstrate that its performance would allow it to return the data necessary to meet the science goals (Section 3.3.1) prior to launch. Due to time constraints during the ground test campaign at JPL and based on the previous experience with the MCS instrument some additional tests on the performance of the spectral filters were also necessary. The author's involvement in the filter performance tests and analysis of the radiometric calibration of the complete instrument are described in this chapter.

Prior to the launch of Diviner, the constituent parts of the instrument required testing. In particular, AOPP was responsible for the construction and testing of the two focal plane assemblies and integration of the filters within them. The spectral responses of most of the filters, windows and blockers were measured prior to instrument integration by Cardiff and Reading Universities, but due to time and measurement apparatus constraints some had not. Once the instrument had been constructed, the calibration of Diviner could proceed. This was performed at the Jet Propulsion Laboratory (JPL) in Pasadena, California, USA, from December 2007 to January 2008, during which time the instrument was subjected to various tests to assess how it would perform when in lunar orbit. These tests consisted of [Paige et al., 2009]:

- Field of view (FOV) calibration, to determine the angular extent of each pixel's FOV for accurate re-construction of surface maps once in orbit.

- Radiometric calibration, to ensure that the detectors inside the instrument correctly measure raw counts that can then be converted into radiances and subsequently surface temperatures.
- Channel spectral response measurements, to check instrument filter spectral responses were as expected post-instrument integration, simplifying the conversion from radiance to brightness temperature and confirming the performance of the mineralogy spectral channels.
- Thermal balancing and cycling, to ensure the instrument would perform as desired under all possible lunar orbit conditions with minimum internal (or at least slow compared to the measurement cycle and well characterised) thermal drift.

The instrument testing was performed by a large team comprising members of the Diviner operational, engineering and science teams, including the author and other members of AOPP. The analysis of the data gathered during the tests was then shared between team members, with the detector radiometric linearity analysis performed by the author. Also, measurements of several filters that were not carried during testing at JPL were completed as part of this project. Specifically, the spectral responses of the KCl blocker and the B2 and B3 filters were measured, and work was done to investigate if the spectral broadening that affected the MCS instrument could be observed in the Diviner mesh filter assemblies (i.e. channel B1-B3).

4.2 Filter Measurements

4.2.1 Introduction

As described in the previous chapter, one of the key requirements for the correct functioning of Diviner is to have filters with well-defined spectral responses. Blocking filters are also

required to remove any out of band spectral leaks, which therefore must also be measured. Before describing the measurements made, however, some details are provided here of the FTIR Spectrometer used to make the measurements.

4.2.1.1 The Brüker IFS66v Fourier Transform Infrared Spectrometer

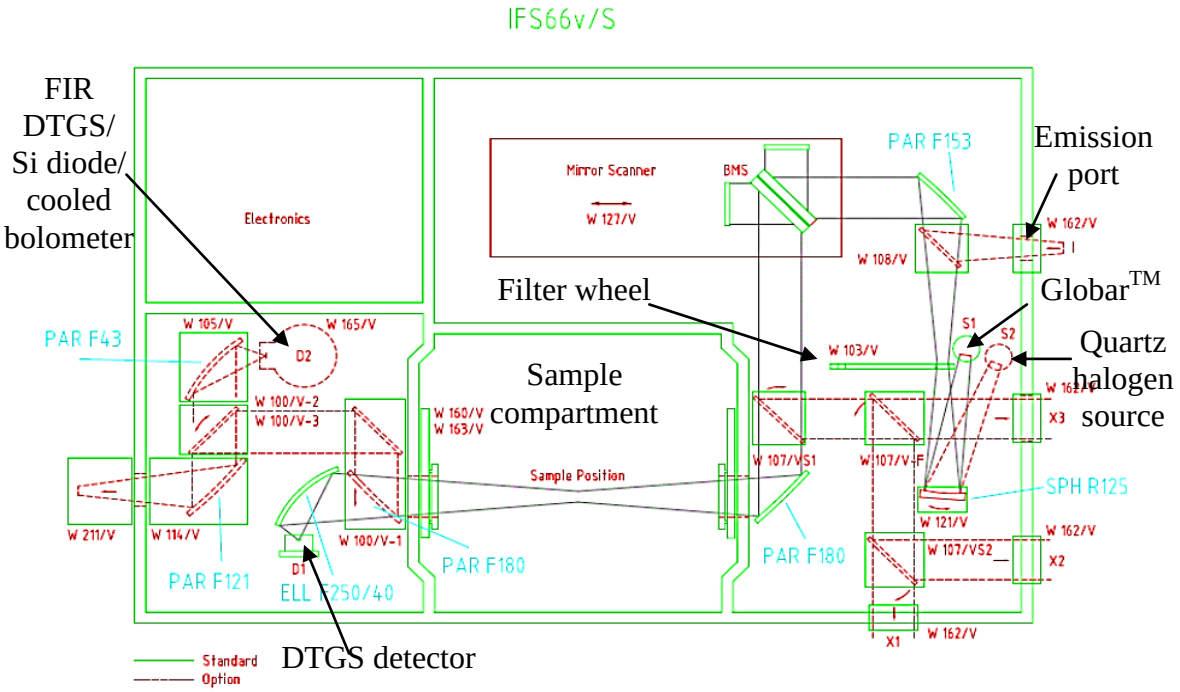

Figure 4-1: The optical layout inside the Brüker IFS 66v FTIR spectrometer, with the main parts labelled, from Brüker Optics Ltd. © [personal communication, 2008]. Almost all of the optional parts (dotted red line) are installed in the instrument at AOPP.

Spectrometer Component		Spectral Range
Beamsplitter	Quartz	14000 - 5500 cm^{-1} (μm)
	KBr	7500 - 370 cm^{-1} (μm)
	Multilayer Mylar	650 - 30
Radiation Source	Quartz Halogen	30000 - 4000
	Globar™	7500 - 30
Detector	Si Diode	Visible/NIR*
	DTGS	Some NIR/MIR/Some FIR*
	FIR DTGS	Some MIR/FIR*

Table 4-1: Brüker IFS 66v FTIR components and their spectral ranges, from the Brüker IFS 66v user's manual. *no figures given.

The primary instrument used at Oxford to characterise the filter material was a Brüker IFS 66v Fourier Transform Infrared (FTIR) Spectrometer (Figure 4-1). It consists of several broadband radiation sources, a Michelson interferometer containing a scan mirror, a beamsplitter, a sample compartment and several detectors. As the scan mirror moves, radiation from the source is modulated into an interference pattern, which then passes through the sample compartment and is recorded by the detector. A computer then performs a Fourier Transform on the measured interferogram to convert it into a spectrum.

The beam in the Brüker IFS 66v FTIR spectrometer converges with a focal ratio of f/4.7 in the sample compartment (Figure 4-1), with the object under investigation placed perpendicular to the beam centre at the point of convergence. An additional repeat measurement can be made to ensure that the spectrometer calibration had not altered during the investigation. Each radiation source and detector functions over a different spectral

range (Table 4-1), so the measurements are made using several different configurations to cover the entire the spectral range.

4.2.2 KCl Blocker

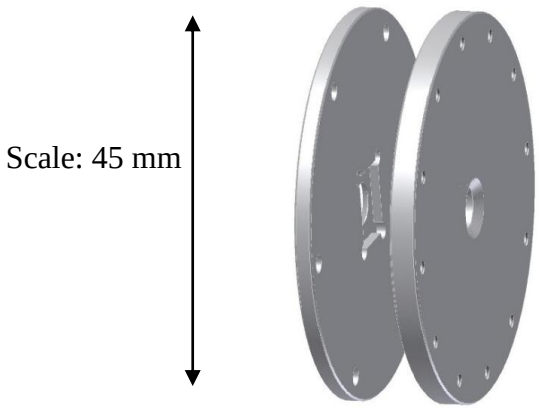

Figure 4-2: Autodesk® Inventor™ CAD drawing of the filter holder manufactured to hold the KCl blockers in the path of the beam inside the spectrometer. To prevent damage to the windows, the holder was made entirely of PTFE, a soft plastic, to avoid scratching the parylene coating.

The KCl blocker in Focal Plane A (FPA), covering channels A1-A6, was only measured by Reading University from 7000 - 250cm^{-1} (1.43 - 40μm), which covers the spectral range of channels 3-6 but not all of channels 1 and 2. Using the Brüker IFS 66v FTIR spectrometer at AOPP, this spectral range could be extended out to 15500 cm^{-1} (645 nm), covering much more of the spectral range of the solar reflectance channels. While this measurement was later repeated during instrument calibration at JPL, it was useful to confirm that: [1] the KCl blocker behaved as expected, and [2] the spectrometer worked in both MIR and NIR, proven by the good overlap of transmission spectra in the three spectral regions and were a good match to the measurements made at Reading. Prior to the start of this project, the

spectrometer had been out of use and had only recently been refurbished, so these measurements provided an essential check of the instrument's measurement reproducibility.

The flight unit focal plane assemblies had already been shipped to JPL for integration, so flight-spare filters were measured instead. Due to the delicacy and flight-ready nature of the blocker, a custom holder with a 10 mm diameter aperture was required to hold the window in place (Figure 4-2). The hygroscopic KCl had been anti-reflection coated with parylene, and so this was constructed of PTFE to avoid scratching of the protective coating.

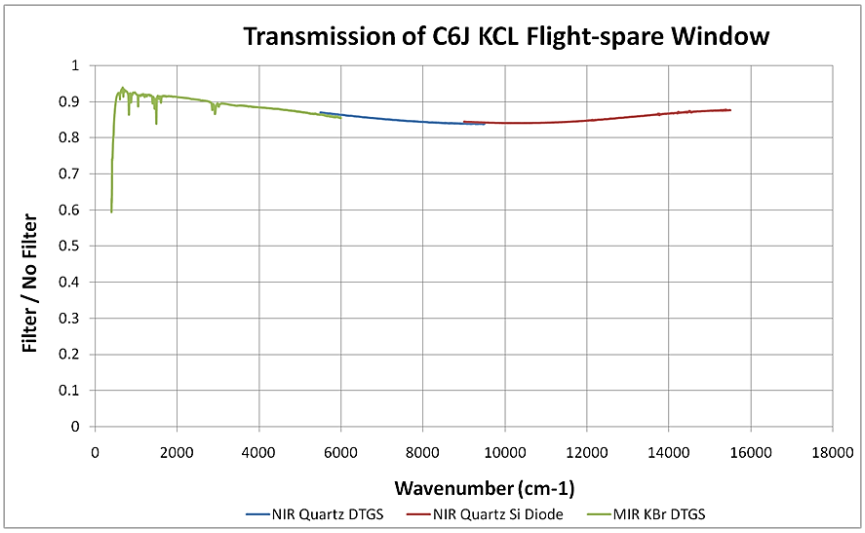

Figure 4-3: The transmission properties of a KCl blocker. Due to the large spectral range, several spectrometer configurations were needed. The spectral features are due to the parylene coating, which is used to protect the hygroscopic KCl from atmospheric water.

Transmission spectra were obtained by making two measurements using the same spectrometer configuration: one with and one without the KCl blocker in the beam of the spectrometer, a simple ratio was then used to calculate the transmission profile. 100 scans were made per measurement at 4cm^{-1} resolution, with suitable gain settings, aperture sizes and scanner velocities chosen so that sufficient signal was recorded with the KCl blocker in position but did not overload the detector when removed. The spectrometer uses a HeNe

reference laser with a wavelength of 633nm, hence the cut-off at 645nm (15500 cm^{-1}), with the longest wavelength dependent on the cut-off of the KBr beamsplitter. Insufficient signal passed through the KCl to allow a measurement to be made in the FIR using the Mylar beamsplitter. The transmission spectrum is shown in Figure 4-3.

4.2.3 B2 and B3 Mesh Filter performance: Avoiding the Problems with MCS

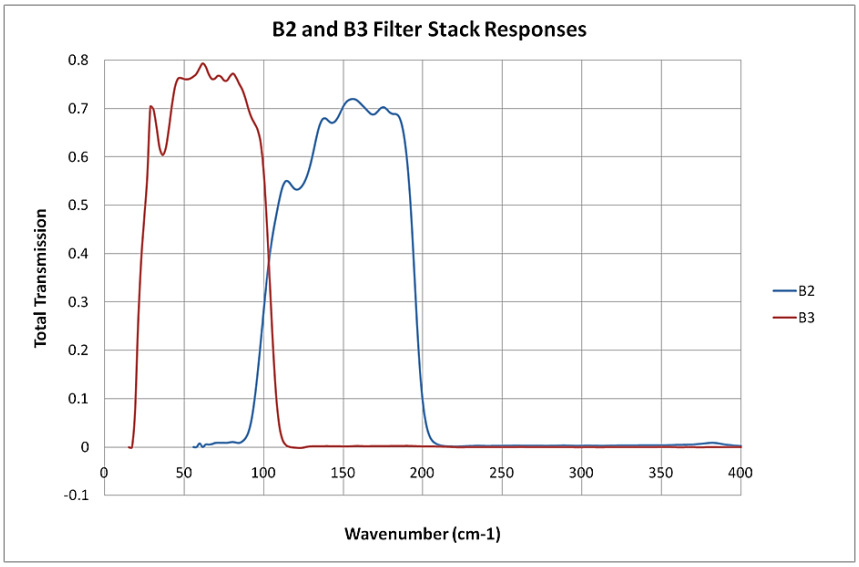

Figure 4-4: B2 and B3 transmission profiles measured during this project. A small leak can be seen in B2 around 380 cm^{-1} (26 µm); however the quartz blocker will remove this.

The B2 and B3 filters are composed of individual meshes of high- and low- pass filters that are stacked together to produce the required spectral response (Section 3.3.4.2). Each mesh was measured individually after manufacture by Cardiff University, but not measured (prior to delivery to Oxford) as complete stacks. After integration into Diviner, the spectral responses of the channels were measured as stacks as part of the calibration process at JPL using a grating monochromator from 0.2 - 56 µm. Whilst adequate to test the response of the A telescope and B1 filters, this range was too limited to characterise the B2 and B3 channels, so spectral responses of the stacks measured in the lab were required to complete

the calibration. These were measured using the same method as for the KCl blocker, except that due to the importance of these measurements, 500 scans were added together to reduce errors due to noise to significantly less than 5%, using the FIR configuration of Multilayer Mylar beamsplitter, Globar^{TM} source and FIR DTGS detector (Table 4-1). The measured transmission spectra of the B2 and B3 flight-spare filters are shown in Figure 4-4.

4.2.4 Quartz Blocker

An attempt was made to measure the Quartz blocker in this project, located in front of the B2 and B3 channels, but the spare sample was too small to allow sufficient radiation to pass through for a measurement to be made. Due to time constraints, this blocker was made from a remainder piece of stock material, that was found to have the required attributes: to block radiation of wavelengths < 50 μm, and have very high transmission in the B2 and B3 region above 50 μm. Due to this somewhat ad-hoc blocker selection, no flight-spare part exists except for small off-cuts, hence the difficulty making spectral measurements. For calibration purposes, it was assumed that the transmission was high and spectrally flat across the B2 and B3 spectral ranges; reasonable when considering the expected performance of the quartz blocker from theoretical calculations [Bowles, personal communication 2008]. Quartz's spectral response varies depending on its type (e.g. amorphous vs. crystalline; trigonal vs. hexagonal) and sample thickness; hence while other samples are available for measurement, their spectral response will differ and be unrepresentative.

4.3 Mesh Filter Broadening

As described in Section 3.3.4.3, the spectral response of the MCS B3 mesh filter was found to have broadened significantly between laboratory measurements post manufacture and those made of the channel instrument during final testing at JPL. As Diviner has an identical

optical design and also utilises mesh filters (albeit of different wavelengths and significantly wider band-pass), it was important to investigate if such broadening was likely to occur again. This was compounded by the inability to measure spectrally the B2 and B3 filters after integration into Diviner, meaning that if the spectral response had changed, the new filter band-passes would be unknown.

This work began prior to this project, carried out by members of the Diviner team[6], with Bowles et al. [personal communication, 2007] observing a small effect in the LRO demonstration model B3 filter around 12 - 17 μm, far below the intended cut-on wavelength of 100 μm, but only when the detector is placed extremely close to the filter (Figure 3-7). This is believed to be caused by random scattering of the out-of-band radiation by the mesh filters, explaining why a larger amount of this radiation hit the detector when it was closer to the filter [Bowles, personal communication 2007]. As the Diviner filter-to-detector distance is extremely small (on the order of ~100 μm), this could have also affected the performance of Diviner, therefore additional non-mesh quartz spectral blockers were added which should significantly reduce this. Therefore the primary concern was of spectral leaks and/or changes in filter band-passes shape, which will not be stopped by the blocker, such as occurred in the MCS instrument. As an integral part of the calibration, any significant changes in spectral shape due to the optical design of Diviner needed to be investigated.

The setup had to effectively recreate the optical layout of Diviner, with a similar f/# number of 1.7 and a variable filter-to-detector distance to allow a systematic investigation of how the spectral shape is modified by the detector filter geometry. Measurements of the longest wavelength channels required the use of the FTIR spectrometer, as the spectral range of AOPP's monochromator is limited to a maximum of ~50 μm, so the setup of Bowles et al.

[6] Hence the large number of references to private, internal team communications. This data is available from the instrument development logs etc. on request.

could not be used. A detector capable of measuring interferograms with adequate response in the FIR also had to be found along with the development of the necessary readout electronics to interface this to the spectrometer. To achieve this, a new experimental setup was developed, described below.

4.3.1 New Apparatus to Investigate Mesh Filter Broadening

Since the final focus in the Diviner instrument uses an f/# 1.7 beam whereas the beam in the spectrometer's internal sample compartment (Figure 4-1) converges with a focal ratio f/4.7, an additional elliptical off axis parabolic focusing mirror was required to change the spectrometer beam passing through the filter and detector under test. Unfortunately a suitable mirror was not available as an off the shelf item so an off-axis paraboloid (OAP) with a focal length of 25.4mm was used instead. This produced a beam with a convergence of approximately f/1.4, closer to the Diviner optical setup and with a spot-size at the focus less than the width of the detector element (2 mm). This parabolic mirror was placed in the sample compartment, directing the beam perpendicularly with the detector at the focus.

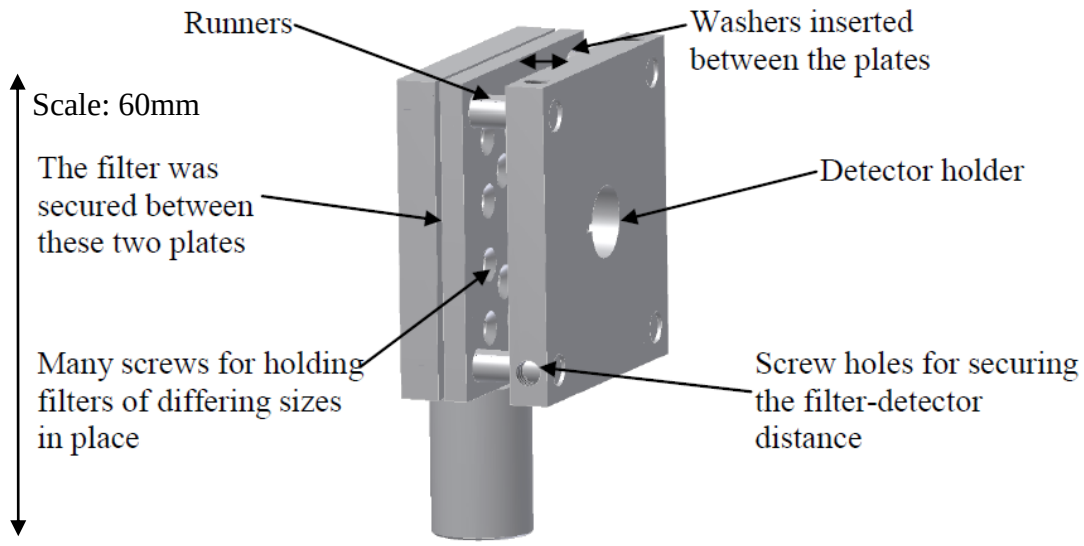

Figure 4-5: A CAD model of the filter holder, designed by the author, with the main parts labelled.

To investigate the effect of varying the detector/filter distance a filter holder was constructed that allowed the distance from filter to detector to be varied from 1000 to 100 µm. The filter holder consists of two plates (Figure 4-5): one holds the detector and remains fixed, while the other holds the filter and is attached on runners, allowing it to slide, varying the distance between the plates. The detector electronics were housed in an electrically shielded box behind the detector, with the output connected directly to the spectrometer's detector input port.

4.3.2 Detector Selection

In order for the detector to be placed as close as 100µm from the filter, the detectors already installed in the spectrometer could not be used, as they have integrated housings (detector 'can') and electronics that can't be removed without destroying the component. Detectors are usually supplied 'canned' by the manufacturer with a filter window placed around the

detector element that prolongs the life of the detector (by e.g. packing the device in dry nitrogen gas) but can reduce the spectral range of the detector (depending on the entrance window) and prevents anything from getting to within a few millimetres of the detector element, again to prevent damage. Therefore, in order to measure at such short distances and across a wide spectral range, it was essential to find a suitable detector and to remove the can and window. Another requirement, for use in the Brüker IFS 66v, was that the detector must have a reasonable response at the relatively high scan frequency (1.6kHz) imposed by the Brüker spectrometer in order for the interferogram to be recorded accurately, ruling out the use of thermopiles as used in the actual Diviner instrument.

Three different pyroelectric type infrared detectors were tested: an Infratec® LIE-332f, an Infratec® LIE-502 and an Infratec® LIE-312f. The latter two were already on loan from Surrey Satellites Technology Limited (SSTL), and came with the can already removed and with detector pre-amplifier electronics integrated by SSTL. The LIE-332f was carefully de-canned on a lathe and a suitable pre-amplification circuit was designed to allow the detector to be connected to the Brüker IFS 66v's analogue to digital converter input.

4.3.2.1 Interfacing the LIE-332f to the Brüker Spectrometer: Amplifier Circuit

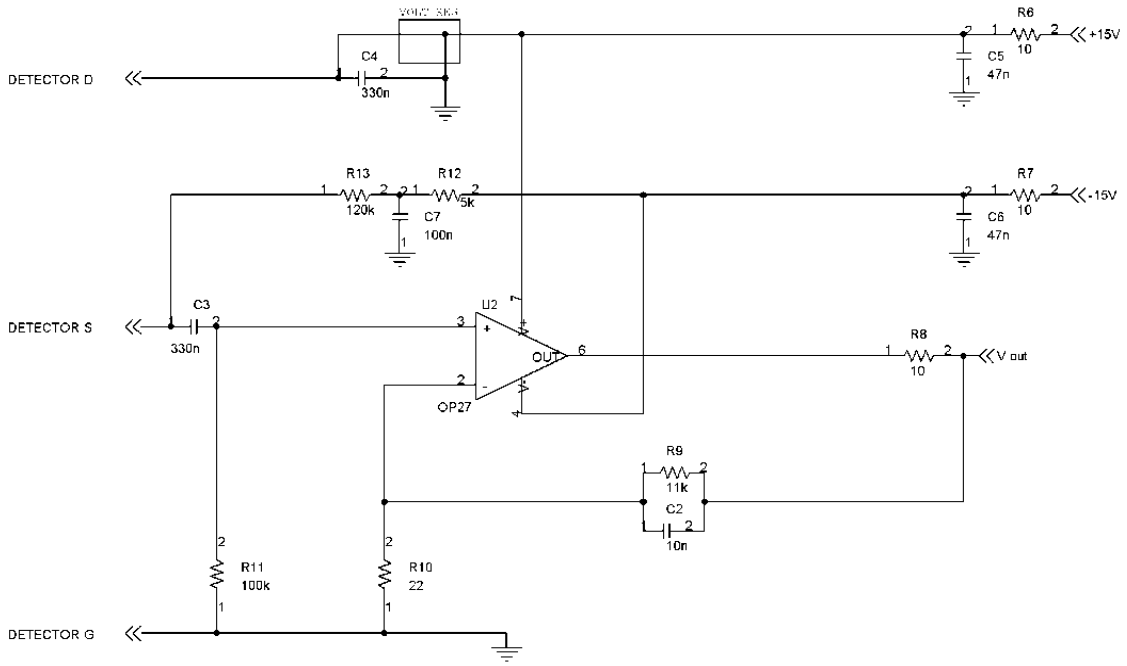

Figure 4-6: A schematic diagram of the pre-amplification circuit constructed for the LIE-332f detector.

The LIE-332f detector required a power supply and pre-amplification of output signal for integration into the Brüker FTIR spectrometer. Before the can was removed from the LIE-332f-16, an initial circuit was prototyped. The bias voltage supply circuit for the detector was taken from the Infratec® detector datasheet, and the amplification and high pass filter were based on the circuit supplied by Brüker for their own detectors. The high pass filter reduces low frequency noise from the recorded interferogram. Initial spectra recorded using this circuit exhibited large periodic spikes, which were attributed to a combination of 50 Hz mains noise and to pick-up in the secondary gain circuit inside the spectrometer itself. The spectrometer gain circuit has a computer selectable gain stage, amplifying the voltage from the detector circuit before recording the signal and calculating the Fourier transform. This problem was solved by adding a voltage regulator to the circuit and by switching off the

spectrometer's own internal gain circuit, thereby decreasing the signal level of the measured spectra but removing the spikes. The final circuit design is shown in Figure 4-6.

4.3.2.2 Detector Testing and selection

Initially, the default Brüker detectors (which are reasonably assumed to have uniform response over their given spectral range) were measured with various beamsplitters in order to distinguish whether low responsivity in several spectral locations was due to the transmission properties of the beamsplitter or due to the response of the detectors being tested. Then the Infratec® detectors were measured and compared to the default Brüker detectors, to check that they had an adequate response across the spectrum. The mirror scanner velocity in the interferometer was also varied to determine which detectors worked at the higher scanner mirror speeds, and therefore took the least amount of time to record an interferogram. The LIE-502 was found to only function well at low mirror scanner velocities, and so was discounted. The LIE-332f performed very similarly to the LIE-312f loaned from SSTL, and so this was chosen as the detector and electronics had already been made. The LIE-312f has a gold-black coating on the detector element and a diameter of 2 mm.

4.3.3 Accurately Determining the Detector to Filter Distance

With a suitable detector selected, the next important part of the setup was accurate measurement of the filter/detector position. To achieve this, a coordinate measuring machine (CMM) was used to determine the relative distance between the front of the detector element and the plate onto which the detector is mounted. The detector element was found to be sufficiently flat, at an angle of 0.67 ± 0.05 degrees to the plate, which equates to an error of 23 ± 2 μm across the width of the detector. The measurements made

on the CMM were then used to determine how plate-to-plate distances correspond to filter-to-detector distances, allowing accurately machined washers to be made that sit between the plates to keep them the desired distance apart. The distance between the detector and the plate where the filter is attached was found to be -1090 ±10 μm (i.e. if no washer is present, the detector element would protrude this distance through the filter (Figure 4-5). Therefore, for filter to detector distances of 50, 100, 200, 500 and 1000 μm, washers of widths 1140, 1190, 1290, 1590 and 2090 μm were required. These were made by machining mild steel washers to within 100 μm of these tolerances, and then grinding down to within ±10 μm of their required width using a surface grinder. The uncertainty in the plate width was ±10 μm, giving a combined uncertainty, by adding in quadrature, of $(23^2 + 10^2 + 10^2)^{1/2} = 27$ μm.

4.3.4 Filter Measurement Procedure

The OAP and filter holder, without filter, were aligned correctly by switching to the quartz-halogen source (visible) in the spectrometer and manually adjusting the distance to find the focus of the beam. The source was then switched to the Globar™ and aligned by maximising the interferogram signal on the detector. Background readings (without a filter present) were taken between all filter measurements, with every washer size. The 50 μm washer was not used, as the detector had a small gold wire embedded into the element, which was in danger of touching the filter at such a short distance away. Before carefully mounting the individual filters that made up a complete filter stack in the correct order, the holder was washed with acetone and left to dry, to keep the filters pristine.

The main cause of differences between measurements was from the jig not being in exactly the same position each time, which did not affect the spectral shape measured, but occasionally caused the amplitudes of spectra to vary by up to 10%. To prevent this from affecting the final filter responses, every spectrum taken was normalised to its peak value

prior to analysis, as the aim of the experiment is to determine if the spectral width of the filter band-pass varies with filter-detector distance.

4.3.5 Filter Measurement Results

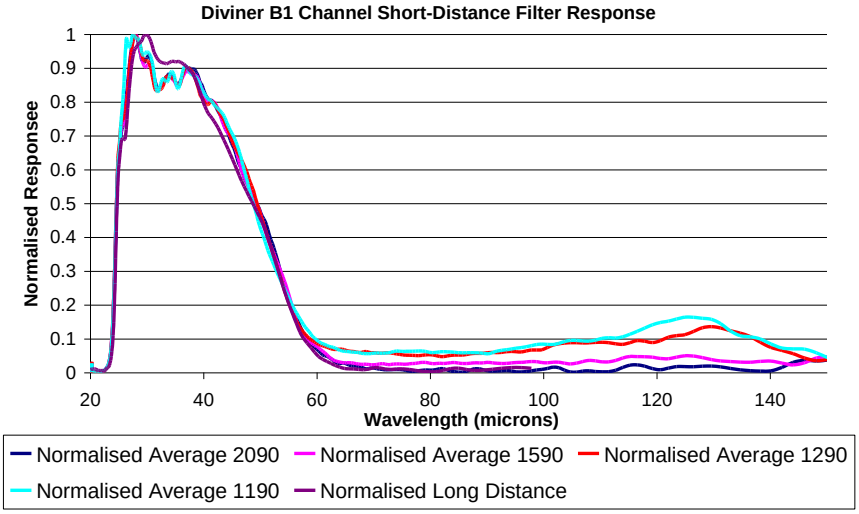

Figure 4-7: The spectral response of the B1 channel at various filter-to-detector distances. No systematic broadening of the channel is seen as the distance is reduced, but a plateau region is observed at beyond the long-wavelength cut-off. This plateau can clearly be seen to increase as the filter-detector distance is reduced, indicating that this is likely to be a spectral leak.

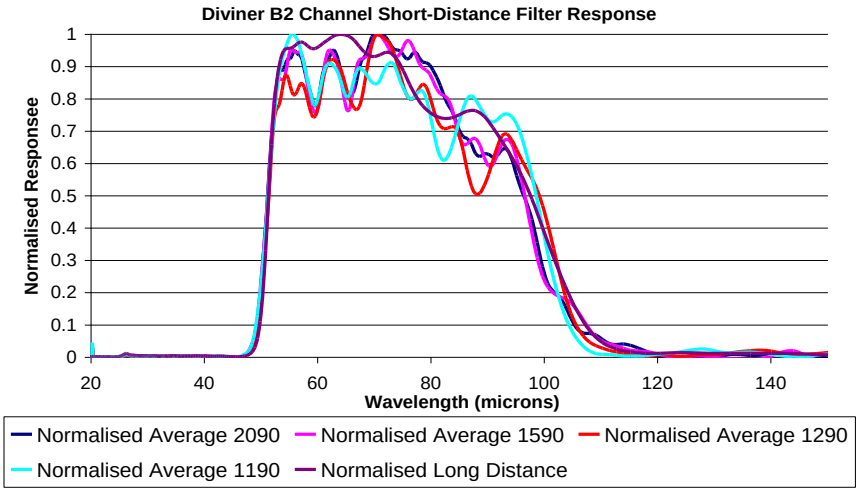

Figure 4-8: The B2 channel measured at various filter-to-detector distances. While there are considerable differences between the measurements of the long-wavelength cut-off, no trend is seen from smallest to greatest filter-detector distance. The differences could be due to "channelling" (Section 4.3.5) as can be seen throughout the entire spectra, or due to the low spectral resolution at high wavelengths.

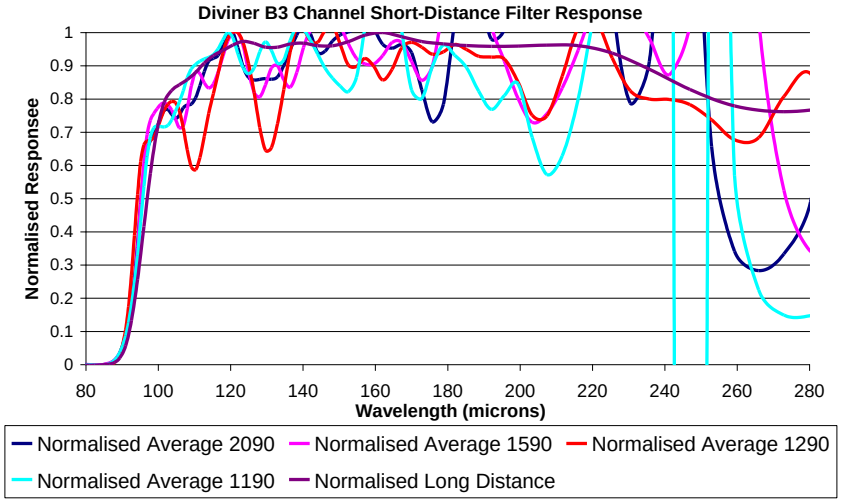

Figure 4-9: The B3 filter response at various filter-detector distances. The oscillations observed here, most likely due to channelling, are significant, therefore only the short-wavelength switch-on is shown. The lower signal in the FIR means that the effects of channelling appear to increase with increasing wavelength, to the extent that the long-wavelength cut-off is indiscernible from these measurements.

As these filters operate in the FIR, the spectra were recorded with the Mylar beamsplitter and Globar™ source (Table 3-1), using a 5 mm aperture and mirror velocity of 1.6 kHz. The number of co-added scans varied between filters: as B1 was the shortest wavelength of the three (25 – 41 μm) it had a high signal throughput, and so only 100 scans were needed, whereas 200 were averaged together for B2 (50 - 100 μm), and 400 for the B3 (100 – 400 μm) filter. 50 scans were used for the background measurements. Each filter was measured three times per washer and averaged. The filter transmission for each washer was then found by dividing the averaged filter response by the averaged background for that specific washer. The results of the B1 filter are shown in Figure 4-7, B2 in Figure 4-8 and B3 in Figure 4-9, with the 1190 μm washer corresponding to a detector-filter distance of 100 μm, 1290 to 200 μm, 1590 to 500 μm, and 2090 to 1000 μm.

The observed oscillations in the band pass are most likely to be due to channelling. This is due to multiple reflections or Fabry-Perot fringing between the filter layers or within the detector element itself, and appears to increase at longer wavelengths, made more prominent by the reduced signal in the FIR. In the B3 channel, this channelling, combined with noise, dominates the spectra taken, making any spectral leaks impossible to be identified at longer wavelengths.

4.3.6 Filter Performance Conclusions

The results suggest that there could be a small amount of spectral broadening seen in the B1 filter but that in general the effect is small and is of a much smaller magnitude than the effect seen in MCS. It should be noted though that the spectral leak seen in the B1 filter will not change the response of the channel in the actual instrument though, because the B1

channel has a blocker with a long-wavelength cut-off at 50 μm, stopping all radiance at wavelengths below that. The B2 and B3 results are less conclusive. At longer wavelengths the radiance incident on the detector is lower, reducing the signal-to-noise ratio of the interferogram, making the results more susceptible to electronic noise. Channelling, caused by the interference of reflected waves within the filters, superimposes a sinusoidal wave onto the resulting transmission spectrum, which can occur when a FTIR Spectrometer is used [Sinclair, 2000], depending on the optical setup and type of filter under investigation. This could explain the origins of the sinusoidal wave apparent in the spectra, which appears to be amplified by the setup, and which increasingly obscures the filter spectral responses as the radiance decreases at longer wavelengths. This decrease in radiance due to the roll-off of the Planck function also helps to reduce the measurement uncertainty though, as the instrument response at very long wavelengths should not significantly affect the response to the scene temperature being viewed [Paige et al., 2009]; investigating the linearity of Diviner's detectors will help to confirm this. This forms part of the radiometric calibration and is discussed in the next section.

4.4 Radiometric Calibration of the Diviner Flight Instrument: Detector Linearity

4.4.1 Introduction

With the individual filters for each of Diviner's channels characterised and seemingly free of the difficulties encountered by the MCS instrument, the next step was to carry out and analyse the performance of the complete flight instrument under thermal-vacuum conditions. These tests included field of view, signal-to-noise ratio, noise equivalent temperature testing etc.; the details of which are beyond the scope of this thesis (see Paige et

al. [2009]). This section, however, describes the radiometric calibration performed by the author, using the results from the filter testing described previously.

The aim of this test was to determine if the detector linearity varies with instrument temperature, which will dictate the accuracy by which the instrument will be able to determine surface radiance and hence temperature and CF variations, following the method of Sam Adlen [2004] for MCS.

4.4.2 Testing Procedure

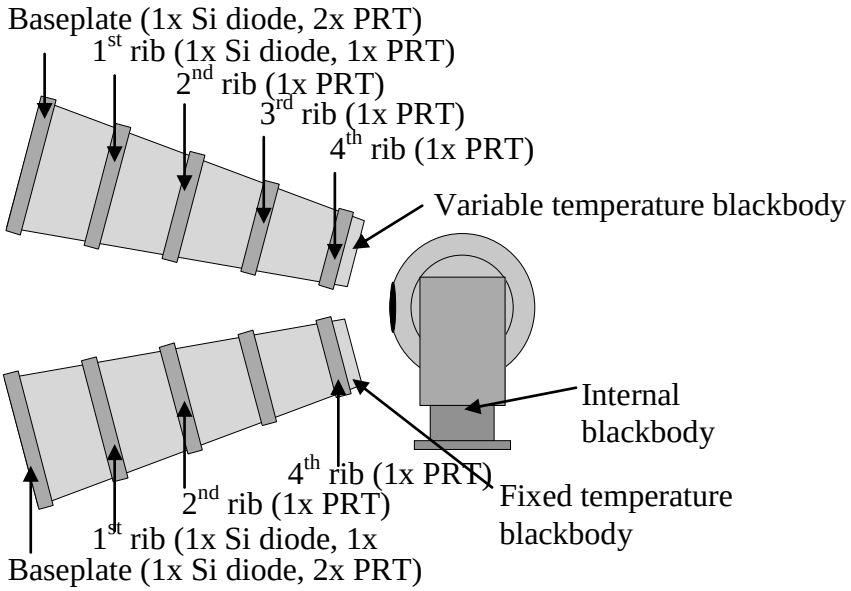

Figure 4-10: Schematic of the Calibration test configuration at JPL, showing the locations of the silicon (Si) diode thermometers and platinum resistance thermometers (PRTs) [Paige et al., 2009].

Radiometric calibration was performed from 12th January 2008 to 16th January 2008 using the same setup as used for calibrating MCS (Figure 4-10). The aim of the test setup was to approximate the measurements and operating conditions that Diviner will experience during

the operational part of the mission. The apparatus was mounted on an optical bench in a vacuum chamber. Inside the vacuum chamber there were internal shrouds around the optical bench cooled with liquid nitrogen to replicate a cold space environment, and two blackbody calibration targets used to replicate the space calibration view and the lunar surface. As described in Section 3.4.2, the instrument is repeatedly calibrated in orbit by observing space and the on-board blackbody between lunar surface measurements, hence this was replicated for the test: one blackbody was held at a constant low temperature, while the other was varied between 20K and 420K to imitate the expected surface temperatures of the Moon. From this, the linearity of each of the instruments channels with respect to wavelength could be found.

4.4.3 Measurement Strategy: Measuring Diviner's Response from the Blackbody Calibration Target Temperatures

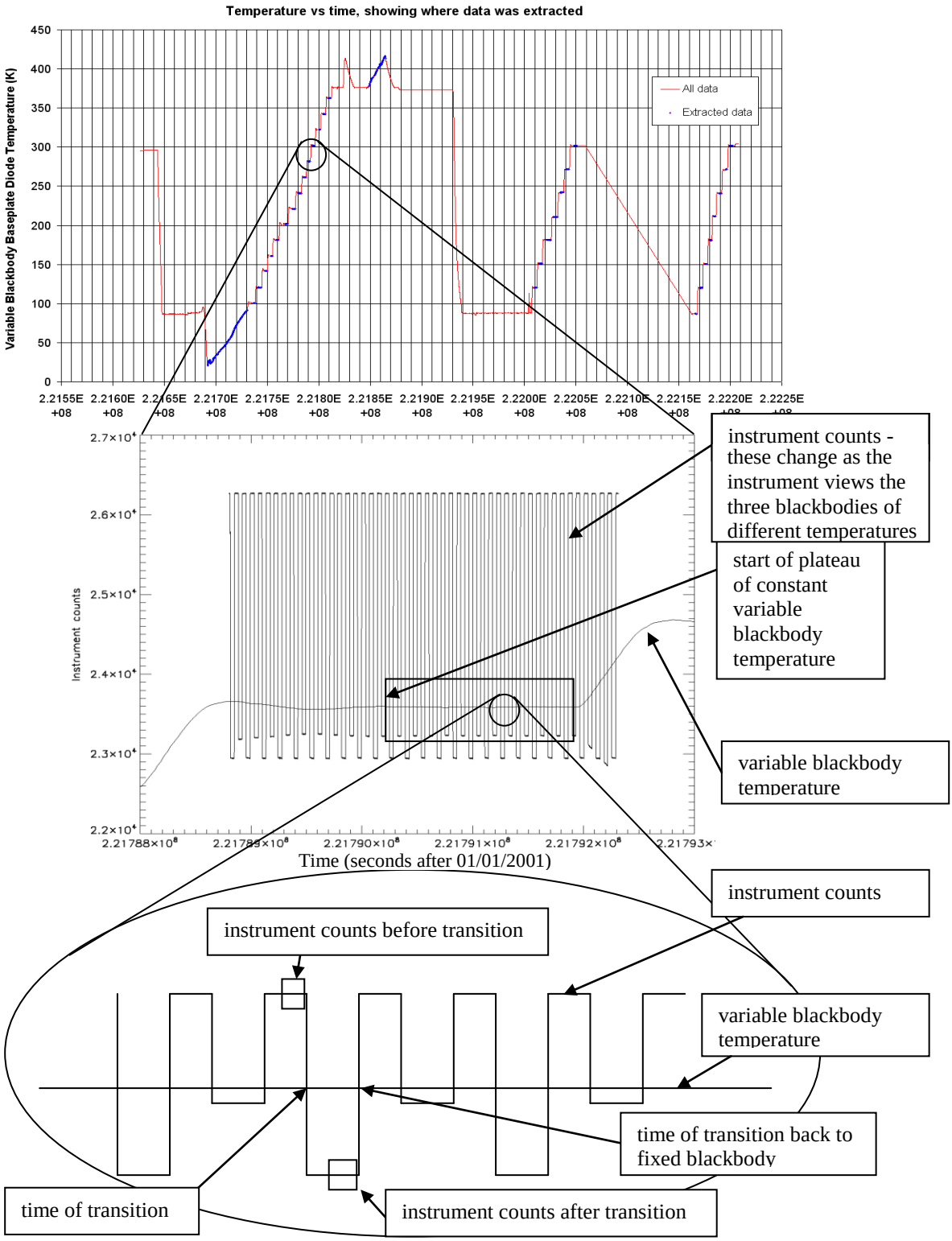

Figure 4-11: Graph (top) showing the variable blackbody temperature over the full time range (red), showing which data were used in the analysis (blue). One particular temperature plateau is then zoomed (middle) with instrument counts overlaid on the variable blackbody temperature plot. This is then zoomed in further (bottom) to show the times where instrument counts were extracted to avoid errors due to thermal lag.

The ‘fixed’ blackbody was used to simulate viewing space and was therefore kept at the constant lower temperature, while the internal blackbody, which is attached to the instrument, was kept at a constant high temperature as occurs in lunar orbit. Practically, the fixed blackbody could not be kept at 3 K, and so was held at 90 K using liquid nitrogen. The temperature of the variable blackbody was increased, first at a constant rate, then in steps, and then at a constant rate again, whilst the instrument was kept as close as possible to 10°C, which has been named “ramp 1”. For ramp 2, the instrument was kept at a constant temperature of 60°C, and the temperature was increased in steps only. Ramp 3 was identical to ramp 2, except that the instrument was at a temperature of 30°C. The variable blackbody temperature ramps are shown in Figure 4-11 (top).

4.4.4 Calibration Target Blackbody Emissivity calculations

The calibration target blackbodies are central to the radiometric testing of the Diviner instrument. As well as knowing the temperature and viewing geometry of the targets, it is also essential that there is a reliable estimate of the emissivity of the targets, which should ideally be as close to 1 as possible across the full spectral range of the Diviner instrument, to determine the radiances measured by Diviner. The emissivity determination was performed in an identical way to the method used for the ISAMS instrument [Nightingale, 1992], as the blackbodies used in calibration were scaled replicas of the ISAMS calibration blackbodies. The entire blackbody cannot be assumed to be isothermal and is therefore divided into ribs (Figure 4-10); each of which contains a temperature sensor. The total blackbody radiance is then a sum of the radiance contribution from each rib, weighted by the average ‘emissive weight’ (See Nightingale [1992] for a complete mathematical description) for each channel, as follows:

$$B(\upsilon_n, T) = \sum_k w_{n,k} \int_\upsilon B(T_k, \upsilon) F_n(\upsilon) d\upsilon \qquad [4\text{-}1]$$

where n corresponds to the *n*th spectral channel (i.e. A1-A6, B1-B3), k corresponds to the *k*th rib of the blackbody (i.e. Baseplate k=1, 1st rib k=2, 2nd rib k=3 etc., see Figure 4-10), $w_{n,k}$ is the emissive weight for each rib of the blackbody, $B(T_k,v)$ is the Planck function of rib *k* with temperature T_k, and F_n is the spectral response of the instrument. The emissive weights vary linearly with surface emissivity, so can be calculated provided the emissivity of the surface of the blackbody is known as a function of wavelength, described in the next subsection.

4.4.4.1 Blackbody Emissivity Determination

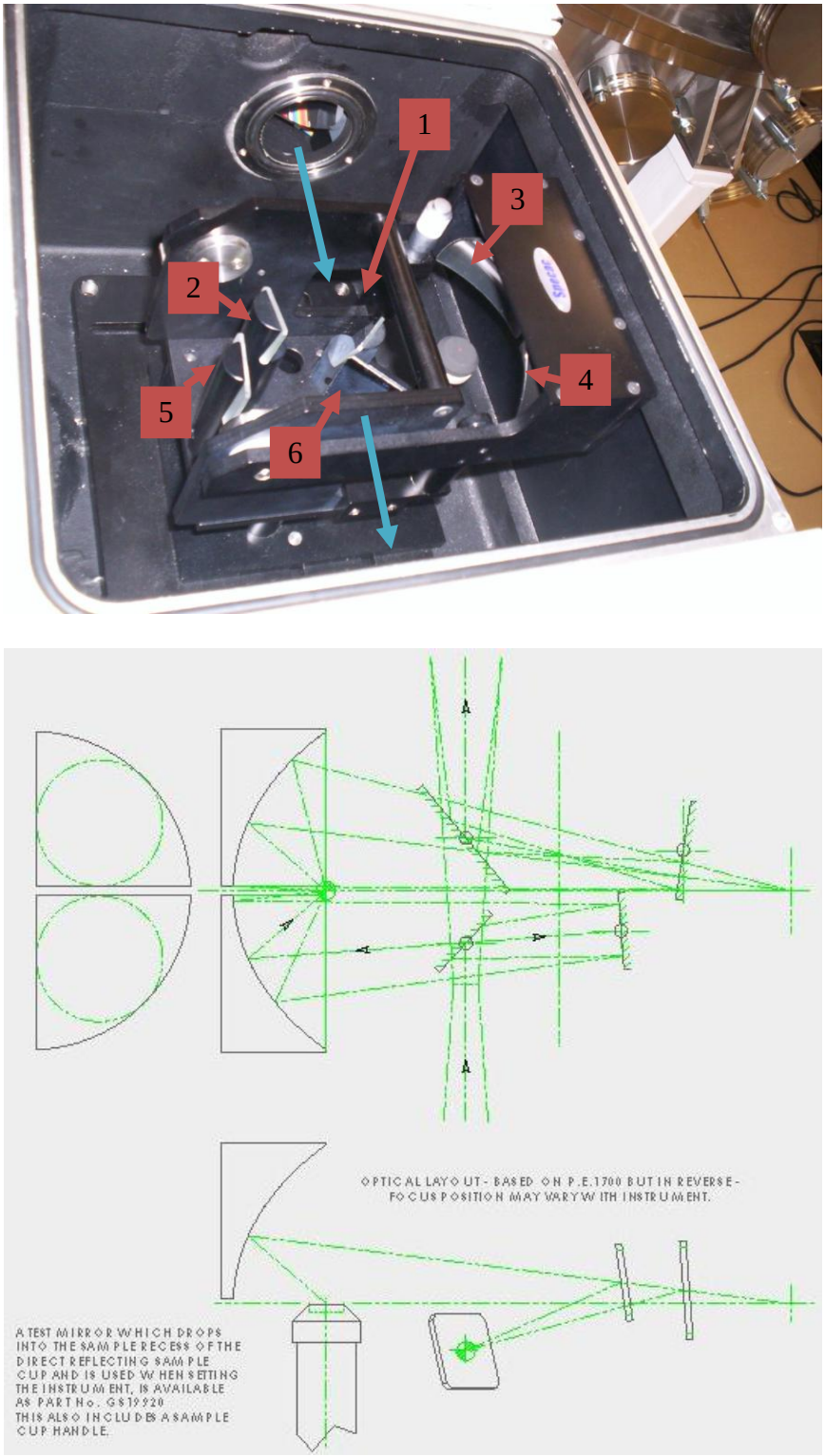

Figure 4-12: Top: Photo of the Specac® Diffuse Selector Accessory showing the input and output beams (blue) and mirrors labelled sequentially in beam order (red). Bottom: A diagram showing how the beam passes through the accessory (Specac ©, private communication 2011).

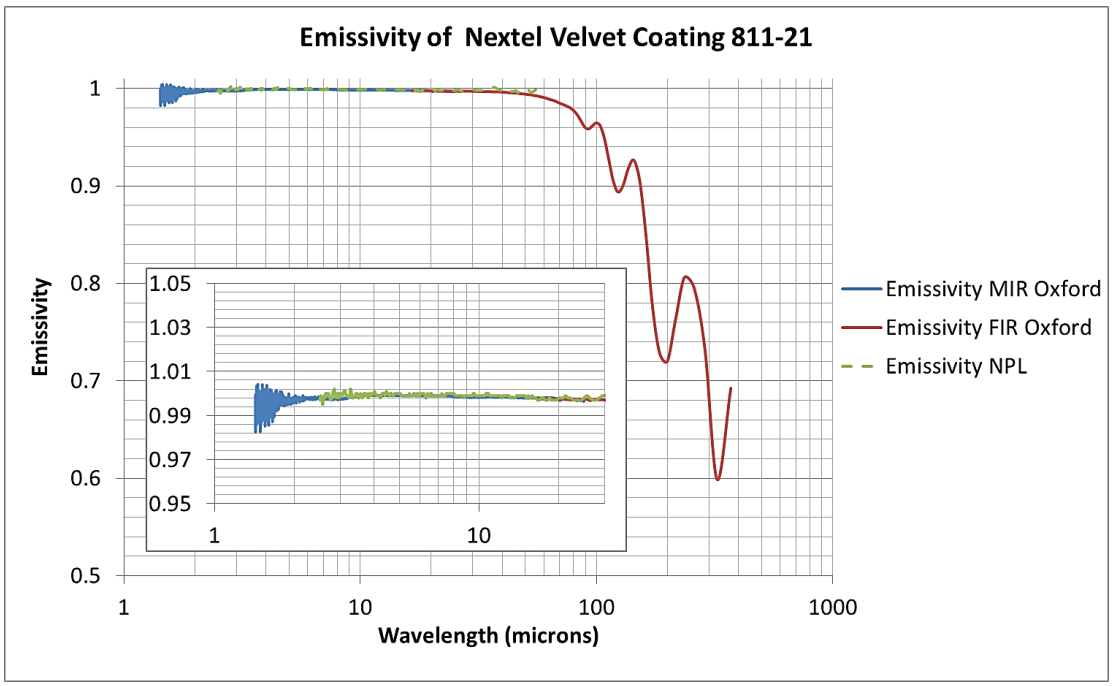

Figure 4-13: Surface emissivity of a sample of aluminium painted with Nextel Black Paint. The green-dashed data were taken by Clarke at the NPL [via Calcutt, personal communication 2008b].

The emissivity of a sample of aluminium coated in Nextel Velvet Coating 811-21[7] was determined at the National Physical Laboratory (NPL) by measuring regular reflectance and using Kirchhoff's Law to convert to emissivity [Calcutt, personal communication 2008b]. Spectra were taken from 4000 cm^{-1} to 180 cm^{-1} (2.5 - 56 μm), in intervals of 20 cm^{-1} from 4000 - 2000 cm^{-1}, 10 cm^{-1} from 2000 - 250 cm^{-1}, and 5 cm^{-1} from 250 - 180 cm^{-1}, which is a relatively coarse resolution compared to a FTIR spectrometer. To obtain higher resolution spectra extended to longer wavelengths to cover all the Diviner channels, the same sample was measured in the Brüker IFS-66v using a Specac® Diffuse Selector Accessory placed inside the spectrometer sample compartment. This accessory directs the beam of the spectrometer onto the sample from a quarter hemisphere and collects the radiation reflected into another quarter hemisphere non-normal to the incident beam (Figure 4-12). While this

[7]A vacuum-compatible high-emissivity paint

bi-conical type of reflectance measurement is not equal to the NPL measurement, it allows the spectra to be extended into the FIR, with the Brüker spectra multiplied by a scaling factor of 1.001 to eliminate the small difference between the two spectra. A small gap was present between the FIR and MIR spectra also, and so the former was also multiplied by a small scaling factor of 0.9985 to force the spectra to overlap. Kirchhoff's Law was again used to convert reflectance to emissivity. The resulting spectrum is shown in Figure 4-13.

Due to the non-uniformity of blackbody emissivity out to longer wavelengths required for Diviner calibration, it was required that equation [4-1] be modified to reflect the wavelength dependency of the emissive weights as follows:

$$B(\nu_n, T) = \sum_k \int_\nu w_k(\nu) B(\nu, T_k) F_n(\nu) d\nu \qquad [4\text{-}2]$$

where all the symbols represent the same quantities as previously described.

4.4.4.2 Calibration Target Temperature Sensors

Using the calculated estimate of the emissivity of the calibration targets accurate silicon (Si) diode and/or platinum resistance thermometer (PRT) temperatures were then required to calculate the radiance of each blackbody target. Although many PRTs were installed throughout the blackbodies, the PRT temperature data were not used, as all the sensors were calibrated only between 91K and 350K (outside the test range of 20 to 420 K). In addition the PRT sensors were also out of calibration since they were last tested in March 2002 [Foote, personal communication 2008]. Only one diode was located in each baseplate and only one diode located in the 1st rib of each blackbody, so for the emissivity calculation it was estimated that the baseplate was at the temperature of the baseplate diode, and all the ribs were at the same temperature as the 1st rib diode. No further data were taken at the time to allow further conclusions to be drawn, but the two diodes on the fixed blackbody showed

good agreement throughout the calibration, with a standard error between the two temperatures of <0.3 K, suggesting that any thermal variations within the blackbodies are minimal when at constant temperature.

4.4.5 Si diode re-calibration

Diode Serial Number	**D73203**	**D69882**	**D73214**	**D73211**
Diode Model	DT-471-SD-10H	DT-471-SD-10H	DT-471-SD-10H	DT-471-SD-10H
Location	Fixed Blackbody Base	Fixed Blackbody 1st Rib	Variable Blackbody Base	Variable Blackbody 1st Rib
Calibration Range	10.0 - 500.0 K	10.0 - 500.0 K	10.0 - 500.0 K	10.0 - 500.0 K

Table 4-2: Detailed descriptions of each of the Si diodes used in the calibration setup [Foote, personal communication 2008].

During the ground calibration test campaign the Si diode voltages were converted into temperatures 'on-the-fly'[8] using a Lake Shore Model 330 Auto-tuning Temperature Controller [Foote, personal communication 2008], which were then logged and the voltages discarded. Unfortunately the wrong calibration curve was used, causing the recorded temperatures to be incorrect by up to 1.5 K. Since each diode had been calibrated individually a specific conversion table should have been used instead of the generic 'Curve

[8] i.e. the calculation was performed automatically by the temperature controller

10’ (see Lake Shore Cryotronics Inc. Form F025-00-00 Revision C [2005] for a full description and coefficients for Curve 10) voltage-temperature lookup table for un-calibrated diodes. Therefore, before the readings could be used, the conversion algorithm was reversed to convert temperatures back into original voltages using the generic curve algorithm provided by the diode manufactures, Lake Shore Cryotronics Inc. This voltage-to-temperature conversion algorithm is, in mathematical terms, a Chebyshev polynomial with calculated fit coefficients based on measurements, but the temperature controller approximates this however, using linear interpolation between voltage set points (see Lake Shore Cryotronics Inc. Form F025-00-00 Revision C [2005]). The voltages were then corrected using the specific calibration curve for each diode, using the Chebyshev polynomial coefficients to convert exactly between the two. While listing all Chebyshev coefficients and voltage-temperature interpolation set-points is beyond the scope of this thesis, some of the technical details of the Si diodes used are shown in Table 4-2. For example, following recalibration, a 44.00 K reading by temperature controller using Curve 10 was recalculated to be 43.58 K for diode 69882 (therefore 1% error), thereby justifying the need for recalibration.

4.4.5.1 Calibration Target Blackbody Uncertainty Analysis

Channel Centre Wavelength (μm)	**Blackbody Temperature (K)**	**% Uncertainty when instrument temperature is:**		
		10°C	30°C	60°C
8 (A3/4/5)	200	0.78	1.2	2.1
8 (A3/4/5)	250	0.079	0.15	0.30
8 (A3/4/5)	300	0.018	0.0037	0.049
18 (A6)	178*	0.27	0.35	0.47
33 (B1)	69*	9.0	10	12
75 (B2)	43*	5.2	5.8	6.5
250 (B3)	20	4.4	4.8	5.3

Table 4-3: The maximum percentage errors due to the non-unity emissivity of the blackbody, assuming the worst-case scenario where the instrument reflection contributes the entire remaining emissivity. *These blackbody temperatures were chosen to represent the minimum mapping temperature of each channel [Paige et al., 2009]. Such errors decrease rapidly when viewing higher-temperature blackbodies.

Each of the steps and unknowns described previously increase the uncertainty in blackbody radiance. These are outlined below:

- Emissivity difference between test sample and actual blackbody due to the number of coats of paint. Four coats were used on the test piece [Calcutt, personal communication 2008b] but the number is unknown for the blackbodies used at JPL. The vast majority of the increase in emissivity of a blackbody over a black plate comes from the shape of the blackbody though, and so even a decrease of emissivity

of 0.1 in the B3 channel only decreases the total emissivity of a 0.9994 blackbody to ~0.9989 (based on Equation [4-2]).

- The assumption that the temperature of the 2nd and subsequent blackbody ribs was equal to the 1st rib temperature. Further investigations were not made into this, and so a worst-case scenario is required. Analysis of the out-of-calibration PRT data showed that the average maximum difference between the ribs of the fixed blackbody is 1.14 K. The emissive weights determine the contribution of each rib to the resulting radiance, with the amount decreasing with distance from the blackbody base. For the B3 (100 – 400 μm) channel, the baseplate contributes ~93% of the emissivity, 1st rib ~6% and 2nd to 4th ribs contribute ~2% to the total. In a calculation of the radiance in the B3 channel, this would result in an error of 0.03% at 40 cm^{-1} (250 μm) when viewing the 90K fixed blackbody, calculated by:

$$\%\sigma_{rib} = \frac{\left(B\left(40cm^{-1},91.1K\right)*0.02 + B\left(40cm^{-1},90K\right)*0.98\right) - B\left(40cm^{-1},90K\right)}{B\left(40cm^{-1},90K\right)} \times 100 \quad [4\text{-}3]$$

  It should be noted though that this error increases as temperature decreases, up to 0.17% for a 30K blackbody view.

- Increased temperature uncertainty due to the diode recalibration and the use of linear interpolation between voltage-temperature set-points by the temperature controller. 'Curve 10' temperatures were recorded to two decimal places, which for diode 69882, for example, equates to an average voltage error of 0.002% when calculated for temperatures from 30 - 90 K in 1 K increments. This corresponds to, for example, an uncertainty in temperature for diode D73214 of 0.01 K at 78 K, and an average error of 0.02 % over the 30 - 90K range.
- Radiance variations due to non-unity blackbody emissivity. If the blackbody does not have unity emissivity, which becomes increasingly true at longer wavelengths, then the remaining component of emissivity must be accounted for as a reflection of

something else off of the blackbody's interior surfaces. Within the chamber, the two possible sources of this are the instrument and the chamber wall, depending on the geometry of the calibration setup within the chamber. The shrouds were held below the temperature of the instrument throughout the test (-100ºC during ramp 1, 20ºC during ramp 2, and -10ºC during ramp 3 [Foote, personal communication 2008]); therefore the worst case scenario is that this extra radiation came entirely from the warm instrument. For example, for ramp 1, the instrument was held at 10°C (283 K) while the blackbody was cooled to its lowest test temperature of 20 K. At 40 cm^{-1} (250 μm) this equates to a 4.4% error in radiance from the formula:

$$\%\sigma_{rad} = \frac{\left(B\left(40cm^{-1},20K\right)*0.9994 + B\left(40cm^{-1},283K\right)*0.0006\right) - B\left(40cm^{-1},20K\right)}{B\left(40cm^{-1},20K\right)} \times 100 \qquad [4\text{-}4]$$

In a non-worst case scenario, for example if only 50% of the extra radiation came from the instrument and 50% from the chamber wall, this error is reduced to 3.4%. 20K is at the limit of detectability of the B3 channel though, and is below the minimum detectable temperature of the shorter-wavelength channels. Measurements of the fixed blackbody at ~90 K resulted in an error of 0.18% at 250 μm, increasing to 0.78% for a 200 K blackbody at 8 μm. For most measurements, errors due to non-unity emissivity (within the temperature range of the channel) are <0.1%. More channel maximum errors are listed in Table 4-3.

While errors such as these will be complexly correlated, a quick addition in quadrature can give an estimate of the combined uncertainty from all of these factors. As such:

0.04% + 0.03% + 0.02% + 0.18% = 0.19%

when viewing a 90 K blackbody using the B3 channel. In reality this will vary between channels and will also be highly dependent on the blackbody temperature being measured,

as the contribution of $\%\sigma_{rad}$ dominates the other terms. Based on this worst-case scenario example, the percentage uncertainty of the calibration setup is outside the required specification (Table 3-2); however in reality the value of $\%\sigma_{rad}$ could be much smaller, becoming negligible when viewing a warmer blackbody target.

4.5 Radiometric Calibration: Linearity Analysis

4.5.1 Introduction

With the emissivity of the black bodies and temperature sensor calibration completed, it was now possible to use the observations made by the Diviner flight instrument whilst under test to derive the radiometric calibration for each of the channels.

4.5.2 Data Retrieval

Data files used in the analysis were extracted from the AOPP Diviner data site, a second repository to the JPL main archive data site. The files contained Level 1A (Section 3.4.3) data in ASCII format, containing approximately one hour of data per file with each row representing an instrument reading each 0.128 seconds including raw detector counts and housekeeping data such as temperatures and actuator states. Diode temperatures were recorded every 30 seconds. All time-stamps, including data files and temperature readings, were converted to seconds after 01/01/2001, the standard time format used throughout the calibration analysis. Three methods of determining the linearity response of the detectors were investigated, to find the maximum radiometric accuracy to show that Diviner can operate within the relevant specifications (Table 3-2).

4.5.3 Radiance versus Interpolated Radiance

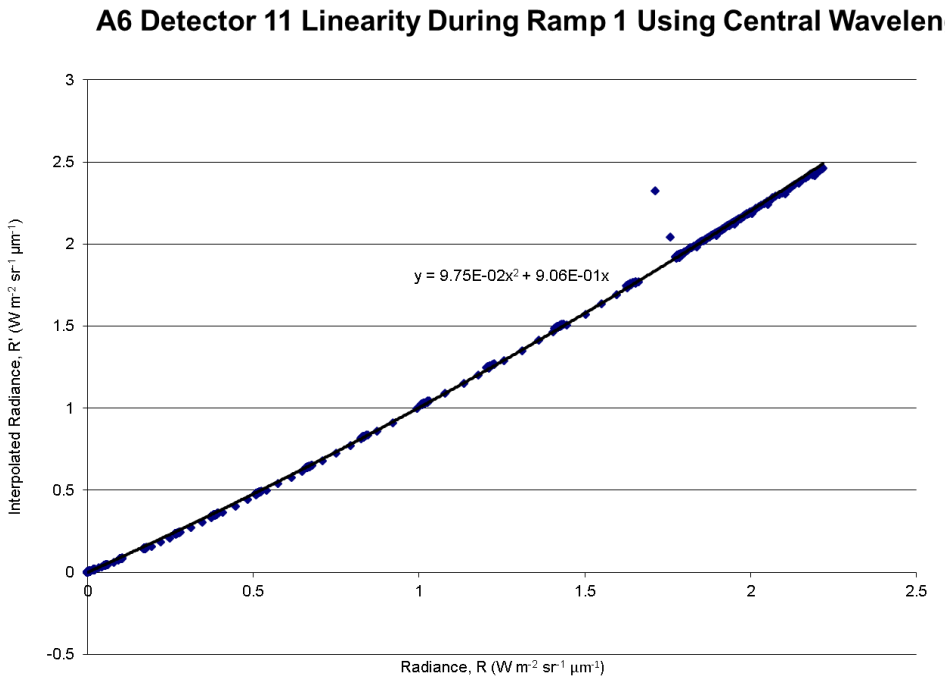

Figure 4-14: Interpolated radiance plotted against radiance for detector 11 of the A6 channel, during the ramp 1 stage of calibration (instrument at 10°C). The erroneous points, likely due to an equipment malfunction or operator error, are removed from the polynomial fit.

The analysis began following the work of Adlen [via Calcutt, personal communication 2008c], who investigated the linearity of the PMIRR detectors flown on the Mars Climate Orbiter spacecraft. In this investigation, the calculated radiance was plotted against interpolated radiance, i.e. the calculated radiance is the actual radiance of the variable blackbody at the time of the view determined from the blackbody temperature and emissivity, and the interpolated radiance is the radiance derived from the detector counts measured by Diviner. The integrated radiance is then calculated by [Adlen via Calcutt, personal communication 2008c]:

$$R_n = \frac{B(\upsilon_n, T_{CT})}{B(\upsilon_n, 300)} \qquad [4\text{-}2]$$

And interpolated radiance by:

$$R' = \frac{(C_{BB} - C_{CT})B(\upsilon_n, T_{SV}) + (C_{CT} - C_{SV})B(\upsilon_n, T_{BB})}{(C_{BB} - C_{SV})B(\upsilon_n, 300)} \qquad [4\text{-}3]$$

Where: C_{CT} is the averaged signal count for the external, calibration target view; C_{SV} is the averaged signal count for the space view target view; C_{BB} is the averaged signal count for the internal blackbody view; $B(v_n,T_{CT})$ is the radiance calculated for the external calibration target view at the central wavelength of channel n; $B(v_n,T_{sv})$ is the radiance calculated for the space view target; $B(v_n,T_{BB})$ is the radiance calculated for the internal blackbody view; and $B(v_n,300)$ is a normalising radiance, corresponding to a 300K blackbody. The values were then plotted in the form:

$$R = aR' + bR'^2 \quad [4\text{-}4]$$

Which is forced to pass through the origin with the linearity of the response determined by the constants a and b. The PMIRR instrument contained only one detector for each of the eight channels present, and so only sixteen coefficients were derived, unlike Diviner which contains 21 detectors x 7 channels (excluding solar reflectance channels) x 2 coefficients x 3 ramps = 882 values, impractical to list here. This method worked well for the narrow mineralogy channels A3-A5, where using only the central wavelength makes a good approximation to the spectrally-narrow channels, for example, a=0.988 and b=0.00162 for detector 11 of the A5 channel in ramp 1, indicating a highly linear relationship. This fails however for the broader thermal channels, where the equivalent coefficients for detector 11 of the A6 channel are a=0.906 and b=0.0975, showing significantly more curvature (Figure 4-14).

4.5.4 Plotting change in radiance against change in instrument counts

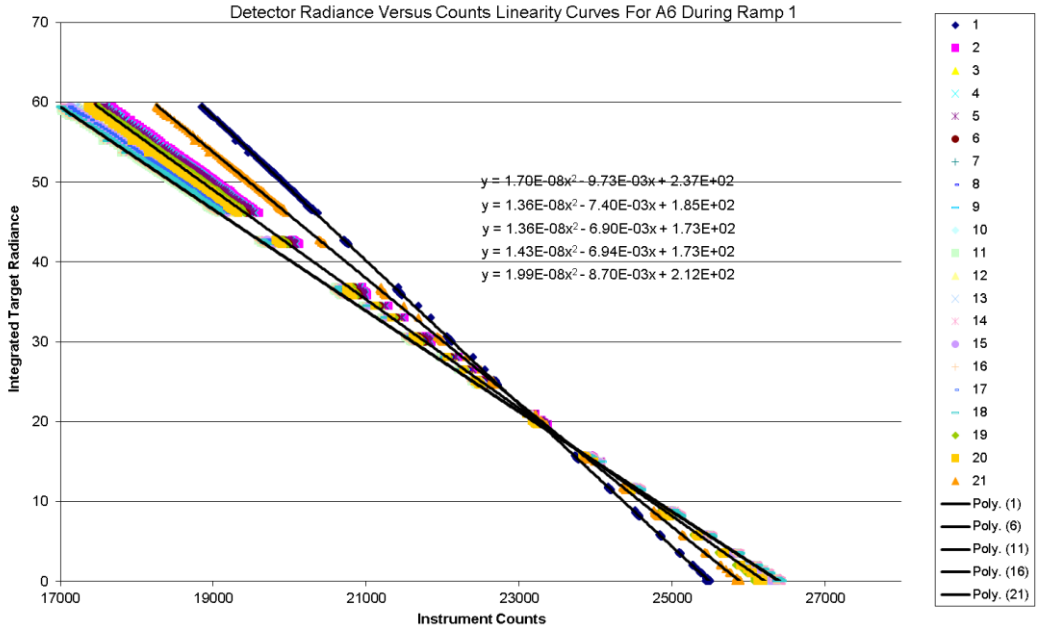

Figure 4-15: Integrated radiance plotted against Diviner instrument counts, for all detector elements of the A6 channel during ramp 1.

Following the advice of Schofield [personal communication, 2008], change in radiance was plotted against change in counts, to ensure that the deviations from linearity were in fact due to using the central wavelength approximation and not due to the response of the detectors varying with wavelength. As the instrument moves from viewing one blackbody to another, the change in radiance between the two blackbodies can be plotted against the change in counts from viewing each blackbody, in order to determine the linearity. This was repeated for each ramp, with a line of best fit of the form:

$$\Delta R = x + y\Delta C + z\Delta C^2 \qquad [4\text{-}5]$$

determined for the data. The results of the A6 channel during ramp 1 are shown in Figure 4-15. Lines of best fit and the corresponding equations have been added for detectors 1, 6, 11, 16 and 21, showing that a high degree of linearity is present in each channel, with values of z below 2 x 10^{-8} even for detectors 1 and 21 at the extremities of the focal plane array.

The central wavelength approximation used by Adlen [via Calcutt, personal communication 2008c] cannot be applied to the broader Diviner channels A6-B3. Therefore the final step was to confirm the detector linearity by removing the approximation, instead integrating the Planck function, blackbody emissivity and channel spectral responses with respect to wavelength for each Diviner blackbody observation, attempting to minimise any errors.

4.5.5 Plotting change in integrated radiance and interpolated change in integrated radiance

To minimise any external influences in the non-linearity coefficients derived in this final investigation, precautions were taken over the previous analyses. When plotting change in radiance against change in instrument counts, the difference in counts was calculated by subtracting the first count after the transition between targets from the first count before the transition. This was found to produce large uncertainties due to the effects of a) not averaging counts to remove noise, and b) not accounting for thermal lag. This lag occurs when the instrument moves to view a new scene with a large difference in radiance from the previous scene. In order to minimise the sources of these errors, for each duration where the instrument was stationary, only the counts from the latter half of the stationary period were averaged together (Figure 4-11). For each variable blackbody temperature plateau, the data were filtered to extract only the periods of time where the temperature of the blackbody diodes remained suitably constant. The five closest diode readings to each transition, within each constant temperature plateau, were used to interpolate the temperature at the time of the transition, in order to minimise fluctuations due to noise. The five closest fixed blackbody diode readings within the same period of time were also interpolated in the same way, along with the internal blackbody temperature, with a check performed to ensure that the temperature of each blackbody remained fairly constant throughout this time.

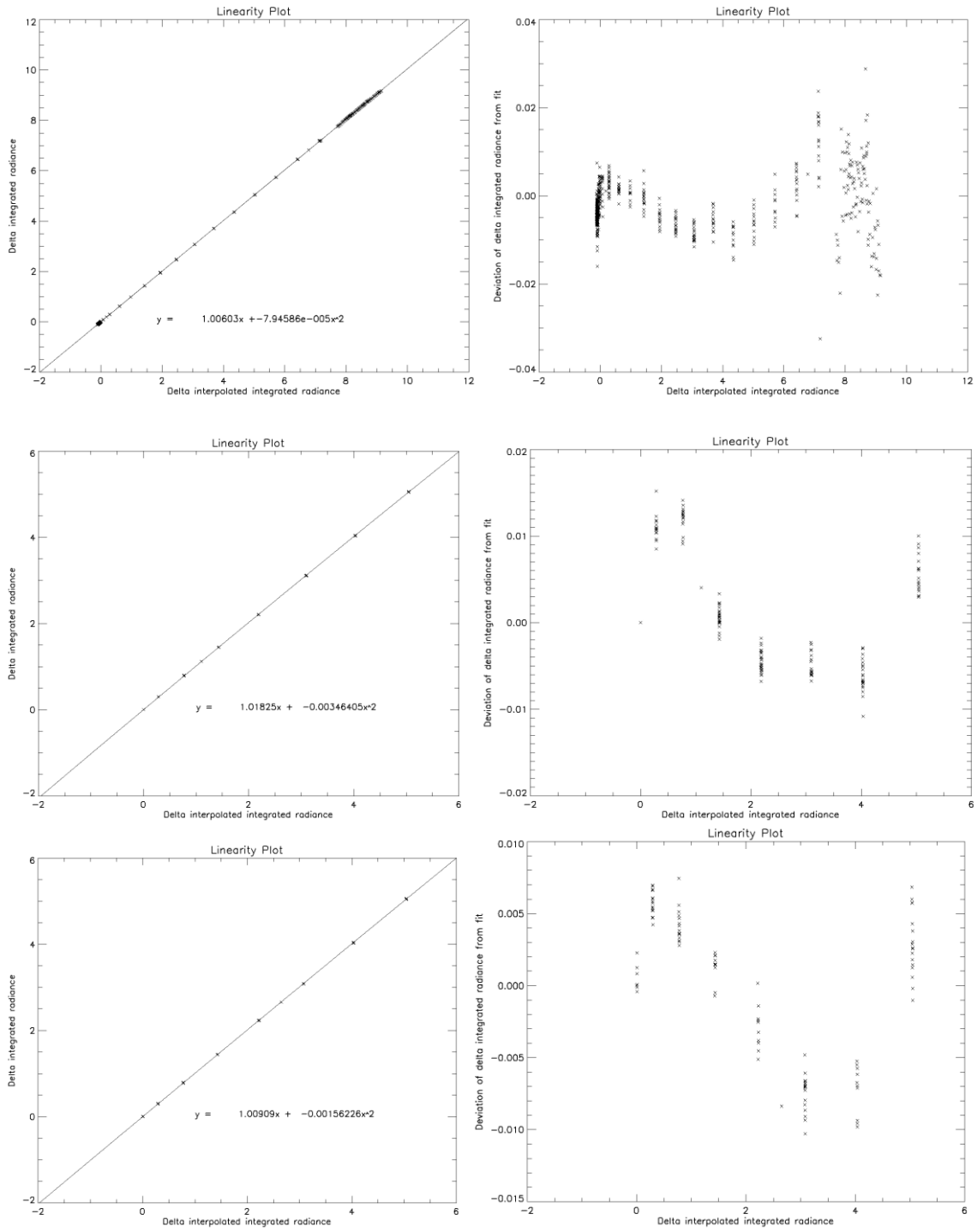

Figure 4-16: Sample linearity plots for detector 10 of the B1 channel, for ramp 1 (top), ramp 2 (middle) and ramp 3 (bottom), with polynomial lines of best fit added (left), and deviations from the fit (right).All axes have the units of integrated radiance, W m^{-2} sr^{-1}.

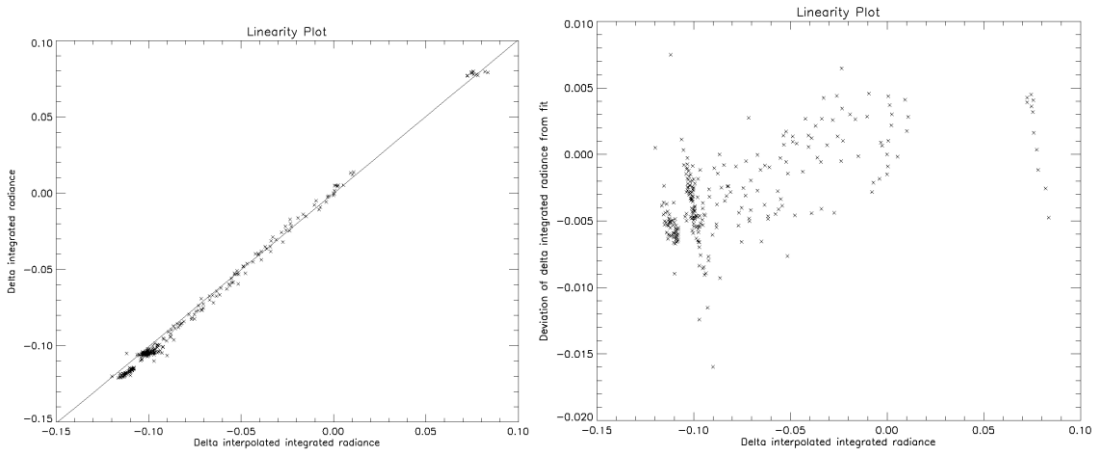

Figure 4-17: A linearity plot (left) for detector 10 of the B1 channel, showing the differing curvature of the negative region of the graph, compared to the line of best fit through the entire data. The deviation of points from the fit is also shown (right).

The four transitions to be considered (Figure 4-11) were: a) viewing internal blackbody to viewing fixed blackbody, b) viewing fixed to viewing variable, c) variable to fixed, and d) fixed to internal. The difference in radiance and difference in counts from each transition were averaged with the opposite transition in the reverse direction. True delta integrated radiance, denoted as ΔR_{fvf}, was then determined from transitions (b) and (c), and interpolated delta integrated radiance is calculated as:

$$\Delta R'_{fvf} = \Delta C_{fvf} \times \frac{\Delta R_{fif}}{\Delta C_{fif}} \qquad [4\text{-}6]$$

Where: ΔR_{fvf} corresponds to the averaged change in radiance from transitions (b) and (c); ΔC_{fvf} is the averaged change in counts from transitions (b) and (c); and ΔR_{fif} and ΔC_{fif} are the average change in radiance and counts from transitions (a) and (b). Next, ΔR_{fvf} was plotted against $\Delta R'_{fvf}$ and a 2nd order polynomial was fitted to the data of the form $\Delta R_{fvf} = a\Delta R'_{fvf} + b\left(\Delta R'_{fvf}\right)^2$ for all the detectors of channels A3-A6 and B1-B3 during every

ramp. As previously, all results cannot be shown due to the number of them, but some sample plots for this data for detector 10 of the B1 channel are shown in Figure 4-16 and Figure 4-17.

Using the integrated radiance, the detectors appear to be much more linear than when using just the central wavelengths for each channel. For example, for the A6 channel during ramp 1 now gives a=1.01 and b=-0.00516 (previously a=0.906 and b=0.0975), considerably lower than before. The mineralogical channels are even more linear: for the A3 channel, a_{mean} = 0.0017 and b_{mean} = 1.0015 averaged over the three ramps, corresponding to a temperature difference (compared to assuming the detectors are linear) of 0.55 K when measuring a 350 K scene.

Deviations from the linearity curves can still be observed though: examples of this curvature can be seen in the B1 detector 10 results when the negative portion of the curve is enlarged (e.g. Figure 4-17). In the end it was decided not to use the polynomial coefficients to correct the small non-linearities detected in the channels, owing mainly to the uncertainties in the calibration procedure (Section 4.4.5.1).

4.6 Filter Measurement and Calibration Conclusion

- The B2 and B3 filters and KCl blocker were successfully measured across the spectral range of the Brüker IFS 66v FTIR Spectrometer. The B1 – B3 filter pass-bands showed no sign of broadening as the distance between the filter and detector was decreased, giving confidence that the filter responses of Diviner have not been compromised by the optical design of the instrument.

- This was further confirmed by the results of the linearity testing, which showed that the quadratic coefficients describing the detectors' responses were sufficiently small that they were approximated to be zero.
- When combined with the other results from instrument testing and calibration (beyond the scope of this thesis; see Paige et al. [2009] for full details), Diviner worked within its specifications and was therefore integrated onto the LRO satellite.

5 Laboratory Mineral Measurements

5.1 Introduction

The study of previous TIR laboratory measurements (Section 2.9.1) concluded that more laboratory spectra were needed to determine lunar surface composition from Diviner observations. In particular, more measurements of terrestrial analogues of lunar minerals were required that had been measured in such a way that they could be directly compared to the data returning from Diviner. The lunar environment creates a thermal gradient in the surface regolith, altering the emission spectra from those measured in ambient conditions on Earth (Section 2.9), so most existing spectral libraries (Section 2.7.3) cannot be related to TIR lunar observations. No working laboratory setup existed for making emissivity measurements in lunar environmental conditions, so an emission chamber was manufactured and a lunar spectral library made, enabling the Diviner compositional measurements to be interpreted (Section 6.3).

5.2 Initial Reflectance Measurements

5.2.1 Reflectance versus Emission

It would have been preferable to measure all the samples under simulated lunar environmental conditions, but this was unachievable within the limited period of the project. Simulated Lunar Emission (SLE) measurements of a single sample take approximately two days to perform, so it was not possible to take emission spectra of the ~ 90 samples collected during the investigation. Instead, reflectance measurements were made, as these could be carried out much more rapidly (~15 - 20 per day), to gain a general insight into the observable spectral features of the samples that were available to the author. An investigation was also conducted into how changes in chamber atmospheric pressure

affected the mineral reflectance spectra, to examine if changes in spectra due to environmental conditions (aside from ambient) could be observed in reflectance measurements.

5.2.2 Diffuse versus Specular Reflectance

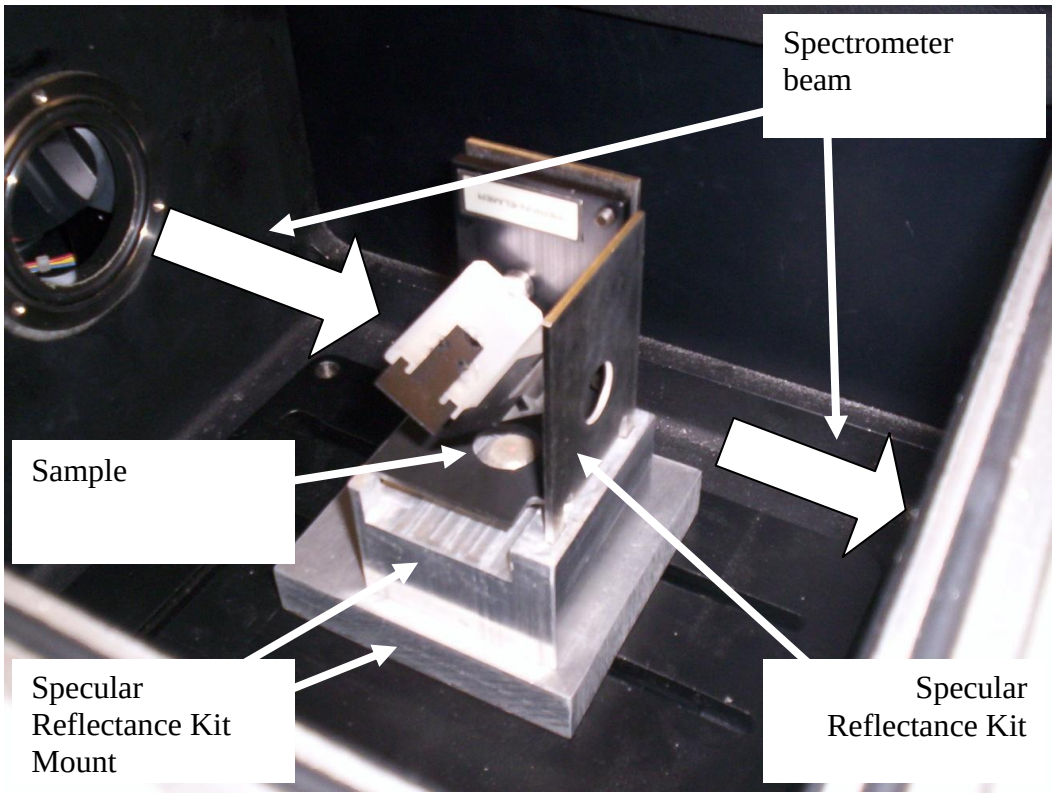

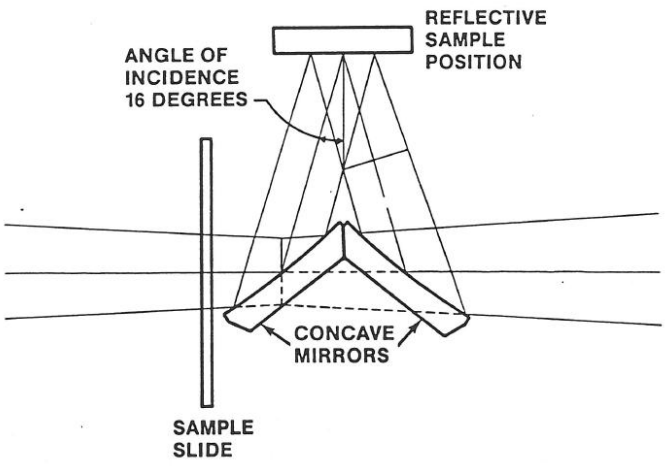

Figure 5-1: Photo (top) and diagram (bottom) [Perkin Elmer, 1987] of the specular reflectance setup, consisting of the two machined aluminium blocks seen in the image, which allows the specular reflectance kit to be mounted upside-down in the spectrometer sample compartment. The sample (or gold mirror reference) is held by the rig in the correct position for a measurement to be made, with arrows showing how the spectrometer beam reflects off the sample and is passed to the detector compartment. Figure © 2012 PerkinElmer, Inc. All rights reserved.

Measurements were made using the same Brüker IFS-66v FTIR Spectrometer used for the filter transmission measurements (Section 4.2). Two types of reflectance measurements could be made using the equipment available in AOPP: either fixed angle specular reflectance, using a Perkin Elmer® Specular Reflectance Kit, or diffuse, using a Specac® Diffuse Selector Accessory. Both accessories were designed to be placed inside the spectrometer sample compartment (Figure 4-1). In general, specular reflectance (Figure 5-1) measures how radiation is reflected where incidence and reflected rays have equal angles, such as when viewing a reflection in a mirror; whereas diffuse reflectance (Figure 4-12) measures how radiation is scattered at other (non-specular) angles. The incident and collected radiation angles are set by the equipment available:

- For specular measurements, the angles of incidence and reflection were 16º from the normal.
- For diffuse, the angles are more complex, each subtending a circular section of a quarter-hemisphere from ~5 – 65º in the x-y plane and from ~0 – 40º in the z plane. A diagram of this is shown in Figure 4-12. It should be noted that this is not a true diffuse measurement, and as such artefacts due to e.g. polarization effects may be present in the measured spectra.

The lunar surface can be considered a diffuse scatterer of radiation, therefore this part of the investigation concentrated on diffuse measurements over specular.

To compare reflectance with emission measurements, reflectance spectra can be converted into emissivities (or vice versa) where [Clarke and Larkin, 1985]:

$$\varepsilon(\lambda) = 1 - [R_d(\lambda) + R_s(\lambda) + T_d(\lambda) + T_s(\lambda)] \qquad [5\text{-}1]$$

Where ε is emissivity, R_d and R_s are the 'true'[9] diffuse and specular components of reflectance and T_d and T_s are the corresponding components of transmission (= 0 for reflectance measurements of thick, opaque mineralogical samples). This is a statement of Kirchhoff's Law, $\varepsilon = 1 - R$, where total reflectance $R = R_d + R_s$. Also, as $R_d > R_s$, diffuse reflectance measurements can be approximately converted to emissivities: comparisons between both types of reflectance spectra are made in Figure 5-6. It should be noted though that this conversion is **only** valid for emission measurements where no thermal gradient is present within the sample [Salisbury et al., 1994], and so cannot be used to convert reflectances to emission spectra made under very low pressure or lunar conditions. Reflectance measurements are converted into ambient-conditions emissivity spectra, and cannot therefore by directly compared to Diviner measurements.

5.2.3 Construction

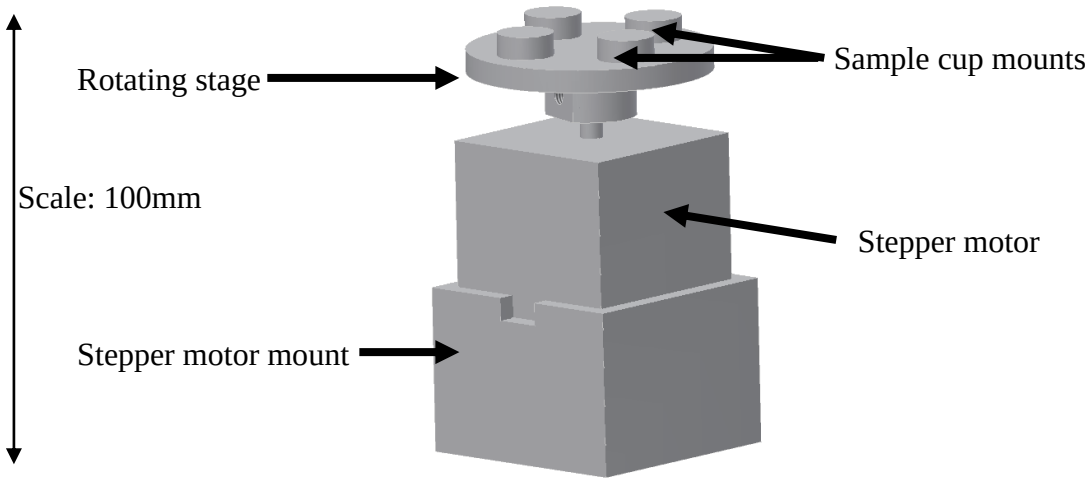

Figure 5-2: 3D CAD drawing of the rotating stage setup designed and manufactured by the author.

[9] The diffuse reflectance accessory available only collects radiation across a limited range of angles, and so cannot be considered a 'true' diffuse measurement. Similarly, the mirrors of the specular reflectance kit are fixed at 16º, preventing measurements at different angles.

To investigate how pressure affects reflectance spectra, attempts were made to pump down the spectrometer to very low pressures using a turbomolecular pump. Difficulties were encountered in evacuating the spectrometer to below a few millibars (the typical minimum pressure using a standard rotary pump) and so a separate sample vacuum chamber was made to fit inside the spectrometer sample compartment. This was connected to a Pfeiffer-Balzers pump and nitrogen bottle through a vacuum port at the front of the spectrometer (Figure 4-1), allowing measurements to be conducted under: [1] air, [2] an overpressure of Nitrogen, and [3] a high vacuum of less than 10^{-3} mbar. To avoid breaking vacuum when making diffuse reflectance measurements, and to achieve accurate calibration of the results, a rotating stage (Figure 5-2) was built so that three samples and one reference standard could be loaded into the chamber simultaneously. The rotating stage consisted of a base, computer-controlled stepper motor and carousel containing sample cup holders, which held the sample under investigation in the correct location and orientation while each measurement was made. First the reference standard was measured, followed by sample 1, then the reference again, and then sample 2 etc., so each sample was preceded and followed by a measurement of the standard, to minimise errors due to changes in the setup (e.g. source brightness fluctuations, spectrometer detector fluctuations etc.).

Additional apparatus was built for making specular measurements: the specular reflectance kit available was designed for use with flat, solid samples, requiring them to be mounted upside-down on the top of the kit. A new setup was manufactured containing a sample cup holder and mount (Figure 5-1) allowing the specular kit to be inverted - instead of the sample - so that powdered minerals could be measured without spillage. Using this mount, however, meant that there was insufficient space below the specular reflectance kit to place the rotating stage (Figure 5-2) and so it was not used to speed up the specular measurement process.

5.2.4 Diffuse and Specular Reflectance Measurement Procedures

5.2.4.1 Reflectance Measurement Calibration

The spectral responses of the spectrometer's components (e.g. the Globar™ source, mirrors, detector and any windows used) have a common affect on the measured mineral spectra regardless of whether a fixed angle specular or diffuse reflectance measurement is being made, i.e. the spectrometer does not have an inherently flat spectral response in the absence of a sample. Removing the spectral response of the instrument from the sample data is achieved by referring to a standard of known reflectance that is (preferably) as spectrally flat as possible. This reference is measured directly before or after the sample, with the sample reflectance spectrum divided by the reference spectra to cancel out any effect of the spectrometer components, allowing absolute reflectance spectra to be derived. Using the available spectrometer sources, detectors and beamsplitters (Table 4-1) enabled the samples to be measured in near-, mid- and far- infrared modes, allowing almost continuous diffuse reflectance spectra to be measured from ~0.4 μm in the visible to ~400 μm in the far infrared.

5.2.4.2 FTIR Spectrometer Settings for Reflectance Measurements

As described above, reflectance spectra are derived by comparing the sample spectrum to that of a reference standard of known reflectivity. This requires the spectrometer settings to be kept constant for both sample and reference measurements. For the Brüker IFS 66v, the following settings are adjustable:

- Aperture size. An aperture wheel is located in the beam after the source (Figure 4-1), controlling the amount of radiation passing through the spectrometer. Using a larger aperture increases the spot size on the sample but reduces the maximum spectral

resolution, so the largest available setting was limited to 10mm for the 4 cm^{-1} resolution desired.

- Amplifier gain. If the interferogram signal is small then errors are increased when the analogue detector readout is converted into digital counts (seen as 'steps' in the interferogram), and so the signal can be amplified prior to this conversion to reduce this error.
- Mirror scan velocity. The detector has increased signal-to-noise performance when interferograms are scanned at a slower rate, though this increases the time taken to make each scan[10].
- Number of scans. Interferograms can be noisy and so it is normal practice to average together many scans before converting them into spectra using a Fourier transform, although each measurement then takes longer. This can be varied between the sample and reference measurements, allowing more scans to be run for samples with lower reflectances.

As described above, ideally, a reflectance standard should be spectrally flat and have a known reflectance (in the geometry being measured, either 'specular' or diffuse). However, powdered mineral samples can often have low specular and diffuse reflectivity, making the choice of reflectance standard problematic.

One option is to calibrate the samples against a 'straight-through' reference measurement, where the beam from the interferometer passes unhindered to the detector, allowing the spectral response of the source, interferometer and detector to be measured. Problems arise when using a 'straight-through' measurement as the reference, as this has a much higher

[10] so introduces the risk of 'drift' in the spectrometer.

signal than the sample measurement, which can saturate the detector due to the inability to change the spectrometer settings between runs (described above). For the NIR and MIR spectral regions, a two-step calibration process was used to overcome this, following the procedure described by e.g. Glotch and Rossman [2009], and is summarised below.

5.2.4.3 NIR and MIR Reflectance Reference Standard

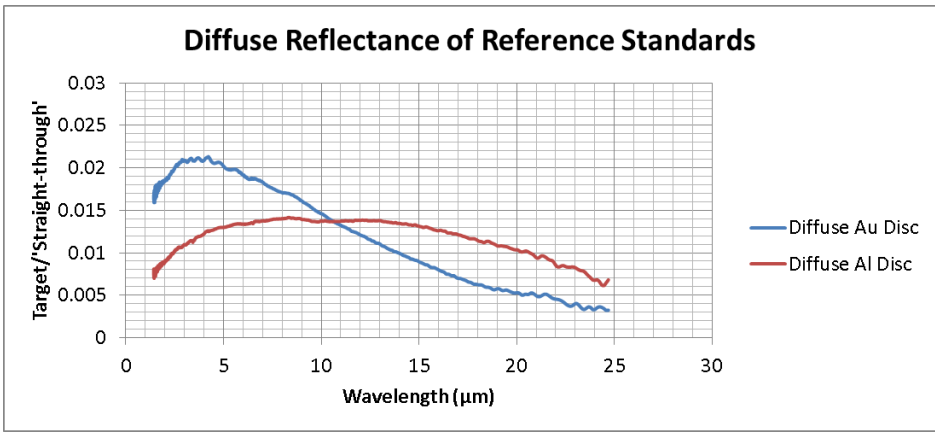

Figure 5-3: A comparison of the diffuse reflectances of the two reference standards used. 'Straight-through' refers to the spectrum measured when no reflectance kit is placed in the spectrometer sample compartment.

For the diffuse reflectance setup, an intermediate reference standard was required of sufficiently high diffuse reflectivity so that it could be calibrated against a 'straight-through' measurement without the detector saturating, which could then, in turn, be used to calibrate the samples without saturating the detector itself. In this two-step process, a diffusely scattering gold disc, and later an aluminium disc, were calibrated against a 'straight-through' measurement using the diffuse reflectance setup (Figure 4-12) to measure their diffuse reflectivity and then used as the reference standard for all the subsequent sample measurements. The diffuse reflectance of the gold disc was found to drop off at longer wavelengths (Figure 5-3); therefore an aluminium reference standard was manufactured

with a higher emissivity to reduce the error due to noise when calculating the sample reflectances. This Al disc was a small cylinder of equal height as the sample cups with a grit-blasted upper surface to give a diffusely scattering, uniform finish; this was then placed on the rotating stage to increase the speed of the measurements.

For the lesser-priority specular measurements, the reflectance standard supplied with the fixed angle specular reflectance kit was a gold-coated metal front mirror with a very high specular (mirror-like) reflectance. This gold mirror was not used as the standard because most of the minerals were poor specular reflectors, and therefore the detector would once again be saturated making the reference measurement with the same spectrometer settings that were used for the sample impossible. The diffuse Al disc had a uniform specular reflectance between that of the minerals and the gold disc, sufficient to be calibrated from measurements made without the reflectance kit in the sample compartment (as for the diffuse setup) but not so high that the detector would saturate when used as a reference for the samples in the specular reflectance setup.

5.2.4.4 Far-Infrared (>25 μm) Reflectance Reference Standard

Neither the gold disc nor this diffuse aluminium disc showed sufficient signal when measured in the FIR region, and so a sample cup filled with crushed polypropylene was instead used as the intermediate reference standard for these measurements. Large polypropylene granules, frozen in liquid nitrogen and ground into small particulates, were placed in a sample cup. Plastics such as polypropylene have few absorption lines in the FIR region, making suitable reference standards, but after several FIR measurements it became clear that the spectra were dependent on the orientation of the polypropylene. This non-uniformity meant that these results were not reliable, so the measurements were discontinued.

5.2.4.5 Sample Preparation

The mineral powder samples were prepared using a standard procedure to try and eliminate any systematic features due to e.g. orientation of the sample cup in the reflectance beam. Prior to measuring, the samples were placed in sample cups and the top surfaces smoothed with a glass slide to achieve a uniform measurement surface. The samples were then placed in a vacuum oven at 50 °C for at least 2 hours to remove contaminants such as water vapour, which may have been absorbed from the air prior to heating. The samples under investigation were then moved immediately from the vacuum oven into the vacuum chamber within the spectrometer, which was immediately evacuated of air to avoid re-contamination. The spectrometer was also evacuated, and measurements were made under both an overpressure of Nitrogen and a high vacuum of less than 10^{-3} mbar.

5.2.4.6 Measurement Method

With the sample in the spectrometer, acquisition of the spectrum could begin. To achieve sufficient signal, it was found through experimentation that an interferogram amplitude of >500 digital counts (without gain) was desirable. Therefore, the spectrometer aperture and scan velocities were optimised to achieve a signal of 500 - 750 counts, with amplifier gain used to increase the signal to around 2000 counts. Diffuse spectra were acquired in the NIR using a 5 mm aperture, 4x gain, with a scanning velocity of 10 kHz, at a resolution of 4 cm^{-1}, with 512 scans averaged per measurement. Each MIR spectra consisted of 800 scans, taken using a 10 mm aperture, 4x gain, 7.5 kHz scanning velocity with 4 cm^{-1} resolution. Much lower signals were observed in the FIR region, with interferograms of >2000 counts only possible using the largest (12 mm) aperture, 1.6 kHz velocity and 16x gain. The largest aperture prevented measurements at resolutions higher than 8 cm^{-1}, and the slowest scanner

velocity meant that only 400 scans were averaged per measurement so that the samples could be measured at a reasonable rate. Even when using the highest signal spectrometer setting, the spectra of most of the interferograms were dominated by noise, which when combined with the variability of the FIR reference standard meant that these results were not deemed reliable and most sample measurements were omitted (Table 5-1). Specular measurements were not made in the FIR.

5.2.5 Lunar Analogue Mineral Sample Suites

Sample Type	**Sample**	**Grain size distribution (µm)**	**Owner**	**NIR**	**MIR**	**FIR**
Calibration	Quartz SiO2	0 - 30	BTG		D, E, S	
		30 - 64	BTG		D, E, S	
		64 - 120	BTG		D, E, S	D
		120 - 450	BTG		D	
Primary	Anorthite (An)(also Plagioclase)	0 - 25	KDH		E	
		0 - 30	BTG	D	D, S	D
		30 - 64	BTG		D, S	
		64 - 120	BTG	D	D, S	D
		120 - 450	BTG		D	
	Augite (Au) (Clinopyroxene)	0 - 25	KDH		E	
		0 - 30	BTG	D	D, E, S	D
		30 - 64	BTG		D, S	
		64 - 120	BTG	D	D, S	D
		120 - 450	BTG		D	
	Enstatite (En)	0 - 30	BTG	D	D, E, S	D

	(Orthopyroxene)	30 - 64	BTG		D, S	
		64 - 120	BTG	D	D, S	D
		120 - 450	BTG		D	
	Fayalite (Fa) (Olivine)	0 - 30	BTG	D	D, E, S	D
		30 - 64	BTG		D, S	
		64 - 120	BTG	D	D, S	D
		120 - 450	BTG		D	
	Forsterite (Fo) (Olivine)	0 - 25	KDH		E	
		0 - 30	BTG	D	D, E, S	D
		30 - 64	BTG		D, S	
		64 - 120	BTG	D	D, S	D
		120 - 450	BTG		D	
	Ilmenite (Il)	0 - 30	BTG		D, S	
		30 - 64	BTG		D, S	
		64 - 120	BTG	D	D, S	
		120 - 450	BTG		D	
	Diopside (Clinopyroxene)	0 - 64	BTG		D	
		64 - 120	BTG		D	
Mixtures	FO40FA60 (40% Fo, 60% Fa)(Olivine)	0 - 30	BTG		D	
		30 - 64	BTG		D	
		64 - 120	BTG		D	
	FO55FA45 (55% Fo, 45% Fa)(Olivine)	0 - 30	BTG		D	
		30 - 64	BTG		D	
		64 - 120	BTG		D	
	FO70FA30 (70%	0 - 30	BTG		D	

	Fo, 30% Fa)(Olivine)	30 - 64	BTG		D	
		64 - 120	BTG		D	
	Mix 1 (44% An, 38% En, 18% Au)	0 - 30	BTG		D	
		30 - 64	BTG		D	
		64 - 120	BTG		D	
	Mix 2 (42% An, 36% En, 17% Au, 5% Il)	0 - 30	BTG		D	
		30 - 64	BTG		D	
		64 - 120	BTG		D	
	Mix 3 (40% An, 34% En, 16% Au, 10% Il)	0 - 30	BTG		D	
		30 - 64	BTG		D	
		64 - 120	BTG		D	
	Mix 4 (39% An, 36% En, 16% Au, 7% Fo, 2% Fa)	0 - 30	BTG		D	
		64 - 120	BTG		D	
	Mix 5 (49% An, 29% En, 13% Au, 7% Fo, 2% Fa)	0 - 30	BTG		D	
		64 - 120	BTG		D	
	Mix 6 (60% An, 22% En, 10% Au, 6% Fo, 2% Fa)	0 - 30	BTG		D	
		64 - 120	BTG		D	
	Mix 7 (87% An, 6% En, 3% Au, 3% Fo, 1% Fa)	0 - 30	BTG		D	
		30 - 64	BTG		D	
		64 - 120	BTG		D	
Plagioclase	Albite (100 - 90%	0 - 25	KDH		E	
		0 - 64	BTG		D, E	

	$NaAlSi_3O_8$)	64 - 120	BTG		D	
		120 - 450	BTG		D	
	Oligoclase	0 - 25	KDH		E	
	(90 - 70%	0 - 64	BTG		D, E	E
	$NaAlSi_3O_8$)	64 - 120	BTG		D	
		120 - 450	BTG		D	
	Andesine	0 - 25	KDH		E	
	(70 - 50%	0 - 64	BTG		D	
	$NaAlSi_3O_8$)	64 - 120	BTG		D	
		120 - 450	BTG		D	
	Labradorite	0 - 25	KDH		E	
	(50 - 70%	0 - 64	BTG		D	
	$CaAl_2Si_2O_8$)	64 - 120	BTG		D	
		120 - 450	BTG		D	
	Bytownite	0 - 64	BTG		D	
	(70 - 90%	64 - 120	BTG		D	
	$CaAl_2Si_2O_8$)	120 - 450	BTG		D	
Silicic	Microcline	0 - 90	TDG		E	
	(Orthoclase)	>90	TDG		E	
	Obsidian	0 - 90	TDG		E	
	(High Silica)	>90	TDG		E	
Other	Shocked Plagioclase	N/A	TDG		E	
	Unshocked Plagioclase	N/A	TDG		E	

	Apollo 11 (10084)	0 – 1000	N/A	S	D, E, S	
	Apollo 16(68810)	0 - 1000	N/A	S	E, S	
	JSC 1A	Wide range. See McKay et al. [2005]	N/A		E, S	

Table 5-1: The samples, grain-size distributions, wavelength ranges and types of measurements made during the project, where S = specular reflectance, D = diffuse reflectance, and E = emission. Sample owners were abbreviated, with BTG = Ben Greenhagen, KDH = Kerri Donaldson-Hanna and TDG = Timothy Glotch.

A lunar analogue mineral sample suite was assembled working with colleagues in the Diviner science team. Samples were provided by Ben Greenhagen (then of UCLA, now of JPL) and Kerri Donaldson-Hanna (Brown University, RI, USA) and consisted of a range of minerals commonly found on the lunar surface. Timothy Glotch (Stony Brook University, NY, USA) also provided several other samples for further specific investigations, which are described in detail in this chapter. These were then split into several sample suites depending on measurement importance: calibration, primary, mixtures, plagioclase, silicic and other. A full list of categorised samples and their owners is shown in Table 5-1. Typically measurements of both diffuse and specular reflectance were attempted. However, some measurements were omitted due to lack of signal (especially in the FIR or those of low-albedo samples), lack of sample mass to entirely fill the sample cup, or due to time constraints. Many of the specular measurements produced the same spectral shape as the diffuse measurements (and took much longer to measure due to reduced signal), so were therefore omitted. Lunar compositional measurements focus on the CF observations made by the Diviner 8 μm channels, therefore reflectance and emission measurements in this region were prioritised. The setup and mineral samples remain available if more measurements are required in the future.

5.2.5.1 Sample Suite Classification

The minerals were classified into separate suites of samples as described below:

- Calibration suite: This was made of the quartz samples of various grain sizes. Quartz samples were measured in all previous relevant laboratory studies and modelled in all previous radiative transfer models, so quartz samples were measured in this investigation to test the laboratory setup and check the new calibration algorithm derived (Section 5.3.5).
- Primary suite: This consisted of many terrestrial minerals found extensively on the Moon that had been analysed to ensure correct composition. Compositions were verified by electron microprobe analysis; more details of verification methods, sample origins, compositional analyses, and preparation procedures of these minerals can be found elsewhere (Greenhagen [2009]). Minerals from Donaldson-Hanna were taken from the ASU repository and had been compositionally analysed (Donaldson-Hanna et al. [submitted 2011]). The primary samples of Greenhagen, with sufficient mass to fill the sample cup, were measured in the TIR in both reflection and emission in this project; the primary samples of Donaldson-Hanna were measured in emission here and reflection at RELab (Section 2.7.3.2).
- Mixtures suite: This suite consisted of various primary suite minerals from Greenhagen mixed in different ratios. Only reflectance measurements were made of this suite.
- Silicic suite: These samples were collected to study regions of the lunar surface that had been identified in the Diviner data for a study by Glotch et al. [2010] (Section). These were measured in emission only.

- Plagioclase suite: Greenhagen and Donaldson-Hanna sourced Anorthite, labradorite, andesine, oligoclase and albite minerals in various grain sizes. Except for anorthite, those from Greenhagen were not compositionally analysed and so were mainly measured in reflectance only. Emissivities were measured of the analysed samples of Donaldson-Hanna.
- Other: The 'other' grouping consisted of various samples acquired during the project that were not pure minerals. Shocked and un-shocked (artificially bombarded) andesine chips were measured in emission, to observe if weathering altered the spectra; plus JSC-1A, a lunar simulant and two Apollo (11 and 16 soil) samples, one of the maria and one of the highlands, were also measured in emission. JSC-1A and the Apollo samples was also measured in reflectance, but due to sample handing restrictions, the Apollo samples could not be measured under full lunar environmental conditions, only under vacuum.

5.2.5.2 Sample Suite Grain sizes

Previous SLE studies (Section 2.9) showed that emissivity spectra were altered by the grain size of the sample; therefore samples were split into grain size distributions to be measured separately (Table 5-1). The primary and calibration suite samples except diopside, from Ben Greenhagen were split into five grain size distributions: 0 - 30 µm, 30 - 64 µm, 64 - 120 µm and 120 - 450 µm. Plagioclase and diopside samples were separated into 0 - 64 µm, 64 - 120 µm and 120 - 450 µm size distributions only. Kerri Donaldson-Hanna minerals consisted of fine and coarse samples, of 0 - 25 µm and 25 - 120 µm; further sample details can be found in Donaldson-Hanna et al. [submitted 2011]. Samples from Timothy Glotch were separated into fine (0 - 90 µm) and coarse (>90 µm) sizes. Once split in to grain sizes, some samples had insufficient mass to be measured in emission, which required a larger sample cup than

for reflectance measurements; hence, some emission measurements of the some of the important samples were not performed (Table 5-1).

5.2.6 Reflectance Spectra Results

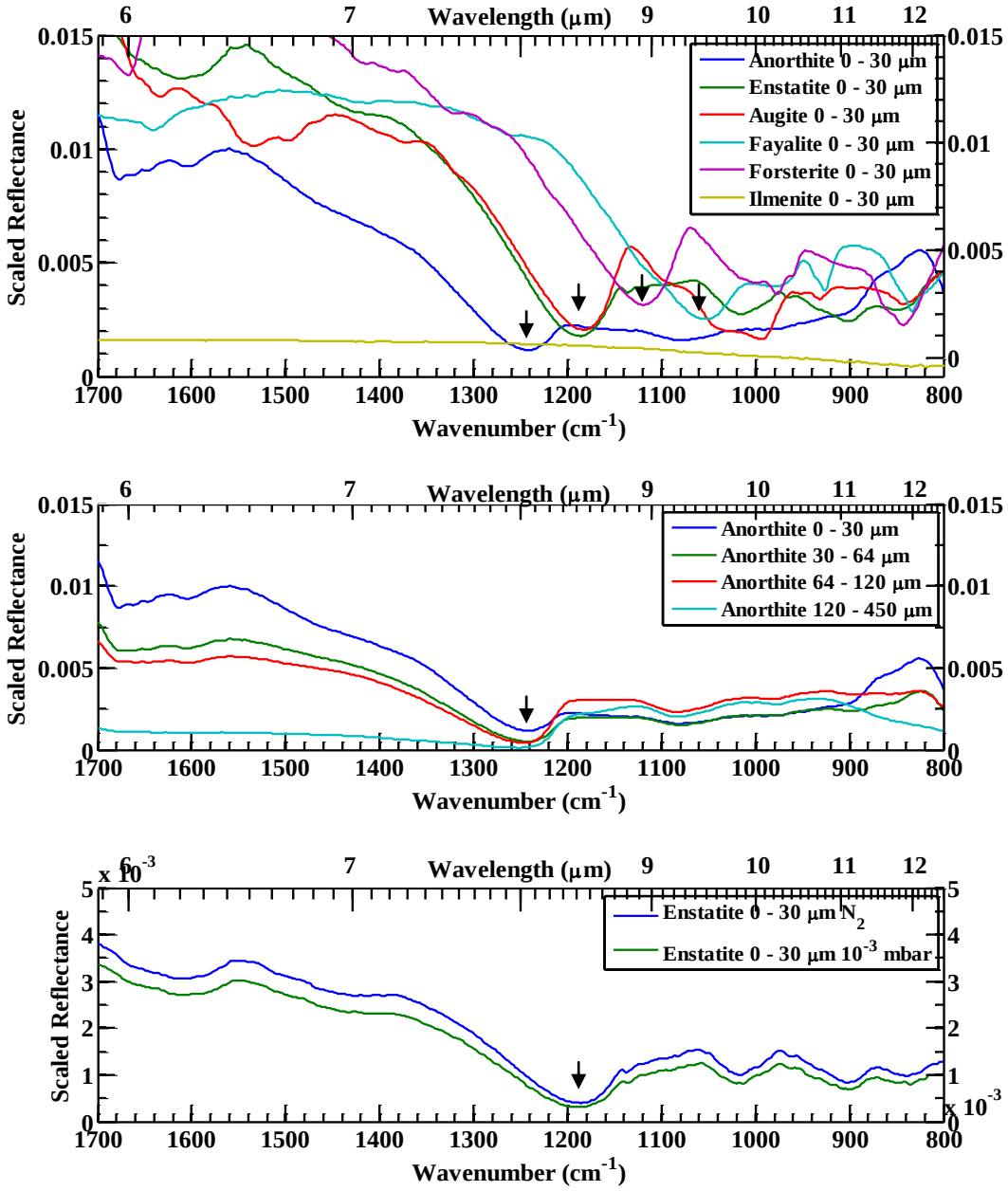

Figure 5-4: Reflectance spectra measured by the author and Ben Greenhagen. These show the effects on diffuse reflectance spectra of varying each parameter individually, e.g. composition (top), grain size (middle) and environmental pressure (bottom). The anorthite grain size spectra are also presented in Greenhagen [2009]. CF locations are shown by tick marks.

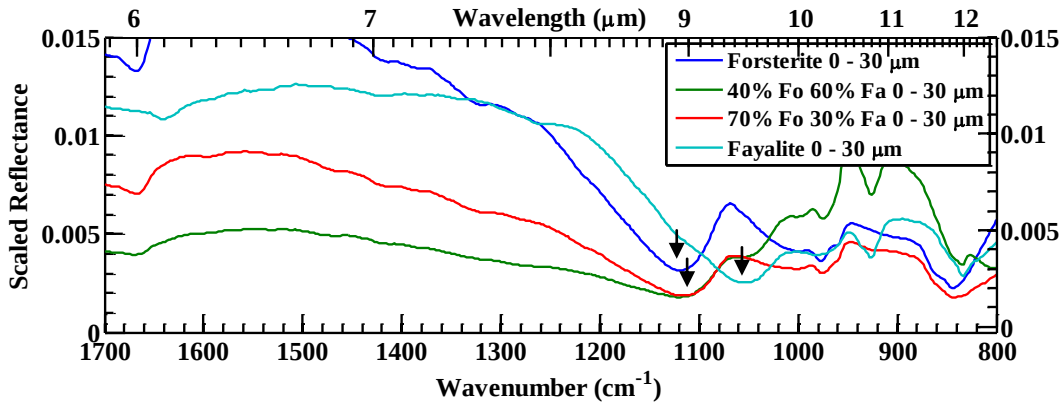

Figure 5-5: The CF of the olivine mixtures varies non-linearly between the Forsterite and Fayalite end-members, with the spectra appearing to retain the spectral features of the former even when the mixture is composed of 60% Fayalite.

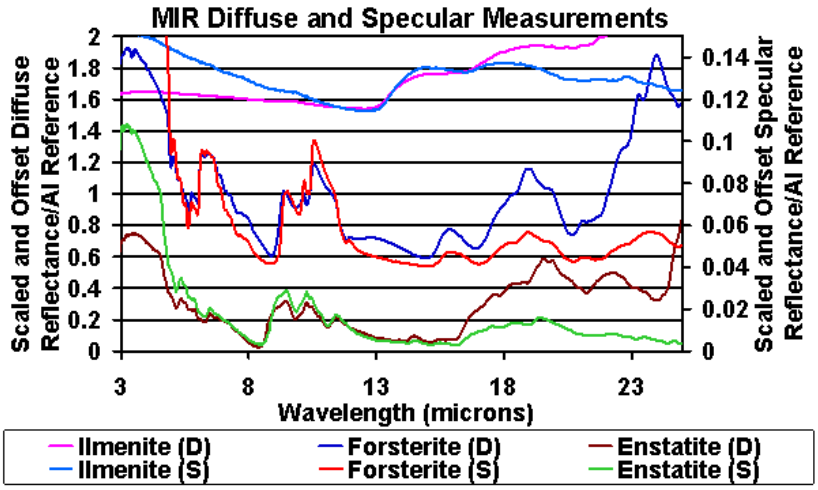

Figure 5-6: Diffuse and specular reflectance spectra of three samples. The spectra have been offset by 0.5 and 1.5 (in diffuse reflectance) for forsterite and ilmenite respectively, with the specular reflectances scaled and offset to overlap the diffuse spectra. The diffuse and specular reflectance spectra are observed to exhibit very similar spectral features, though the specular features are less pronounced, shown by the scale of the secondary y-axis.

Due to the number of spectra generated, not all measurements can be displayed in this thesis: selected results of primary suite measurements are shown in Figure 5-4. The CF is observed to shift to longer wavelengths with increasing abundance of mafic minerals, from Quartz to Fayalite, as expected [Salisbury, 1997], but changes minimally due to grain size and pressure effects, as no thermal gradient is induced in reflectance measurements, even under very low pressures. Restrahlen and other spectral bands can be seen at either side of the CF. Results of the olivine mixtures are shown in Figure 5-5 and diffuse and specular measurements are compared in Figure 5-6. More reflectance spectra and further discussion of the results are given in Greenhagen [2009].

5.3 Thermal Emission measurements

A review of previous laboratory emission measurements is described in detail in Section 2.9; only the most important details are repeated here.

5.3.1 Experimental Requirements of the Simulated Lunar Environment Setup

The lunar thermal environment affects emission spectra due to the creation of a large temperature gradient within the uppermost layers of the lunar regolith [Logan and Hunt, 1970; Logan et al. 1973; Henderson et al., 1996; Henderson and Jakosky, 1997 etc.]. Therefore the most important requirement for the setup is the ability to measure the TIR emission spectra of laboratory samples while a lunar-like thermal gradient exists within them, which previous studies have shown can be achieved in two ways. Logan and Hunt [1970] used a solar-like lamp to heat the samples from above, whereas Henderson et al. [1996] showed that heating the samples from below, using a heated sample cup of the correct temperature, produces equally valid results, is less technically complex to develop and calibrate, and allows cross-calibration with other existing emission setups (Section

2.7.3.2). For this work, an emission setup was made to create a thermal gradient by heating the samples from below, in a similar way to Henderson et al. [1996], except that higher spectral resolution and a larger spectral range were required. For these reasons, the Brüker IFS 66v FTIR spectrometer was chosen over a grating spectrometer or circular variable filter as was used in previous studies. To create the required thermal gradient, the system needed:

- A sample cup capable of being heated to and held at 500 K.
- A radiation shield surrounding the sample cup, cooled to ~100 K.
- A pump and vacuum chamber sufficiently airtight that it could be pumped to a pressure $<10^{-6}$ bar and held at such low pressures while the radiation shield is cooled.
- A method of passing sufficient radiation emitted from the sample into the relevant external source port of the spectrometer.
- Accurate temperature sensors to determine the temperatures of the cup, shield and mirror within the vacuum chamber.
- A calibration routine to convert raw spectra generated by the experiment into emissivities.

5.3.2 Prototyping

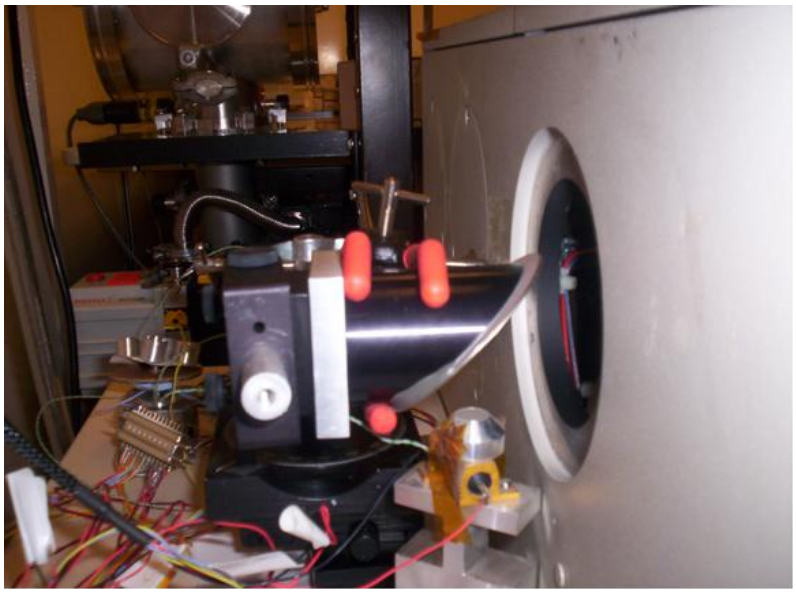

Figure 5-7: A current was passed through the large resistor, heating the sample cup containing the JSC-1A, a lunar regolith simulant. The off-axis paraboloid is set in a position where the radiation emitted from the sample is directed into the emission port in sufficient amount that a spectrum could be recorded.

Firstly it needed to be checked that the Brüker IFS 66v could be setup to make emission measurements, as this had not been tested before using this instrument. The first, crude, proof of concept setup for generating raw spectra of minerals in air was built and spectra were taken of JSC-1A lunar (Figure 5-7). No blackbody was available at this point to convert the raw spectrum of the JSC-1A into emissivity, but as a raw spectrum could be measured, this test proved that an emission chamber could work on this spectrometer.

5.3.3 Design

After ensuring that the spectrometer was suitable, the lunar environment emission chamber was developed and tested at various stages. The developments of the parts that make up the setup are described below.

5.3.3.1 Chamber

The vacuum chamber used for the reflectance measurements was converted into an emission chamber. This chamber had already proved capable of holding the low pressures required, and already had the correct vacuum fittings to connect to the existing pump and pressure gauges. The chamber also included ports where the incident and reflected beams entered and exited the chamber during the reflectance measurements. One of these ports was used for passing the emitted radiation into the spectrometer, while the other was used to provide the cooling power for the radiation shield via a liquid nitrogen feed-through.

5.3.3.2 Emission Port

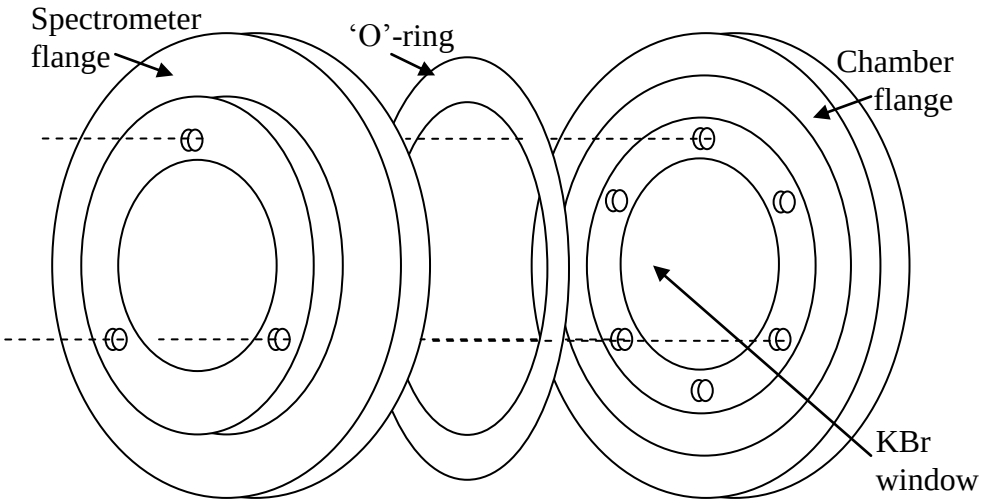

Figure 5-8: The chamber flange, containing the KBr window is first attached to the emission chamber to prevent air entering the chamber. The spectrometer flange, without a window, is then attached to the Brüker IFS 66v. Screws are inserted from the inside of the spectrometer through the clearance holes in the spectrometer flange into the tapped holes in the chamber flange (dotted lines). When tightened, the two flanges press together onto the large 'o'-ring between them to create a seal allowing the spectrometer to be evacuated and keeping the two flanges parallel to each other.

An interface to join the emission ports of the chamber and spectrometer was made that allowed both the Brüker and the chamber to be pumped down separately, with a single KBr window between them, allowing radiation to pass into the spectrometer. This interface was constructed of two Brüker external window flanges (Figure 5-8), one containing the KBr window, joined together with a large 'o'-ring between them. KBr windows do not have perfect transmittance, and so the use of only one KBr window increases the signal reaching the detector and reduces errors due to radiation reflecting off the window into the beam path. The optical design used a 90° off-axis paraboloid (OAP) to direct the radiation emitted from the sample into the spectrometer. Due to the short distance between the mirror and the

sample, the mirror filled a large field of view of the sample, and therefore required cooling with the shield.

5.3.3.3 Cold Finger

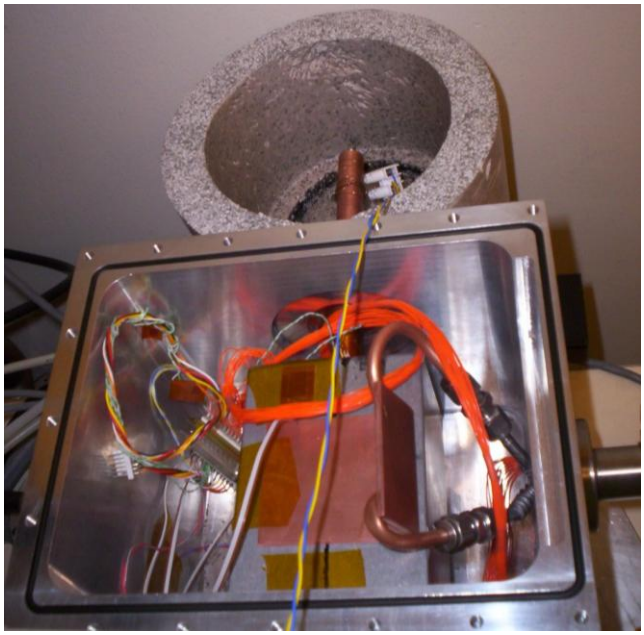

Figure 5-9: The cold finger can be seen at the top of this picture within the liquid nitrogen Dewar. Within the emission chamber, the grey box is the radiation shield and the copper piping is the liquid nitrogen feed-through prior to removal of the Swagelok® fittings.

The first cooling system used a copper cold finger to cool the mirror and radiation shield (Figure 5-9). The cold finger passed through a steel port window into the chamber, on which the radiation shield and mirror were entirely mounted, with the opposite end of the copper rod placed in a Dewar of liquid nitrogen. If the cold finger were to cool down the flange assembly, the radiation shield would be prevented from attaining lower temperatures and the ‘o’-rings within the flange could freeze, potentially breaking vacuum. Therefore the port window was made of poor-thermally conducting stainless steel, machined to have a thickness of only ~1 mm to prevent this. The top of the copper finger was a few centimetres from the rim of the Dewar so that it could be completely immersed in the cryogenic liquid.

Heater wire was wrapped around the cold finger, reducing the time taken to bring the equipment back to above freezing point, at which temperature the chamber can be opened without ice forming on the shield or mirror.

5.3.3.4 Thermal Modelling

Using only the cold finger, the temperature of the shield could not be reduced beyond -60°C while the sample holder was being heated, insufficient to replicate lunar thermal gradients. Additional cooling power was provided using a feed-through pipe, where liquid nitrogen could be flowed directly into the box, circulating around a copper plate attached to the top of the shield. To check that this approach was feasible, a thermal model of the system was made using the finite element analysis software ALGOR to determine whether this method of cooling would work. The model results showed that the cooling power of the liquid nitrogen was sufficient to cool the shield while the sample cup is heated, and showed that the emission chamber wall temperature is relatively unaffected by the cold shield, remaining close to room temperature. The stainless steel supports upon which the sample cup stands were shown to be sufficient to thermally isolate the heated cup.

5.3.3.5 Liquid Nitrogen Feed-through

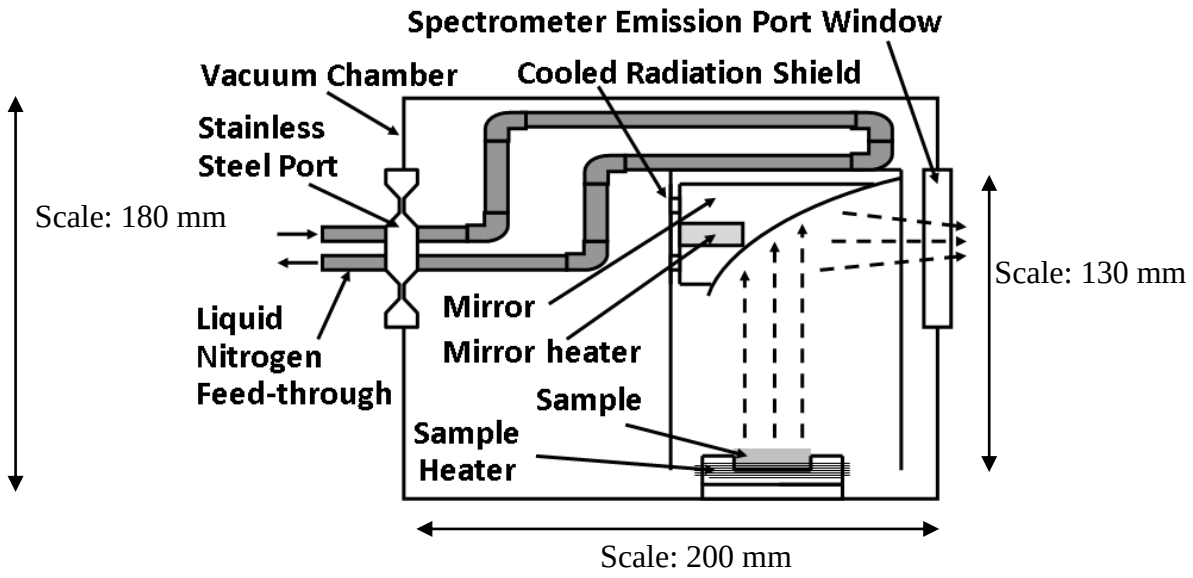

Figure 5-10: A schematic diagram of the final emission chamber design, with the main components labelled.

After a few initial leaks using Swagelok fittings (used to allow the feed-through to be removed from the chamber if required), these fittings were removed and replaced with a single, continuous pipe, permanently hard-soldered into the chamber. The cold finger was cut and the feed-through was run through the centre of the finger, with the input pipe attached to a 30 litre liquid nitrogen Dewar and the output sending the nitrogen gas into an external exhaust. A new, larger, aluminium radiation shield, painted with Nextel Velvet Black high-emissivity paint on the inside, was made to increase the distance between the hot sample and cooled shield and mirror, and to allow the samples to be placed close to the floor of the chamber. The mirror was in good thermal contact with the inside of the shield, and therefore was cooled down when making measurements, meaning that almost the entire field of the view of the sample could be cooled. A schematic diagram of the final version of the emission chamber is shown in Figure 5-10.

5.3.3.6 Sample Cup

The sample cups needed to be sufficiently deep that the thermal gradients (and hence emissivity spectra) were not affected by the boundary between the sample and the bottom of the cup. Past experiments (Section 2.9.1) have shown that the thermal gradient exists only in the top 1 mm of the sample, below which the sample is isothermal. Therefore, 3 mm deep sample cups were manufactured.

Similarly, the cups required a larger diameter than the extent of the spectrometer field of view (FOV) at the location of the sample cup to prevent any horizontal thermal gradient (i.e. heating of the sample by the sample cup sides) from affecting the measured spectra. This FOV size depends on the mirror used and the acceptance angle of the spectrometer's emission port: this angle was known for the Brüker IFS 66v [Turner, personal communication 2008] and so the optimum mirror and sample cup diameter required to fill the spectrometer field of view could be calculated. A suitable sample cup diameter was chosen based on several factors:

- Sample mass. The sample cups need to be filled for each measurement, so the maximum diameter was ultimately dependent on the amount of each sample available.
- Flux required for measurements. A larger spot size allows more radiation to be collected by the spectrometer, reducing noise and therefore reducing scan times.
- Distance between the sample cup and radiation shield. A larger sample cup requires more heating power, and sits closer to the cooled radiation shield making cooling the shield more difficult.

A sample cup diameter of 20 mm was chosen, the maximum size for the mass of samples available, and therefore an off-axis parabolic mirror was selected for a spot size of 16 mm.

Measurements were made to confirm the spot size: firstly spectra were taken of an empty heated sample cup, which was then covered by an ambient temperature baffle containing a 16 mm hole and more spectra taken. All measurements were identical, confirming that no part of the baffle was obscuring the FOV of the spectrometer - therefore the actual spot size must be equal (or smaller) than the 16 mm calculated spot size.

The sample cups were made from aluminium, a good thermal conductor, to ensure that the cups were heated uniformly, and were wrapped in Omegalux^{TM} Rope Heater wire, capable of withstanding temperatures of 482°C and suitable for vacuum use on a conducting surface. The sample cups were supported on 3 small stainless steel screws, securing the sample cup to the chamber baseplate while minimising the loss of heat to the baseplate.

5.3.3.7 Temperature Sensors

Radiation shield and mirror temperatures were monitored using Class B (±0.3 K at 273 K; ±1.3 K at 73 K & 473 K) 2-wire PRT sensors connected to an Agilent 34970A Data Acquisition Unit. To confirm that the shield was cooled uniformly, PRTs were placed at both the top and bottom of the shield. The sample cup temperature was maintained by a Cal 3200 PID temperature controller connected to the sample cup heater wire and to another PRT mounted to the underside of the cup. K-type thermocouples, connected to the radiation shield, inside chamber wall, emission port window flange and liquid nitrogen feed-through were also used during early measurements to confirm the PRT readings and to monitor temperatures within the chamber, but were removed for later measurements.

5.3.3.8 The Calibration Blackbody

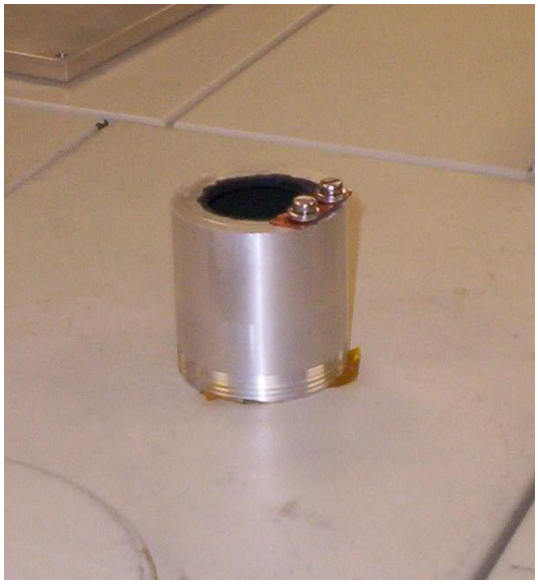

Figure 5-11: The blackbody manufactured specifically for the emission chamber.

A blackbody was required for calibration, to convert the raw mineral spectra output from the spectrometer into emissivities, which needed to be small enough to fit within the radiation shield (in place of the sample cup) and to have a sufficiently large aperture to fill the spectrometer field of view while also having a high emissivity. A blackbody was manufactured with a 40 mm deep aluminium cavity containing a 45º cone and 30 mm aperture (Figure 5-11). The inside of the cavity was painted with Nextel Velvet Black high-emissivity paint (Section 4.4.3). To control the blackbody temperature, the PID temperature controller from the sample cup was used, which was connected to a PRT mounted to the blackbody and a longer thread of the Omegalux^{TM} Rope Heater wire wrapped around the blackbody exterior.

The emissivity of the blackbody was verified at the Planetary Emissivity Laboratory, a European spectroscopy facility at the Deutsches Zentrum für Luft- und Raumfahrt (DLR) in Berlin. There it was measured at 70ºC and compared to a standard industry blackbody

measured using the same spectrometer in the same geometry. The emissivity was found to be >99% in the CF region from 500 – 1740 cm^{-1} (5.75 – 20 μm), decreasing to 97% by 2500 cm^{-1} in the region where the thermally emitted radiation decreases due to the shape of the Planck function.

5.3.4 Experimental Procedure

MIR measurements were made using the KBr beamsplitter, KBr emission port window and DLATGS detector, measured from 300 – 7000 cm^{-1} (1.4 – 33 μm) at 2cm^{-1}(0.013 μm at 8 μm) resolution using the slowest (1.6 kHz) scan mirror velocity, usually with 4x amplifier gain. High-resolution blackbody spectra were made, typically at 60ºC and 90ºC, by co-adding 300 scans together per measurement to be used for calibration (Section 5.3.5).

When measuring the samples, the temperature controller and thermal gradients could take some minutes (up to 5 on occasion) to stabilise, an effect observable by making multiple scans. Therefore, to ensure that the spectra were reproducible, after a delay of 5 minutes, several spectra were measured to ensure that they were reproducible: initially two spectra of 100 scans each were averaged together per measurement. Spectra made of 50 scans were found to have sufficiently low noise, and so this was later changed to three spectra composed of 50 scans each. The complete list of samples measured is shown in Table 5-1. Uncertainties due to the calibration procedure are calculated in Section 5.3.6.

5.3.4.1 Reference Target and Mirror Heater – Kapton Tape contamination

Some of the early emissivity spectra measured consecutively, exhibited a common absorption line at 8.00 μm, regardless of the composition of the sample. After several tests, an absorption line at 8.00 μm was discovered in transmission measurements of melted

Kapton tape, suggesting that this was due to a contamination by burnt tape vapour. The maximum operating temperature of Kapton tape (250ºC) is above the required sample cup temperature, but it is possible that some had been in contact with the sample cup heater wire, which could have been at a higher temperature than this. This tape, that held one of the PRTs in place, was replaced by a metal holder and the chamber was thoroughly decontaminated in a vacuum oven.

To avoid further contamination issues, an extra rope heater was inserted into the hollow interior of the off-axis paraboloid (OAP). This heated the mirror as the box cooled, so that if another contaminant were to be released under vacuum, the radiation shield would reach colder temperatures first, sparing the OAP from most of the contamination. In addition, a copper reference target painted with Nextel Velvet Black paint was added to the chamber. After the sample measurements were made, a stepper motor moved this target into the spectrometer field of view in place of the sample, which was then measured while the radiation shield remained cold. While this reference target is not strictly a blackbody (and therefore can't be used for calibration), its emissivity spectra can be checked for absorption lines, which could then be removed from the mineralogical sample spectra by comparing the two. No further contaminant was detected, and so these extra reference measurements were never required. With the 8.0 μm region being the most important for comparison to Diviner CF measurements, the contaminated spectra were re-measured.

5.3.5 Simulated Lunar Environment Calibration Algorithm

Calibration of the spectrometer was achieved in a similar way to other FTIR emission setups [Christensen and Harrison, 1993; Ruff et al., 1997; Maturilli et al., 2006 etc.], but without assuming that the sample is isothermal. The principal equation describing the function of a FTIR spectrometer is [Christensen and Harrison, 1993]:

$$V_{meas}(\lambda,T) = [\varepsilon_{samp}(\lambda)B_{samp}(\lambda,T) + R_{samp}(\lambda)\varepsilon_{env}(\lambda)B_{env}(\lambda,T) - \varepsilon_{inst}(\lambda)B_{inst}(\lambda,T)]F \quad [5\text{-}1]$$

Where $\varepsilon_{samp}B_{samp}$ is the radiance from the sample, $R_{samp}\ \varepsilon_{env}B_{env}$ is the radiance from the environment reflected off the sample, and $\varepsilon_{inst}B_{inst}$ is the spectrometer radiance. As shown by Ruff et al. [1997], two high-resolution measurements of a blackbody, V_{BB}, at two different temperatures, T_1 and T_2,can be used to calculate the spectrometer response function, F, and the instrument radiance, B_{inst}, as follows:

$$F(\lambda) = \frac{V_{BB}(\lambda,T_1) - V_{BB}(\lambda,T_2)}{B_{BB}(\lambda,T_1) - B_{BB}(\lambda,T_2)} \qquad [5\text{-}2]$$

$$\varepsilon_{inst}(\lambda)B_{inst}(\lambda,T) = B_{BB}(\lambda,T) - \frac{V_{BB}(\lambda,T)}{F} \qquad [5\text{-}3]$$

where B_{BB} is the radiance of an ideal blackbody at temperature T from the Planck equation. Other setups [e.g. Ruff et al., 1997; Maturilli et al., 2006] then assume that R_{samp}= 1 - ε_{samp}, but this cannot be used for lunar environment spectra due to the presence of a large thermal gradient within the sample [Salisbury et al., 1994]. Though, with a cooled radiation shield:

$$B_{env}(\lambda,T) << B_{samp}(\lambda,T), B_{inst}(\lambda,T) \quad [5\text{-}4]$$

Hence equation [5-1] can be simplified and rearranged to:

$$\varepsilon_{samp}(\lambda) = \frac{\varepsilon_{inst}(\lambda)B_{inst}(\lambda,T) + (V_{meas}(\lambda,T)/F)}{B_{samp}(\lambda,T_{samp})} \qquad [5\text{-}5]$$

Therefore, the sample temperature, T_{samp}, could be fitted so that ε_{samp}= 1 at the peak of the CF. Further discussion of using this method to calibrate emission spectra is presented in Section 7.3.2. Emissivity measurements made under nitrogen or a few mbar of pressure were calibrated in the same way as the other setups referenced, using Kirchhoff's Law that R_{samp}= 1 -ε_{samp}, applicable for samples where a negligible thermal gradient exists. It should be noted that measurements made in very low pressure using an ambient temperature

radiation shield cannot technically be calibrated, as it must be assumed that either the radiation shield has negligible radiance or that no thermal gradient is created.

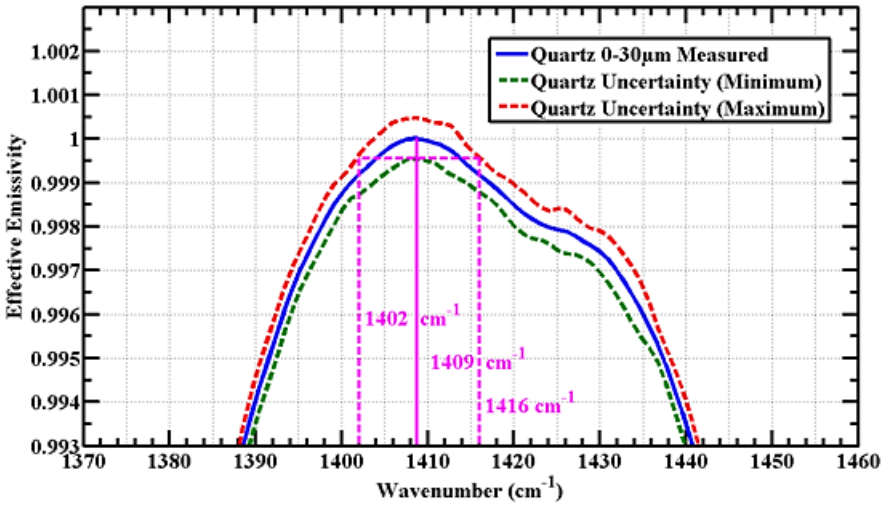

Figure 5-12: Calculation of the maximum uncertainty in the measurement of quartz 0-30µm. In wavelength space, this corresponds to a CF at 7.10 µm ± 0.03 µm. A similar uncertainty will apply to all mineral measurements.

5.3.6 Calibration Uncertainty

For simplicity, all errors were assumed to be uncorrelated, and therefore could be added together in quadrature. It was also assumed that the error on calculating the ideal blackbody (Planck) radiance is negligible. The error in spectrometer response function is derived from equation [5-2] as:

$$\Delta F(\lambda) = \frac{1}{B_{BB}(\lambda, T_1) - B_{BB}(\lambda, T_2)} \sqrt{\left(\Delta V_{BB}(\lambda, T_1)\right)^2 + \left(\Delta V_{BB}(\lambda, T_2)\right)^2} \qquad [5\text{-}6]$$

Where the variables are the same as previously described, with a Δ symbol indicating the uncertainty in that variable. The error in spectrometer instrument radiance is calculated from equation [5-3]:

$$\Delta\left(\varepsilon_{inst}(\lambda)B_{inst}(\lambda,T)\right)=\left(\frac{V_{BB}(\lambda,T_2)}{F}\right)\sqrt{\left(\frac{\Delta V_{BB}(\lambda,T_2)}{V_{BB}(\lambda,T_2)}\right)^2+\left(\frac{\Delta F}{F}\right)^2} \qquad [5\text{-}7]$$

Therefore the error in sample radiance is:

$$\Delta\left(\varepsilon_{samp}(\lambda)B_{samp}(\lambda,T_{samp})\right)=\sqrt{\left(\Delta\left(\varepsilon_{inst}(\lambda)B_{inst}(\lambda,T)\right)\right)^2+\left(\Delta\left(V_{meas}(\lambda,T)/F\right)\right)^2} \qquad [5\text{-}8]$$

$$\Delta\left(\varepsilon_{samp}(\lambda)B_{samp}(\lambda,T_{samp})\right)=\sqrt{\left(\left(\frac{V_{BB}(\lambda,T_2)}{F}\right)\sqrt{\left(\frac{\Delta V_{BB}(\lambda,T_2)}{V_{BB}(\lambda,T_2)}\right)^2+\left(\frac{\Delta F}{F}\right)^2}\right)^2+\left(\left(\frac{V_{meas}(\lambda,T)}{F}\right)\sqrt{\left(\frac{\Delta V_{meas}(\lambda,T)}{V_{meas}(\lambda,T)}\right)^2+\left(\frac{\Delta F}{F}\right)^2}\right)^2} \qquad [5\text{-}9]$$

The uncertainties in $V_{BB}(\lambda,T_1)$, $V_{BB}(\lambda,T_2)$ and $V_{meas}(\lambda,T)$ were determined by running single scans of the quartz 0 - 30 µm sample, and a blackbody at the two calibration temperatures. The standard deviation, $\sigma_{\Delta V}$, was calculated for each, and the standard error was determined from:

$$\Delta V\,(\lambda,T)=\frac{\sigma_{\Delta V}}{\sqrt{n}} \qquad [5\text{-}10]$$

Where n is the number of scans taken, i.e. 300 for each blackbody, and 100 for each sample. When applied to the quartz calibration measurement, this equalled a maximum uncertainty in the CF peak wavelength of approximately ±0.03 µm, as shown in Figure 5-12.

5.4 Emissivity Results

5.4.1 Quartz

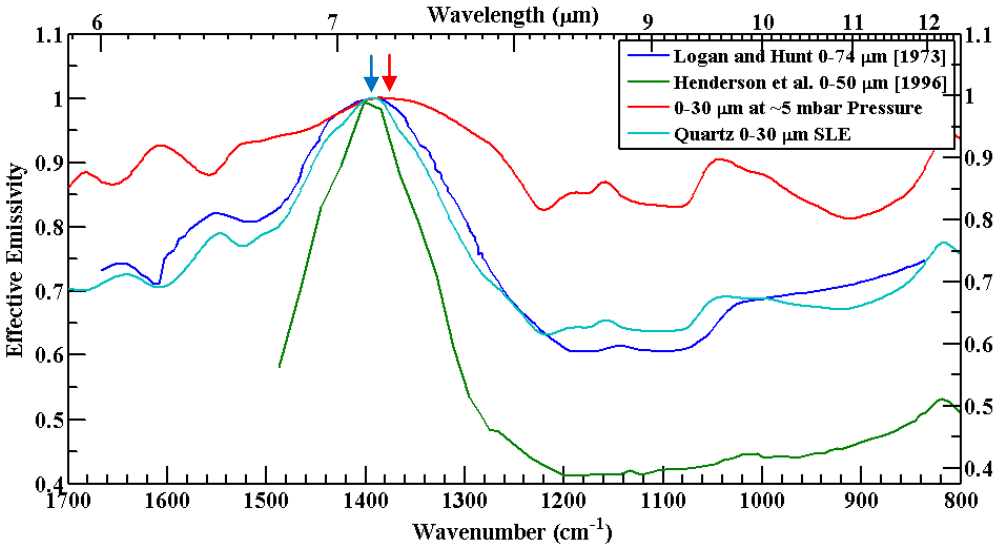

Figure 5-13: Comparison of emissivity spectra of Quartz 0 - 74 µm heated from above (digitised from Logan et al. [1973]) and Quartz 0 - 30 µm heated from below, measured in this investigation. The CF can be seen to shift to shorter wavelength and the spectral contrast increases under SLE conditions (blue and green) when compared to a 5 mbar pressure measurement (red). The spectral contrast varies with grain size, but the CF remains constant. The lower resolution of the Henderson et al. [1996] measurements can also be seen to make it hard to discern the emissivity peak.

Quartz, while not being a known major constituent of the lunar surface, had been measured previously both by heating-from-above by Logan et al. [1973] and heating-from-below by Henderson et al. [1996]; both of which had published the emission spectra (not just the CF maximum value as for most other measurements). This made it the ideal sample measurement for verifying the chamber calibration, calibration algorithm and heating-from-below method. A comparison of the emissivity spectrum of the quartz 0 – 30 µm grain size sample with the laboratory results of Logan et al. [1973] and Henderson et al. [1996] is shown in Figure 5-13.

5.4.2 Primary Suite

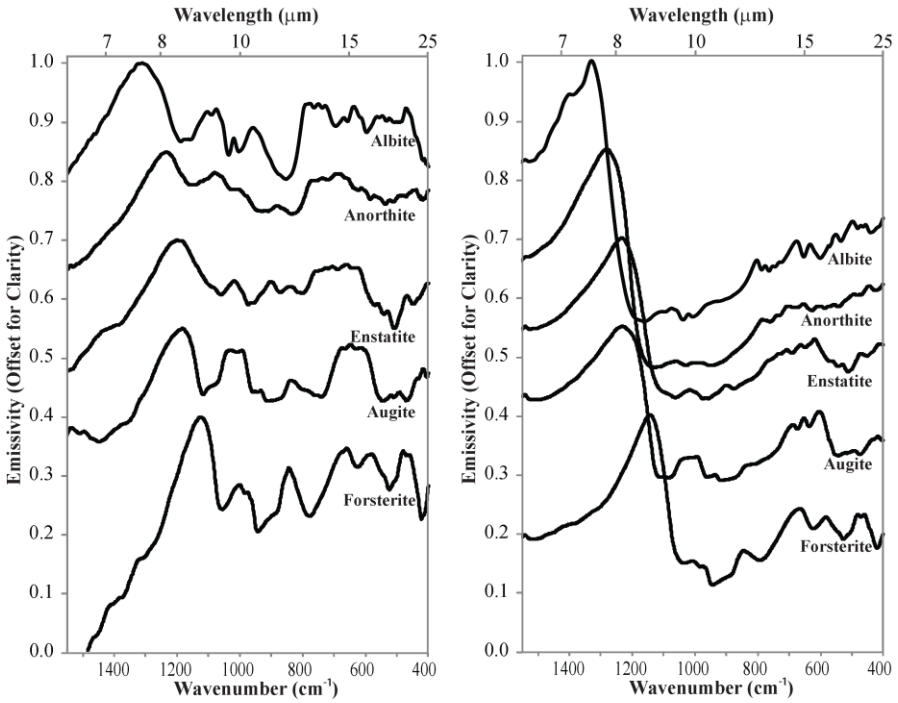

Figure 5-14: The emissivity spectra of the 0 – 25 μm grain size primary suite minerals measured in this project in a nitrogen atmosphere (left) and in a SLE (right) [Donaldson-Hanna, accepted 2011]. For clarity, the spectra are offset by 0.15 units from each other. The CF shifts to shorter wavelength and the spectral contrast is increased for all the minerals measured.

Selected lunar environment emission spectra, measured by the author, of the primary suite minerals are shown in Figure 5-14. Anorthite, a plagioclase feldspar representative of the lunar highlands, has a CF of 7.82 μm (0 – 25 μm grain size), while the pyroxenes augite and enstatite have intermediate CFs of 8.13 μm (for both augite 0 – 25 μm and 0 – 30 μm grain sizes) and 8.12 μm (0 – 30 μm) respectively. The olivines forsterite and fayalite were found to have the longest wavelength CFs, from 8.68μm (forsterite 0 – 30 μm) and 8.76 μm

(forsterite 0 – 25 µm) to 8.99µm (fayalite 0 – 30 µm). Comparisons of these values to Diviner observations are made in Section 6.3.

5.4.3 Silicic Minerals

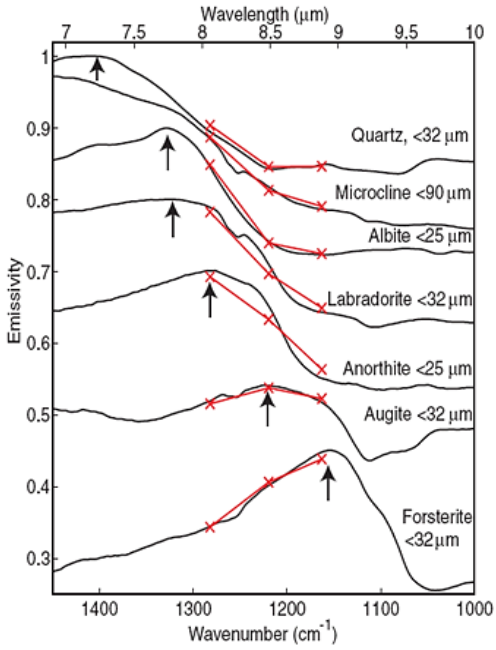

Figure 5-15: SLE mineral spectra (black) from Glotch et al. [2010] (reprinted with permission from AAAS), measured in this project and convolved to Diviner 8 µm channel pass bands (red). The spectra are offset by 0.1 units from each other for clarity. CF maxima are highlighted by arrows.

The silicic minerals were measured by the author for a separate study by Glotch et al. [2010] after it was discovered that very low wavelength CFs were observed for certain regions on the lunar surface (Figure 5-15). Only high silica-content (e.g. quartz, microcline, obsidian etc.) and calcic plagioclase (e.g. albite) minerals were observed to exhibit CFs much shorter than can be constrained by Diviner. The application of these results to Diviner data is described in Section 6.5.

5.4.4 Plagioclase Series

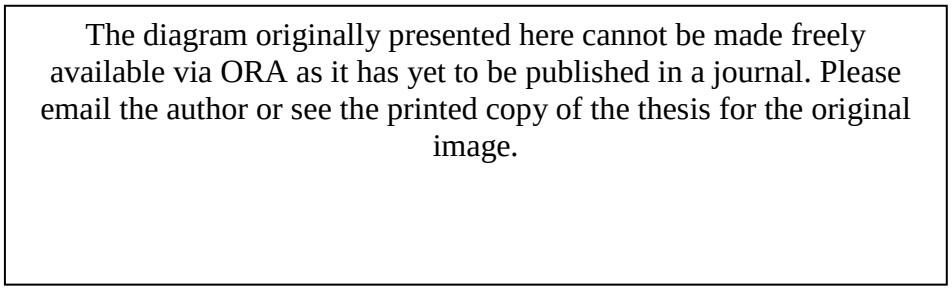

Figure 5-16: The plagioclase minerals measured by the author during this project, with each mineral type offset by 0.1 units from each other. The CF shifts to shorter wavelengths as the sodium:calcium ratio increases, though the effect is non-linear with the intermediate minerals lying closer to the albite end-member.

The CF maxima of the plagioclase minerals (described in Section 1.2.4.2) were measured to be of shorter wavelengths (Figure 5-16), from 7.51 μm and 7.53 μm for albite 0 – 64 μm and 0 – 25 μm grain-sized minerals, to 7.82 μm for the anorthite 0 – 25 μm sample. The intermediate plagioclase minerals lie between these values, with CFs closer to albite than anorthite. No bytownite sample exists, as the chemistry of the anorthite was found to be on the boundary between the two (i.e. 90% anorthite, 10% albite). Again, comparisons with Diviner observations of the lunar surface are given in Section 6.4.

5.4.5 Weathered Anorthosite

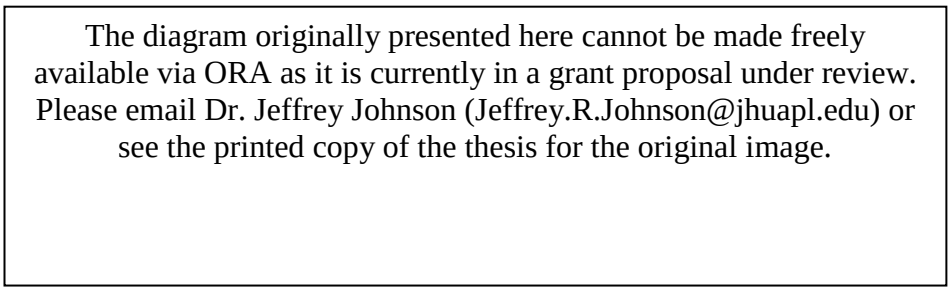

Figure 5-17: Spectra of two samples of andesine measured in SLE and ambient conditions [Johnson, 2010], where one was shocked with 56.5GPa of pressure. Samples containing larger grains are not ideal for this type of comparative study, as they exhibit fewer differences between ambient and lunar conditions and tend to have flat emissivity short-wave of the CF making identification difficult (here, it is approximately located with tick marks around 8 μm). The CF appears to shift to longer wavelengths due to the artificial weathering, but this shift cannot be described quantitatively from the data. Ambient spectra were measured using the emission setup at ASU.

Two samples of andesine (composition: 30 – 50% Anorthite, 50 – 70% Albite) chips were measured in this project where one had been artificially weathered using a powder propellant gun to impact the sample [Johnson, 2010]. Both samples were measured in ambient conditions at ASU and in SLE here (Figure 5-17). The samples were too large-grained to exhibit any real differences in spectra between measurements made in air and in SLE, but this itself confirmed an earlier conclusion: that large-grained samples do not exhibit the change in spectral shape caused by the presence of a thermal gradient. In addition, the results showed that mineral spectra could change as a direct consequence of space weathering, shifting the CF to longer wavelength, and not only due to the mixing of the surface by such weathering processes.

5.4.6 Apollo Samples

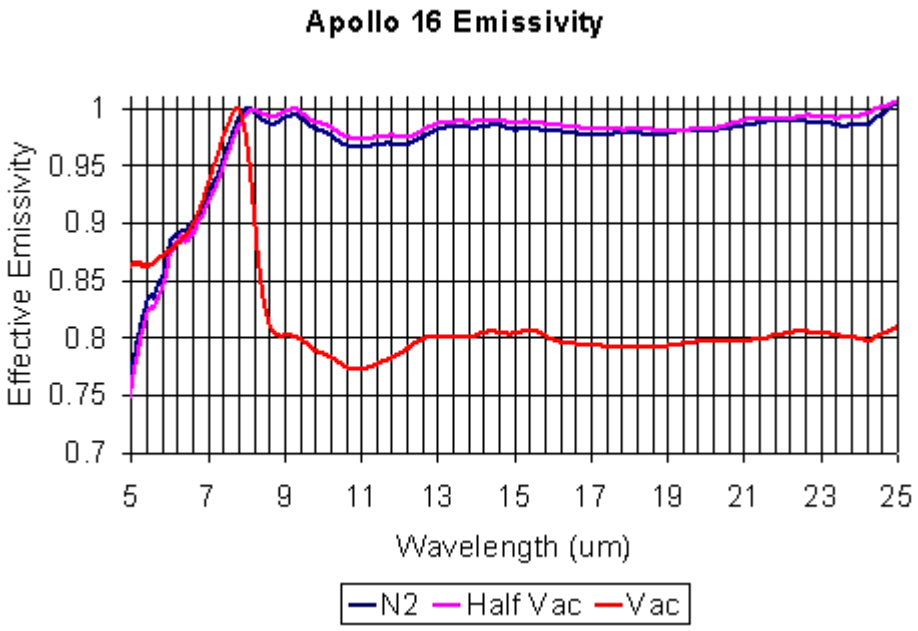

Figure 5-18: Emissivity spectra of Apollo sample 68810, taken from the lunar highlands, under various environmental conditions.

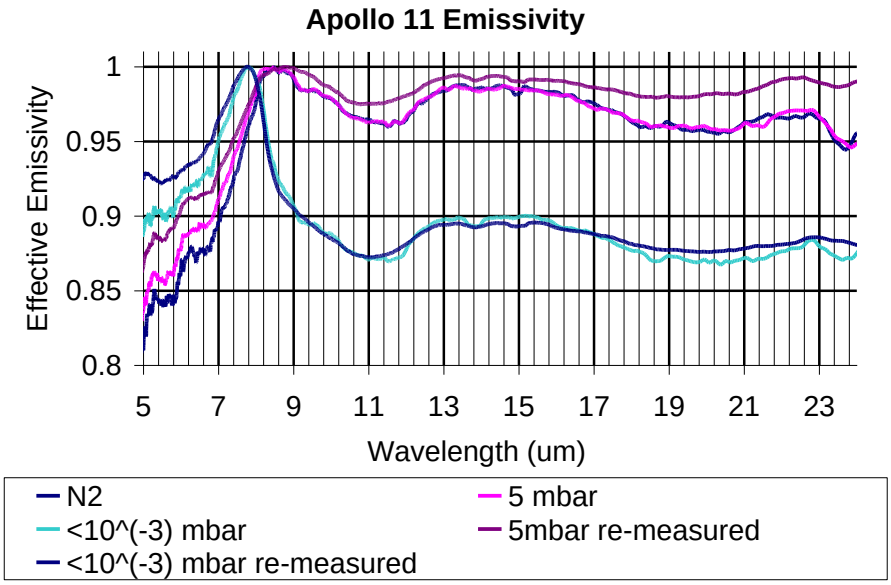

Figure 5-19: Measurements of two different samples of 10084, a mare basalt from the lunar surface by Apollo 11 astronauts, measured under several environments. Some variation is observed between the two samples, but the CF locations for each environmental condition match each other.

Two lunar samples, 68810 and 10084, returned from the Moon during the Apollo program were obtained and measured in the emission chamber. Due to restrictions imposed by the NASA Astromaterials Acquisition and Curation Office, the samples could not be heated to the temperature required for a full SLE measurement to be made, so instead were measured in nitrogen gas, 5 mbar of pressure and $<10^{-3}$ mbar (with ambient temperature shield) to investigate how the emissivity spectra of the lunar surface were affected by pressure. Sample 68810 was collected by the Apollo 16 mission from the lunar Descartes highlands, and was described as one of the most plagioclase-rich samples [Paige, personal communication 2010]. This was reflected in the measurements, having a CF of 8.04 under nitrogen, 8.16 under low pressure and 7.75 under vacuum (Figure 5-18). This final measurement used an ambient cold shield and low pressure and so the result may not be

valid (Section 5.3.5), possibly explaining why this CF appears to be of a shorter wavelength than expected. The flat emissivity beyond the CF in the higher-pressure environments is routinely observed in reflectance measurements of Apollo samples [e.g. Salisbury et al., 1997].

More data is available for Sample 10084. It was returned by the Apollo 11 mission from Mare Tranquillitatis, and was a mature (highly weathered) sample, composed mainly of mare basalt and agglutinates respectively comprising 24% and 52% (modal values) of the sample [Simon and Papike, 1981]. It was found to have a value of 8.47 in both nitrogen and when pumped down to 5 mbar, but unexpectedly shifted to 7.84 under pressures of $<10^{-3}$ mbar (Figure 5-19). Again, this result may not be valid due to the calibration algorithm, but due to such a large deviation from what was expected of a mare sample (>8.2 μm), a different sample of 10084 was then measured, which resulted in similar CF values (Figure 5-19). Possible explanations of why the results for both Apollo samples could be wrong and possible future solutions are described later (Section 7.4.1).

5.4.7 FIR (>25 μm) Measurements of Oligoclase

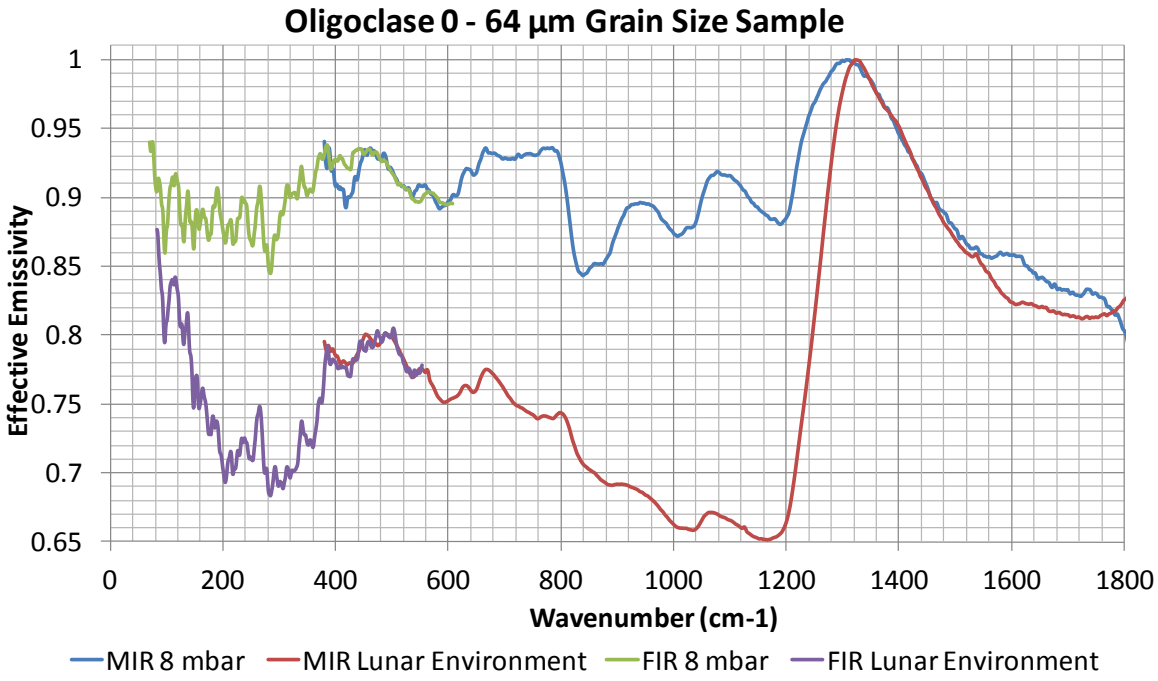

Figure 5-20: Combined MIR and FIR spectra of oligoclase. The spectra appear to show some overlap around the 400 - 600 cm^{-1} region in both the 8 mbar and vacuum measurements. Future work needs carrying out (Section 7.4.1.6) to check the validity of this result.

Attempts were made to determine the emissivity spectrum of oligoclase in the FIR, potentially allowing mineral spectra to be compared with the Diviner thermal channels in addition to the 8 μm channels. The KBr emission port window was replaced by one made of polyethylene, which is transparent in the FIR (Table 4-1), the Mylar beamsplitter was added and the DTGS detector replaced by the FIR DTGS detector. The lower flux of a thermally-emitting sample in the FIR region required more time per measurement. Blackbody measurements were again made using a 1.6 kHz scan mirror velocity and 4x amplifier gain, with three spectra of 300 scans each averaged together for each blackbody measurement, made at 60ºC and 90ºC. The oligoclase 0 – 64 μm grain size sample was heated to 100ºC

and measured in 5 mbar of air and under vacuum ($<10^{-3}$ mbar). Due to a lower flux in the FIR, 150 scans were co-added per spectrum, three of which were averaged together for each measurement. An SLE measurement was attempted but as the cold shield temperature reduced, this increased the radiative cooling of the sample, which reduced the sample temperature and therefore the emitted radiance. It may have been possible to take spectra if longer scans were made, but a larger liquid nitrogen Dewar would be required to keep the shield cold.

When calibrating FIR spectra, no point in the spectrum can be assumed to have an emissivity of one, therefore the calibration of the spectra must be done differently to the MIR. Instead, a value of T_{samp} in equation [5-5] was selected to make the FIR emissivity overlap the MIR emissivity (Figure 5-20). Investigating the validity of this result is beyond the scope of this thesis, but the measurements appear to produce a valid spectrum. Further discussion of this result is made in Section 7.4.1.6.

5.4.8 Comparison of Christiansen Feature Maxima to Heating-from-Above Measurements

This project SLE			Logan et al. [1973] Packed Samples in SLE			
Sample	**Owner**	**CF (μm)**	**Sample (0 - 5 μm)**	**CF (μm)**	**Sample (0 – 74 μm)**	**CF (μm)**
Albite (0 – 64 μm)	BTG	7.51	Albite	7.47	Albite	7.53
Albite (0 – 25 μm)	KDH	7.53				
Fayalite (0 – 30 μm)	BTG	8.99	Olivine	9.25	Olivine	8.88
Forsterite (0 – 30 μm)	BTG	8.68				
Forsterite (0 – 25 μm)	KDH	8.76				
Anorthite (0 – 25 μm)	KDH	7.82	Labradorite	7.88	Labradorite	7.75
Labradorite (0 – 25 μm)	KDH	7.60				
Quartz (0 – 30 μm)	BTG	7.12	Quartz	7.18	Quartz	7.15
Quartz (30 – 64 μm)	BTG	7.11				

Table 5-2: The CF wavelength maxima, measured by heating-from-below are shown adjacent to the corresponding figures from Logan et al. [1973]. 0 – 5 μm grain size samples are included for completeness, and are not representative of the lunar surface [Logan et al., 1975; McKay, 1991] or of the 0 – 30 μm samples used in this project. Initials of sample owners are given in Table 5-1. The anorthite sample measured in this study was composed of 89% anorthite [Donaldson-Hanna, personal communication 2010]; hence the closest comparable mineral is labradorite (up to 70% anorthite). Olivine chemical analysis is not given by Logan et al. [1973]: from these results it appears to be composed primarily of fayalite. Such large CF differences between Olivine (0 - 5 μm) and Olivine (0 – 74 μm) found from their data are unusual for only a change in grain size.

There is good agreement between the CF of the minerals measured in this investigation and those measured previously by Logan et al. [1973] (Table 5-2; Section 2.9.1). Some differences are observed, especially between the 0 – 5 μm grain sized samples, but these samples were not expected to be comparable. Logan et al. [1975] stated that:

> "Analysis of the 0 – 5 μm samples shows that they contain very few particles larger than 1 μm, most being considerably smaller. Consequently, such samples represent a limiting case for particle size distribution and are unrealistic as analogues of remote targets with particulate surfaces."

The radiative properties of the samples, and hence the change in emissivity and enhancement of the CF by the lunar environment is governed by the transmission spectrum and source function of the sample (Section 2.9.3.2). Transmission spectra are relatively insensitive to particle size [Logan et al., 1975]; however source functions show large variations. Source functions of larger, more reasonable grain sizes of quartz (e.g. 44 – 53 μm, 74 – 88 μm, 135 – 149 μm and 250 – 297 μm) exhibited much smaller differences between each other than between the 0 – 5 μm sample [Logan et al., 1975]. Hence, the 0 – 74 μm samples, which contained less of the smallest sized grains, were considered adequate lunar analogues [Logan et al., 1975], which matched well to the spectra measured for this project (Table 5-2). Some differences are seen, but without compositional information of the minerals measured by Logan et al. [1973], it is difficult to make any conclusions.

5.5 Conclusions

5.5.1 Accounting for the Effects of the Lunar Environment

This and previous studies (Section 2.9.1) have shown that many factors affect the CF position. A summary of such factors and how they were approached in this study are described below:

- Particle size: Several particle sizes were investigated, though attention was mainly paid to the small grain sizes, as small particles dominate the spectral features observed [Logan and Hunt, 1972] and most surface lunar regolith is composed of fine-grained particles [Salisbury et al., 1973]. Grain size distributions provide only a loose description of the sample characteristics – much of the variations are due to the way in which the samples were sourced and prepared – which skew the distributions. Measuring two similar grain sized samples (0 – 25µm and 0 – 30 µm) that were sourced individually and prepared differently [Greenhagen, 2009; Donaldson-Hanna, submitted 2011] allowed comparisons to be made, which have been shown to affect the CF position minimally.
- Soil, rock and mineral differences: In addition to variations in particle size due to preparation method, the type of sample may also affect the emissivity spectra. Minerals are composed of pure, regularly structured crystalline solids and are therefore preferable for spectral measurements, but may differ from measurements of the lunar surface, which consists of rock or soil mixtures. Aside from previous measurements of Apollo samples (Figure 2-16) that had been mineralogically characterised, it is unknown how such mixtures affect the CF shape.
- Vacuum conditions: In all SLE measurements, the pressure in the chamber was sufficiently low to replicate the lunar environment [Wechsler and Glaser, 1965].

- Shield temperature: The radiation shield was cooled sufficiently during SLE measurements that the shield approximated cold space, e.g. at 1250 cm^{-1}, the % error in radiance between a 350K sample and the shield vs. cold space is calculated by:

$$\frac{B_{samp}\left(1250\,cm^{-1},350K\right)-B_{shield}(1250\,cm^{-1},100K)}{B_{samp}\left(1250\,cm^{-1},350K\right)-B_{shield}(1250\,cm^{-1},3K)}\times 100=99.99\% \quad [5\text{-}12]$$

- Sample packing: The CF dependency on the amount of sample packing was not investigated in this study, so every sample was prepared by the author in the same way, with the sample poured into the sample cup and excess wiped away to leave a flat upper surface in line with the top of the sample cup.

- Type of heating: Models show an equal thermal gradient developed within the sample through either heating-from-above or heating-from-below experiments, confirmed by the measurement of quartz (Section 5.4.1) and previous laboratory measurements (Section 5.4.8), provided the correct sample cup and radiation shield temperatures are used.

- Insolation angle: These measurements replicate the environmental conditions of the lunar surface when the sun is directly overhead, to produce the maximum thermal gradient in the sample. Other sun angles have not been considered in this project, but would be expected to reduce the temperature gradient, therefore shifting the CF to longer wavelengths.

- Space weathering: An attempt was made to quantify the shift due to sample maturity. Shocked and un-shocked andesine chips were measured in SLE but the samples were not ideal for this type of measurement due to the large size of the chips, which we were unable to reduce. Two Apollo samples were measured, but the mafic sample exhibited an unusually-short wavelength CF (Figure 5-18; Figure 5-19), due to several possible factors discussed in Section 7.4.1.

All of these factors can affect both the CF position and spectral contrast, the only lunar surface parameters measureable by Diviner. Large differences in spectral contrast had been observed between previously measured SLE emissivity spectra and Apollo samples (Section 2.9.1), with the latter having less spectral contrast than almost all mineral measurements. Therefore, to compare laboratory SLE spectra to Diviner data (Section 6.3) the CF is assumed to depend primarily on composition, with the other factors contributing to an uncertainty in the spectral location of the CF peak.

5.5.1.1 Uncertainty in CF Position

With insufficient large-grained sized samples measured, these uncertainties were derived from the SLE CF values of Logan et al. [1973], by comparing the shift in CF due to the type of sample packing (i.e. 'packed' versus 'fairy castle'; Section 2.9) and due to the sample particle size distribution (0 - 5 μm versus 0 – 74 μm). Averages, calculated as the mean of the absolute CF differences, were found to be 0.13 μm due to the difference in packing and 0.28 μm due to the difference in particle size. The latter large difference can at least be partly attributed to using an unrealistic lunar particle size (Section 2.9.2) [Logan et al., 1975; McKay, 1991], but without more data, a better estimate cannot be made. The variations between the CFs of 0 – 25μm and 0 – 30 μm samples are small (maximum 0.08 μm; Table 5-2), strongly suggesting that this error may be smaller for more realistic lunar particle size distributions. Many other unquantifiable uncertainties also exist, such as the effects of space weathering, differences in CFs between pure minerals and rocks, and the effects of spectral mixing, which require further investigation beyond the scope of this thesis.

5.5.2 Comparing the Effects of the Lunar Environment

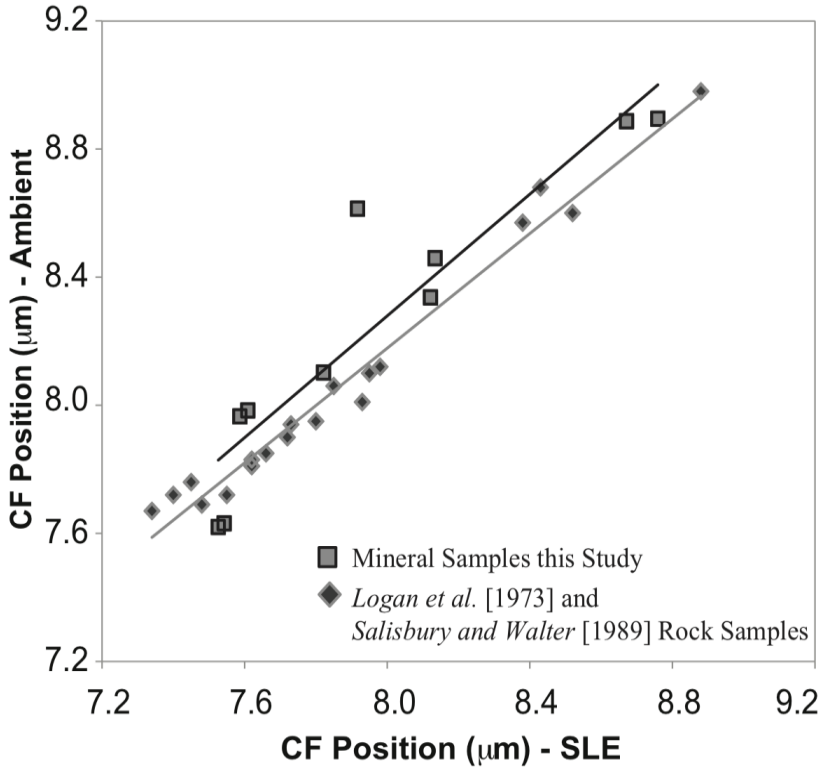

Figure 5-21: The figure shows the relationship between CF wavelength in a nitrogen environment and SLE measured in the emission chamber (squares), measured by the author and Kerri Donaldson-Hanna, plotted in a study by Donaldson-Hanna et al. [accepted, 2011]. Also plotted (diamonds) is the CF wavelength of the rock samples measured in SLE by Logan et al. [1973] and in reflectance by Salisbury and Walter [1989].

A study by Donaldson-Hanna et al. [submitted, 2011] compared the CF wavelengths of spectra taken in SLE and nitrogen conditions in the chamber, similar to that performed by Salisbury and Walter [1989] who measured the reflectance of the samples used by Logan et al. [1973]. A plot of CF measured in nitrogen versus CF measured in a SLE is shown in Figure 5-21.

6 Preliminary Results Using Diviner Data

After entering into an elliptical orbit around the Moon, during which the on-board systems and instruments were checked, LRO successfully transitioned into a 50km mapping orbit in September 2009 and has since been returning data taken by all instruments with minimal disruptions. This chapter describes some of the unique studies made possible by the Diviner dataset:

- Polar surface temperature maps
    - by the author, for an ESA landing site study
    - by Paige et al. [2009], which utilised the filter measurements (Section 4.2) and instrument calibration (Section 4.5) performed by the author
- Compositional maps:
    - by the author, combining Diviner TIR and Kaguya Multiband Imager UV/Vis datasets
    - by Glotch et al. [2010], using mineral emissivity measurements made in this project (Section 6.5) to constrain lunar surface mineralogy.

6.1 Polar Temperature Mapping 1: Searching for Permanently Illuminated Regions

Diviner's measurable temperature range is sufficiently large (~24 K to >400 K) that the surface temperature at any location on the Moon can be measured. This has important implications for future human missions to the lunar poles, as some locations are permanently illuminated throughout a full diurnal cycle while the coldest areas exist in permanent shadow (Section 2.2).

6.1.1 Landing Site Study

During this project a European Space Agency study of potential landing sites for an unmanned lander arose, investigating three regions believed to be near-permanently illuminated from previous work [Crawford, personal communication 2010]. This gave a good opportunity to utilize the unique Diviner dataset, to determine the diurnal and seasonal temperature variations of these sites, important for determining the engineering requirements of future landing craft. The locations were:

- Shackleton Rim (-89.779º, -153.435º)
- Connecting Ridge (-89.463º, -137.490º)
- Malapert Peak (-86.024º, +2.613°)

where the numbers in brackets signify their latitude and longitude. Selenographic coordinates are used in this project, where latitudes are measured in degrees between +90º (north pole) and -90º (south pole). Longitudes are defined as 0º at prime meridian, with negative values for locations to the east of this line and positive to the west, from -180º to +180º.

6.1.2 Aims

Lunar surface temperatures are dependent upon the position of the sun. The surface local time of a region (measured in hours from 0 - 24) is a measurement of the subsolar longitude (the surface longitude where the Sun is directly overhead, relative to that region's longitude), where the directly overhead at midday. As the Moon rotates with respect to the Sun, this diurnal cycle causes regular heating and cooling (Figure 2-2). At the poles however, the temperatures can also have a seasonal dependence as the subsolar latitude varies between ±1.54° each cycle. At ±75° latitude, for example, regolith temperatures are

expected to oscillate between 80 - 280 K during a lunar day, but at 89° latitude the regolith is expected to vary between 40 - 180 K due to the season cycle [Paige et al., 2009]. Therefore, variations in surface temperature across both diurnal and seasonal cycles were required to be investigated.

6.1.3 Data Retrieval and Mapping Procedure

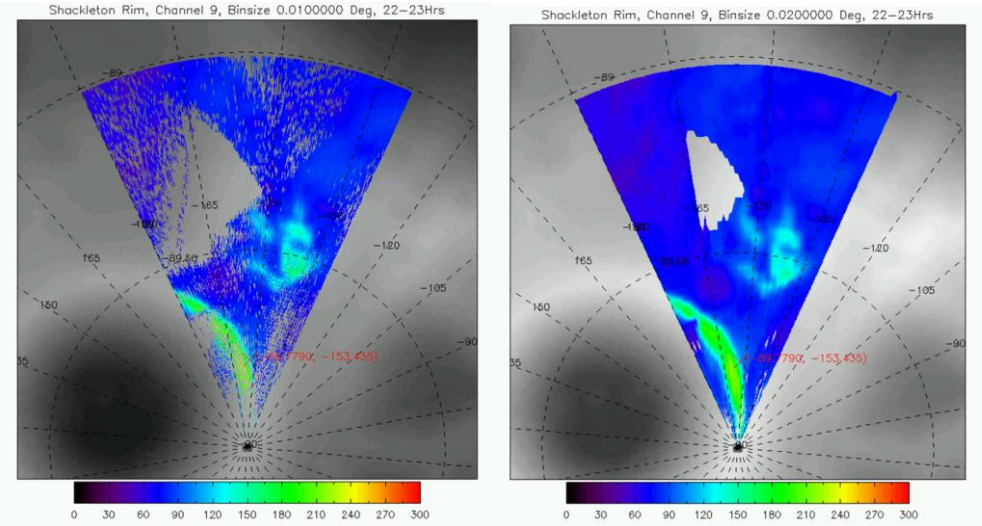

Figure 6-1: Lunar south pole surface temperatures measured by Diviner channel 9, overlaid on a Kaguya LALT topographic base map [Araki et al., 2009], showing data from the selected region at 10 - 11pm local surface time. The binning resolution used on the left (0.01° lat x 0.1° lon) was too high, hence the gaps in the data; using a resolution of 0.02° (latitude) x 0.5° (longitude) resolved this. The red cross indicates the location of Shackleton Rim.

Using a radiometer (over using a camera or spectrometer, for example) with a two-point calibration (Section 3.4.2) simplifies the conversion of instrument's digital counts into radiances and hence into temperatures without the need for complex corrections. Spacecraft geometry and timing are added to the Diviner data from the LRO SPICE (Spacecraft, Planet, Instrument, C-matrix (pointing), and Events) kernel files provided by JPL, therefore

brightness temperature maps can be produced directly from the lower-level Diviner data without the need for further calculations. The data used in this polar study was retrieved from the UCLA servers up to the 15th June 2010 using the Diviner Web Query Tool. Longitude, latitude, brightness temperature, lunar local time and subsolar latitude were extracted for the regions under investigation.

For the analysis, a two-dimensional grid was made in latitude and longitude space and all points that were located within each grid square, or bin, were averaged together to make a polar map. This binning process provides a regular grid onto which the data is plotted to create complete maps from the many Diviner swaths passing over the poles. The data were binned by longitude, latitude, and into 24 lunar local hour (i.e. subsolar longitude) segments for each location. The number of Diviner observations governs the resolution of the bins: if the spatial resolution is too high then the bins are sparsely populated i.e. many bins contain no data, making incomplete maps (Figure 6-1). Conversely, if it is too low then spatial resolution is lost when the data in each bin is averaged. A binning resolution of 0.02° (lat) x 0.5° (lon) was found to fill >90% of the local surface time bins at the desired regions.

6.1.4 Results: Permanently Illuminated Regions

6.1.4.1 Temperature versus Surface Local Time

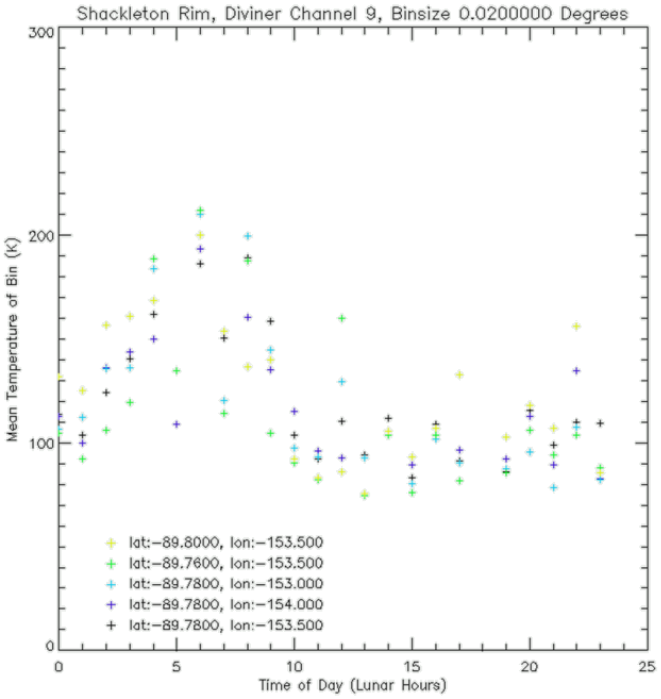

Figure 6-2: Channel 9 mean (binned) brightness temperature variations across the full diurnal cycle for Shackleton Rim (black crosses) and adjacent bins (other colours).

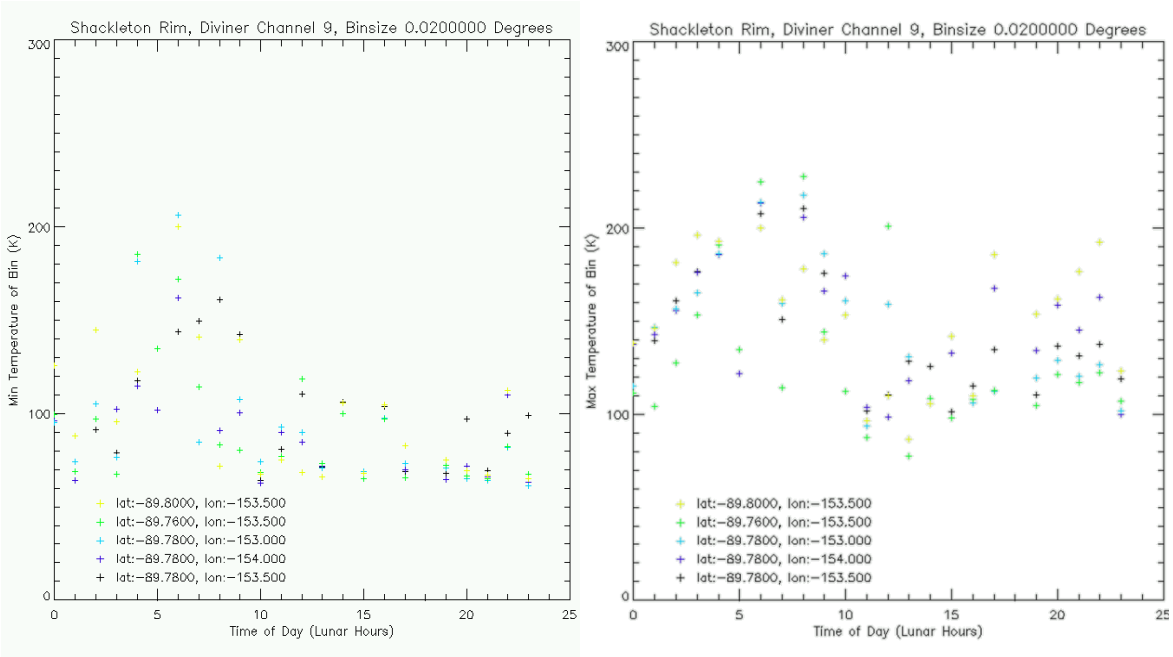

Figure 6-3: Channel 9 minimum and maximum brightness temperatures for Shackleton Rim and adjacent bins.

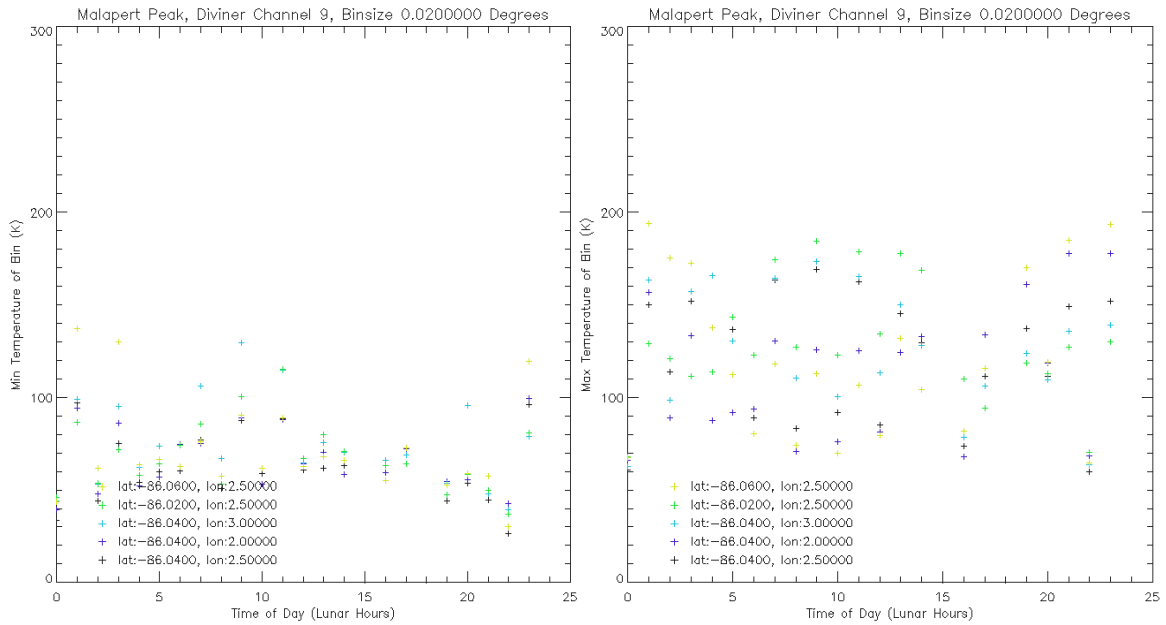

Figure 6-4: Channel 9 minimum and maximum brightness temperatures for Malapert Peak and adjacent bins.

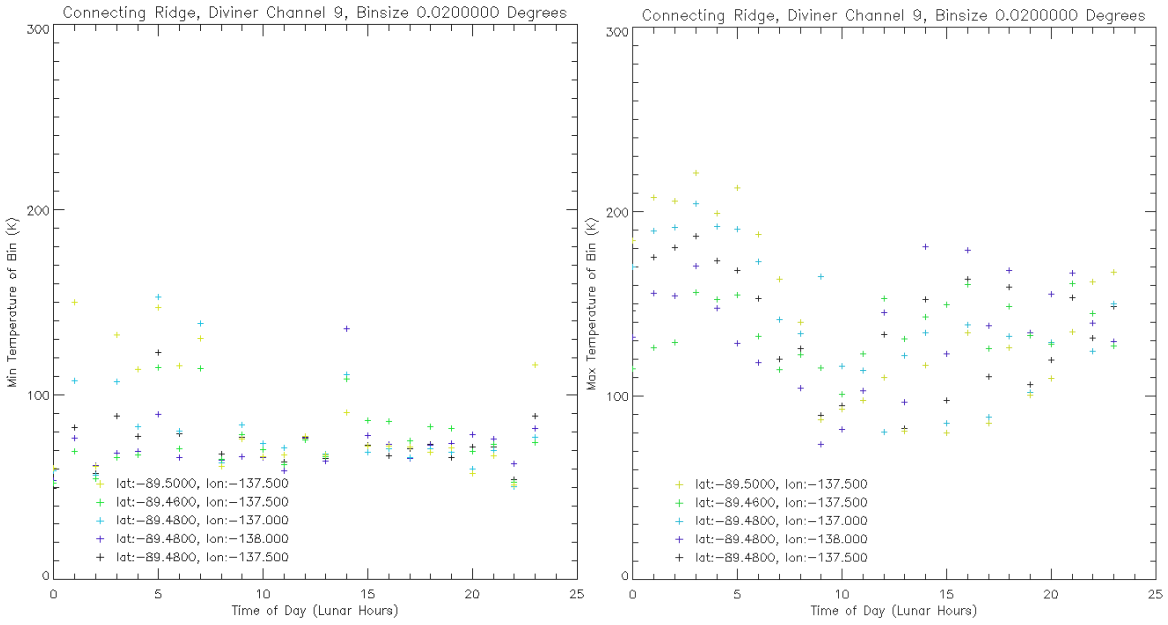

Figure 6-5: Channel 9 minimum and maximum brightness temperatures for Connecting Ridge and adjacent bins.

Diurnal curves of brightness temperature (i.e. temperature assuming unity emissivity) against local surface time were plotted for these regions (Figure 6-2). Temperatures for the bins to the north, south, east and west were also plotted to provide a comparison to the surrounding region. A clear diurnal cycle is observed, with higher temperatures (200 K) measured around 6 am, corresponding to the time when the sun is directly overhead -90° longitude. This agrees with the local topography, with the slope of Shackleton Rim facing this direction (Figure 6-1), indicating that this region is preferentially sunlit from this direction. Temperatures away from 6 am are similar to the typical night-time temperatures for mid-latitudes (~90 - 100 K; Figure 2-2), but are higher than the expected temperatures of ~40 K expected during lunar winter [Paige et al., 2009]. By analysing the minimum and maximum temperatures detected per bin, the spread of temperatures could also be investigated (Figure 6-3). Within the 600 m bin containing the Shackleton Rim location, the minimum surface temperature never drops below 65 K, reaching 165 K at optimal illumination conditions. The maximum surface temperatures in this region rarely drop below 100 K, consistently higher than the average temperature (Figure 6-2) indicating how strongly influenced the surface temperature is by topography at the poles.

Temperatures at the other locations chosen for the study were also investigated: Malapert peak (Figure 6-4) and Connecting Ridge (Figure 6-5) showed smaller diurnal variations in minimum and maximum temperatures, though the minimum temperatures observed at the former were consistently lower than those at Shackleton Rim. Next, the effects of lunar seasonal variations are investigated.

6.1.4.2 Temperature versus Subsolar Latitude

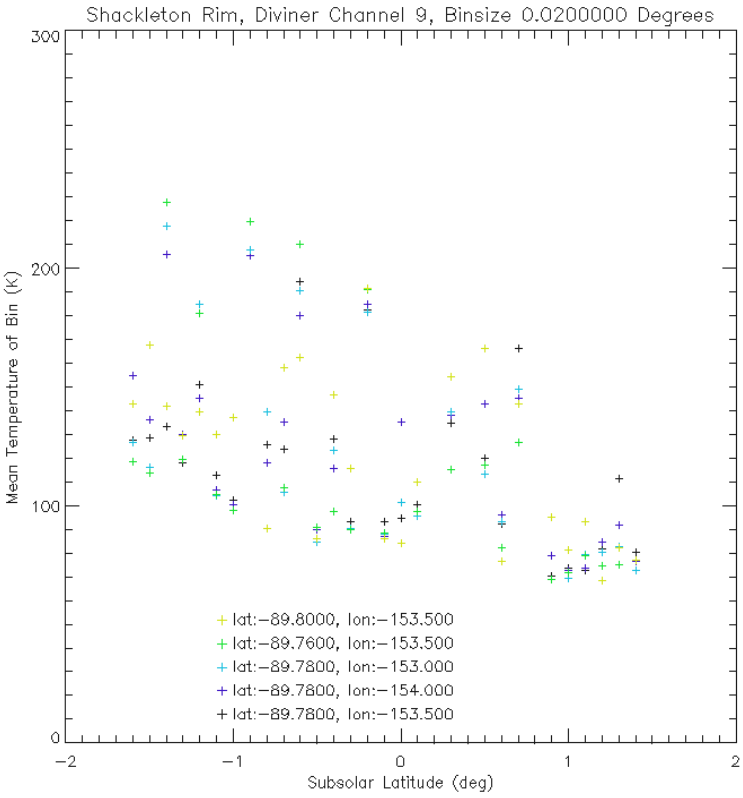

Figure 6-6: Mean channel 9 binned temperatures, plotted against subsolar latitude for Shackleton Rim and the surrounding bins.

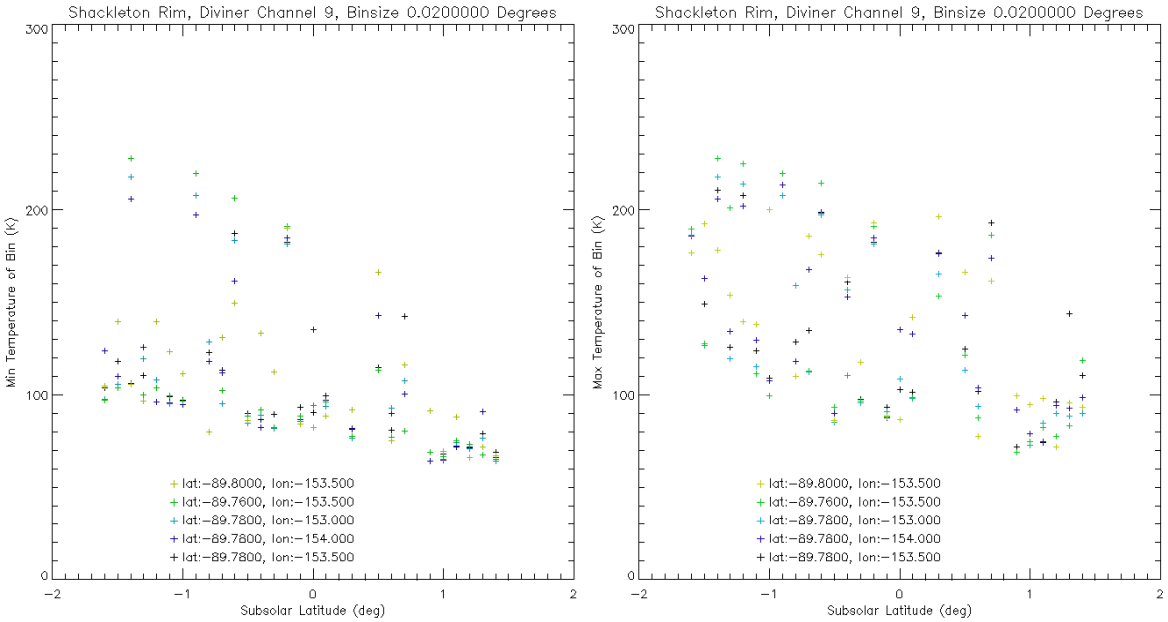

Figure 6-7: Minimum and maximum binned temperature versus subsolar latitude for Shackleton Rim and surroundings bins, measured by channel 9.

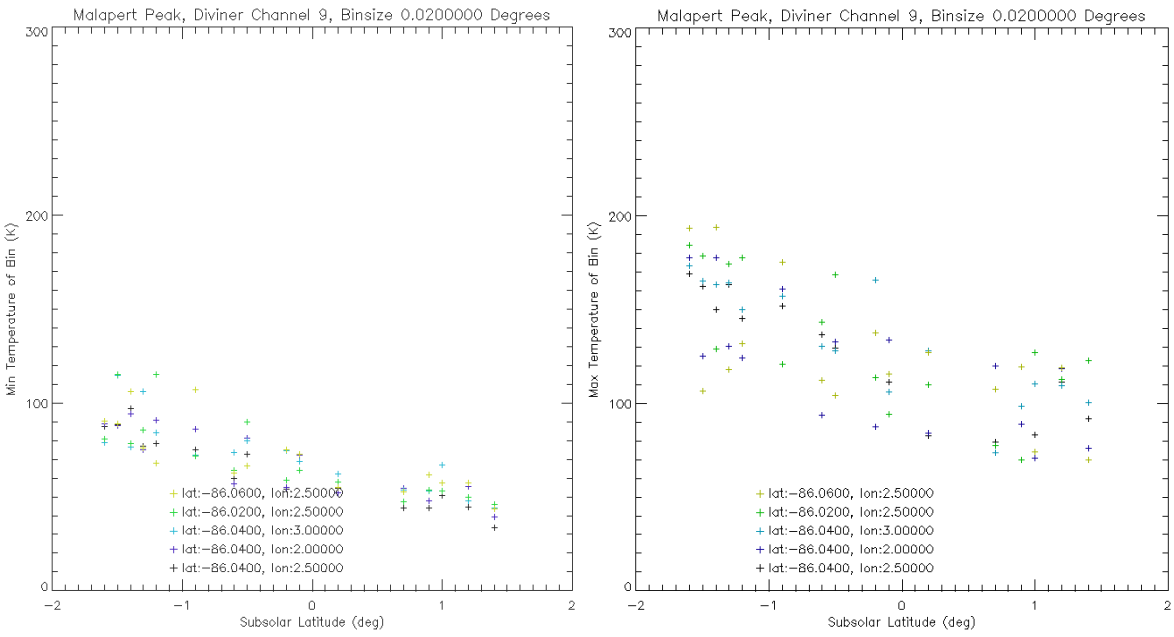

Figure 6-8: Minimum and maximum binned temperature versus subsolar latitude for Malapert Peak and surroundings bins, measured by channel 9.

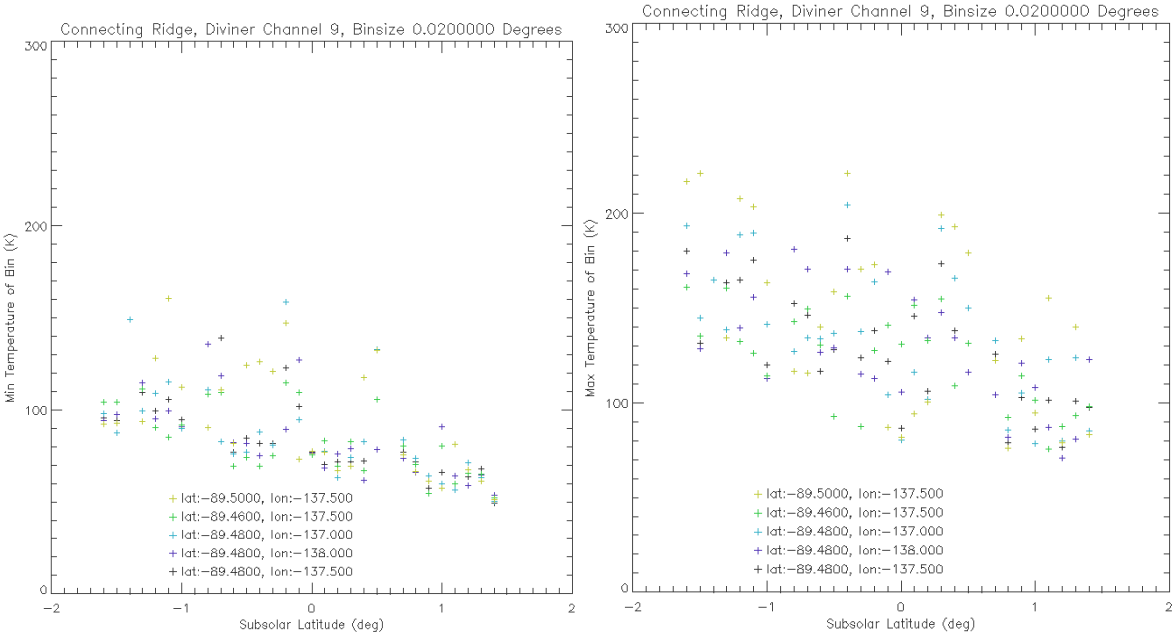

Figure 6-9: Minimum and maximum binned temperature versus subsolar latitude for Connecting Ridge and surroundings bins, measured by channel 9.

This analysis was carried out as in Section 6.1.4.1, except that the temperature measurements were binned into 0.1° subsolar latitude bins instead of surface local time. The mean temperature per bin was plotted against subsolar latitude to investigate the seasonal

dependence on temperature (Figure 6-6). Minimum and maximum temperatures measured are also shown (Figure 6-7). A seasonal variation is clearly seen, with lunar **south** pole temperatures decreasing for larger (more-positive) subsolar latitudes, when the Sun is **north** of the equator. Minimum temperatures rise from 70 - 190 K, but generally remain between 65 and 110 K, with most maximum temperatures lying around 70 - 140 K. Again, these are above the minimum expected for these latitudes [Paige et al., 2009]. A similar seasonal dependence is also observed at Malapert Peak (Figure 6-8) and Connecting Ridge (Figure 6-9).

6.1.5 Conclusions

The Diviner observations suggest that the topography around Shackleton Rim and Connecting Ridge is contributing to a preferential increase in surface temperatures over the expected values for their latitudes. The temperatures at Malapert Peak follow a trend more similar to that expected, and so appear to be less consistently illuminated. However, there may be other factors contributing to these results, mainly arising from the relatively small amount of data taken at this early stage in the mission. These factors are described below:

- Insufficient data: by June 2010, only nine months of mapping data were available. Measurements were made under a wide range of illumination angles due to the inertial orbit of Diviner (Section 3.4.4), but some preferential biases could exist (e.g. towards lunar seasons, explored below) or could be affected by large-scale topography at the poles (e.g. illuminated slopes hiding cooled regions due to the difference in magnitudes of their respective Planck radiances). With more data available, multiple diurnal curves could be made for different subsolar latitudes, to ensure that the minimum and maximum regional temperatures are measured.

- Spatial resolution: with insufficient data available, it is likely that the spatial extent of each bin is too large. At Shackleton Rim, for example, 0.02° corresponds to a ~600m bin on the surface (less so in the longitude direction). For a crater rim such as this, it is possible that only a small region is permanently illuminated, which is therefore obscured by the large bin size.

From an engineering perspective however, these preliminary results are useful. For a spacecraft with a landing accuracy of 600 m, the minimum and maximum temperatures measured are a useful constraint on the thermal design and power requirements (if powered by solar cells) of the lander. With Diviner expected to make many years of measurements (Section 3.4.4.2), and new analysis tools being developed (Section 7.4.3), spatial and diurnal/seasonal resolution will increase substantially.

6.2 Polar Temperature Mapping 2: Permanently Shadowed Regions by Paige et al. [2010]

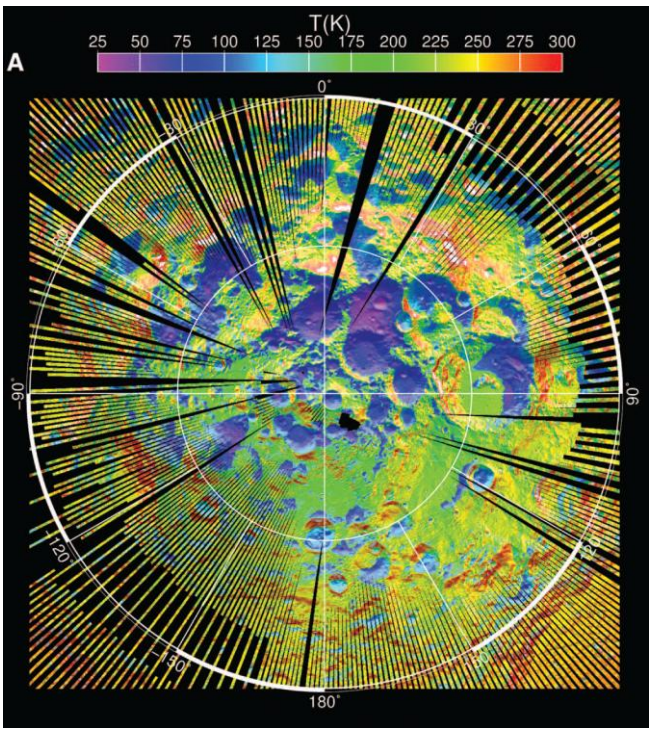

Figure 6-10: Lunar south pole daytime temperature map from Diviner measurements made as the Moon approached southern summer solstice (from Paige et al., [2010], reprinted with permission from AAAS). The inner and outer circles correspond to -85° and -80° latitude respectively.

Another important factor when planning future manned missions to the Moon is the presence of life-sustaining resources. In particular, it was believed that water could have been trapped within the regions of the permanent shadow at the poles of the Moon (Section 2.3). Paige et al. [2010] analysed the lunar south pole data, which used the B2 and B3 filter measurements and calibration procedure to ensure accurate results (Section 4), to find the regions in permanent shade during the (southern) summer solstice period (Figure 6-10). Temperatures of ~35 K were observed on the edge of the floor of Hermite Crater, with

regions on the edges of the floors of Peary and Bosch Craters measured to be almost as cold [Amos, 2009]. Such temperature maps made by Diviner "played a key role" in the choice of impact site for the LCROSS mission [Shopland & Wolpert, 2010], with the Cabeus B crater measured to have a temperature of only 37 K, capable of retaining water-ice for billions of years (Section 2.3.2). The LCROSS impactor successfully crashed into Cabeus region on 9th October 2009, ejecting water vapour, 155 ± 12 kg of which was then detected by the secondary spacecraft, confirming that the water exists on the Moon [Colaprete et al., 2010].

6.3 Global Compositional Mapping using the Christiansen Feature

6.3.1 Global Compositional Mapping Introduction

The principal aim of the three 8 μm channels is to map the peak wavelength of the CF across the lunar surface (Section 2.9.3.2). The CF is a good measure of silicate composition, where the peak wavelength primarily depends on surface composition (Section 2.9.3.2) and can be compared to laboratory spectra measured in lunar environmental conditions (Section 5.3). The method used to calculate CFs, devised by Greenhagen et al. [2009], is outlined below, and is essential to determine surface composition using the new laboratory spectra described in the thesis.

6.3.2 Compositional Mapping Method

CFs were calculated from Diviner Level 1B data, using latitude, longitude, brightness temperature, radiance, local surface time and spacecraft orientation. CF peaks increase in prominence when a thermal gradient is present within the top microns of the surface (Section 2.9.1) and hence are best observed where the temperature of the surface is highest (i.e. smaller solar incidence angle). Therefore, daytime data were extracted for mid-latitudes

between ±60°. The inertial orbit of LRO will eventually observe the entire surface at all times of day given sufficient time in orbit, but the CF cannot be mapped above 60° latitudes due to the small axial tilt of the Moon with respect to the Sun. After calculation of the CF, Greenhagen et al. made corrections to account for variations in local time of day and latitude, described below.

6.3.2.1 Christiansen Feature Calculation

The calculation method assumed that the CF is parabolic in shape. Temperatures are non-linear w.r.t. radiances, so simply plotting a parabola through the three temperature measurements would introduce extra measurement error. Instead, for each bin, a parabola is fitted to the three 8 μm channel average temperatures and the maximum temperature at the peak of the curve is found. This is assumed to be the point where the emissivity of the surface is equal to 1, therefore making this the surface brightness temperature. This brightness temperature is then converted into a 'brightness radiance' for each channel, from which the three 8 μm channel average radiances are divided to calculate emissivities. A three-point parabolic (after e.g. Greenhagen et al. 2010) fit is made to these emissivities, and the CF peak wavelength is estimated from this through re-arrangement of the quadratic equation:

$$\varepsilon_n = A\lambda_n^2 + B\lambda_n + C \qquad [6\text{-}1]$$

Where ε_n = emissivity and λ_n = channel central wavelength of the n^{th} channel (n=3, 4, 5). The maximum was then found by differentiating to find the maximum point (i.e. where the gradient = 0), therefore the CF wavelength is calculated as:

$$CF_{\max} = \lambda_{\max} = -B/2A \qquad [6\text{-}2]$$

Where A and B are calculated from fits to the observed data of Diviner channels 3-5. A more detailed description is given in the Supporting Online Material (SOM) of Greenhagen et al. [2010].

6.3.2.2 Empirical Corrections

Empirical corrections were made to correct for variations in the solar incidence angle due to the local time of day and latitude of the observations. CF variations with respect to latitude were corrected using a polynomial fit based on the assumption that all the regions of the highlands have the same CF value. Similarly, cosine fits to the highland observations were then used to correct for CF wavelength variations due to differences in local time of day from equatorial, noon values. While this assumption may not be entirely valid, as mixing, age and highland composition (e.g. anorthite versus albite, Section 1.2.4) vary, it is sufficient given the large area encompassed by the highlands and the expectation that none of these factors should be dependent on latitude (or local time of day, obviously).

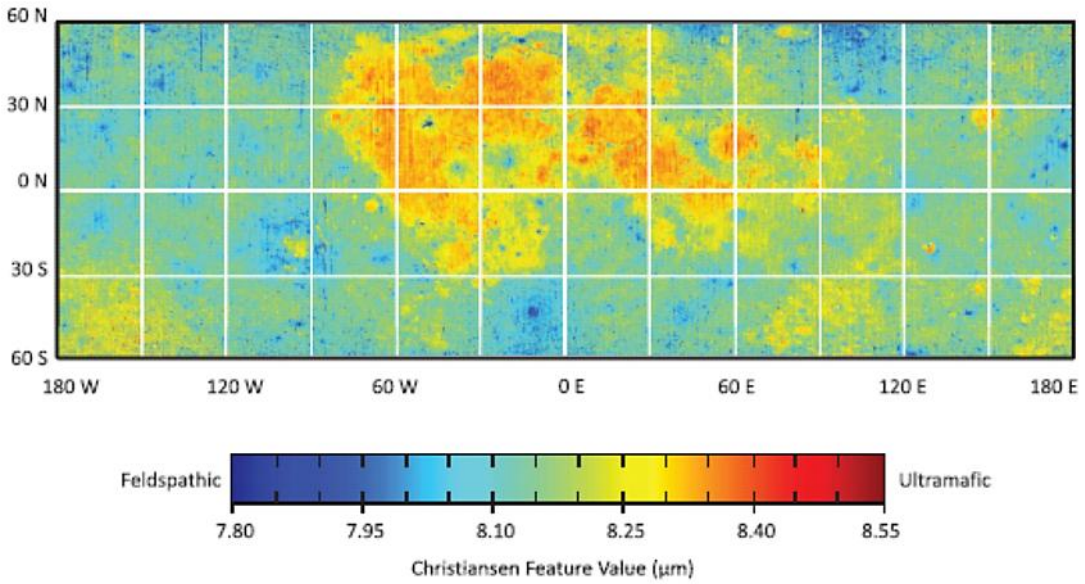

Figure 6-11: Global lunar CF map by Greenhagen et al. [2010] (reprinted with permission from AAAS), calculated from daytime Diviner observations between ±60° latitudes. The regions of mare (red) have longer CFs than the highlands (blue) as expected.

6.3.3 Results

The results (Figure 6-11) show a clear CF variation between mare and highland regions, with more mafic compositions having longer wavelength CFs than the corresponding anorthositic compositions as expected by previous Earth-based observations (Section 2.8.1) and lunar environment laboratory measurements on returned Apollo samples (Section 2.9.1) and terrestrial mineral analogues (Section 2.9.3). This correlation with CF could also be caused by space weathering: measurements of Tycho crater (a very young 100Myr crater) showed that the difference between the young crater and its ancient highland surroundings is around 0.2 μm, which can be considered an upper limit on this effect [Greenhagen et al., 2010]. Diviner is also able to investigate the nature of the highlands further, such as determining the type of plagioclase present, as detailed in the study below.

6.4 Differentiation of Regions of Previously Observed Plagioclase Feldspar: Application of the New Emissivity Spectral Library.

6.4.1 Aims

Name	Latitude (deg)	Diameter (km)	Geological province	Fresh	Location	Crater Mean CF
Jackson	22.00	71.00	Highland	Yes	Central Peak	7.78
Kant	-11.00	33.00	Highland	Yes	Central Peak	7.95
Orientale (Inner Rook North)	-10.00	327.00	Highland	Yes	Central Peak	7.78
Orientale (Inner Rook Massif)	-21.00	327.00	Highland	Yes	Central Peak	7.84
Petavius	-25.00	188.00	Highland	Yes	Central Peak	7.88
Proclus	16.00	28.00	Highland	Yes	Wall/ Ejecta	7.79
Byrgius A	-24.10	20.00	Highland	Yes	Wall/ Ejecta	7.85
Virtanen (East rim)	16.00	40.00	Highland	Yes	Crater Wall	7.83
Golitsyn J	-27.10	20.00	Highland	Yes	Crater Wall	7.83
King	6.00	77.00	Highland	No	Central Peak	7.93
Robertson	22.00	88.00	Highland	No	-	7.80
Tsiolkovsky	-20.00	185.00	Highland	No	Central Peak	7.91
Vavilov	-1.50	99.00	Highland	No	Central Peak	7.90
Gassendi E	-18.00	9.00	PKT	No	Wall/ Ejecta	7.81

Table 6-1: Locations containing areas of PAN at latitudes less than ±30°, of craters >5 km diameter and sorted by optical maturity i.e. age, with fresh craters included higher, from Ohtake et al. [2009]. Crater-averaged CFs were taken from the SOM (supporting online material) of Greenhagen et al. [2010]. Reprinted with permission from AAAS.

One of the abilities of UV/Vis/NIR instruments is to distinguish surface concentrations of plagioclase from other lunar rocks and minerals by detecting the 1.25 μm plagioclase band (Section 2.7.3.1): the Multiband Imager on the Kaguya satellite, for example, was capable of distinguishing regions of 98% or higher of pure anorthosite (herein referred to as PAN) [Ohtake et al., 2009]. This instrument consists of two cameras with narrow filters centred on wavelengths of 415, 750, 900, 950 and 1,000 nm in camera 1 and 1,000, 1,050, 1,250 and 1,550 nm in camera 2.

As TIR instruments such as Diviner can measure variations in silicate mineralogy by mapping the wavelength of the CF, different types of anorthosite (Section 1.2.4.2) should be distinguishable from one another based on laboratory measurements (Section 5.4.4). A study of the CF of the regions of PAN identified by Ohtake et al., [2009] was made by Greenhagen et al. [2010] (SOM), primarily to justify the empirical corrections made to the highland regions, which assumed global-scale CF values to be constant (Section 6.3.2.2). The CFs of the 24 regions of PAN suitable for comparison (e.g. not above ±60° latitude) had a mean of 7.85 μm, ranging from 7.76 to 7.98 μm. Compared to laboratory experiments (Section 5.4.4, Figure 5-16), this appears to suggest almost exclusively anorthite, though such CF values could be measured of more sodic plagioclase mixed with other lunar minerals, which generally have much longer wavelength CFs. This global-scale, low-resolution study measured the average CF of the crater without correlating it to the specific regions of pure anorthosite, which were typically small and confined to the central peak or wall of craters [SOM, Ohtake et al., [2009], supporting this conclusion.

Therefore the aim of this study, conducted by the author, was to relate laboratory measurements to only the regions of PAN, to attempt to determine plagioclase composition,

removing the effects of compositional mixing from the calculation of the mean CF. The region exhibiting the shortest wavelength CF was Leibnitz South, though this crater is amongst the smallest (2 km diameter) and is located at a relatively high latitude (40° from the equator). Hence the second option, Jackson crater, was chosen for this initial study (71 km diameter, 22° latitude). The PAN regions are detailed in Table 6-1.

6.4.2 Data Retrieval

This study required analysis of the Kaguya Multiband Imager UV/Vis and NIR data in conjunction with Diviner's 8 μm channels. At the time of writing, only radiance data from the UV/Vis and NIR cameras was publicly available. These datasets must be photometrically calibrated to convert radiances into reflectances and this requires accurate knowledge of surface topography; therefore publicly available altimetry data were also needed. The Laser Altimeter (LALT) instrument, also on the Kaguya satellite, produced global topographic maps at 16 pixels per degree resolution, while LOLA (Section 3.2), on board LRO, collected much higher resolution data (512 px/deg) but coverage has been limited so far (at the time of writing).

Data from the Multiband Imager and LALT instruments were retrieved from the JAXA website. The data is in the form of image cubes with dimensions of longitude x latitude x spectral channel, taken by the two cameras with co-aligned boresights. The required Diviner data for calculation and correction of the CF is described in Section 6.3.2. Corrected CF values were retrieved for the desired region.

6.4.3 Analysis Method

The analysis of the Multiband Imager (MI) data followed the procedure of Ohtake et al. [2009], detailed by Pieters [1999], whereby the radiances are:

- Scaled by a gain and offset, converting digital counts into radiances
- Photometrically corrected, allowing measured radiances to be corrected for viewing geometry
- Converted to reflectances, using correction factors derived from viewing regions of known composition, with NIR camera reflectances scaled to match UV/Vis observations
- Transformed into spectral absorption depths, for comparing with laboratory data
- Binned into a regular latitude-longitude grid, to create a map from many separate images

This procedure is detailed below.

6.4.3.1 Photometric Correction

The photometric correction used by Ohtake et al. [2009] was originally developed for the Clementine UVVIS camera by McEwen [1996] and subsequently refined by McEwen et al. [1998]. The photometric correction converts measured reflectance data into reflectances of a standard geometry to remove differences between observations due to differing solar incidence angle, i, phase angle, α, and emission angles, e. The correction accounts for the variations between the different wavelength channels and for the limb-darkening effects of the non-lambertian (non-uniformly scattering) lunar surface. In this case, the standard geometry chosen was that of the RELab spectroscopy facility (Section 2.7.3.2), allowing direct comparisons to be made between this ground-based laboratory and the orbiting

instrument. In RELab geometry, $i = \alpha = 30°$ and $e = 0°$, but MI geometries varied throughout the mission and also varied with topography.

Filter	A_L	B_L	C_L	Bo	H	E	F	G2
415 nm	-0.019	0.242×10^{-3}	-1.46×10^{-6}	2.31	0.062	-0.222	0.5	0.39
750 nm				1.6	0.054	-0.218	0.5	0.4
Other channels				1.35	0.052	-0.226	0.5	0.36

Table 6-2: Parameters derived by McEwen et al. © [1998] used in the photometric correction. While the equations and coefficients derived by McEwen et al. [1998] were for the Clementine UVVIS channels (415 - 1000nm), covering only half the MI channels, the 1000nm coefficients can also be applied to the longer wavelength channels on MI [Ohtake, personal communication 2011].

The photometric correction, based on the work of Hapke [1981], consists of a normalisation function, $X_L(i,e,\alpha)$, and a phase function, $F(\alpha)$, empirically derived from previous lunar observations. MI digital counts were first multiplied by a gain parameter and added to an offset parameter contained in the header of each data file to produce radiance values. Radiances in the RELab geometry, R_{RELab}, were calculated from the radiances measured by MI, R_{MI} by [McEwen, 1996]:

$$R_{RELab} = R_{MI}(i,e,\alpha)\frac{X_L(30°,0°,30°)}{X_L(i,e,\alpha)}\frac{F(30°)}{F(\alpha)} \quad [6\text{-}3]$$

Where X_L is the Lunar-Lambert function given by:

$$X_L(i,e,\alpha) = 2L(\alpha)\frac{\cos(i)}{\cos(i)+\cos(i)} + (1-L(\alpha))\cos(i) \quad [6\text{-}4]$$

And L is the limb-darkening parameter:

$$L(\alpha) = 1.0 + A_L\alpha + B_L\alpha^2 + C_L\alpha^3 \quad [6\text{-}5]$$

The phase function was calculated as:

$$F(\alpha) = B(\alpha, h, B_0)\left((1-F)P(\alpha, g_1) + FP(\alpha, g_2)\right) \quad [6\text{-}6]$$

Where:

$$P(\alpha, g) = \frac{1-g^2}{1+g^2+2g\cos(\alpha)^{1.5}} \quad [6\text{-}7]$$

The backscatter function was defined as:

$$B(\alpha, h, B_0) = 1 + \frac{B_0}{1+\tan(\alpha/2)/h} \quad [6\text{-}8]$$

And $B_0 = 19.9 - 59.6\lambda + 59.9\lambda^2 - 20.1\lambda^3$. g_1, the narrowness of the backscattering lobe, was set to be independent of albedo, and hence $g_1 = E$, *a constant*. The values of the other variables were determined by empirical fits to previous datasets (Table 6-2).

6.4.3.2 Conversion to Reflectance

Once the photometric correction had been performed, a spectral calibration correction factor for each channel was applied; to account for differences between photometrically corrected observations and laboratory measurements. The Apollo 16 site is well suited to calibrations: sample 62231, a soil sample taken from a more homogeneous area to the north of the landing site [Meyer, 2010] was chosen as the calibration standard for both the Clementine UV/Vis and Kaguya MI cameras. The method was the same as used for the UVVIS camera by Pieters [1999], starting by converting the spectrum of Apollo sample 62231 into that measured by each of the camera's filters, accounting for the filter transmission profiles and solar radiance. The correction factor was then found by dividing this converted filter spectra by the photometrically corrected Apollo 16 site observations. Once these correction factors had been found, observations of the Moon could be converted into reflectance by multiplying by this correction factor and applying the photometric correction, as performed on both UVVIS Camera and MI data.

Due to the MI instrument being effectively two separate cameras, in some spectra there is a small difference between the reflectance spectrum in the 1000nm channel in the visible camera and the 1000nm in the NIR camera. In these cases, the NIR bands were multiplied by a further small correction factor so that they overlap at 1000nm.

6.4.3.3 Conversion to Absorption Depth

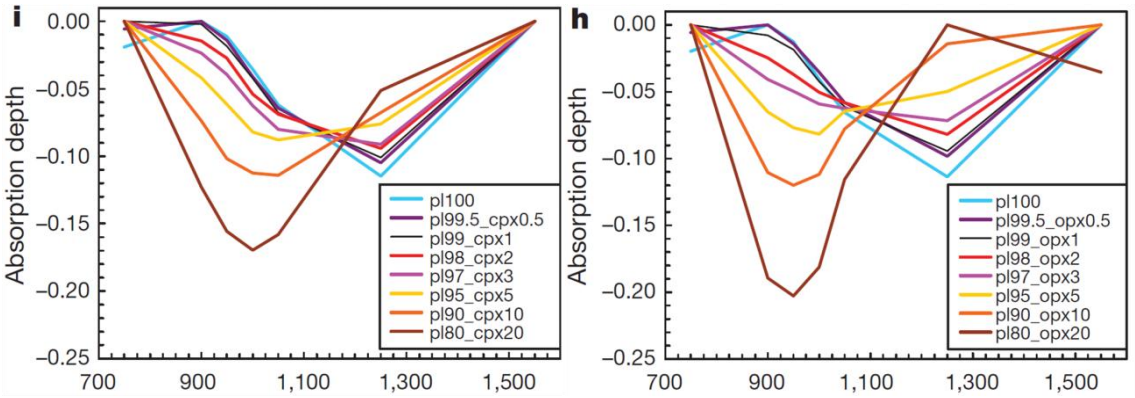

Figure 6-12: Absorption depths of plagioclase (pl) mixed with increasing amounts of clinopyroxene (cpx) and orthopyroxene (opx) measured by Ohtake et al. [2009] (reprinted by permission from Macmillan Publishers Ltd.). The numbers in the legends refer to the relative % abundances.

Reflectance spectra are typically logarithmic curves with small absorption bands superimposed on this curve. Hence, to make easier comparisons between mineralogical absorption bands, the continuum is removed. From Ohtake et al. [2009]:

> "Absorption depths were derived by dividing each reflectance spectrum by its continuum. A continuum was defined as a line connecting the reflectance values in the log-scale between two optimized wavelengths (750nm or 900nm, and 1,250nm or 1,550nm) selected for each spectrum"

Surface composition is then determined from these absorption depth spectra, through comparisons made to laboratory spectra of the main lunar crustal rock groups (Figure 6-12). 2% of orthopyroxene or clinopyroxene alters the spectra sufficiently that this technique is highly sensitive to PAN.

6.4.4 Multiband Imager Results

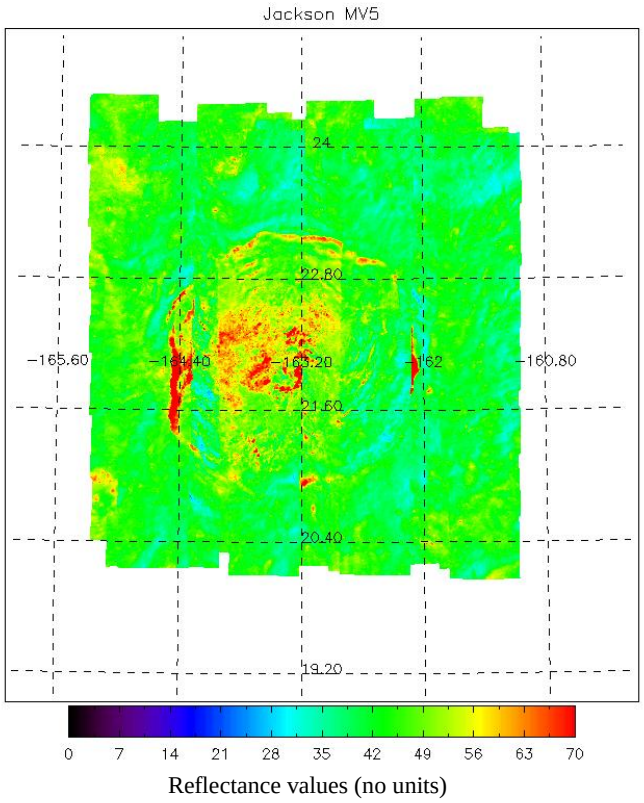

Figure 6-13: 1000 nm (visible camera) map showing all the observations of Jackson crater binned into regular grid, plotted in IDL by the author.

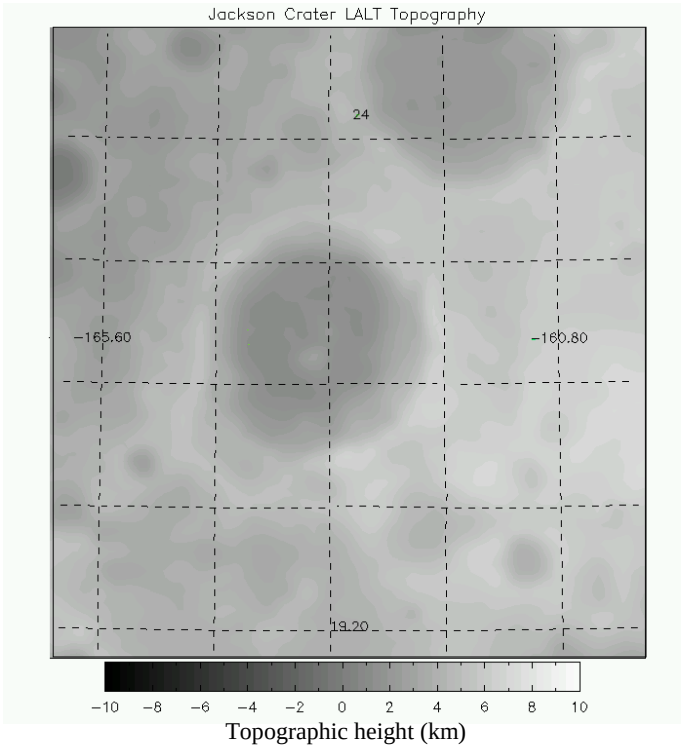

Figure 6-14: Topographic map of Jackson crater made by the LALT instrument, plotted in IDL by the author. The same spatial scale is used in all figures.

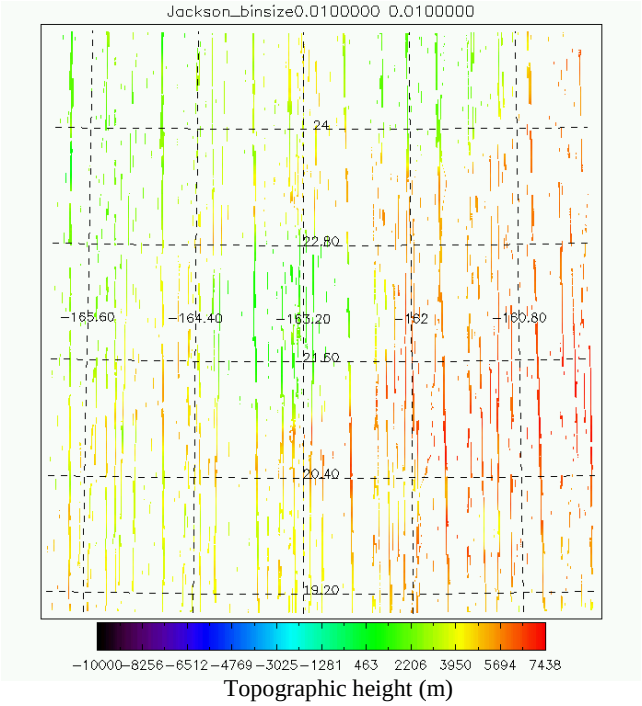

Figure 6-15: LOLA data for Jackson crater, taken from September 2009 to December 2010. The elevation values are given in metres.

Photometrically (but not topographically) corrected reflectances of Jackson crater measured by MI are shown in Figure 6-13. However, the absorption depths do not appear to fit the spectra expected for regions of PAN, which could be due to the topography used in calculating the photometric correction. The LALT data (Figure 6-14) has very low spatial resolution compared to the MI data which is binned in 20 x 20m bins. Ohtake et al. [2009] used the MI instrument itself to generate topographic data derived from the parallax of measurements made at different viewing geometries. This dataset is not publicly available; however LOLA data is, though coverage is limited in this region (Figure 6-15). Once more data become available, this method should allow PAN regions to be fully constrained, allowing quantitative comparisons of Diviner and UV/Vis and NIR data. At this time however, such observations can only be made of Jackson crater as Ohtake et al. [2009] provided additional information (Figure 2-9) as to the exact location of the PAN deposit.

6.4.5 Christiansen Feature Variation of Anorthosite in Jackson Crater

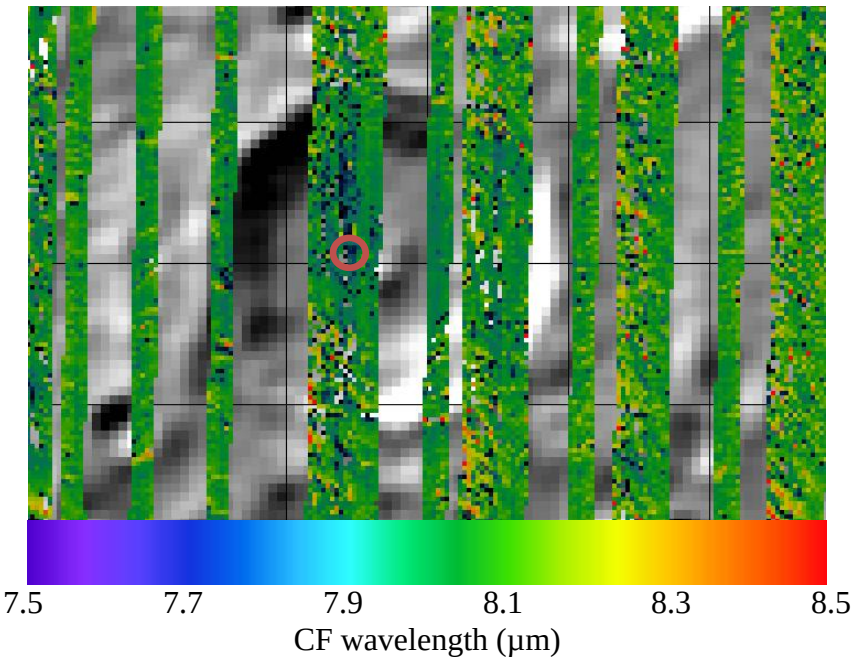

Figure 6-16: Diviner CF wavelength map for Jackson Crater, plotted over a LALT topographic map (greyscale) in JMoon, a java-based mission-planning and analysis tool by the ASU Mars Scientific Software Team. The approximate region of PAN discovered by Ohtake et al. [2009] is highlighted. The grid lines are separated by 1º, from -164.5º to -162.2º (longitude) and from +21.1º to +23º (latitude).

Diviner CF maps were plotted for Jackson crater (Figure 6-16) and show that approximately for the region of PAN, the CF peak wavelength varies between 7.72 and 8.03 μm with a mean of 7.92 μm. When compared to plagioclase mineral spectra measured in a SLE (Figure 5-16) this would suggest a range of compositions from labradorite or bytownite to anorthite, potentially indicating a more sodic-rich region than the highland region visited by the Apollo 16 astronauts (typically >90% anorthite content [e.g. Laul et al. 1974]). Clearly, this is very preliminary work, given the current data, but does demonstrate a possible technique for investigating the nature of such regions. Future work, aside from

improvements in the topographic maps for photometric correction of MI data, is described in detail in Section 7.4.3.

6.5 Detection of Silica- Rich Regions of the Lunar Surface – Further Application of the New Spectral Emissivity Library by Glotch et al. [2010]

Another study of the Diviner dataset by Glotch et al. [2009] discovered some regions of the Moon where the CF fitting method of Greenhagen et al. [2009] produced an error, indicating either extremely short- or long-wavelength CF peaks outside the range identifiable by Diviner's 8 μm channels. Laboratory emission spectra, made by the author, were therefore required to determine the possible surface compositions that could result in these observations.

6.5.1 CF Detection

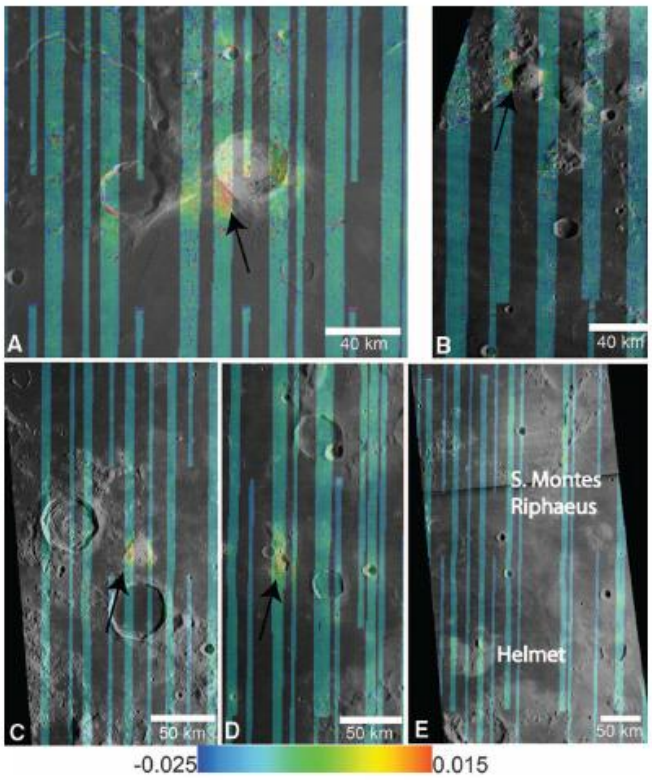

Figure 6-17: Concavity values (*c*) for Aristarchus Crater (A), Gruithuisen Domes (B), Hansteen Alpha (C), Lassell (D), and Helmet and Southern Montes Ripheus (E) regions on the Moon, from Glotch et al., [2010] (reprinted with permission from AAAS). Positive values indicate silicic compositions.

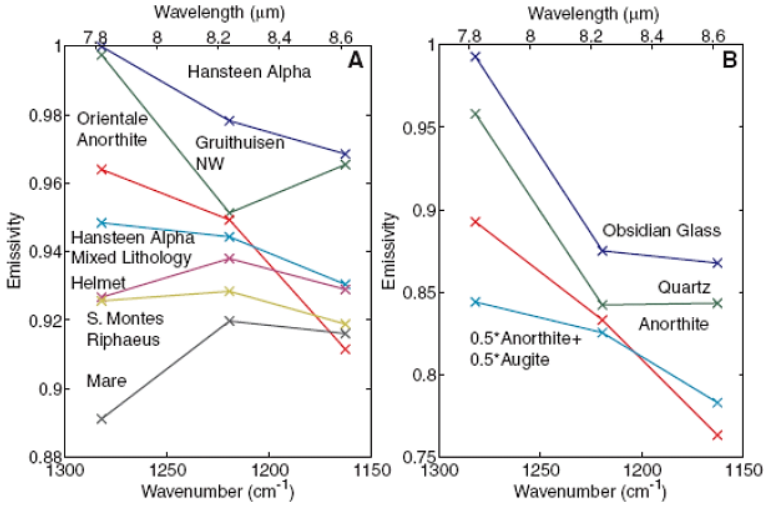

Figure 6-18: Lunar surface spectral shapes derived from Diviner channel 3 - 5 data, from Glotch et al., [2010] (reprinted with permission from AAAS). Obsidian and Quartz have distinct shapes with large values of *I* and highly positive values of *c*, as determined during this project.

To match lunar emissivity spectra of these regions to those measured in the laboratory, two new parameters were devised, based on the shape of the spectra observed [Glotch et al., 2010]:

- Spectral index (*I*): This is the difference in emissivity (calculated using the method described in Section 6.3.2.1) between channels 3 and 4, where $I = \varepsilon_3 - \varepsilon_4$.
- Concavity (*c*): This is a measure of the difference between the measured channel 4 emissivity and the emissivity of channel 4 when linearly interpolated between the emissivities of channels 3 and 5. A positive value indicates that the measured emissivity is less than the interpolated value, and hence has a ‘concave up’ shape.

Previously flown UV/Vis, NIR and gamma-ray instruments have been unable to identify the surface composition of these regions, but have observed low iron and titanium concentrations [Bruno et al., 1991]. However, when measured by Diviner (Figure 6-17),

these regions exhibited high spectral index values and positive concavities (Figure 6-18), and therefore must be composed of something with an unusually short wavelength CF. From previous measurements (not necessarily those in made in lunar conditions, e.g. Section 5.2), such short CFs are indicative of compositions more silica-, sodium- or potassium-rich, such as quartz (SiO_2), albite (Na end-member of the plagioclase series; Figure 1-2) or microcline ($KAlSi_3O_8$, end-member of the anorthoclase series).

6.5.2 Laboratory Measurements

SLE emission measurements were made by the author of microcline and obsidian (Section 5.4.3) in addition to the spectra of the plagioclase series and main lunar minerals already measured. Microcline had smaller concavity and spectral index values than obsidian, quartz or albite, more similar to that of labradorite which had a slightly positive concavity. Deposits of pure albite or labradorite would be detected as PAN regions, with large concave spectra suggesting that more unusual silicic materials were being observed such as quartz and obsidian (Figure 6-18). The composition of such regions cannot be exactly determined using only the three 8 μm channels on Diviner, especially when attempting to measure CFs outside of the spectral range, but it could be constrained in combination with SLE laboratory measurements.

6.5.1 Formation Theories

This discovery led to several theories of formation to explain how such silicic minerals could form on the Moon, given the cooling required to have occurred over a sustained period of time, after the initial cooling of the magma ocean. Glotch et al. [2010] proposed that they could have been caused by:

- The residual melt of later stages of the magma ocean. This could have produced large granitic plutons, which were then subsequently excavated by later impacts.
- Basaltic underplating. This occurs when the anorthositic crust is melted by basaltic magma intruding into it, forming large amounts of silicic magmas which would then rise to the surface. This could be possible as all the regions identified are located within KREEP terrain (Section 2.7.1) where heat-producing elements and evidence of magmatism are abundant.

7 Conclusion

7.1 Scope of the Project

7.1.1 First Steps in Using Mid-Infrared Lunar Observations

This project represents some of the first steps in using the TIR spectral region to understand new elements of the Moon's surface composition and history. Working as a part of the Diviner instrument and science teams consisting of engineers, physicists and geologists, much of the work carried out was guided by the overall mission requirements at the time. Hence, this thesis consists of some (at points) seemingly unconnected tasks, though when combined with the work of others delivered a calibrated instrument for the LRO mission and generated excellent science output. Specifically, the requirements fulfilled by the author towards this objective were as follows:

- The final uncharacterised filters and blockers were measured. Further work was carried out to ensure that the filter responses for the long-wavelength channels were not affected by the instrument design, as had possibly occurred to MCS, Diviner's predecessor (Section 4.3).
- Assistance was given to the calibration of Diviner at JPL and the detectors' responses to radiance were found to be so linear within experimental error that any non-linear polynomial coefficients were not used (Section 4.5) in the subsequent automated data analysis pipeline.
- A lunar environment emission chamber was developed and calibrated. A spectral library of common lunar terrestrial analogues was measured in reflectance, with the most important samples measured in emission in a SLE (Section 5.3); essential if the

results from the compositional channels are to be used to retrieve TIR surface composition.

- Early data returned by Diviner were analysed. This included a study of the temperatures of permanently illuminated regions motivated by a requirement from ESA as part of a future landing site study (Section 6.1) and a preliminary investigation has begun into the composition of the pure anorthosite detected in Jackson crater (Section 6.4) by the Kaguya spacecraft.
- Studies by other Diviner science team members which utilised the instrument filter measurements, calibration and SLE emission measurements were described briefly. This included investigations of permanently shaded regions, the discovery of highly silicic regions, and global compositional mapping capabilities from measurements of the CF wavelength (Section 6).

Some of the work described above is of a preliminary nature, due to the time constraints imposed by the mission for the delivery and calibration of Diviner, and by the start date and duration of this D.Phil thesis. The remainder of this chapter details possible considerations for future work, in terms of both improving the results presented here and in proposing new experiments, building on the results from this project and from the Diviner mission as a whole.

7.2 Instrument Calibration

7.2.1 Filter Measurements

The two main difficulties in improving the filter measurements are:

- Wide spectral range of the channels. In particular, the long wavelengths of B2 and B3 channels prevent the use of grating spectrometers to measure the actual spectral

response of the filters when integrated into the instrument. An FTIR spectrometer is required to make these measurements, and hence the thermopile detectors used in Diviner would need to be replaced by detectors with a faster response time to be able to measure the interferogram, or a step-scan mode added to the instrument available in AOPP.

- Export restrictions. The International Traffic in Arms Regulations (ITAR) forbids transportation outside the USA of military-related items or data without a specific strictly enforced export license, which includes Diviner's detectors and optical assemblies. This adds difficulty in replicating the Diviner optical layout for measuring the filters in the arrangement as in the instrument. Hence, in the experiment a variety of filter-to-detector distances were measured to determine if any correlation between distance and changes in spectrum could be found.

7.2.2 Instrument Calibration

Given sufficient time, the entire thesis could have been devoted to the calibration of Diviner. This, however, would only have delivered improved radiometric performance after launch had already occurred, requiring the re-analysis of the entire dataset up to that time. Uncertainties in launch date (Diviner was originally scheduled to launch in 2008 when this project began) meant that the primary aim was to ensure that the instrument operated as designed, with improvements in radiometric accuracy a lower priority. Below is detailed some further improvements based on the four uncertainties in the instrument linearity calibration that arose from insufficient knowledge of the blackbodies used for the testing:

- The emissivity of the paint used in the blackbody was unknown. This could be remedied by measuring the reflectance of a sample of the paint across the

wavelength range of Diviner channels 3-9, or in hindsight could have been solved by repainting the blackbodies prior to testing.

- The six blackbody PRTs were out of calibration, therefore only the two Si diodes located in the baseplate and 1st rib could be considered reliable, with the other blackbody ribs assumed to be at the same temperature as rib 1. Assuming the blackbodies have not been altered since Diviner calibration, the PRTs (and therefore the blackbody temperatures) could be back-calibrated to reduce or remove this error. Alternatively, additional calibrated temperature sensors could be attached to the ribs and the testing procedure rerun without the instrument.
- The diode temperatures required re-calibration post-testing, which introduced an error because the original temperature readings were recorded to two decimal places using a linear interpolant. As the original voltages were discarded, it is unlikely that any significant decrease in this uncertainty can be achieved without taking any of the steps outlined in the previous bullet point.
- The uncertainty in radiance due to the non-unity emissivity, which in the worst-case scenario was assumed to be a reflection of Diviner itself. A thermal model of the setup with the vacuum chamber would be likely needed to investigate this, taking into account the pointing vector of each detector. This uncertainty was much larger at lower temperatures, overwhelming the other three uncertainties towards the detection limit of each channel (Table 4-3).

As this final error was so great, and due to the lack of time to create a thermal model of calibration setup to reduce these errors, it was decided to assume a linear response from each detector with respect to radiance (Section 4.5.5). From the curves (Figure 4-16), this appears to be good assumption, with typical quadratic coefficients a factor of 10^3 smaller than the linear counterparts.

7.3 Interpretation of Spectra measured in a Simulated Lunar Environment

Although FTIR spectrometers are the preferred choice for measuring emissivities in modern laboratories [Christensen and Harrison, 1993; Ruff et al., 1997; Glotch et al., 2007; Maturilli et al., 2006 etc.], this project was the first time that one had been used to measure SLE emissivity spectra. This caused added complication (below) and required a new calibration algorithm, due to the thermal gradients in the samples and the unique way in which FTIR instruments are calibrated (Section 5.3.5).

7.3.1 Using a Fourier Transform Spectrometer

One of the peculiarities of FTIR spectrometry is that if the object under investigation is of equal temperature (assuming it has unity emissivity) as the spectrometer, no signal is measured. If it is below this temperature, the signal becomes inverted, but is recorded as positive when the Fourier transform is applied (unlike grating spectrometers). The spectrum can be simply re-inverted if this is known, but any spectrum containing both negative and positive signal at different wavenumbers results in an unusable spectrum. Initially this caused confusion due to the difference in emissivity of the CF and the rest of the spectrum (i.e. the continuum) caused by the lunar conditions: the CF would be highly positive while other parts were negative as the sample was heated up to the temperatures required for SLE measurements. Fortunately, the midday lunar surface is hotter than the spectrometer and so the spectra were entirely positive when heated sufficiently, but this may not be a viable method of measuring samples for other times of day (or other airless bodies in near-Earth orbits, for example). Simulating environments of airless bodies cooler than the Moon would

be possible however, by inverting the measured spectra, an effect utilised in some methods of spectroscopy [e.g. Baldridge and Christensen, 2009].

7.3.2 Spectrometer Calibration Improvements

7.3.2.1 CF Fitting

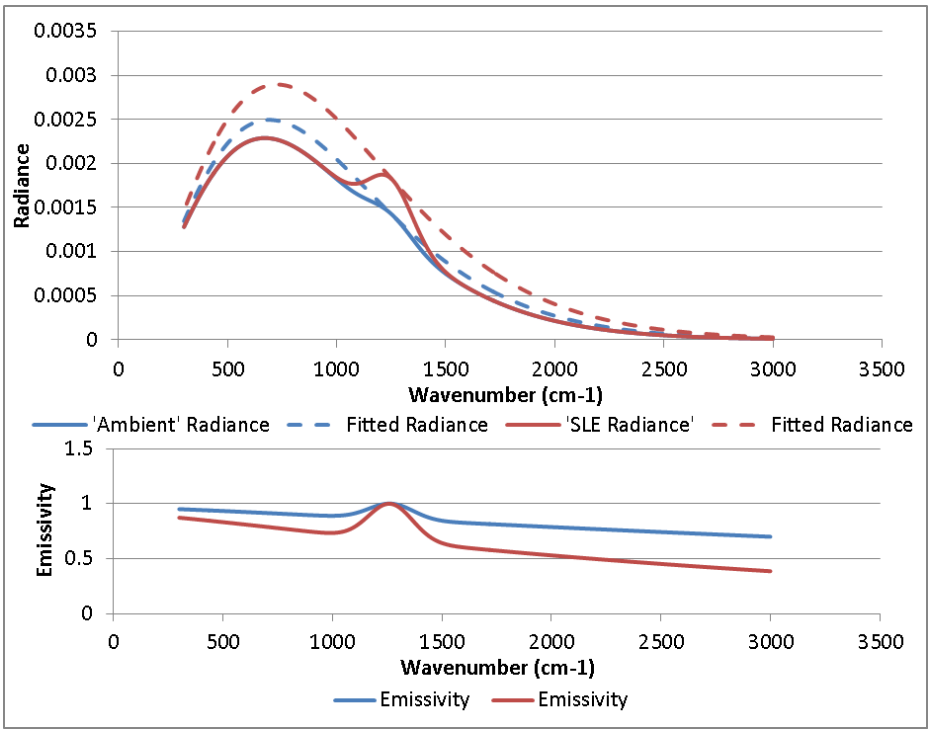

Figure 7-1: Two radiance spectra showing how the calibration algorithm fits a Planck function to the peak of the CF (top). This method of fitting creates an increasingly sloped emissivity continuum as the CF becomes more pronounced (bottom).

In these experiments, the calibration algorithm assumed that the emissivity at the CF wavelength, $\varepsilon(\lambda=\lambda_{CF})$ = 1, and a fit was made to calculate each spectrum, as in other emission setups [Ruff et al., 1997; Maturilli et al., 2006 etc.]. However, unlike measurements made under ambient conditions, SLE spectra of small grain sized samples exhibit a large emissivity difference between CF and continuum, which can produce unusual results using this assumption. For example, consider a sample under ambient conditions that

has a CF emissivity close to its continuum emissivity (e.g. $\varepsilon(\lambda=\lambda_{CF}) = 1.01 \times \varepsilon(\lambda\neq\lambda_{CF})$), which when under SLE then became more pronounced (e.g. $\varepsilon(\lambda=\lambda_{CF}) = 1.3 \times \varepsilon(\lambda\neq\lambda_{CF})$) where the emissivity of the continuum $\varepsilon(\lambda\neq\lambda_{CF})$ remains the same. When the spectrum is fitted, the emissivity of the continuum appears to change due to the shift in the Planck function peak (Figure 7-1). An alternative to this is to apply the fit to the continuum to calculate the emissivity, then scale this emissivity so that the $\varepsilon(\lambda_{CF}) = 1$. This effect does not affect the CF peak wavelength (and therefore Diviner channel 3-5 observations); however it does change the continuum and would therefore affect any fits made to longer wavelength channels or to other MIR lunar observations.

7.3.2.2 Short Wavelength Emissivity Increase

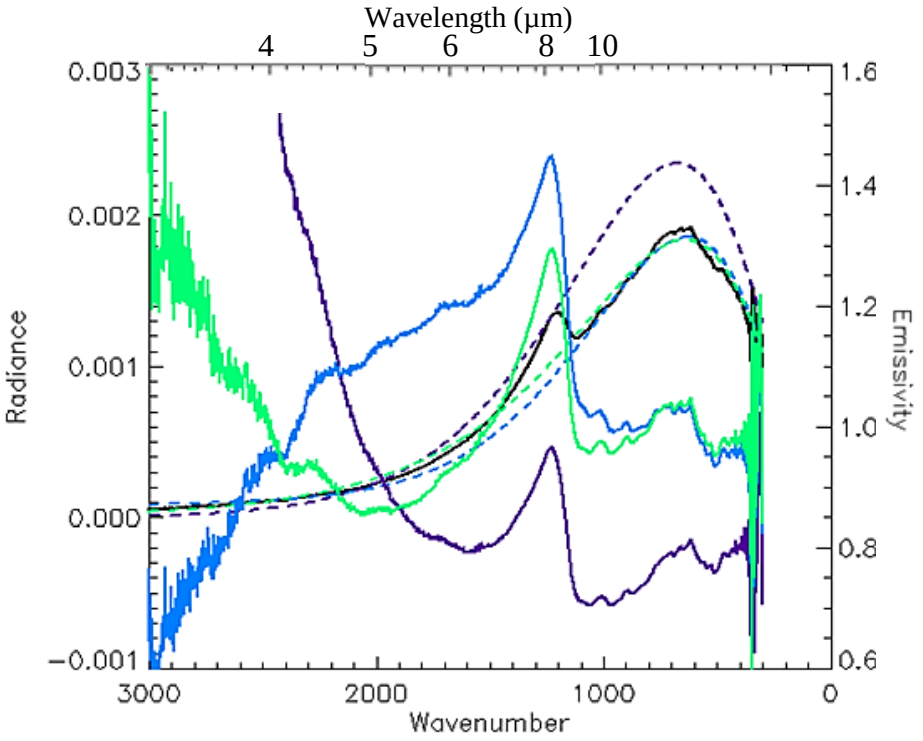

(a)

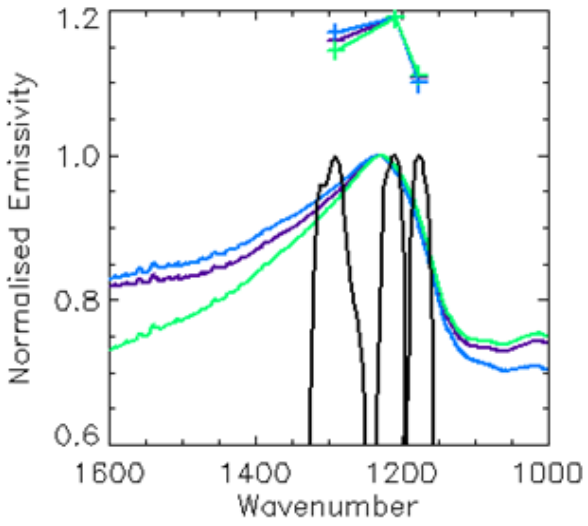

(b)

Figure 7-2: (a) Enstatite 0 - 30 μm emissivity spectra, calibrated using the original method (purple), using a fitting algorithm including a component of the Globar™ source to fit to the non-CF regions (blue), and including a component of the 500 K sample cup (green). (b) The same spectra after normalisation, overlaid on Diviner 3-5 channel band-passes showing how Diviner would observe these spectra.

One of the features of several of the emissivity spectra measured in a SLE is an observed increase in emissivity, at wavelengths below ~6 μm, to greater than that at the CF. This can be best shown by plotting sample radiance (black line, Figure 7-2 (a)). The corresponding Planck function used to convert from radiance to emissivity is also displayed (purple dotted line), with the two curves equal to each other at the CF (thereby making emissivity equal to 1 at this point). As can be seen, the sample radiance increases above the Planck radiance above 2000 cm^{-1} (<5 μm) for this mineral, sending the emissivity above 1 (purple solid line). This effect becomes more pronounced when larger grain-sized samples are measured, so it was initially believed to be due to a property of the samples, such as an increase in sample transparency at increasing wavenumbers. A similar trend was also observed by Henderson et al. [1996] where the data point at 6.6μm shows a dramatic increase in emissivity in both measured spectra.

It was also suspected that it could be due to a reflection within the spectrometer. Such an increase in emissivity at higher wavenumbers can only be accounted for by a higher temperature source, and therefore was assumed to be caused by either the spectrometer Globar™ source (1200 K temperature) or the heated sample cup (500 K). A chi-squared minimisation-fitting algorithm determined the optimum fit to the continuum region of the spectrum, assuming that a percentage of the radiation measured originated from these external sources. Therefore, instead of fitting a Planck function of a single temperature to the data, it instead fits a sum of two Planck functions: one for the sample and one for the higher temperature heat source. The sample radiance is reduced greatly at shorter wavelengths (e.g. Figure 7-1) and hence only a very small percentage change was required for the emissivity to remain below one. For example, for the enstatite 0 - 30 μm sample (Figure 7-2), a fit of 0.09% of the 1200K source combined with 99.91% sample radiance

(blue dotted line), or a fit of 6.5% 500K with 93.5% sample radiance (green dotted line) were sufficient to achieve this. As for the modifications for the CF fitting algorithm (Section 7.3.2.1), the CF remained unchanged at 8.14 μm by applying this fit (Figure 7-2 (b)).

7.3.2.3 Blackbody Calibrations

Blackbody calibrations consisted of two spectra of 300 scans each. This took considerable time and so the blackbodies could not be measured immediately before and after each sample as would have been ideal. Fast calibration spectra composed of only 50 scans were found to be too noisy, and so the spectrometer was calibrated every ~10-15 measurements. The instrument response function and instrument radiance, the two parameters gained from the blackbody calibration, did not differ significantly throughout the experiments (e.g. average 1.2% difference between 1240 - 1260cm^{-1}) and so it was assumed that the instrument calibration remained constant throughout the experiment. The spectrometer remained switched on, including the heated Globar^{TM} source, throughout the experiment and the emission chamber was thermally isolated from the spectrometer within a temperature-controlled room.

7.4 Combining Diviner Data and the Lunar Spectral Library

Including the effects of lunar environment on emission spectra is essential when creating a TIR lunar spectral library. However, some variations have still been observed between spectra measured by Diviner and those measured in the laboratory, which are described and explained below.

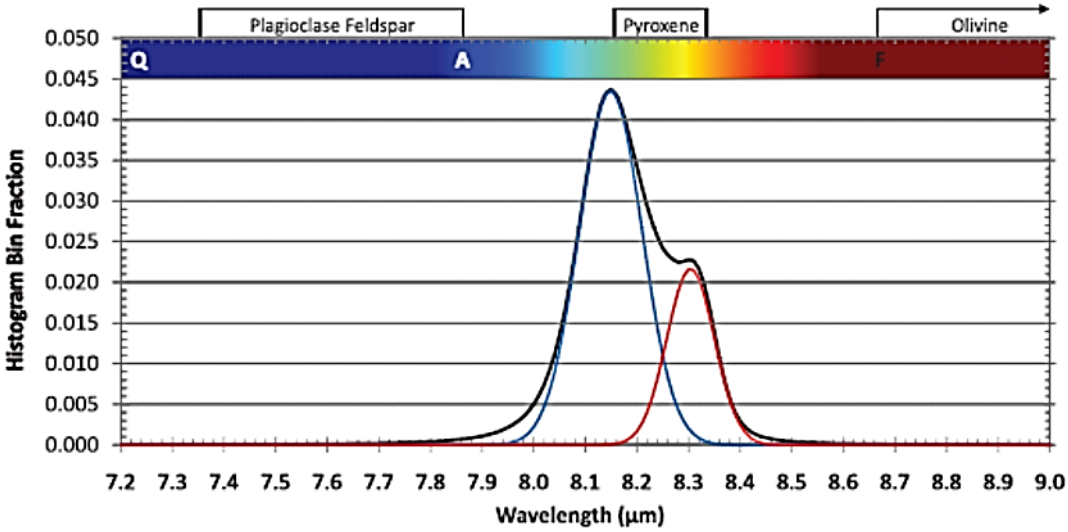

Figure 7-3: Histogram of CF wavelength in relation to the fraction of the lunar surface between ±60° latitude by Greenhagen et al. [2010] (black line). The CFs fit well to two distributions centred on ~8.15 µm (highlands, blue) and ~ 8.3 µm (mare, red). The top boxes refer to the expected CFs based on laboratory measurements made during this project, with the CFs of quartz (Q), anorthite (A) and forsterite (F) shown by their respective initial. Reprinted with permission from AAAS.

7.4.1 Comparing the Spectra of Pure Minerals and Rock Mixtures

7.4.1.1 CF Comparison

Almost all of the CF values measured by Diviner lie within a small wavelength range (Figure 7-3). Much less variation in wavelength is observed than in the laboratory mineral spectra, measured both in this study and previously, with the modal CF values of the highlands and mare appearing to lie close to the CFs of pyroxene minerals. However, the lunar surface CFs match better with previous SLE laboratory measurements of Apollo samples (Figure 2-16), suggesting that, as might be expected, pure minerals are bad lunar analogues, the lunar surface is very mixed, or the lunar CF distribution is affected by the empirical corrections made to the dataset.

7.4.1.2 Spectral Contrast Comparison

A clear difference is also observed between the spectral contrast (between the CF and the emissivity continuum) of the Apollo and terrestrial mineral samples, seen in both heating-from-above and heating-from-below experiments e.g. between the primary mineral suite (Figure 5-14) and the previous Apollo soil (Figure 2-16). The spectral contrasts of minerals in both heating-from-above (Section 2.9.1) and heating-from-below (Section 5.4) experiments agree however, as do the Apollo soil spectral contrasts, suggesting that this is primarily due to the sample type rather than the method of heating. Due to the scarcity of Apollo samples however, terrestrial lunar analogues were measured instead to provide a starting point for analysis of the Diviner data.

7.4.1.3 Explanation of the Observed Differences

Both of these differences between minerals and Apollo soils can be explained in terms of the composition of such samples. Apollo samples are highly-weathered and may have been

altered by space weathering, micrometeorite bombardment, the solar wind etc. many times (Section 1.2.3), consisting of mixtures of many compositional types, containing large size-variation grains and other more unusual constituents such as nano-phase iron and glasses. While all the grains in a narrow grain sized mineral sample will have similar optical depths (from Mie theory, see Millan et al. [2011] for details), the radiative transfer properties of mixtures will vary between the different grains. A mixture of optical depths within a sample would alter the structure of the near-surface thermal gradients sufficiently to change the shape and wavelength of the CF and could reduce the spectral contrast, as was observed. Nano-phase iron and glasses in the Apollo soils could have other radiative properties, affecting the measured spectrum further.

This could also explain why the Apollo CF wavelengths measured when heated from below did not agree with those when heated from above (comparing Figure 2-16 with Figure 5-19). Clearly the Apollo samples did not exhibit the expected CF wavelengths in the former, suggesting that a different thermal gradient was set up within the sample with the different types of heating. Therefore, to alleviate this, the setup which most resembles the actual lunar conditions, i.e. heating from above, must be used. This requires modifications to the existing setup to instead heat such samples using a solar-like source. In future new measurements may need to focus on lunar samples, artificially weathering or mixing the pure minerals; or may require new experiments to improve the empirical corrections, described below.

7.4.1.4 Mixing of Samples

Reflectance spectra of the olivine mixtures revealed that the CF shifts non-linearly with composition between the fayalite and forsterite end-members (Figure 5-5). This suggests that the CF, when measured in SLE emissivity, could also shift non-linearly to variations in mixing ratio, hampering characterisation of possible outcrops of olivine-rich materials.

Future work would need to measure various mixtures, with the aim of developing a mixing ratio equation to describe such CF shifts, using a setup capable of correctly setting up lunar thermal gradients within such mixtures.

7.4.1.5 Space weathering effects

Future work would need to address the variations in CF due to space weathering effects. Comparing weathered Apollo sample spectra to those of pure minerals is difficult, with Apollo and lunar CFs lying in a much narrower range than that of pure minerals (Figure 7-3). The measurements of the andesine chips (Figure 5-17) showed that the weathered and un-weathered spectra of large chips do differ in the MIR, though this is inconclusive in relation to the minerals measured in this project.

7.4.1.6 FIR Emissivity

A FIR measurement of Oligoclase (Section 5.4.7) was attempted; however it is uncertain if this is realistic or not at present. The emissivity of the surface is believed to be relatively flat across these broadband channels; however these have never been measured previously in the laboratory. Further work is required to determine if this result is correct.

7.4.2 New Experimental Setups

7.4.2.1 Heating from Above

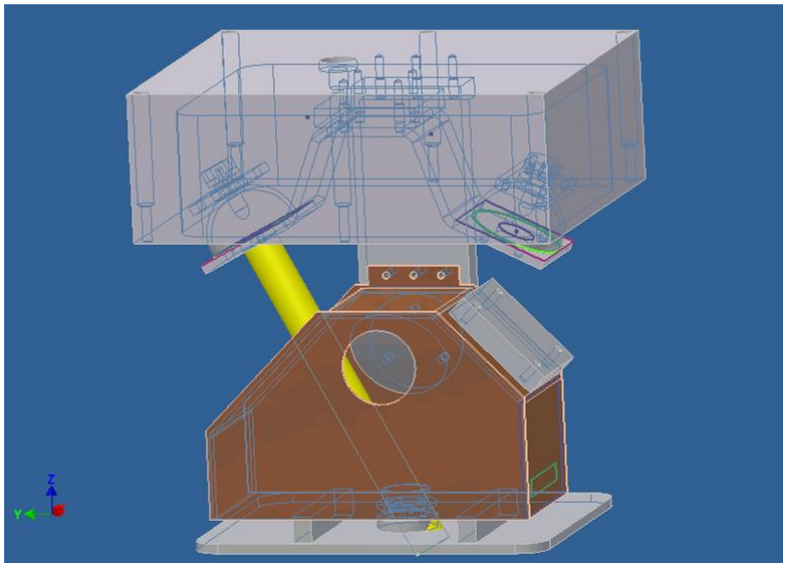

Figure 7-4: CAD drawing of the new solar heating experiment for measuring Apollo samples under lunar conditions, currently in development. A lamp assembly heats the sample through an aperture in the copper radiation shield. The lower part of the outer emission chamber is omitted for clarity.

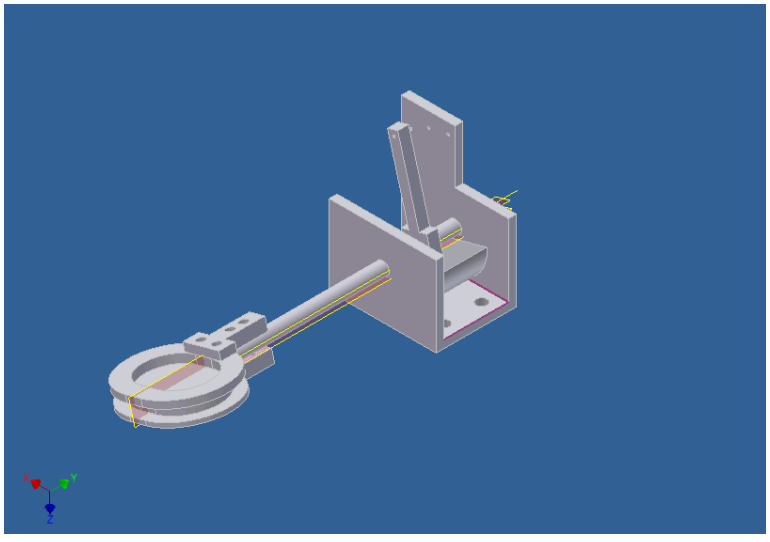

Figure 7-5: CAD drawing of the angled sample cup. The angle can be set at 0°, 15° and 30° using the guide holes in the baseplate attachment. The oval sample cup was made to keep the sample in the spectrometer field of view when rotated up to 30°.

As discussed previously (Section 7.4.1), Apollo soils, mixtures, and other non-pure mineral samples (e.g. those created through artificially weathering) may need to be heated from above using a solar-like source in order to set up the correct thermal gradient within the sample. This would require modifications to the existing setup, which are currently ongoing (Figure 7-4).

Such a setup could also be used to investigate the effects of topography: Logan et al. (1975) studied this briefly, concluding that higher angles changed the spectral contrast between the CF and the emissivity continuum, but

> "no discernible shift occurred in the wavelength of the emissivity maximum".

For this purpose, an angled sample cup (Figure 7-5) has been made with the intention of repeating this experiment using an Apollo sample, to ensure that the difference in composition and thermal properties of lunar and terrestrial samples does not change the result. A goniometer (Section 7.4.2.2) would be needed to investigate this fully.

7.4.2.2 Thermal Infrared Laboratory Goniometry

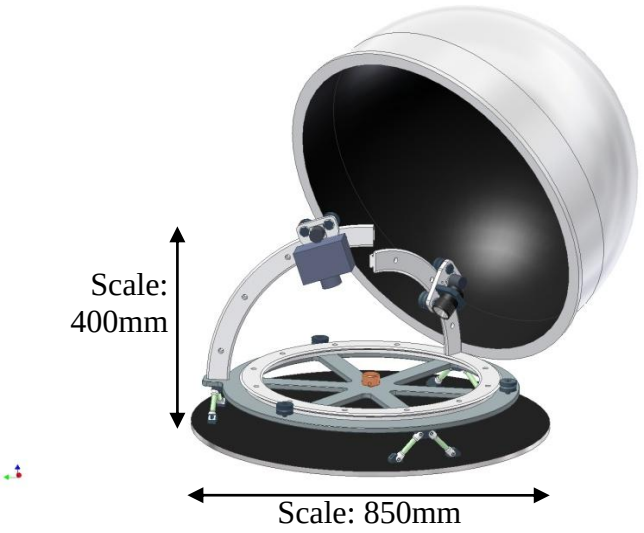

Figure 7-6: CAD design of a TIR lunar goniometer from Bowles [personal communication, 2011]. The sample is placed in the centre and a solar source and radiometer (utilising the spare Diviner filters, for example) are mounted on rotatable arms. The apparatus is placed in a vacuum chamber: the low pressure and cold radiation shield simulate the lunar environment.

To remove the latitude- and time of day- dependent corrections from the data, experiments need to measure how the CF is affected by variations in solar incidence and emission angles. One way to do this is through goniometry [e.g. Johnson and Grundy, 2003], although such experiments would need to be carried out under lunar conditions. This is possible (Figure 7-6) although measurements would take a considerable length of time and therefore such an approach could not be used to measure a full spectral library. Instead, it is envisaged that several Apollo samples would be investigated in this way, and compared to similar measurements made by Diviner. A TIR goniometer is in development, but further studies are required: for example, soil temperatures need to be modelled to investigate if a

FTIR spectrometer can be used (to avoid phase inversion, Section 7.3.1) or if an arm-mounted radiometer would instead be preferable.

7.4.3 Improved CF Mapping

7.4.3.1 Increased Dataset

Depending on the SMD orbit chosen (Section 3.4.4.2), similar data will be acquired over many years. This would allow the entire surface to be mapped closer to lunar midday, reducing the effects of the empirical time of day fit.

7.4.3.2 Pfootprint Algorithm

New tools to improve the analysis of Diviner data are continually being made. The latest, at the time of writing, is the pfootprint command by Jean-Pierre Williams at UCLA. This analysis tool provides better binning of the Diviner data by accounting for the spatial extent of each pixel's field of view (FOV) and the topography at the observation site. The longitudes and latitudes in the dataset denote the coordinates of the centre of the FOV, therefore when binned at high spatial resolution some bins are unpopulated even though they are within the FOV of a detector. Furthermore, the extent of each FOV is also affected by surface slopes, especially for detectors 1 and 21 which point furthest from nadir in a pushbroom mapping instrument like Diviner. The pfootprint tool combines Diviner and LOLA data to calculate a number of points within the each pixel's FOV and populates all the bins within this view, improving temperature [Williams, personal communication 2011] and CF maps [Glotch, personal communication 2011]. Further tools will be developed in the future.

At the time of writing (late 2011), the instrument and the spacecraft continue to perform nominally. LRO orbit transition successfully occurred on the 11th December 2011: the spacecraft is now in its initial elliptical commissioning phase orbit, where it will have sufficient fuel to remain for many years. The ground teams continue to process and archive data efficiently, while the Diviner team are continuing to develop new data analysis techniques and devise new observations e.g. lunar surface measurements away from nadir, observations during lunar eclipses etc.

8 References

Adlen, S. (2004), Remote sounding of the Martian atmosphere with Mars Climate Sounder, AOPP D.Phil thesis, University of Oxford.

Amos, J. (2009), "BBC News - 'Coldest place' found on the Moon", Retrieved from: http://news.bbc.co.uk/1/hi/8416749.stm.

Angelo, J. (2006), Encyclopedia of Space and Astronomy, 753. Infobase Publishing.

Araki, H., S. Tazawa, H. Noda, Y. Ishihara, S. Goossens, S. Sasaki, N. Kawano, I. Kamiya, H. Otake, J. Oberst, and C. Shum (2009), Lunar Global Shape and Polar Topography Derived from Kaguya-LALT Laser Altimetry, Science, 323, doi:10.1126/science.1164146.

Arnold, J. R., (1979), Ice in the Lunar Polar Regions, J. Geophys. Res., 84, pp.5659-5668.

Baldridge, A. M. and Christensen, P. R., (2009), A Laboratory Technique for Thermal Emission Measurement of Hydrated Minerals, Applied Spectroscopy, 63, pp. 678-687.

Baldridge, A. M., S.J. Hook, C.I. Grove and G. Rivera, (2009), The ASTER Spectral Library Version 2.0. Remote Sensing of Environment, 113, pp. 711-715.

Bandfield, J., (2010), Rock abundance and landing sites, personal communication. Email correspondence.

Bandfield, J. L., R. R. Ghent, A. R. Vasavada, and D. A. Paige, (2010), Mapping Lunar Surface Rock Abundance and Regolith Thermophysical Properties Using LRO Diviner Data, Lunar and Planetary Institute Science Conference Abstracts, 41.

Bansal, B. M., S. E. Church, P. W. Gast, N. J. Hubbard, J. M. Rhodes, and H. Wiesmann, (1972), The chemical composition of soil from the Apollo 16 and Luna 20 sites, Earth and Planetary Science Letters, 17, doi:10.1016/0012-821X(72)90256-7.

Benz, W., Slattery, W. L. and Cameron, A. G. W., (1986), The origin of the moon and the single-impact hypothesis I, Icarus, 66 (3), pp. 515-535.

Birkebak, R. C., C. J. Cremers, and J. P. Dawson, (1970), Thermal Radiation Properties and Thermal Conductivity of Lunar Material, Science, 167, 724-726, doi:10.1126/science.167.3918.724.

Blewett, D. T., P. G. Lucey, B. R. Hawke, and B. L. Jolliff, (1997), Clementine images of the lunar sample-return stations: Refinement of FeO and TiO2 mapping techniques, Journal of Geophysical Research, 102, 16319-16326, doi:10.1029/97JE01505.

Bowles, N. E., (2007), personal communication: "Bowles, N. E., A. Camilletti, & Gordon, (2005), LRO team meeting presentation, personal communication". Email correspondence.

Bradley, J. P., H. J. Humecki, and M. S. Germani, (1992), Combined infrared and analytical electron microscope studies of interplanetary dust particles, The Astrophysical Journal, 394, 643-651, doi:10.1086/171618.

Bruno, B. C., P. G. Lucey, and B. R. Hawke, (1991), High-resolution UV-visible spectroscopy of lunar red spots, Lunar and Planetary Science Conference Proceedings, 21, 405-415.

Burke, J. D., (2011), "Moon". In Encyclopædia Britannica. Retrieved from http://www.britannica.com/EBchecked/topic/391266/Moon.

Bush, G. W., (2004), "President Bush Announces New Vision for Space Exploration Program". Retrieved from: http://history.nasa.gov/Bush%20SEP.htm, 2011.

Bussey, D. B. J., P. D. Spudis, and M. S. Robinson, (1999), Illumination conditions at the lunar south pole, Geophysical Research Letters, 26, 1187-1190, doi:10.1029/1999GL900213.

Calcutt, S. B., (2007), DLRE end item data product, personal communication. Email correspondence.

Calcutt, S. B., (2008a), personal communication.

Calcutt, S. B., (2008b), personal communication: “Clarke, F. J., (1997), NPL Certificate of Calibration”. Email correspondence.

Calcutt, S. B., (2008c), personal communication: “Adlen, S., (unknown year), PMIRR Calibration Analysis Report".

Campbell, B. A. et al., (2003), Radar Imaging of the Lunar Poles, Nature, 426, pp. 137-138.

Carrier, W. D., III, (1973), Lunar Soil Grain Size Distribution, Moon, 6, 250-263, doi:10.1007/BF00562206.

Chin, G. et al., (2007), Lunar Reconnaissance Orbiter Overview: The Instrument Suite and Mission, Space Sci. Rev., 129, pp.391–419.

Christensen, P. R. and S. T. Harrison, (1993), Thermal infrared emission spectroscopy of natural surfaces: Application to desert varnish coatings on rocks, Journal of Geophysical Research, 98, 19819-19834, doi:10.1029/93JB00135.

Christensen, P. R., and 25 colleagues, (2001), Mars Global Surveyor Thermal Emission Spectrometer experiment: Investigation description and surface science results, Journal of Geophysical Research, 106, 23823-23872, doi:10.1029/2000JE001370.

Christensen, P. R., J. L. Bandfield, V. E. Hamilton, D. A. Howard, M. D. Lane, J. L. Piatek, S. W. Ruff, and W. L. Stefanov, (2000), A thermal emission spectral library of rock-forming minerals, Journal of Geophysical Research, 105, 9735-9740, doi:10.1029/1998JE000624.

Christiansen, C., (1884), Untersuchungen über die optischen Eigenschaften von fein vertheilten Körpern - Erste Mittheilung, Ann. Phys., 23, pp. 298-306.

Clark, R. N., (2009), Detection of Adsorbed Water and Hydroxyl on the Moon, Science, 326, 562-doi:10.1126/science.1178105.

Clarke, F. J. J. and J. A. Larkin, (1985), Measurement of total reflectance, transmittance and emissivity over the thermal IR spectrum, Infrared Physics , 25, 359-367, doi:10.1016/0020-0891(85)90108-3.

Colaprete, A., P. Schultz, J. Heldmann, D. Wooden, M. Shirley, K. Ennico, B. Hermalyn, W. Marshall, A. Ricco, R. C. Elphic, D. Goldstein, D. Summy, G. D. Bart, E. Asphaug, D. Korycansky, D. Landis, and L. Sollitt, (2010), Detection of Water in the LCROSS Ejecta Plume, Science, 330, 463-doi:10.1126/science.1186986.

Compton, W. D., (1989), Where no Man has Gone Before; a History of Apollo Lunar Exploration Missions, NASA Special Publication, 494.

Cooper, B. L. et al, (2002), Midinfrared Spectral Features of Rocks and Their Powders. J. Geophys. Res., 107, pp. 1-16.

Crawford, I., (2010), personal communication. Email correspondence.

Diviner website, (unknown year), "LRO Diviner Lunar Radiometer: Data Product Descriptions", Retrieved from: http://diviner.ucla.edu/data_products.shtml

Donaldson Hanna, K. L., M. B. Wyatt, I. R. Thomas, N. E. Bowles, B. T. Greenhagen, A. Maturilli, J. Helbert, and D. A. Paige, (2011), Thermal infrared emissivity measurements under a simulated lunar environment: Application to the Diviner Lunar Radiometer Experiment, J. Geophys. Res., doi:10.1029/2011JE003862, in press.

Donaldson Hanna, K. L., M. B. Wyatt, J. Helbert, A. Maturilli, and C. M. Pieters, (2009), Constraining Lunar Surface Mineralogy with Combined Thermal- and Near-Infrared Spectral Data, Lunar and Planetary Institute Science Conference Abstracts, 40, 2286.

Eckert, J. O., Jr., L. A. Taylor, and C. R. Neal, (1991), Spinel Troctolite from Apollo 17 Breccia 73215: Evidence for Petrogenesis as Deep-seated Lunar Crust, Lunar and Planetary Institute Science Conference XXII Abstracts.

Eichelman, W. F., & W. W. Lauderdale, (1974), Apollo scientific experiments data handbook. NASA Technical Memorandum.

Elphic, R. C., (1998), Lunar Fe and Ti Abundances: Comparison of Lunar Prospector and Clementine Data. Science, 281(5382), 1493-1496. doi:10.1126/science.281.5382.1493.

Elphic, R. C., D. J. Lawrence, W. C. Feldman, B. L. Barraclough, S. Maurice, A. B. Binder, and P. G. Lucey, (2000), Lunar rare earth element distribution and ramifications for FeO and TiO2: Lunar Prospector neutron spectrometer observations, Journal of Geophysical Research, 105, 20333-20346, doi:10.1029/1999JE001176.

Epstein, S. and H. P. Taylor Jr., (1973), The isotopic composition and concentration of water, hydrogen, and carbon in some Apollo 15 and 16 soils and in the Apollo 17 orange soil, Lunar and Planetary Science Conference Proceedings, 4, 1559.

Farmer, V. C., (ed.), (1974), The Infrared Spectra of Minerals. Mineralogical Society of Great Britain & Ireland. Surrey: Adlard & Son Ltd.

Feldman, W. C., S. Maurice, A. B. Binder, B. L. Barraclough, R. C. Elphic, and D. J. Lawrence, (1998a), Fluxes of Fast and Epithermal Neutrons from Lunar Prospector: Evidence for Water Ice at the Lunar Poles, Science, 281, 1496-doi:10.1126/science.281.5382.1496.

Feldman, W. C., B. L. Barraclough, S. Maurice, R. C. Elphic, D. J. Lawrence, D. R. Thomsen, and A. B. Binder, (1998b), Major Compositional Units of the Moon: Lunar Prospector Thermal and Fast Neutrons, Science, 281, 1489-doi:10.1126/science.281.5382.1489.

Foing, B. H. et al., (2006), SMART-1 mission to the Moon: Status, first results and goals, Advances in Space Research, 37 (1), pp. 6-13.

Foote, M. C., (2008a), "DLRE Radiometric Test Report JPL D-42958". unpublished draft. Email correspondence.

Foote, M. C., (2008b), DLRE filter responses, personal communication. Email correspondence.

Foote, M. C., E. W. Jones, and T. Caillat, (1998), Uncooled thermopile infrared detector linear arrays with detectivity greater than 10^9 cmHz^1/2/W, IEEE Transactions on Electron Devices, 45, 1896-1902, doi:10.1109/16.711353.

Gaidos, E. et al, (20060, Terrestrial Exoplanet Light Curves, Proc. International Astronomical Union Colloquium 200, pp. 153-158.

Glotch, T. D., (2011), "pfootprint comparison", personal communication. Email correspondence.

Glotch, T. D. and G. R. Rossman, (2009), Mid-infrared reflectance spectra and optical constants of six iron oxide/oxyhydroxide phases, Icarus, 204, 663-671, doi:10.1016/j.icarus.2009.07.024.

Glotch, T. D. et al, (20070, Mid-infrared (5-100 μm) Reflectance Spectra and Optical Constants of Phyllosilicate Minerals, Icarus, 192, pp. 605-622.

Glotch, T. D., Lucey, P. G., Bandfield, J. L., Greenhagen, B. T., Thomas, I. R., Elphic, R. C., Bowles, N., et al., (2010), Highly silicic compositions on the Moon, Science, 329(5998), 1510-1513.

Goets, A. F. H., (1968), Differential Infrared Lunar Emission Spectroscopy, Journal of Geophysical Research, 73, 1455-doi:10.1029/JB073i004p01455.

Greenhagen, B. T. & Paige, D. A., (2006), Mapping Lunar Surface Petrology Using the Mid-Infrared Emissivity Maximum with the LRO Diviner Radiometer, 37th Annual Lunar and Planetary Science Conference, no. 2406.

Greenhagen, B. T. & Paige, D. A., (2009), Overview of the 2009 LRO Diviner Lunar Radiometer Compositional Investigation, Lunar and Planetary Institute Science Conference Abstracts Vol. 40, pp. 2255-2256.

Greenhagen, B. T., (2009), Thermal Emission Remote Sensing Of The Moon: Design And Development Of Diviner, Ph.D. Thesis, UCLA.

Greenhagen, B. T., Lucey, P. G., Wyatt, M. B., Glotch, T. D., Allen, C. C., Arnold, J. A., Bandfield, J. L., et al., (2010), Global silicate mineralogy of the Moon from the Diviner lunar radiometer, Science, 329(5998), 1507-1509.

Grieger, B. et al., (2008), Investigating a peak of (almost) eternal light close to the lunar south pole with SMART-1/AMIE Images, EPSC Abstract, 3, EPSC2008-A-00205

Gupta, A. K., (1998), Igneous Rocks, Allied Publishers.

Hand, E., (2010), "Nature News Blog: Hot rocks help scientists map Moon’s terrain", Retrieved from: http://blogs.nature.com/news/2010/07/hot_rocks_help_scientists_map.html.

Hanel, R. A. et al., (2003), Exploration of the Solar System by Infrared Remote Sensing, Cambridge: Cambridge University Press.

Hapke, B., (1981), Bidirectional reflectance spectroscopy I - Theory, Journal of Geophysical Research, 86, 3039-3054, doi:10.1029/JB086iB04p03039.

Hapke, B., (1996), A model of radiative and conductive energy transfer in planetary regoliths, J. Geophys. Res., 101, pp. 16817-16831.

Hartmann, W. K., (1968), Lunar Crater Counts VI: The Young Craters Tycho, Aristarchus, and Copernicus, Communications of the Lunar and Planetary Laboratory, 7, 145-156.

Hartmann, W. K. and D. R. Davis, (1975), Satellite-sized planetesimals and lunar origin, Icarus, 24, 504-514, doi:10.1016/0019-1035(75)90070-6.

Haruyama, J. et al, (2008), Lack of Exposed Ice Inside Lunar South Pole Shackleton Crater, Science, 322, pp. 938-939.

Heiken, G. H., Vaniman, D. T., & French, B. M., (1991), Lunar sourcebook - A user's guide to the moon, 753, Cambridge University Press.

Henderson, B. G. & Jakosky, B. M., (1994), Near-surface thermal gradients and their effects on mid-infrared emission spectra of planetary surfaces, Journal of Geophysical Research, 99, pp. 19063.

Henderson, B. G. & Jakosky, B. M., (1997), Near-surface thermal gradients and mid-IR emission spectra: A new model including scattering and application to real data, Journal of Geophysical Research, 102, pp. 6567-6580.

Henderson, B. G., et al., (1996), New laboratory measurements of mid-IR emission spectra of

simulated planetary surfaces, Journal of Geophysical Research, 101, pp. 14969-14975.

Hunt, J. M., M. P. Wisherd, & L. C. Bonham, (1950), Infrared Absorption Spectra of Minerals and Other Inorganic Compounds, Anal. Chem., 22 (12), 1478–1497, DOI:10.1021/ac60048a006.

Irwin, P. G., (1991), Remote sounding of the Martian atmosphere, AOPP D.Phil thesis, University of Oxford.

Isbell, D., D. Morse, and B. Rische, (1999), Moon Water Still a Mystery". Science@NASA. http://science.nasa.gov/newhome/headlines/ast13oct99_1.htm.

Jakosky, B. M., (1986), On the thermal properties of Martian fines, Icarus, 66, 117-124, doi:10.1016/0019-1035(86)90011-4.

Johnson, J. R. and W. M. Grundy, (2003), Two-Layer Visible/Near-Infrared Radiative Transfer Modeling Using Bloomsburg University Goniometer (BUG) Observations of Dust-coated Rocks, Sixth International Conference on Mars, 3150.

Johnson, J.R., (2010), Thermal infrared spectral analyses of experimentally shocked minerals and rocks under lunar conditions and at microscopic scales, Planetary Geology and Geophysics Program 2010 Proposal.

Johnson, N. L., (1979), Handbook of Soviet lunar and planetary exploration, American Astronautical Society, Univelt Inc. San Diego.

Jolliff, B. L. et al., (eds.), (2006), New Views of the Moon, Mineralogical Society of America: Reviews in Mineralogy & Geochemistry, 60.

Kerr, R. A., (ed.), (2009), A Primal Crust Found on the Moon, While Mercury’s Proves Elusive, Science Magazine, 324, pp. 161.

Laul, J. C., D. W. Hill, and R. A. Schmitt, (1974), Chemical studies of Apollo 16 and 17 samples, Lunar and Planetary Science Conference Proceedings, 5, 1047-1066.

Lawrence, D. J., (1998), Global Elemental Maps of the Moon: The Lunar Prospector Gamma-Ray Spectrometer, Science, 281, pp1484-1489.

Logan, L. & Hunt, G. R., (1970), Emission spectra of particulate silicates under simulated lunar conditions, Journal of Geophysical Research, 75, pp. 6539-6548.

Logan, L. M., G. R. Hunt, S. R. Balsamo, and J. W. Salisbury, (1972), Mid-infrared emission spectra of Apollo 14 and 15 soils and remote compositional mapping of the moon, Lunar and Planetary Science Conference Proceedings, 3, 3069.

Logan, L M., et al., (1973) Compositional Implications of Christiansen Frequency Maximums for Infrared Remote Sensing Applications, Journal of Geophysical Research, 78, pp. 4983-5003.

Logan, L. M., G.R. Hunt and J.W. Salisbury, (1975), The use of mid-infrared spectroscopy in remote sensing of space target. In: C. Karr, Jr., (ed.), Infrared and Raman Spectroscopy of Lunar and Terrestrial Minerals, Academic Press, New York, pp. 117–142.

Lolachi, R., (2010), MCS filter responses, personal communication. Email correspondence.

Lolachi, R., (2011), personal communication.

Lucey, P., (2010), Planetary science: Mantle of the Moon exposed?, Nature Geoscience, 3, 517-518, doi:10.1038/ngeo904.

Lucey, P. G., (1991), Comparison of thermal emission spectroscopic measurements of the lunar surface - 1968-1990, Lunar and Planetary Science Conference Proceedings, 21, 417-423.

Lucey, P. G., B. R. Hawke, and B. C. Bruno, (1989), Thermal Infrared Spectroscopy of the Moon, Bulletin of the American Astronomical Society 21.

Lucey, P. G., D. T. Blewett, and B. L. Jolliff, (2000), Lunar iron and titanium abundance algorithms based on final processing of Clementine ultraviolet-visible images, Journal of Geophysical Research, 105, 20297-20306, doi:10.1029/1999JE001117.

Lucey, P. G., D. T. Blewett, and B. R. Hawke, (1998), Mapping the FeO and TiO2 content of the lunar surface with multispectral imagery, Journal of Geophysical Research, 103, 3679-doi:10.1029/97JE03019.

Lundeen, S., (2008), Moon Mineralogy Mapper Data Product Software Interface Specification, Retrieved from: http://img.pds.nasa.gov/documentation/M3_DPSIS.PDF.

Lyon, R. J. P. (1964), Analysis of rocks by spectral infrared emission (8 to 25 Microns), Econ. Geol., vol. 60, p. 717-736 (1964)., 60, 717-736.

Maturilli, A., Helbert, J., Witzke, A., & Moroz, L., (2006), Emissivity measurements of analogue materials for the interpretation of data from PFS on Mars Express and MERTIS on Bepi-Colombo, Planetary and Space Science, 54(11), 1057-1064.

Maxwell, J. A. and H. B. Wiik, (1971), Chemical composition of Apollo 12 lunar samples 12004, 12033, 12051, 12052 and 12065, Earth and Planetary Science Letters, 10, 285-doi:10.1016/0012-821X(71)90032-X.

McCleese, D. J. et al, (2007), Mars Climate Sounder: An investigation of thermal and water vapour structure, dust and condensate distributions in the atmosphere, and energy balance of the polar regions, J. Geophys. Res., 112, E05S06.

McEwen, A. S., (1996), A Precise Lunar Photometric Function, Lunar and Planetary Institute

Science Conference Abstracts, 27, 841.

McEwen, A., E. Eliason, P. Lucey, E. Malaret, C. Pieters, M. Robinson, and T. Sucharski, (1998), Summary of Radiometric Calibration and Photometric Normalization Steps for the Clementine UVVIS Images, Lunar and Planetary Institute Science Conference Abstracts, 29, 1466.

McKay, D. S., G. H. Heiken, R. M. Taylor, U. S. Clanton, D. A. Morrison, and G. H. Ladle, (1972), Apollo 14 soils: Size distribution and particle types, Lunar and Planetary Science Conference Proceedings, 3, 983.

McKay, D. S., Heiken, G. H., Basu, A., Blanford, G., Simon, S., Reedy, R., French, B. M., et al., (1991), The lunar regolith. Annual Review of Earth and Planetary Sciences, 5, p. 285–356, Cambridge University Press.

McKay, D. S., J. L. Carter, W. W. Boles, C. C. Allen, and J. H. Allton, (1993), JSC-1: A new lunar regolith simulant, Lunar and Planetary Institute Science Conference Abstracts, 24, 963-964.

Mendell, W. W., (1976), Ph.D. Thesis. Rice University, Houston, TX.

Mendell, W. W. & Wieczorek, M. A., (1993), Thermogeologic Mapping of the Moon from Lunar Orbit, Lunar and Planetary Inst., 24th Lunar and Planetary Science Conference. Part 2: G-M pp. 977-978.

Meyer, C., (2010), "62231.pdf", NASA Lunar Sample Compendium, Retrieved from: http://curator.jsc.nasa.gov/lunar/lsc/62231.pdf.

Mignard, F., (1979), The evolution of the lunar orbit revisited. I, Moon and Planets, 20, pp. 301-315.

Murcray, F. H., et al., (1970), Infrared emissivity of lunar surface features. 1. Balloon-borne observations, Journal of Geophysical Research, 75, pp. 2662-2669.

Narendranath,S. , P.S. Athiray, P. Sreekumar, B.J. Kellett, L. Alha, C.J. Howe, K.H. Joy, M. Grande, J. Huovelin, I.A. Crawford, U. Unnikrishnan, S. Lalita, S. Subramaniam, S.Z. Weider, L.R. Nittler, O. Gasnault, D. Rothery, V.A. Fernandes, N. Bhandari, J.N. Goswami, M.A. Wieczorek and the C1XS team, (2011), Lunar X-ray fluorescence observations by the Chandrayaan-1 X-ray Spectrometer (C1XS): Results from the nearside southern highlands, Icarus, 214, pp. 53-66, doi:10.1016/j.icarus.2011.04.010.

Nash, D. B., J. W. Salisbury, J. E. Conel, P. G. Lucey, and P. R. Christensen, (1993), Evaluation of infrared emission spectroscopy for mapping the Moon's surface composition from lunar orbit, Journal of Geophysical Research, 98, 23535-doi:10.1029/93JE02604.

Neugebauer, M., C.W. Snyder, D.R. Clay, B.E. Goldstein, (1972), Solar wind observations on the lunar surface with the Apollo-12 ALSEP, Planetary and Space Science, 20 (10), p1577-1591, doi: 10.1016/0032-0633(72)90184-5.

Neumann, G. A., M. T. Zuber, D. E. Smith, and F. G. Lemoine, (1996), The lunar crust: Global structure and signature of major basins, Journal of Geophysical Research, 101, 16841-16864, doi:10.1029/96JE01246.

Nightingale, T. J., (1992), Investigation of the radiometric performance of the Improved Stratospheric and Mesospheric Sounder, AOPP D.Phil thesis, University of Oxford.

Nozette, S., and 34 colleagues, (1994), The Clementine Mission to the Moon: Scientific Overview, Science, 266, 1835-1839, doi:10.1126/science.266.5192.1835.

Nozette, S. et al., (1996), The Clementine Bistatic Radar Experiment, Science, 274, pp. 1495-1498.

Ohtake, M., and 31 colleagues, (2009), The global distribution of pure anorthosite on the Moon, Nature, 461, 236-240, doi:10.1038/nature08317.

Paige, D. A., et al., (2004), "Diviner LRO Proposal AO NNH04ZSS003O; Measurement Investigation and Implementation", Initial DLRE mission proposal.

Paige, D. A., et al., (2009), The Lunar Reconnaissance Orbiter Diviner Lunar Radiometer Experiment, Space Science Reviews, pp. 66.

Paige, D. A., (2010), personal communication. Email correspondence.

Paige, D. A., and 26 colleagues, (2010), Diviner Lunar Radiometer Observations of Cold Traps in the Moon's South Polar Region, Science, 330, 479-doi:10.1126/science.1187726.

Perkin Elmer Ltd., (1987), Fixed Angle Specular Reflectance Accessory Instructions, Perkin Elmer Instruments Ltd.

Pieters, C. M., (1983), Strength of mineral absorption features in the transmitted component of near-infrared reflected light - First results from RELAB, Journal of Geophysical Research, 88, 9534-9544, doi:10.1029/JB088iB11p09534.

Pieters, C. M., (1999), The Moon as a Spectral Calibration Standard Enabled by Lunar Samples: The Clementine Example, Workshop on New Views of the Moon II: Understanding the Moon Through the Integration of Diverse Datasets, 8025.

Pieters, C. M., et al., (1993), Optical effects of space weathering on lunar soils and the role of the finest fraction, Lunar and Planetary Institute Science Conference Abstracts, 24, pp. 1143-1144.

Pieters, C. M., and 28 colleagues, (2009), Character and Spatial Distribution of OH/H2O on

the Surface of the Moon Seen by M3 on Chandrayaan-1, Science, 326, 568- doi:10.1126/science.1178658.

Pieters, C. M., and 26 colleagues, (2011), Mg-spinel lithology: A new rock type on the lunar farside, Journal of Geophysical Research (Planets), 116, doi:10.1029/2010JE003727.

Potter, A. E. and T. H. Morgan, (1981), Observations of Silicate Reststrahlen Bands in Lunar Infrared Spectra, Lunar and Planetary Institute Science Conference Abstracts, 12, 854-856.

Praezisions Glas & Optik GmbH., (unknown year), "PYREX Technical Borosilicate glass" Retrieved from: http://www.pgo-online.com/intl/katalog/pyrex.html, 2011.

Presley, M. A. & Christensen, P. R., (1997), Thermal Conductivity Measurements of Particulate Materials 2. Results, J. Geophys. Res., 102, pp. 6551-6566.

Ruff, S. W., P. R. Christensen, P. W. Barbera, and D. L. Anderson, (1997), Quantitative thermal emission spectroscopy of minerals: A laboratory technique for measurement and calibration, Journal of Geophysical Research, 102, 14899-14913, doi:10.1029/97JB00593.

Salisbury, J. W., G. R. Hunt, and L. M. Logan, (1973), Infrared spectra of Apollo 16 fines, Lunar and Planetary Science Conference Proceedings, 4, 3191.

Salisbury, J. W. and L. S. Walter, (1989), Thermal Infrared (2.5-13.5 um) Spectroscopic Remote Sensing of Igneous Rock Types on Particulate Planetary Surfaces, Journal of Geophysical Research, 94, 9192-9202, doi:10.1029/JB094iB07p09192.

Salisbury, J. W., A. Wald, and D. M. D'Aria, (1994), Thermal-infrared remote sensing and Kirchhoff's law 1. Laboratory measurements, Journal of Geophysical Research, 99, 11897-11911, doi:10.1029/93JB03600.

Salisbury J. W. et al, (1997), Thermal Infrared Spectra of Lunar Soils, Icarus, 130 (1), pp. 125-

139.

Sanderson, K., (2007), “The sunniest spot on the Moon”. Nature News. Retrieved from: http://www.nature.com/news/2007/071023/full/news.2007.182.html.

Schofield, J. T., (2008), personal communication. Email correspondence.

Shopland, M., and S. Wolpert, (2010), "Lunar 'permafrost': Evidence for widespread water ice on the moon". Science Daily. Retrieved from: http://www.sciencedaily.com-/releases/2010/10/101022022904.htm.

Simon, S. B. and J. J. Papike, (1981), The Lunar Regolith: Comparative Petrology of the Apollo and Luna Soils, Lunar and Planetary Institute Science Conference Abstracts, 12, 984-986.

Sinclair, P., (2000), Long path Fourier transform absorption spectroscopy for investigating pollution in the urban boundary layer, AOPP D.Phil thesis, University of Oxford.

Solomon, S. C. and J. Longhi, (1977), Magma Oceanography: 1. Thermal Evolution, Lunar and Planetary Institute Science Conference Abstracts, 8, 884.

Specac Ltd., (2011), Email correspondence.

Spencer, J. R. et al., (1989), Systematic Biases in Radiometric Diameter Determinations, Icarus, 78, pp. 337-354.

Spencer, J. R., (1990), A Rough-Surface Thermophysical Model for Airless Planets, Icarus, 83, pp. 27-38.

Sprague, A. L., F. C. Witteborn, R. W. Kozlowski, D. P. Cruikshank, M. J. Bartholomew, and A. L. Graps, (1992), The moon - mid-infrared (7.5- to 11.4-microns) spectroscopy of selected

regions, Icarus, 100, pp. 73-84, doi:10.1016/0019-1035(92)90019-4.

Spudis, P. D. and D. B. J. Bussey, (1997), “Clementine Explores the Moon: Second Edition" Retrieved from: http://www.lpi.usra.edu/publications/slidesets/clem2nd.

Spudis, P. D., (2001), What is the Moon made of?, Science, 293(5536), 1779-1781.

Staid, M. I. and C. M. Pieters, (1996), Craters as Indicators of Compositional Stratigraphy in Mare Tranquillitatis and Serenitatis, Lunar and Planetary Institute Science Conference Abstracts, 27, 1259.

Stevenson, D. J., (1987), Origin of the moon - The collision hypothesis, Annual Review of Earth and Planetary Sciences, 15, 271-315, doi:10.1146/annurev.ea.15.050187.001415.

Sunshine, J. M., T. L. Farnham, L. M. Feaga, O. Groussin, F. Merlin, R. E. Milliken, and M. F. A'Hearn, (2009), Temporal and Spatial Variability of Lunar Hydration As Observed by the Deep Impact Spacecraft, Science, 326, doi:10.1126/science.1179788.

Swinyard, B. M., K. H. Joy, B. J. Kellett, I. A. Crawford, M. Grande, C. J. Howe, V. A. Fernandes, O. Gasnault, D. J. Lawrence, S. S. Russell, M. A. Wieczorek, B. H. Foing, and The SMART-1 team, (2009), X-ray fluorescence observations of the moon by SMART-1/D-CIXS and the first detection of Ti K_alpha; from the lunar surface, Planetary and Space Science, 57, 744-750, doi:10.1016/j.pss.2009.01.009.

Taylor, F.W., (2005), Elementary climate physics, OUP, Oxford, UK.

Thomson, J. L. and J. W. Salisbury, (1993), The mid-infrared reflectance of mineral mixtures (7-14 microns), Remote Sensing of Environment, 45, 1-13.

Todd, N. S., (2011), “Top 10 Scientific Discoveries from Apollo”, Retrieved from http://curator.jsc.nasa.gov/lunar/lunar10.cfm.

Tompkins, S. & Pieters, C. M., (1999), Mineralogy of the Lunar Crust: Results from Clementine, Meteoritics & Planetary Science, 34 (1), pp. 25-41.

Tooley, C. R., M. B. Houghton, R. S. Saylor, C. Peddie, D. F. Everett, C. L. Baker, and K. N. Safdie, (2010), Lunar Reconnaissance Orbiter Mission and Spacecraft Design, Space Science Reviews, 150, 23-62, doi:10.1007/s11214-009-9624-4.

Turner, P., (2008), Brüker Coventry personal communication. Email correspondence.

Urquhart, M. L. and B. M. Jakosky, (1995), Can We Use Remote Thermal Emission Observations to Derive Lunar Surface Properties?, Lunar and Planetary Institute Science Conference Abstracts, 26, 1433.

Urquhart, M. L. & Mellon, M. T., (2007), A New Model for Determining Lunar Rock Abundance and Landing Hazards, 38th Lunar and Planetary Science Conference, pp. 2171.

Vasavada, A. R. et al., (1999), Near-Surface Temperatures on Mercury and the Moon and the Stability of Polar Ice Deposits, Icarus, 141, pp. 179-193.

Viatour, L., (2006), "Full Moon view from Earth in Belgium (Hamois)", Retrieved from: http://www.lucnix.be/v/Astronomy/Pleine+Lune+Luc+Viatour.jpg.html

Vondrak, R., J. Keller, G. Chin, and J. Garvin, (2010), Lunar Reconnaissance Orbiter (LRO): Observations for Lunar Exploration and Science, Space Science Reviews, 150, 7-22, doi:10.1007/s11214-010-9631-5.

Ward, W. R., (1975), Past Orientation of the Lunar Spin Axis, Science, 189, pp. 377-379.

Warren, P. H., (1985), The magma ocean concept and lunar evolution, Annual Review of Earth and Planetary Sciences, 13, 201-240, doi:10.1146/annurev.ea.13.050185.001221.

Watson, K. et al., (1961), The Behaviour of Volatiles on the Lunar Surface, J. Geophys. Res. Vol. 66, pp. 3033-3045.

Wechsler, A. E. and P. E. Glaser, (1965), Pressure Effects on Postulated Lunar Materials, Icarus, 4, 335-doi:10.1016/0019-1035(65)90038-2.

Wicander, R., J. S. Monroe and E. K. Peters, (2005), Essentials of geology, Thomson Brooks/Cole.

Wilhelms, D. E., (1993), To a rocky moon - A geologist's history of lunar exploration, University of Arizona Press.

Williams, D. R., (2011), "Lunar Exploration Timeline". Retrieved from http://nssdc.gsfc.nasa.gov/planetary/lunar/lunartimeline.html.

Williams, J. P., (2011), "pfootprint: A New Pipes Tool in Development for Creating Gridded Data Products", personal communication.

Willman, B. M. et al., (1995), Properties of Lunar Soil Simulant JSC-1, Journal of Aerospace Engineering, 8 (2), pp. 77-87.

Wood, J. A., J. S. Dickey Jr., U. B. Marvin, and B. N. Powell, (1970), Lunar Anorthosites, Science, 167, 602-604, doi:10.1126/science.167.3918.602.

Yamamoto, S., R. Nakamura, T. Matsunaga, Y. Ogawa, Y. Ishihara, T. Morota, N. Hirata, M. Ohtake, T. Hiroi, Y. Yokota, and J. Haruyama, (2010), Possible mantle origin of olivine around lunar impact basins detected by SELENE, Nature Geoscience, 3, 533-536, doi:10.1038/ngeo897.